MECHANICAL AND ACOUSTIC PROPERTIES OF POROUS STEEL MANUFACTURED BY LOST CARBONATE SINTERING

Thesis submitted in accordance with the requirement of the
University of Liverpool for the Doctor degree of Philosophy

by

Miao LU

October 2011

ABSTRACT

Over the last few decades, porous metals have received a large amount of interest in industry due to the rapid advancement in manufacturing techniques, design and possible applications. Their unique properties and multi-functionality allow them to be utilized in many different applications throughout different industrial sectors.

This thesis manufactured porous steel using the Lost Carbonate Sintering (LCS) method and studied their mechanical and sound absorption properties. The dissolution, decomposition and re-sintering routes were studied and compared.

The mechanical properties of the specimens manufactured by LCS via the dissolution and decomposition routes were measured by compression and three-point bending tests. The compression strength, elastic modulus and flexural strength of the porous steel specimens manufactured with both routes increased with increasing relative density, pore size and compaction pressure. Increasing the sintering temperature and time in the decomposition route served to increase the compression strength, elastic modulus and flexural strength. The advantages and disadvantages of the dissolution and decomposition routes were analyzed. The porous steel specimens manufactured by the decomposition route had better mechanical properties than those manufactured by the dissolution route.

The acoustic absorption performance of porous steel manufactured by the LCS process via the dissolution route was assessed using the standing wave impedance tube method. The single layer specimens showed excellent sound absorption properties at high frequencies. Pore size of the porous steel had no significant effect on the sound absorption coefficient. Sound absorption at low frequencies can be improved by increasing the thickness of specimens, or by introducing an air gap behind the absorber.

The sound absorption properties of the porous specimens of multi-layer assemblies with different porosities, pore sizes, thicknesses and air-gap depths were assessed. The porosity of the first layer of multi-layer-assembled specimens had a critical effect on the sound absorption coefficient and frequency of peak. Increasing this porosity increased the sound absorption coefficient at all frequencies after the peak. The effects of the porosities of the subsequent layers were smaller. When the first layer had a high porosity, increasing the porosity of the second layer increased the frequency of peak. When the first layer had a low porosity, increasing the porosity of the second layer enhanced the sound absorption coefficient of peak. The effects of pore size were not significant. Increasing the thickness of specimens and the depth of air-gap behind the specimens decreased the frequency and coefficient of the peak in the sound absorption curve.

CONTENTS

Abstract.....i

Acknowledgements.....vii

Publications.....viii

CHAPTER 1 INTRODUCTION.....1

1.1 Porous Metals.....1

1.2 Applications of Porous Metals.....3

1.3 Porous Steel.....3

1.4 Structure of Thesis.....5

CHAPTER 2 LITERATURE REVIEW.....7

2.1 Manufacturing Technologies for Porous Metals.....7

2.1.1 Liquid state methods.....7

2.1.1.1 Melt foaming.....7

2.1.1.2 Powder compact foaming.....9

2.1.1.3 Solid–gas eutectic solidification.....11

2.1.1.4 Investment casting.....12

2.1.1.5. Casting around space holders.....12

2.1.1.6. Spray forming.....13

2.1.2. Solid state methods.....14

2.1.2.1 Metal powder sintering.....14

2.1.2.2 Fiber sintering.....15

2.1.2.3 Powder sintering around space holders.....16

2.1.2.4 Slurry foaming.....17

2.1.2.5 Metallic hollow sphere sintering.....17

2.1.3 Lost carbonate sintering (LCS) 18
2.1.4 Comparison of porous structures.....19
2.2 Mechanical Characteristics of Porous Metals.....22
2.2.1 Compressive behaviour of porous solids 22
2.2.2 Compressive strength 24
2.2.3 Elastic modulus.....28
2.2.4 Energy absorption.....31
2.2.5 Flexural strength.....32
2.2.6 Scaling law.....33
2.3 Acoustic Properties.....39
2.3.1 Absorption of Sound at Surface.....39
2.3.2 Sound absorption of porous materials.....41
2.3.3 Sound absorption Models 43
2.3.3.1 Biot–Allard model 43
2.3.3.2 Helmholtz resonators and viscous resistance.....46
2.3.3.3 Equivalent Electrical Circuit Approach 49
2.3.4 Measurements of acoustic absorption coefficient.....49
2.3.5 Acoustic properties of porous materials.....51
2.3.5.1 Non-rigid porous materials.....51
2.3.5.2 Porous metals.....53
2.3.5.3 Multi-layer assemblies.....59
2.4 Applications of Porous Metals.....63
2.4.1 Structural and mechanical applications.....64
2.4.2 Acoustic applications.....65
2.5 Objectives of the Research.....65

CHAPTER 3 EXPERIMENTAL.....79

3.1 Fabrication of Specimens.....79
3.1.1 Raw materials.....79

3.1.2 Preparation of containers.....80
3.1.3 Mixing and compaction.....81
3.1.4 Dissolution route.....82
3.1.4.1 Sintering 83
3.1.4.2 Preform shaping.....83
3.1.4.3 Carbonate dissolution.....84
3.1.4.4 Re-sintering.....84
3.1.5 Decomposition route.....85
3.1.5.1 Sintering 85
3.1.5.2 Preform shaping.....86
3.2 Property Tests.....86
3.2.1 Density Measurements 86
3.2.2 Compression tests.....87
3.2.3 Flexure tests.....88
3.2.4 Airflow Resistance Tests.....89
3.2.5 Acoustic Tests.....91

CHAPTER 4 MECHANICAL PROPERTIES OF POROUS STEEL.....98

4.1 Porous Steel Manufactured by Dissolution Route.....98
4.1.1 Effects of relative density.....98
4.1.2 Effects of pore size.....102
4.1.3 Effects of compaction pressure.....104
4.2 Porous Steel Manufactured by Decomposition Route.....106
4.2.1 Effects of relative density.....106
4.2.2 Effects of pore size.....107
4.2.3 Effects of compaction pressure.....109
4.2.4 Effects of sintering temperature.....111
4.2.5 Effects of sintering time.....112
4.3 Comparison of Two Routes.....114

4.3.1 Mechanical properties.....114
4.3.2 Re-sintering specimens.....116
4.3.3 Advantages and disadvantages of decomposition route.....117
4.4 Scaling Law Parameters 118

CHAPTER 5 ACOUSTIC PROPERTIES OF POROUS STEEL.....150

5.1 Homogeneous Single-layer Specimens 150
5.1.1 Air flow resistance.....150
5.1.2 Effects of porosity.....151
5.1.3 Effects of pore size.....154
5.1.4 Effects of cell shape.....156
5.1.5 Effects of specimen thickness.....159
5.1.6 Effects of air-gap depth 162
5.1.7 Effects of metal matrix.....170
5.2 Multi-layer assemblies.....174
5.2.1 Assemblies with different porosities.....174
5.2.1.1 Two-layer-assemblies 174
5.2.1.2 Four-layer assemblies 178
5.2.1.3 Five-layer assemblies 182
5.2.2 Assemblies with different pore sizes.....184
5.2.3 Assemblies with different thicknesses.....185
5.2.4 Assemblies with different air-gap depths.....187
5.2.5 Equivalent Electrical Circuit Approach analysis.....189

CHAPTER 6 CONCLUSIONS AND FUTURE WORKS 241

6.1 Conclusions.....241
6.1.1 LCS process.....241
6. 2 Mechanical properties 242

6. 3 Acoustic absorption properties 243

6.2 Future Work.....245

REFERENCES.....247

ACKNOWLEDGEMENTS

I would like to thank my PhD supervisor, Dr Yuyuan Zhao, for his extraordinary patience and constant encouragement. He gave me great help by providing me with necessary teaching, advice of great value and inspiration of new ideas. It is his suggestions that draw my attention to a number of deficiencies and make many things clearer. Without his strong support, this thesis would not have been in the present form.

My heartfelt thanks also go to Dr. Liping Zhang for her priceless assistance with test specimen preparation and experimental work. Her enthusiasm and kindness have been an inspiration to me.

I am grateful to Dr. Gary Seiffert, Dr Carl Hopkins, Mr. Stephen Pennington, Mr. Jijimon Mathew and Mr. Dave Atkinson, for their great help with sample preparations, mechanical tests and acoustic absorption tests.

I would like to acknowledge Mr. Xiaobing Xue, Mr. Xingfu Tao, Mr. David Thewsey, Mr. Zhu Xiao and Mr. Fanjing Yang, for their invaluable assistance. They graciously made many comments and suggestions to the outline of this thesis.

Finally, I would particularly like to express my gratitude to my parents for their support. It is a great help for me to finish this thesis successfully.

PUBLICATIONS

Lu M., Hopkins C., Zhao Y. and Seiffert G. (2009), Sound absorption characteristics of porous steel manufactured by lost carbonate sintering, Materials Research Society Symposium Proceedings, Vol. 1188, pp. 207-212.

Lu M. and Zhao Y. (2010), Mechanical properties of LCS porous steel: comparison between dissolution and decomposition routes, TMS Annual Meeting, Vol. 2, pp. 137-142.

CHAPTER 1 INTRODUCTION

1.1 Porous Metals

A porous material is a material containing pores. The skeletal portion of the material is usually a solid and is often called as the matrix. The pores are typically filled with a fluid. Porous materials or foams exhibit novel properties and afford great potential for weight savings (Gibson & Ashby, 1997). Polymer foams have long been used to absorb vibration, noise and impact energy. However, structural applications of polymer foams are limited to low-stress components because of the relatively low strength compared with other engineering materials. For these reasons, considerable attention has been devoted to porous metals because of their much higher strength, stiffness, energy absorption during deformation, and substantial weight savings relative to conventional metallic components. Over the last few decades, porous metals have received a large amount of interest in industry because of advancement in manufacturing techniques and growing possible applications. Porous metals can be produced with different metals and different porous structures giving a combination of different properties. Their unique properties and multi-functionality allow them to be utilized in many different components throughout different industrial sectors.

The first porous metals used in engineering applications were manufactured by the sintered powder method. Sintered powder has been used with success for filters,

batteries and self-lubricated bearings since the 1920's (Capus, 2000). The sintered powder porous metals are still used today.

The earliest reference to metallic foams is a French patent published in 1925 (Meller, 1925). The commercialization of metallic foams started in the late 1950's in the USA. Little activity remained until a second surge of worldwide R&D activities started in the 1990's, which is still ongoing. With the recent developments, foam materials became commercially available in a wide variety of structures and properties.

Many international and national R&D programs have focused on porous metals, for example, the US Multidisciplinary Research Initiative on Ultraligth Metals (MURI) launched in 1996, and different European research projects funded within the 4th and 5th EU Framework programs (Degischer, 2002).

A biennial conference series (Metfoam) reviews the latest progress since the late 1990's (Banhart, Ashby & Fleck, 1999; Banhart; Ashby & Fleck, 2001; Banhart, Fleck & Mortensen, 2003; Nakajimma & Kanetake, 2005; Lefebvre, Banhart & Dunand, 2007; Foroughi, Degischer & Kottar, 2009). These conference proceedings are a good source of information on recent developments of the cellular, porous or foamed metals, including materials development, manufacturing technologies, characterization and applications.

1.2 Applications of Porous Metals

Porous metals have an increasingly wide range of applications. The type of applications depends on many conditions, such as type of pores, porosity, pore size, total internal surface area, type of metal or alloy, microstructure, easiness of shaping and suitability for mass production (Banhart, 2001). The properties of porous metals particularly important for industrial applications include impact energy absorption properties, acoustic, thermal and electrical properties. Some examples of typical existing applications include lightweight panels for building and transport, impact absorption panels, sound and thermal insulation materials, heat sinks, heat exchangers, structural parts for aircraft, heat shields, electromagnetic shields, loudspeaker enclosures, filters and condensing towers. Development of low-cost production methods will make many types of porous metals a cheap alternative to expensive, engineering materials.

1.3 Porous Steel

Although the majority of the applications employ porous metals with light weight metal matrices such as Al or Mg, there have been some attempts to apply the steel to be the matrix (Park & Nutt, 2000) steel poses special difficulties stemming from its higher melting point and lower melt viscosity.

Steel foam offers several potential advantages over Al foam, including higher specific strength and stiffness, lower raw material cost, higher service temperature, and compatibility with steel structures. Potential applications utilizing the mechanical properties include cores for beams and sandwich panels, weight-critical components, and energy absorbing components and structures.

Process control of the manufacture of porous metals is critical for controlled pore structures and consistent properties. This is currently a formidable challenge. Development of manufacturing technology will innovate structural application of porous steel because of its inherent advantages.

This thesis manufactures porous steel by the Lost Carbonate Sintering (LCS) process, a novel technique developed by Zhao *et al* (2005), and studies its properties of interest to industrial applications. The LCS method involves sintering metal powder particles around carbonate particles. It is a highly controllable process and can produce a variety of porous metals with controlled porosity, pore size and pore shape.

The mechanical and acoustic properties of porous steel are of particular interest. The inherent strength of steel combined with the reduced density of porous steel makes it an ideal material with reasonable strength, greatly reduced density, and highly efficient energy absorption. The special microstructure of LCS porous steel makes it an ideal candidate for use as an acoustic absorber in harsh environments. The

combination of a rigid construction, acoustic properties and relatively light weight of LCS porous steel would allow it to be used in a wide range of engineering applications where conventional absorbers are not suitable.

1.4 Structure of Thesis

The primary objective of this thesis is to investigate the mechanical and acoustic properties of LCS porous steel specimens with different structural properties, manufactured using two different routes. The mechanisms involved in these manufacturing routes will be analysed, with an aim to identify the optimum structural properties giving rise to the best mechanical and acoustic performance.

Chapter 2 evaluates the literature that is relevant to the present work. The methods currently used to manufacture porous metals will be reviewed. An overview of existing porous metals and their properties will also be given in this chapter.

Chapter 3 gives a detailed description of the experimental procedures used in this work, including the LCS process used to produce the porous steel samples, the characterization techniques for mechanical properties, and the measurement procedures for acoustic absorption coefficient and air flow resistance. The equipment and process conditions used in the experiments are described.

Chapter 4 presents the results of mechanical properties of the porous steels produced by the dissolution and decomposition routes of the LCS process. Particular attention is paid to the effects of porosity, pore size, compaction pressure, sintering temperature and sintering time. The effects of structure and production route on the flexural strength, compression strength and elastic modulus are described and discussed.

Chapter 5 presents the results of acoustical properties of the porous steels produced by the LCS process. Particular attention is paid to the effects of porosity, pore size, pore shape, sample thickness, air-gap depth, and assembly order. The effects of structure and production route on the sound absorption coefficient are described and discussed.

Chapter 6 summarises the conclusions drawn from this study and recommends a few areas for future research.

CHAPTER 2 LITERATURE REVIEW

2.1 Manufacturing Technologies for Porous Metals

There are many methods for manufacturing porous metals. Some methods are similar to the techniques used for polymer foams. Some are designed by taking advantage of characteristic properties of metals, such as their sinterability. These methods can generally be classified according to whether the metal is in liquid or solid state during manufacturing. This section gives a brief overview of the common manufacturing methods and their characteristics.

2.1.1 Liquid state methods

2.1.1.1 Melt foaming

In melt foaming methods, metallic foam is formed by directly injecting gas, such as air, nitrogen or argon, bubbles into the liquid metal (Babcsan *et al*, 2003). The bubbles tend to rise rapidly to the surface of the melt because of the high buoyancy force of the high-density liquid metal. This rise can be reduced by increasing the viscosity of the melt by adding fine ceramic particles in the melt. The result is a more even pore distribution in the manufactured foam.

There are two ways of adding gas into a metallic melt: to inject gas into the melt from an external source, as shown in Figure 2.1.1, or to cause the gas formation in the melt by mixing a blowing agent in the molten metal.

In the gas-injection method for manufacturing Al foam, the aluminum melt is prepared to contain silicon carbide or aluminum oxide or magnesium oxide particles to enhance the viscosity of the melt. The liquid metal matrix composites (MMCs) melt is then foamed by injecting gases (air, nitrogen or argon) into it using specially designed rotating impellers or vibrating nozzles. The function of the impellers or nozzles is to create very fine gas bubbles in the melt and distribute them uniformly. The viscous mixture of bubbles and metal melt subsequently floats up to the surface of the liquid and turns into fairly dry liquid foam as the liquid metal drains out. Before solidification, the semisolid foam can be flattened by means of one or more top-mounted rolls to yield a foam slab with closed and fairly even upper and lower skins (Banhart, 2001). The porosity of porous metal manufactured by this method is in the range 80-97%, and the pore size is in a wide range of 5μm-25mm.

The second way of making Al foams is adding a blowing agent into the molten aluminum (Elliot, 1956). The blowing agent decomposes and releases gas under the high temperature of the melt. The gas expands in the melt, which forms a solid cellular structure after cooling. The blowing agent in this way is usually a metal hydride, such as TiH_2 or ZrH_2; other compounds can also be used. The porosity of

porous metals manufactured by this method is in the range 91-93%, and the pore size is in the range of 2mm-10mm.

Advantages of the melt foaming process include the large volume of foam which can be continuously produced and the low densities which can be achieved. The main disadvantage of this manufacturing method is that the as-produced samples usually have a high porosity at the centre of the foam and the pore size and its distribution cannot be controlled accurately.

An approach to overcome the inhomogeneity problems is using high speed mixing (Davies & Zhen, 1983). This method can disperse the blowing agent throughout the molten metal in a very short space of time. More uniform pore distribution throughout the structure can be achieved. Thickening the melt makes it maintain the fluid state for a longer time without collapsing and gives more time for the foaming agent to be added into the molten metal. Increasing viscosity of the molten metal results in smaller pores and a more even pore distribution.

2.1.1.2 Powder compact foaming

This technique was developed by Fraunhofer-Institute in Bremen (Baumeister, 2010). The method is often called 'powder metallurgical method' because the starting materials are metal powders. The production process begins with the mixing of metal

powders — elementary metal powders, alloy powders or metal powder blends — with a blowing agent. The mix is then compacted to yield a dense, semi-finished product. The next step is heat treatment at a temperature near the melting point of the matrix material. The blowing agent, which is homogeneously distributed within the dense metallic matrix, decomposes at this temperature. The released gas forces the compacted precursor material to expand. Highly porous structure is formed by this force, as shown in Figure 2.1.2. The full expansion time depends on the temperature and the size of the precursor. The range of the heat treatment time is from a few seconds to several minutes. The porosity of porous metals manufactured by this method is in the range 60-90%, and the pore size is 10μm-32mm.

In principle, the compaction of powder mix can be done by any technique that ensures that the blowing agent is embedded uniformly into the metal matrix without any notable residual open porosity. Examples of such compaction methods are hot uniaxial or isostatic compression, rod extrusion or powder rolling. Which compaction method is chosen depends on the required shape of the precursor material. Extrusion is considered to be the most economical method (Baumgartner *et al*, 2000). Thin sheets can be obtained by rolling rectangular profiles with various cross-sections. The manufacture of the precursor has to be carried out very carefully because any residual porosity or other defects will lead to poor results in further processing.

2.1.1.3 Solid–gas eutectic solidification

This method is based on the fact that some liquid metals form a eutectic system with hydrogen gas (Shapovalov *et al*, 1998). In this method, the metal is melted in a hydrogen atmosphere under a pressure higher than 50 atm, resulting in a melt charged with hydrogen. When the melt is cooled, it undergoes a eutectic transition to a heterogeneous two-phase system of 'solid + gas'. If the composition of the system is close to the eutectic concentration, there will be a segregation reaction at one temperature. Removal of heat from the melt from one end leads to directional solidification. As solidification proceeds through the liquid, at a velocity ranging from 0.05 to 5 mm/s, the hydrogen content near the solidification plane increases and gas bubbles are formed. The process parameters have to be chosen such that the bubbles remain near the solidification zone and are entrapped in the solid (Apprill *et al*, 1998). The resulting pore morphologies, as shown in Figure 2.1.3, are largely determined by the hydrogen content, the pressure over the melt, the direction and rate of heat removal, and the chemical composition of the melt.

The porous metals manufactured by this method have elongated pores orientated in the direction of solidification. They only appear spherical when observed in this direction. Pore diameters range from 0.01 to 10 mm, pore lengths from 0.1 to 300 mm, aspect ratios from 1 to 300 and porosities from 5 to 75% (Shapovalov *et al*, 1998). The pore size distribution is non-uniform because of concurrent growth of small and

large pores and coalescence. Pores may be conical or even corrugated.

2.1.1.4 Investment casting

The investment casting method manufactures foam from a molten metal without directly foaming the metal. It uses open-cell polymer foam, such as polyurethane foam, as a precursor (Hintz *et al*, 1999). The polymer foam is filled with a slurry of heat resistant materials, e.g. a mixture of phenolic resin and calcium carbonate (Yosida & Hayashi, 1990) or simply plaster (Yamada *et al*, 2000). The polymer foam is then removed by thermal treatment to form a ceramic mould. The molten metal is cast into the resulting open voids, as shown in Figure 2.1.4. In order to ensure the liquid metal filling the narrow cavities, pressure and heating of the mould is often necessary. After solidification of the metal and removal of the mould material, a metallic structure is obtained which is an exact replica of the original polymer foam. The porosity of porous metals manufactured by this method is in the range 80-97%, and the pore size is in the range 2-25mm. Difficulties in this process include achieving a complete filling of the cavities and removing the mould material without damaging the fine structure.

2.1.1.5. Casting around space holders

In this method, porous metals are produced by casting liquid metals around removable

granules, or space holders such as sodium chloride particles, as shown in Figure 2.1.5 (Zhu & Chung, 1991; Chen & He, 1999). After solidification of the metal, the granules are removed by leaching in a suitable solvent or acid or by thermal treatment. This can be done successfully if the content of the space holding fillers is so high that all the granules are interconnected. Polymer spheres can also be used as space holders if the solidification of the melt is sufficiently fast. The latter requires high pressure infiltration, e.g. in a die-casting machine (Ma & Song, 1998). The porosity of porous metals manufactured by this method is less than 65%, and the pore size is the same as the diameter of the space holder, generally between 5μm-25mm.

2.1.1.6. Spray forming

This method atomizes metallic melt continuously and creates a spray of fast flying small metal droplets, as shown in Figure 2.1.6. The droplets are collected on a substrate and grow to a deposit in a given shape, with various degrees of porosity. The characteristics of spray-formed materials include low oxide content, fine grain size or a high content of metastable alloy phases (Lavernia & Grant, 1988). Spray foaming allows for processing a variety of different metals and alloys. The porosity of porous metals manufactured by this method is no more than 60%, and the pore size is in the range 10μm-1mm. This combination of properties usually cannot be obtained by conventional casting methods.

When the spray is deposited on the substrate, powders such as oxides, carbides or pure metals can be injected into it and react with or be wetted by the liquid metal droplets. Metal powders incorporated into the foam can modify the properties of the deposit. This feature makes the spray process especially attractive to some applications. Babcsan *et al.* (2003) created porous steel by injecting silicon oxide or manganese oxide into a carbon steel spray, thus creating large amounts of carbon monoxide in the deposition zone in a chemical reaction of the type $SiO_2 + 2C \rightarrow Si + 2CO$. The porosities achieved in this way can range up to 60% but the pore morphologies still lack uniformity.

2.1.2. Solid state methods

2.1.2.1 Metal powder sintering

Sintering is a process of particle coalescence of a powdered aggregate by diffusion. During the time that the powder particles are being heated, the contact of particles with each other grows by the action of capillary or surface tension forces. The manufacture process generally includes two steps: compaction and sintering (Neumann, 1999). If during the compaction process a binder is used, it has to be removed before or during sintering. The sintering is accomplished by firing at an elevated temperature which is lower than the melting temperature. Application of pressure could increase the contact area and quantity but is not always necessary. With

increasing sintering time, particle boundaries develop on each contact and the space between the particles develops into a pore. In the advanced stages of sintering, the necks between the particles increase in size, resulting in a reduction in the pore size. Mass movements which happen during the sintering result in the reduction of total porosity by repacking. In the final stage, metal atoms move along crystal boundaries to the internal pore walls, redistributing mass from the internal bulk of the object and smoothing pore walls. A typical structure of the porous metals produced by the sintering method is shown in Figure 2.1.7.

The porosity of the as-produced porous metals is relatively low, usually between 40% and 60% (Davies & Zhen, 1983), and the pore size is in the range 10-100μm. Generally, the metal powder sintering method is used in applications where a high porosity and relatively low pore size are not required. For higher porosities, spacing agents or space holders can be added to the powder before sintering.

2.1.2.2 Fiber sintering

Like metal powders, metal fibers can also be sintered to form porous metals with some unique properties. Various methods are used to produce the fibers, which are then sintered using conventional techniques. After sintering, the metal fibers retain their strength. The porosity of sintered metal fibers is controllable to some extent and the pore structure has a high permeability. The porosity of porous metals

manufactured by this method is in the range 20-80%. The pore size is difficult to be defined because the porous structure in sintered fibers is highly inter-connected. The high permeability makes porous metals manufactured using this technique an ideal candidate for use as filters. Metals used in this process include copper, stainless steel, nickel and Ni-Cr alloys (Yarnton, 1966).

2.1.2.3 Powder sintering around space holders

In this method, a metal powder is mixed with a removable powder, as shown in Figure 2.1.8 (Stiller *et al*, 1998; Bram *et al*, 2000). Ceramic particles or hollow spheres, polymer grains or hollow polymer spheres, salts or even metals can be used as space holders. The mix is compacted at room temperature. The mixture is heated at a high temperature and the sintering process starts between the metal powder particles. The space holder is finally removed to form a porous structure. If the metal content is low enough, it is possible to remove the space holder completely, because the network formed is interconnected. The removal of the space holder can be done by thermal treatment, leaching, or by use of an aqueous solvent. A final sintering step can be applied to further density the porous metallic network. The porosity of porous metals manufactured by this method is in the range 10-70%, and the pore size is the same as the diameter of the space holder particles, normally 10μm-10mm.

The Sintering and Dissolution Process (SDP) (Zhao and Sun, 2001) and the Lost

Carbonate Sintering (LCS) process (Zhao *et al*, 2005) are two examples of using the space holder methods. The former uses NaCl as space holder and the latter uses carbonate. The LCS process will be reviewed separately in 2.1.3.

2.1.2.4 Slurry foaming

The slurry foaming method produces metallic foams by preparing a slurry of metal powders, creating pores using blowing agents and some reactive additives, and consolidating metal particles by powder metallurgy. The process starts by mixing a metal powder and a foaming agent to form a slurry (Drolet, 1977). The mixture slurry is whipped into foam and then heated to create a solid porous structure. The slurry can be poured into moulds to form the required shapes. When foaming has completed, the foam is sintered to impart strength and improve the mechanical properties. This technique can be used for many metals such as nickel, iron, copper and beryllium as well as stainless steel and bronze. Generally, the porosity of porous metals manufactured by this method is less than 93%, and the pore size is in the range 10μm-1mm.

2.1.2.5 Metallic hollow sphere sintering

The metallic hollow sphere sintering method uses hollow spheres made of copper, nickel, steel or titanium to create highly porous structures by bonding the individual

spheres together by sintering. The metallic hollow spheres can be made by a process called Advanced-Pore-Morphology technology (Baumeister, 2010). In this technology, a metal powder mixture containing a foaming agent is compacted to yield a foamable precursor material. Wires made of the foamable precursor material are chopped into small pellets. The resulting granulated material runs through a belt foaming furnace where it is expanded into numerous foamed spheres, as shown in Figure 2.1.9. These spheres are coated with an adhesive and heated at a low temperature (e.g. 180°C) to activate the adhesive to improve the contact between the individual spheres (Clark *et al*, 1999). They are then packed and sintered. The spheres are deformed to polyhedral bodies by applying forces during sintering, in order to increase sintering contacts and reduce the degree of open porosity. The porosity of the porous metals manufactured by this method is no more than 80%, and the pore sizes are in the range 0.8-8mm. An alternative method is to bond oxide spheres together with oxide slurry and to carry out the reduction and sintering in one step.

2.1.3 Lost carbonate sintering (LCS)

The LCS process is a powder metallurgy method using carbonate as a space holder, as shown in Figure 2.1.10 (Zhao *et al,* 2005). The particle size of the carbonate grains is selected according to the intended pore size of the final foam. The particle size of the metal particles must be smaller than the carbonate particles.

The LCS process was first used to produce porous Cu (Zhao *et al*, 2005; Tao *et al*, 2007; Zhang & Zhao, 2007). In producing porous Cu, the Cu and K_2CO_3 powders were mixed with a volume fraction of Cu ranging from 0.15 to 0.5 of all solid materials excluding pores in the mixture. Ethanol was added during mixing as the binder. The volume of ethanol was approximately 1 vol. % of the Cu–K_2CO_3 mixture. The Cu–K_2CO_3 powder mixture was poured into a mild steel tube and both ends were sealed with layers of iron powder in order to protect Cu from extensive oxidation. The mixture was compressed by a hydraulic press at 200 MPa. The debinding was carried out either at 200 °C for 1h in order to evaporate the ethanol in the perform or by heating the samples slowly (10 °C/min) to the sintering temperature. As the melting point of K_2CO_3 is 891°C, at which it also starts to decompose, three different routes of sintering and carbonate removal can be used. In Route A (the dissolution route), the preform was sintered at 850°C for 4h, cooled to room temperature and then placed in running water for 5h. The carbonate was dissolved by the water. In Route B, the preform was sintered at 850°C for 4h, heated at 950°C for 0.5h to melt and decompose the carbonate and then cooled to room temperature. In Route C (the decomposition route), the preform was heated to 950°C and maintained at this temperature for 2h before being cooled to room temperature.

2.1.4 Comparison of porous structures

Porous metals manufactured by the methods described above have different porosities,

pore types and pore sizes. Table 2.1 summarizes the typical metal matrices, pore types, pore sizes and porosities of all the production methods discussed in this section.

The liquid state methods are normally used for Al or Zn matrix because they have low melting temperatures. The solid state methods can be used for high melting temperature metals such as steel. The most common pore type of porous metals produced by the liquid state methods is closed, while the solid state methods generally produce open pores.

The pore size and porosity of the porous metals produced by melt foaming, powder compact melting, solid-gas eutectic solidification, slurry foaming and metallic hollow sphere sintering are very hard to be controlled accurately because the gas bubbles are not homogeneous. The investment casting, casting around space holder, powder sintering around space holder and LCS methods can control the pore size and porosity well because the size and number of pores are the same as the polymer skeleton or space holder used.

The casting around space holder, powder sintering around space holder and LCS methods all have a wide range of porosities and pore sizes. Among these three methods, LCS has the widest range of porosities and is the simplest process. The solid–gas eutectic solidification, metallic hollow sphere foaming and slurry foaming methods also have wide ranges of porosities and pore sizes, but these methods cannot

control the porosity and pore size very well because they use blowing agents to generate the pores.

Table 2.1 Summary of metal matrix, pore type, pore size and porosity of porous metals produced by different methods.

Methods	Matrix	Cell	Pore size	Porosity(%)
Liquid state processing				
Melt foaming (gas)	Al Zn	Closed	5μm-25mm	80-97
Melt foaming (agent)	Al Zn	Closed	2mm-10mm	90-93
Solid–gas eutectic solidification	Cu Al Ni	Closed	10μm-10mm	5-75
Powder compact melting	Al Zn Pb	Closed	10μm -32mm	60-90
Investment casting	Al Zn	Open	2-25mm	80-97
Casting around space holder	Al Pb Cu	Open	10μm -10mm	≤ 65
Spray forming	Steel Cu	Closed	10μm-1mm	≤ 60
Solid state processing				
Metal powder sintering	Steel Cu	Open	10-100μm	40-60
Fiber sintering	Steel	Open	-----	20-80
Powder sintering around space holder	Ti	Open	10μm -10mm	≤ 70
Slurry foaming	Al	Open	10μm-1mm	≤ 93
Metallic hollow sphere sintering	Steel	Closed	0.8 -8mm	≤ 80
Lost carbonate sintering (LCS)	Cu (Steel)	Open	50μm -1.5mm	≤ 85

2.2 Mechanical Characteristics of Porous Metals

2.2.1 Compressive behaviour of porous solids

The stress-strain curve obtained in the compression of a porous material often has three distinct deformation regions: elastic region, stress plateau region and densification region as shown in Figure 2.2.1 (Ashby *et al*, 2000; Theis, 2002). The porous material undergoes elastic deformation in the linear elastic region, as in the compression of a solid material. The plateau region, in which the stress is nearly constant over a wide range of strain, is a process of pore collapse, cell wall buckling and fracture. When the cells have almost completely collapsed opposing cell walls touch and further strain compresses the solid itself, leading to a final region of rapidly increasing stress. Depending on the material from which the foam is made, different deformation mechanisms can be observed.

Many investigations have been made on compression behaviour and energy absorption performance of porous metals in recent years. Porous metals usually show a ductile behaviour which is similar to many polymer foams. In the compression test, loading at small strains of a ductile porous material results in bending and compression of cell walls. If the stresses in the walls are higher than the compressive strength of the solid, plastic strain appears and the deformation is not reversible. Because of the inhomogeneous structure of real porous metals, the stress

concentrations exceed the compressive strength in some places at relatively low strains, which leads to plastic deformation in these places. Therefore the linear elastic region of the stress-strain curve of a ductile porous material is in general hardly developed. When the load on the porous materials increases, the cell walls are buckled in weaker regions of the porous materials. A deformation band appears perpendicular to the loading direction. This is the beginning of the plateau region in the stress-train curve. With increasing strain, additional deformation bands appear until most of the cells have collapsed, and the densification region is reached. Depending on the porous structure and the properties of the matrix, the plateau region of the stress-strain curve may slightly sloped or jagged. Two extreme cases are depicted in Figure 2.2.2, showing the behaviours of a ductile aluminum foam with a smooth plateaus and a brittle alumina foam with a jagged plateau, respectively (Degischer & Kirszt, 2002).

Figure 2.2.3 shows the stress-strain curves of Alulight aluminum foams with different densities in compression (Degischer & Kirszt, 2002). It is clearly shown that the compressive strength increases with increasing density. Different methods exist for the determination of the compressive strength, depending on the course of the stress-strain curve. If there is a stress peak at the beginning of the plateau, this peak or a clear flat section stress will be taken as compressive strength. In the absence of a stress peak the plateau region will be extrapolated to lower strains and the intersection with the initial elastic line gives the compressive strength.

2.2.2 Compressive strength

Previous work showed that the compressive strength of the porous metals affected by relative density. The production method, metal matrix, pore shape, and the thickness, amount of defects and orientation of the cell-wall are also important factors affecting the mechanical properties of the porous metals.

Kunze *et al* (1993) studied the mechanical properties of Al foams manufactured by a hydrogen technology method with very low densities. The compressive strength of these materials depends strongly on the relative density, varying in the range of 1.7-11.4 MPa with the relative density in the range of 0.1-0.25. The compressive strength and elastic modulus also increased with increasing cell-wall thickness but not significantly. The experimental results conformed to the scaling law, which will be discussed in 2.2.6.

San Marchi and Mortensen (2001) studied compressive behaviour of high-purity Al foams produced by a space holder (salt) method. These foams had homogeneous open-porosity, cell sizes of ≈500μm and relative densities of 0.19-0.31. The compressive strength depended on the relative density and varied from 2.2 to 6.9 MPa. They found that the low-strain response was not elastic from the onset, but was after a small strain increment. The stress-strain curve then displayed a linear elastic response with stiffness proportional to the square of the relative density.

Wen *et al* (2004) showed that the compressive strength of Al foams manufactured by a sintering method varied from 0.79 to 1.6 MPa with the relative density varied from 0.19 to 0.27 and pore size varied from 0.5 to 1 mm. The stress-strain curves of the Al foams exhibited a plateau region with a nearly constant flow stress. The stress in the plateau region increased with increasing relative density. On the other hand, the densification strain decreased with increasing relative density. Observation of the deformed cells revealed that for the Al foams produced by the sintering method plastic collapse was dominated by the bending of cell walls.

Goodall *et al* (2007) measured the compressive properties of open-cell Al foams with spherical or angular pores. It was shown that the effect of cell shape on mechanical properties was negligible if the cells were roughly equiaxed. The compressive strength of spherical-pore Al foam ranged in 0.11-1.6 MPa, while that of angular-pore Al foam ranged 0.17-1.17 MPa for relative density ranges of 0.075-0.26 and 0.1-0.24, respectively.

Thornton and Magee (1975) studied the compressive behaviour of Al, Al-7Mg and Al 7075 alloy foams. The porosity of the Al and Al alloy foams varied from 0.80 to 0.95. The compressive strengths of Al, Al-7Mg and Al 7075 foams were in the ranges of 0.4-2.1 MPa, 0.7-13.2 MPa and 1.5-13.5 MPa, respectively. In all cases, a greater-than-linear increase in compressive strength with increasing relative density

was exhibited. The reason of the proportional relationship between the compressive strength and relative density was that the foams collapsed by different modes at different densities.

Prakash *et al* (1995) examined the mechanical response of a Al-SiC composite foam in compression. The foam had a closed cell structure with a pore size of 600μm and had an Al matrix embedded with SiC particles. The mechanical responses of the foams were complex because the cell walls had a complex microstructure. In compression, deformation localized in a band which extended outward with increasing strain. The compressive strength of the composite foam varied in 0.64-2.57 MPa with relative density in the range of 0.1-0.2.

Simone and Gibson (1998) studied closed-cell Al–Si–Mg alloy (nominal composition: Al–7wt% Si–0.3wt% Mg) foams with a pore size of 600μm, made by two liquid-state methods: gas injection method and mixing with blowing agent method. The results showed that the mechanical properties of the specimens manufactured by the gas injection method were lower than that manufactured by the mixing with blowing agent method. The compressive strength of the specimens manufactured by the mixing with blowing agent method ranged in 0.063-2.9 MPa with relative density range in 0.03-0.14. They found that the mechanical properties of the specimens produced by both processes were significantly improved through the elimination of defects in the cell structure.

Banhart and Baumeister (1998) investigated the deformation behaviour of Al–6Si–4Cu and Zn–4Cu foams by uniaxial compression testing. A series of measurements was carried out at different directions on the samples with varying the foaming directions. It was shown that the form of the stress-strain curves depended on the density of the foam, on the orientation of the testing relative to the foaming direction, and on the orientation of cell-walls. Higher densities led to higher compressive strengths. The compressive strength of the Al-Si-Cu alloy varied from 5.9 to 23.7 MPa when the relative density varied from 0.07 to 0.29; the compressive strength of the Zn-Cu alloy foam varied from 5.8 to 21.2 MPa when the relative density varied from 0.14 to 0.27. A parallel orientation of the cell-walls with respect to the applied force led to a higher strength.

Silva and Ramesh (1997) studied the compressive properties of porous pure iron with a pore size of 400μm, prepared by cold isostatic pressing and subsequent heat-treatment. The relative densities of the specimens ranged from 0.69 to 1.0 and the compressive strengths ranged from 180 to 450MPa. They formulated a finite deformation visco-plastic model, treating the porous material as a composite of the matrix material and the porosity. Numerical simulations based on this model were able to provide reasonable predictions of the observed behaviour.

Wang *et al* (2001) investigated the compressive behaviour of a porous bronze

containing 10% tin and a porous pure iron, fabricated by powder metallurgy. The compressive strength of the iron foam varied from 43 to 168 MPa when the relative density varied from 0.67 to 0.89; the compressive strength of the bronze foam varied from 53 to 129 MPa when the relative density varied from 0.61 to 0.83. The plastic response of the materials was similar under different strain rates, but the compressive strength was rate-sensitive, particularly for the iron samples. Both porous iron and bronze samples showed a strong bi-linear behaviour in terms of strain. The behaviour of the materials could be predicted using approximate models with significant simplicity.

Zhang and Wang (2004) studied the compressive behaviour of porous copper manufactured by a space holder method, with a pore size of 600μm. The compressive strength had a linear relationship with porosity. The porous coppers with high relative densities behaved more like a solid metal than a foam material. It has also been shown that the compressive strength increased with decreasing porosity and increasing powder size. The compressive strengths of porous Cu with Cu powder sizes of 5μm and 45μm ranged from 30 to 129 MPa and from 28 to 45 MPa for relative densities of 0.43-0.94 and 0.43-0.65, respectively.

2.2.3 Elastic modulus

Gibson and Ashby (1982) investigated homogeneous deformation of cellular solids.

They measured and calculated the elastic modulus of flexible or rigid polyurethane with open or closed cell structure. The elastic moduli of the open-cell flexible polyurethane with relative densities between 0.01 and 0.05 were in the range of 0.004-0.032 GPa. They established a model to correlate relative elastic modulus and relative density of the cellular solids, but found some inconsistency with the experimental results. They attributed this to the fact that the elastic modulus of the solid they used in the model could be incorrect.

Hagiwara and Green (1987) measured the elastic modulus of open-cell aluminum foams as a function of relative density. The elastic modulus was in the range of 3-24 MPa with the relative densitiy between 0.08 and 0.3, in good agreement with the scaling law. The measured values were found to be sensitive to the microstructure of the cell struts, especially porosity within these struts. The Al foams contained some closed cells, but they were not found to have a major effect on the elastic behaviour. Anisotropy was observed in terms of the fraction of open to closed cells in these materials, but this was not translated into anisotropic behaviour. This is consistent with the idea that the presence of the cell faces does not have a significant effect on the elastic behaviour.

Simone and Gibson (1998) measured the elastic modulus of closed-cell Alporas Al alloy foams. There was a linear relationship between elastic modulus and relative density of the Al alloy foams. The elastic moduli of the close-cell Alporas foams, with

relative densities between 0.02 and 0.15, were in the range of 0.14-0.7 GPa. The Alporas foam outperformed the Alcan foams in terms of elastic modulus and plastic collapse stress. They found it is difficult to quantify the degree to which micro-structural variations and cell wall defects influence the material properties.

Zhang and Wang (2004) examined the elastic behaviour of porous copper manufactured by a space holder method and compared it with that of porous Ti (Wen *et al*, 2002). The elastic moduli of the porous copper (5μm Cu powder) with relative densities between 0.65 and 0.92 were in the range of 6-115 GPa. The elastic moduli of the porous copper (45μm Cu powder) with relative densities between 0.42 and 0.65 were in the range of 1.2-6.4 GPa. The elastic moduli of the porous Ti with relative densities between 0.1 and 0.65 were in the range of 3-11 GPa. The elastic modulus of the porous copper had an exponent relationship with porosity and did not vary with pore size.

Friedl *et al* (2007) fabricated porous steels from 316L stainless steel hollow spheres by sintering and studied their mechanical behaviour under compression and tension. The elastic modulus of the porous steels was between 200 and 640MPa. The cell wall morphology affected the elastic modulus of the porous structure.

2.2.4 Energy absorption

The selection of cellular materials for applications such as inner liners of cycle helmet and bumpers for automobiles or motor cycles is based on their energy absorption ability. Porous materials absorb energy by their irreversible deformation. Many porous solids are good energy absorbers because of their deformation at a nearly constant stress level over a wide range of strain (Gibson & Ashby, 1997). Metal foams are better than conventional foams, e.g. polymer foams, because of their much higher strengths. The energy absorption for a porous material can be evaluated by integrating the area under the stress-strain curve, namely:

$$W_p = \int_0^{\varepsilon_d} \sigma(\varepsilon) d\varepsilon \tag{2.1}$$

$$W = \frac{W_p}{\rho} \tag{2.2}$$

where ε is strain, σ is stress, ε_d is the densification strain, which can be obtained by the intersection of the tangent lines of plateau and densification curves, W_p is the specific absorbed energy per unit volume (J/m^3), W is the specific absorbed energy per unit weight (J/g), ρ is the density of porous material.

Banhart (2001) suggested some general criteria for a good energy absorber: (i) energy absorption characteristics as ideal as a flat stress–strain curve, i.e. yielding only after the maximum tolerable stress has been reached and progressive deformation at this plateau stress; (ii) a high absorption capacity per unit volume, length or mass; and (iii) isotropy of energy absorption, i.e. good absorption characteristics for at least a wide

range of impact directions.

Han *et al* (1998) studied the energy absorbing characteristics of Al and Al alloy foams by compression test. They found that the energy absorption capacity of foamed Al increases as the compressive strength and the plateau stress increase. Brittle or as-cast Al alloy foam showed a much higher capacity than the plastic Al foam. The peak values of energy absorption of Al and Al alloy foams were obtained at relatively low strains, generally from 0.15 to 0.35, depending on the relative density. The peak value shifted toward a lower strain as the relative density increased.

Mukai *et al* (1999) studied the dynamic response of a close-celled aluminum foam with a relative density of 0.1 and a pore size of 2.6mm by compression with different strain rates. The energy absorption value in the dynamic test was about 50% higher than that in the quasi-static test.

2.2.5 Flexural strength

Flexural strength is defined as a material's ability to resist bending deformation. The transverse bending test is most frequently employed. In the test, a rod specimen having either a circular or rectangular cross-section is bent until fracture using a three point or four point flexural test. The flexural strength represents the highest stress experienced within the material at its moment of rupture.

Kwan *et al* (2000) measured flexural modulus and strength for a range of porous Al specimens with different initial powder particle sizes and final porosities, manufactured by sintering. A power or an exponential function could adequately describe the porosity dependence of flexural strength. The flexural strength of the porous Al with relative densities between 0.55 and 0.95 were in the range of 22-840 MPa. The strength values obtained were test method dependent. They were also significantly lower for specimens with sintering aids. No dependence of mechanical properties on powder particle size was observed.

Tao *et al* (2007) examined the mechanical response of a sintered porous copper under three-point bending and Charpy impact conditions. They found that the apparent modulus, flexural strength and energy absorption capacity increased exponentially with increasing relative density. The increase in the flexural strength and the bending energy absorption capacity was observed when the compaction pressure of the copper powder during the manufacturing process was increased. This was a direct result of reduced sintering defects. The flexural strength of the porous copper with relative densities between 0.15 and 0.35 were in the range of 0.4-5.5 MPa.

2.2.6 Scaling law

The compressive properties of porous metals depend greatly on the relative density of

the materials (Gibson & Ashby, 1997). There is a strong correlation between the relative density (or porosity) and the compressive strength of a porous metal. The relative compressive strength and relative density are used widely to understand the relationship between the compressive strength and density of various porous materials. The relative compressive strength (σ_c/σ_s) is the ratio between the compressive strength of a porous material (σ_c) and the compressive strength of its cell wall solid (σ_s). The relative density (ρ/ρ_s) is the ratio between the density of the porous material (ρ) and the density of its cell wall solid (ρ_s).

Gibson and Ashby (1982) modeled three-dimensional open cell foam as a cubic array of solid members of length l and square cross section of side t (Figure 2.2.4). Adjoining cells are staggered so that their members meet at their mid-points. The relative density of the cell, ρ/ρ_s, is in direct proportion to the $(t/l)^2$. If the cell-wall material has a plastic yield point, then the foam as a whole may show plastic behaviour. Plastic collapse occurs when every point on a cross section of a member has reached the compressive strength, σ_S, of the cell wall material. The fully plastic moment, M_p, is

$$M_p = \frac{1}{4}\sigma_S t^2 l \qquad (2.3)$$

If a force F acts in bending on a member of the length l in a cellular material, the maximum moment in the member is proportional to Fl, and the overall plastic collapse stress for the foam, σ_c, is proportional to F/l^2, i.e., proportional to M_p/l^3, Combining these expressions gives

$$\frac{\sigma_C}{\sigma_S} = C\left(\frac{\rho}{\rho_S}\right)^n \tag{2.4}$$

where C is a constant for the geometric effect, and n is the density exponent, which is a constant giving the relative density dependence of the compressive strength of a porous material. For the model open-cell porous material, $n = 3/2$.

The compressive strength of actual porous metals is affected by many factors. The factors for porous metals produced by sintering include metal matrix, relative density (or porosity), pore size, pore shape, compaction pressure, sintering temperature and sintering time. Obviously, the compressive strength of the porous metals increases with the compressive strength of the metal matrix and relative density. The geometric effect constant C maybe affected by pore size and pore shape. The density exponent n may be affected by the integrity of the cell struts, which increases with increasing compaction pressure, sintering temperature and sintering time. Other variables, such as the geometrical arrangement of the cell elements, may also be important. The values of C and n may depend on whether the material is periodic or not.

Gibson and Ashby (1997) reviewed the compressive strength of several Al and Al alloy foams and concluded that the scaling law (equation 2.4) holds for metal alloy foams, with $C \approx 0.3$ and $n = 3/2$ for the above Al and Al alloy foams.

Table 2.2 Relative density, compressive strength and scaling law parameters for various porous metals.

Material	Relative density	Compressive strength (MPa)	C	n
Al–7Si–0.3Mg (SiC) [1]	0.03–0.14	0.063–2.9	0.25	2.5
Al [2]	0.06–0.14	0.4–2.1	0.26	2.4
Al–7Mg [2]	0.05–0.21	0.7–13.2	0.27	2.1
Al 7075 [2]	0.1–0.21	1.5–13.5	0.21	2.6
Al–6Si–4Cu [3]	0.07–0.29	5.9–23.7	0.32	1.89
Zn–4Cu [3]	0.14–0.27	5.8–21.2	0.34	2.01
Al (SiC) [4]	0.1–0.2	0.64–2.57	0.3	1.5
Al [5]	0.1–0.25	1.7–11.4	0.29	1.9
Al [6]	0.19–0.27	0.79–1.6	0.27	1.63
Al [7]	0.19–0.31	2.2–6.9	0.28	2.5
Al (spherical pore) [8]	0.075–0.26	0.11–1.6	0.25	2.3
Al (angular pore) [8]	0.1–0.24	0.17–1.17	0.25	2.3
Cu (5 μm) [9]	0.43–0.94	30–129	0.21	1.8
Cu (45 μm) [9]	0.43–0.65	28–45	0.22	1
Fe [10]	0.67–0.89	43–168	0.23	4.9
Cu–Sn [10]	0.61–0.83	53–129	0.24	2.9
Fe [11]	0.69–1.0	180–450	0.2	2.4

[1] Simone & Gibson, 1998; [2] Thornton & Magee, 1975; [3] Banhart & Baumeister, 1998; [4] Prakash *et al*, 1995; [5] Kunze *et al*, 1993; [6] Wen *et al*, 2004; [7] San Marchi & Mortensen, 2001; [8] Goodall *et al*, 2007; [9] Zhang & Wang, 2004; [10] Wang *et al*, 2001; [11] Silva & Ramesh, 1997.

Table 2.2 summarises the relative density, compressive strength, and the geometric constant, C, and density exponent, n, for a range of metallic foams reported in the literature. The C values for all the materials are in the range of 0.2 to 0.35. The work

of goodall *et al* (2007) showed that pore shape does not affect C. The n values of the materials with periodic pore structure (Prakash *et al*, 1995; Kunze *et al*, 1993; Wen *et al*, 2004; Zhang & Wang, 2004;) are close to 3/2, while the other porous materials with disordered structures have higher n values. It is interesting to note from Table 2.2 that for porous metals with low relative density in the range of 0.03-0.3 the values of n are in a relatively small range of 1.5–2.6 and for porous metals with higher relative density in the range of 0.3-1, there is a large variation in the n values from 1.0 to 4.9. This may be because the geometry and denseness of the cell struts are more varied with a higher relative density.

When the porous materials have low relative densities, experimental results indicate that elastic modulus (E) is related to density (ρ) through the relation (Gibson & Ashby, 1988):

$$\frac{E}{E_S} = C'\left(\frac{\rho}{\rho_s}\right)^{n'} \tag{2.5}$$

where E_s is the elastic modulus of the solid material. The value of n' is generally in the range 1-4. For the model open-cell porous material shown in Figure 2.2.4, $n' = 2$ (Gibson & Ashby, 1988). Gibson and Ashby (1997) determined the C' and n' values for several Al and Al alloy foams and found that the scaling law (Equation 2.5) holds for the foams with $C' \approx 1$ and $n' = 2$.

Table 2.3 summarises the relative density and elastic modulus, and the C' and n' values for a range of porous materials reported in the literature. The C' values of the

materials produced by liquid state processes (Gibson & Ashby, 1982; Hagiwara & Green, 1987; Simone & Gibson, 1998) are close to 1 and *n'* values are close to 2. The *C'* of the materials produced by the solid state processes (Zhang & Wang, 2004; Friedl *et al*, 2007) are lower than 0.75 and the *n'* values are higher than 2.5. This may be because the cell struts of the materials produced by the solid state process are not as dense as those produced by the liquid state processes.

Table 2.3 Relative density, elastic modulus and scaling law parameters for various porous metals.

Material	Relative density	Elastic modulus (MPa)	*C'*	*n'*
Polyurethane [1]	0.01-0.05	0.4 - 3.2	0.89	2.1
Al foam [2]	0.08-0.3	3 - 24	0.92	2.4
Alporas foams [3]	0.02-0.15	140 - 700	0.91	2.3
Porous Cu 5μm [4]	0.65-0.92	6000 - 115000	0.67	2.7
Porous Cu 45μm [4]	0.42-0.65	1200 - 6400	0.68	2.7
Porous Ti [4]	0.1-0.65	3000 - 11000	0.74	2.4
Porous HS-316L [5]	0.04-0.08	200-640	0.73	4.3

[1] Gibson & Ashby, 1982; [2] Hagiwara & Green, 1987; [3] Simone & Gibson, 1998; [4] Zhang & Wang, 2004; [5] Friedl *et al*, 2007.

2.3 Acoustic Properties

2.3.1 Absorption of sound at surface

Sound energy is the vibration of air particles and can be dissipated in the form of heat. When a sound wave travels through air and hits a surface covered with an acoustical material, a component of the sound wave is reflected to the air and another part of sound wave is transmitted into the acoustical material. A result of the reflection is the heat loss in the air, which is significant at high frequencies (Everest, 2001) but very poor at low frequencies (Evans & Bazley, 1964). The velocities of sound wave in the material and air are different because of the different densities of the material and air. At the air/material interface, the direction of sound wave travel will be refracted due to the difference of sound velocities between the material and air. When the sound wave penetrates the material, friction between the vibrating air particles and the material will cause more energy loss in the form of heat.

The amount of sound absorbed by a material depends on its structure. Solid acoustic materials yield slightly by the fact that they are never perfectly rigid. When the sound wave hits solid materials, the air flow causes the structure to vibrate. Porous materials allow a certain amount of air to transmit across the surface of the structure, generating an effective motion of the surface. The reaction of the surface can be described in terms of its specific surface impedance, which is the ratio between the pressure at the

surface and the normal velocity at the surface (Morse, 1948).

Another measure of a material's acoustic absorption is its absorption coefficient (Morse 1948). There are two kinds of absorption coefficient: the Sabine absorption coefficient, a, and the energy absorption coefficient, α. The Sabine absorption coefficient is based on the arithmetic mean of a number of incident surfaces, and is defined as a fraction of acoustic power absorbed by a unit area. The energy absorption coefficient is defined as a fraction of the transmission sound wave energy at the surface of the material over the incidence sound wave energy. The Sabine absorption coefficient and the energy absorption coefficient are related by:

$$a = -\log(1-\alpha) \tag{2.5}$$

Another theory uses sound velocity in a porous material and its elastic modulus to predict its sound absorption behaviour (Gibson & Ashby, 1997). When the porosity of the porous material is very low (≤ 0.1), the velocity in the porous material can be calculated as $v = \sqrt{E/\rho}$, where E is the elastic modulus of the porous material, ρ is the density of the porous material, and v is the sound velocity in the porous material. The transmission and reflection part of sound energy in a porous material can be calculated by the acoustic impedance, Z, which is:

$$Z = \rho v = \sqrt{\rho E} \tag{2.6}$$

Sound frequency, pore size and pore shape do not affect the sound absorption properties of the porous material significantly when the porosity is low. The reflection coefficient, R_c, and the transmission coefficient, T_c, are calculated by surface impedance as:

$$R_c = \frac{Z - Z_0}{Z + Z_0},$$

$$T_c = 1 - R_c \tag{2.7}$$

where Z_0 is acoustic impedance of air ($= \rho_0 c_0$). ρ_0 is the density of air (1.186 kg/m^3), and c_0 is the velocity of sound in air (343 m/s).

This theory is not suitable for high porosity materials. When the material has a high porosity, sound velocity is affected by the elastic response of air in the pores and the reflection of the cell walls. A large amount of sound wave transmits across the hollows on the surface into the porous material, some part of which is reflected by the cell walls and transmits across the surface out from the porous material. The sound absorption properties of high porosity materials cannot be calculated by the transmission and reflection coefficients, as they are significantly affected by pore size, pore shape and thickness.

2.3.2 Sound absorption of porous materials

The acoustic absorption ability of porous materials mainly depends on the viscosity

resistance of air in the pores. Since sound wave is a kind of vibration of air particles and the energy of it can be transformed into heat (Pizzirusso, 1981), the air in open cells and pores has good acoustic resistance because friction between the vibrating air particles and the surface of pores will dissipate more energy in the form of heat. In fact, the sound energy dissipation has several mechanisms: air viscous losses when the air is pumped in and out of the porous material's cavities by sound pressure, mechanical damping in the structure of the porous materials by sound wave, thermo-elastic damping by heat exchange, Helmholtz resonance and vortex shedding from sharp edges. However, these mechanisms are difficult to analyze because the pores in the materials have complex structures.

The acoustic absorption properties of the porous structure depend on the frequency of the incident wave, the flow resistivity, the porosity and the effective air density (Morse, 1948). The flow resistivity, r_p, under steady-state conditions can be described by:

$$r_p = \frac{u_x}{d\Delta p} \tag{2.8}$$

where u_x is the volumetric airflow rate passing through the test specimens, Δp is the pressure drop across the porous material and d is the thickness of the material (Morse, 1948).

When the back face of the absorbing material is placed against an impervious backing,

the velocity of the sound wave adjacent to the backing will be zero. A sound wave entering the pores will cause the air pressure inside them to increase. If the pores within the material are small enough, the air within them can lose its heat to the pore walls.

When materials are selected specifically for sound absorbing purposes, highly permeable substances are the obvious choice. Open cell polymer foams and glass or mineral fiber materials are generally used. The disadvantage of using polymer foams is that they are flammable when subjected to high temperatures. Fibrous materials are generally regarded as excellent acoustic absorbers, but have a tendency to wear down and erode over time due to air flow and vibration within their structure (Degischer and Kriszt, 2002).

2.3.3 Sound absorption models for porous materials

2.3.3.1 Biot–Allard model

There are two kinds of dilatational waves in a homogeneous porous medium which is loaded by an acoustic wave (Biot, 1956a, b). The fast wave of propagation type is named as the wave of the first kind and the slow wave of diffusive type, which is highly attenuated at low frequencies, is named as the wave of the second kind. Expressions for the velocity and attenuation of shear waves and compression waves

were derived in terms of permeability, viscosity and elastic constant of rocks. Berrymann (1980) predicted the sound absorption behaviour of porous structures using the Biot theory. Plona (1980) identified the slow wave by experiments and found good agreement with the previous theoretical predictions.

Some acoustical parameters of porous materials required for the Biot theory, such as sinuosity, are relatively difficult to measure. Therefore, the acoustical models with least unknown parameters are desirable when a given accuracy of calculation can be satisfied. The Biot–Allard model (Allard, 1993) includes relatively few unknown parameters and has acceptable calculating accuracy. The sound absorption characteristics of porous sintered metals have been calculated using the model and validated by impedance tube measurements.

In the Biot–Allard model, a layer of equivalent fluid with the effective density, ρ_{eff}, and bulk modulus, K_{eff}, replaces a layer of porous material. The effective density, ρ_{eff}, and bulk modulus, K_{eff}, can be written, respectively, as:

$$\rho_{eff} = \alpha_\infty \rho_0 \left(1 + \frac{\sigma\phi}{i\omega\rho_0\alpha_\infty}\right)$$

$$K_{eff} = yP_0 / [y - (y-i)F(B^2\omega)] \qquad (2.9)$$

where

$$F(B^2\omega) = \left[1 + \frac{\sigma\varphi}{i\omega\omega^2\rho_0\alpha_\infty} G_c(s)\right]^{-1}$$

$$G_c(s) = \frac{s\sqrt{-i}}{4}\frac{j_1(s\sqrt{-i})}{j_0(s\sqrt{-i})}\Big/\left[1-\frac{2}{s\sqrt{-j}}\frac{j_1(s\sqrt{-i})}{j_0(s\sqrt{-i})}\right]$$

$$\mathrm{s} = \mathrm{c}\left(\frac{8\omega\rho_0\alpha_\infty}{\sigma\phi}\right)^{1/2} \tag{2.10}$$

In these equations, α_∞ is the sinuosity factor, ρ_0 the static density of air, σ the static flow resistivity, ϕ the porosity, ω the angular frequency of the excitation, c a shape factor, B^2 the Prandtl number and y the air specific heat ratio c_p / c_v; $j_0(\cdot)$ and $j_1(\cdot)$ are the Bessel functions of zero and first order, respectively, i^2=-1, and P_0 is the static pressure of air.

The characteristic impedance Z_c, complex wave number k, and the sound absorption coefficient α of porous materials at normal incidence can be calculated as:

$$Z_c = \sqrt{K_{eff}\rho_{eff}}$$

$$k = \omega\sqrt{\frac{\rho_{eff}}{K_{eff}}}$$

$$Z_f = Z_c \coth kd$$

$$\alpha = 1-\left|\frac{Z_f - Z_0}{Z_f + Z_0}\right|^2 \tag{2.11}$$

where Z_0 is the acoustic impedance of air, 414 Pa s/m at 18°C, Z_f is the acoustic impedance of the specimen, and d is the thickness of the specimen. This model is

suitable to calculate the acoustic absorption coefficient of rock and porous fiber materials.

2.3.3.2 Helmholtz resonators and viscous resistance

The Helmholtz resonator is a very simple concept to analyze the sound absorption behaviour of porous materials. It has been the subject of investigations for over 100 years, perhaps most notably by von Helmholtz, Lord Rayleigh and Ingard (1953). Helmholtz resonators can take two principal forms: single resonators or distributed resonators. All the resonators have two characteristic features in common: a cavity and a relatively small open neck through which the sound energy enters the cavity. In distributed Helmholtz resonators the cavity is shared by the resonator openings. The Helmholtz resonator is both an absorber and a scatterer. The sound absorption characters are determined by the system resistance, and can be predicted with reasonable accuracy. The system resistance is determined by considering the energy dissipation in the resonator system. The exact mechanisms involved in the energy dissipation in fluids are complex (Morse & Ingard, 1968), and include surface energy dissipation and fluid internal energy dissipation.

Surface energy dissipates by thermal conductivity and viscosity. The surface energy dissipations take place in thin layers close to the surfaces. The widths of thermal losses layer, d_h, and viscous losses layer, d_v, as given by Morse and Ingard (1968) are:

$$d_h = \sqrt{\frac{2\kappa}{\rho_0 \omega C_p}} \approx \frac{2.4\text{mm}}{\sqrt{f[\text{Hz}]}},$$

$$d_v = \sqrt{\frac{2\mu}{\rho_0 \omega}} \approx \frac{2.2\text{mm}}{\sqrt{f[\text{Hz}]}}, \tag{2.12}$$

where μ is the coefficient of viscosity of air (=17.9 μNs/m^2), κ is the thermal conductivity of air (=23.1 mW/Km), and C_p is heat capacity of air at constant pressure (=1.01J/Kkg).

The thermal resistance, R_h, and viscous resistance, R_v, of a surface area of ΔS, are:

$$R_h = \left(\frac{\gamma - 1}{\rho_0 c_0^{\,2}} \omega d_h \Delta S \right)^{-1}$$

$$R_v = \frac{1}{U^2} \rho_0 \omega d_v |v|^2 \Delta S = \frac{1}{U^2} \sqrt{2\mu\rho_0\omega} |v|^2 \Delta S \tag{2.13}$$

where U is the volume flow rate across the surface, γ is the ratio of specific heats of air (=1.4), ρ_0 is the density of air (=1.186 kg/m^3), c_0 is the velocity of sound in air (343 m/s), ω is the angular frequency (=$2\pi f$), and v is the sound velocity in porous material (=$\sqrt{E/\rho}$). Figure 2.3.1 shows the results of R_h, and R_v values for a porous metal specimen with a density of 7.1 g/cm^3 calculated by Equation (2.13). The thermal resistance decreases and the viscous resistance increases with increasing frequency.

The porous metal has a high thermal resistance and a low viscous resistance at the surface.

Fluid internal energy dissipation in porous materials is mainly determined by thermal conductivity, fluid viscosity and molecular energy equitation. The main part of the energy dissipation in Helmholtz resonators takes place inside the necks, where the velocity is highest. The amount of energy dissipation depends on the velocity profile in and around the resonator neck. Because this velocity profile is impossible to calculate analytically even for quite normal geometries, the prediction of dissipation is not trivial. Under the assumption of a large radius of curvature compared to the viscous boundary layer thickness and uniform flow in the neck, Ingard (1953) found analytically that the combined acoustic resistance R_n of a cylinder hole of radius r_{ca} and neck length l is:

$$R_n = \frac{1}{\pi r_{ca}^{\ 2}} \sqrt{2\mu\rho_0\omega} \frac{1}{r_{ca}} (l + r_{ca}) \tag{2.14}$$

This equation is suitable for calculating the acoustic resistance of lotus-type porous metals. The viscous resistance at the neck of the Helmholtz resonator, R_v', was given by:

$$R_v' = \frac{2}{\pi r_{ca}^{\ 2}} \rho_0 \omega d_v \tag{2.15}$$

As shown in Figure 2.3.2, the viscous resistance in the resonator neck is higher than the thermal resistance.

2.3.3.3 Equivalent Electrical Circuit Approach

The Equivalent Electrical Circuit Approach (EECA) is one of the most popular approaches in acoustic system analysis. Munjal (1987) found that there is a correspondence between the impedance approach in acoustical systems and the frequency-domain analysis of electrical transmission networks. The sound pressure is analogous to the electromotive force, particle velocity to electrical current, acoustic impedance to electrical impedance, flow resistance to electrical resistance, inertance to inductance, and compliance to capacitance.

2.3.4 Measurements of acoustic absorption coefficient

There are three methods to measure the acoustic absorption coefficient of a material: the reverberation chamber method, the tone-burst method and the impedance tube method.

The reverberation chamber method consists of a large room with highly reflective walls, floor and ceiling. The high reflectivity of the internal wall chamber gives rise to

a very long reverberation time. The test process uses a large sample of the material laid on the floor of the chamber to test. The standard size of the sample used in this test is 8×9 Ft (Everest, 2001). The reverberation time is then measured and compared to the reverberation time of the empty chamber. The difference can be attributed to the amount of sound absorbed in the test sample, and the absorption coefficient can be calculated.

The tone-burst method can measure the sound absorption coefficient of a material at any desired angle of incidence (Everest, 2001). A sound pulse hits the sample surface from the desired angle and the magnitude of the reflected pulse is measured. The absorption coefficient can be calculated by the difference in intensity between the incident and reflected sound pulses. The system uses short pulses of sound, which make anechoic acoustical measurements possible in ordinary rooms. The short pulses allow the sound waves to be fired and measured before external interference has time to be detected.

The impedance tube method is a convenient way of measuring the acoustic absorption performance of small sized test samples (Everest, 2001). This method is generally used to measure the performance of porous materials. The method employs the same basic theory as with the tone-burst method, in that it measures the difference in intensity between an incident and reflected sound wave. A disadvantage of using this measurement process is that the incident sound source is directed in one direction

down the impedance tube to the test sample. The direction of the incident wave is therefore only in one direction, normal to the surface of the absorber. In reality, the source of sound comes from all directions and the absorption of sound waves arriving from different angles of incidence cannot be measured.

2.3.5 Acoustic properties of porous materials

2.3.5.1 Non-rigid porous materials

Wassilieff (1996) measured the sound absorption coefficients of materials made from compressed Pinus radiata wood fibers with a medium comprised of slit shaped apertures. The results are shown in Figure 2.3.3. Raylrigh model was used to predict acoustic properties of porous materials by modelling the air space within the material as parallel cylindrical pores. Agreement between measurement and Raylrigh model for commercial particle board was possible only with very high assumed values for tortuosity. An empirical relationship between the bulk density of the fibers, and the porosity, airflow resistivity and tortuosity, has been established.

Zhou *et al* (2006) studied sound absorption coefficients of polymer materials composed of polymer micro-particles and polyurethane foam by impedance tube method. The sound absorption coefficients of the polymer materials are shown in Figure 2.3.4. Their measurements showed that polymer micro-particles have a strong

effect on the absorption performance of the composite materials because of their microstructures. The sound energy attenuation in polymer micro-particles material may most likely consist of two parts, viscous attenuation of air inside the pores and the friction energy caused by the oscillation of polymer particles. The average sound absorption coefficient of the polymer micro-particles materials is 0.4 and the maximum is up to 0.92. In the low-frequency region, it has a higher sound absorption coefficient than porous sound absorption materials such as PU foam with the same thickness.

Ismail *et al* (2010) measured the sound absorption coefficients of the Arenga pinnata natural fiber material with different thicknesses by the impedance tube method. The results (Figure 2.3.5) showed that sound absorption coefficients of Arenga pinnata from 2000 Hz to 5000 Hz, being within the range of 0.75 – 0.90. The optimum sound absorption coefficient was obtained from the thickness of 40 mm.

A large amount of sound absorption measurement work of non-rigid porous materials has been conducted in the past forty years. Ma (1983) collected the sound absorption coefficients of a range of materials, which is shown in Table 2.4.

Table 2.4 Sound absorption coefficients of non-rigid porous materials.

Materials	Thickness (cm)	Sound absorption coefficients / Frequency					NRC
		250Hz	500Hz	1000Hz	2000Hz	4000Hz	
Wood fiber	3	0.045	0.036	0.087	0.042	0.058	0.05
Sugarcane fiber	3	0.19	0.28	0.44	0.76	0.88	0.42
Bakelite	3	0.11	0.26	0.61	0.93	0.97	0.48
Polyurethane	5	0.28	0.78	0.79	0.81	0.84	0.67
Carpet	2	0.06	0.15	0.25	0.3	0.35	0.19
Velour	0.5	0.12	0.35	0.45	0.38	0.36	0.33
Arenga pinnata	4	0.11	0.14	0.27	0.78	0.83	0.33
Three-ply board	3	0.12	0.11	0.1	0.16	0.19	0.12

2.3.5.2 Porous metals

Porous metals have good mechanical properties and the porous structure makes them ideal contenders for acoustic absorption applications for use in hostile surroundings (Han *et al*, 2003). A main parameter affecting the acoustic absorption properties is the air-flow resistance of the porous metals. In the case of open cell porous metals, the air flowing into the absorber is able to penetrate the pores and interstices within the structure, so that the energy can be dissipated. Generally, open cell porous metals exhibit good acoustic absorption characteristics (Davies & Zhen, 1983). Porous metals with closed pores are generally poor absorbers because the air flow is unable to penetrate the internal pores of the structure.

Lu *et al* (1999) studied a closed-cell aluminum alloy foam (Alporas) and concluded

that closed cell foams do not absorb sound well; however, the sound absorption behaviour can be enhanced when the foams are rolled or compressed so that the wall of the cells is broken and some cracks are formed on them. These cracks enable the air flow to penetrate in and out of the pores, so that the energy is dissipated more effectively. The sound absorption coefficients of the Al alloy foams with different porosities and pore sizes are shown in Figure 2.3.6.

The acoustic absorption behaviour of semi-open pore aluminum foams was also analyzed by Lu *et al* (2000). The semi-open pore aluminum foams were produced using a negative-pressure infiltration method, using a preform consisting of water soluble spherical particles. They measured acoustic absorption coefficient and static flow resistance of six samples and studied the effects of porosity, pore size and pore opening. They found that selected samples exhibit an acoustic absorption coefficient greater than 0.8 at frequencies between 800 and 2000Hz. There was no clear correlation between acoustic absorption coefficient and pore size or porosity of semi-open pore aluminum foams. A relationship was found between the acoustic absorption and the pore opening size, with the absorption coefficient increasing as the opening size decreases.

Han *et al* (2003) studied the acoustic absorption behaviour of open-cell aluminum foam samples manufactured by a melt infiltration process, with the porosity ranging between 57% and 61% and pore size ranging between 0.5mm and 3.5mm (Figure

2.3.7). These samples showed better sound absorption properties at high frequencies (>1000Hz) than commercial metal foams. They found that decreasing pore size and increasing foam thickness improve sound absorption. At low frequencies (<1000Hz), the absorption performance was enhanced by the introduction of an air-gap behind the absorber. The main sound dissipation mechanisms involved were viscous and thermal losses with no air gap present, and Helmholtz resonant absorption when an air-gap was present.

Berg *et al* (2003) measured the sound absorption coefficient of a series of aluminum foams. They made a comparison between open-cell pore structures and closed-cell pore structures with cracks on the cell wall. The open pore foams, with pore sizes between 2 mm and 3.5 mm exhibited a low air-flow resistance compared with typical absorber materials such as mineral fibers. The peak sound absorption coefficient is higher than 0.8. The sound absorption coefficient of the closed pore samples, which have a high air-flow resistance, was significantly lower than that of the open pore samples.

Kovacik *et al* (1999) studied the noise attenuation of a series of closed-cell aluminum foams with cracks on the cell wall. The dissipation of acoustic energy in the aluminum foam was predominantly due to friction in the cracks in the structure and the vibration of pore walls. The pore walls were thinner when the foams had higher porosities. The foams achieved higher loss factors because the foams had a large number of cracks in

the cell wall. They found that the absorption properties of metal foams could be improved significantly when particles were added into the porous matrix because of the additional interfaces introduced to the structure.

Wu *et al* (2002) extended this idea in their research on the acoustic absorption properties of aluminum matrix composite foams (closed-cell, melt foaming method) and porous A356/SiC (open-cell, casting around space holder method). The results are shown in Figure 2.3.8. They found that the A356/SiC foams had better damping and sound absorption qualities than aluminum foams because of the large amount of Al/SiC interfaces in the matrix, where the interfaces could improve the absorption of vibration energy.

Albracht and Lotze (1999) investigated the acoustic behaviour of melt extracted and commercially available metal fibers. The acoustic absorption coefficient was determined over a frequency range of 200Hz to 2000Hz, on both sintered and non-sintered test specimens. They reported that the sintering process degraded the acoustic absorption capabilities of the metal fiber networks.

Xie *et al* (2004) studied the acoustic absorption of a lotus-type porous copper with the porosity range between 30% and 62%, and pore size range between 270 μm and 867 μm. The sound absorption coefficients of Cu foams with different porosities and pore sizes are shown in Figure 2.3.9. The sound absorption coefficient increased with

increasing frequency, porosity and specimen thickness, and decreased with increasing pore size. They found that when the thickness of the sample was increased to above 20 mm, the pores became more difficult to permeate as the length of elongated pores was limited in this type of porous copper.

The sound absorption coefficients of some metallic foam in the literature are summarized in Table 2.5. Noise Reduction Coefficient (NRC), which is the arithmetic average of the absorption coefficients at the frequencies of 250, 500, 1000 and 2000 Hz, is also listed (Bell, 1982).

Porosity has a significant effect on the sound absorption ability of the metallic foams. The sound absorption coefficient of the Alporas foam with 91% porosity is higher than that with 87% and 85% porosity at the frequency range 200-1500Hz, as shown in Figure 2.3.3 (Lu *et al*, 1999). Al-SiC foam with 85% porosity shows a higher sound absorption coefficient than that with 80% porosity at the frequency range 200-1600Hz (Wu *et al*, 2002). The sound absorption coefficient of the lotus-type Cu foams with 62% porosity is higher than that with 43% porosity at low frequencies, as shown in Figure 2.3.6 (Xie *et al*, 2004). These results show that sound absorption coefficient of porous materials increases with increasing porosity at low frequencies (<1600Hz).

Table 2.5 Sound absorption coefficients of metallic foams.

	Porosity (%)	Pore size (mm)	Sound absorption coefficient/Frequency (Hz)					NRC
			250	500	1000	2000	4000	
Alporas 10mm	91	2- 4	0.04	0.02	0.19	0.36		0.15
[1] 10mm	87	2- 4	0.05	0.03	0.16	0.5		0.19
10mm	85	2- 4	0.05	0.12	0.1	0.24		0.13
6mm	91	2- 4	0.02	0.02	0.06	0.38		0.12
20mm	91	2- 4	0.04	0.1	0.37	0.3		0.21
40mm	91	2- 4	0.08	0.35	0.22	0.3		0.24
50mm	91	2- 4	0.17	0.12	0.12	0.22		0.16
Al foam [2]	57	0.5	0.2	0.3	0.4	0.5	0.6	0.46
20mm	60	1.5	0.2	0.1	0.3	0.6	0.4	0.35
	59	2.5	0.05	0.05	0.2	0.3	0.5	0.3
	61	3.5	0.2	0.3	0.6	0.5	0.4	0.5
Al/SiC foam [3]	80	< 0.01	0.05	0.06	0.28	0.85	0.51	0.3
25mm	85	< 0.01	0.06	0.06	0.4	0.88	0.64	0.2
lotus-type Cu	62	0.38	0.04	0.03	0.14	0.16	0.92	0.12
[4]	55	0.38	0.04	0.03	0.04	0.16	0.82	0.08
10mm	43	0.38	0.04	0.03	0.06	0.16	0.78	0.07
	58	0.46	0.04	0.08	0.1	0.18	0.82	0.13
	58	0.55	0.04	0.08	0.1	0.14	0.76	0.11
	58	0.66	0.04	0.08	0.1	0.14	0.7	0.1

[1] Lu *et al*,1999; [2] Han *et al*, 2003; [3] Wu *et al*, 2002; [4] Bell, 1982.

The frequencies of peak sound absorption coefficient decreases with increasing thickness of foams. The peak sound absorption coefficient of the Alporas foams with thicknesses of 50mm and 10mm appeared at 400Hz and 1400Hz, respectively, as

shown in Figure 2.3.6 (Lu *et al*, 1999). Pore size does not affect the sound absorption coefficient very much. When the pore size of the Al foams increased from 0.5 mm to 3.5mm, the sound absorption coefficients did not show any significant changes with increasing pore sizes (Han *et al*, 2003). The matrix of solid foams also affects the sound absorption ability. Al-SiC foams have higher sound absorption coefficients than the Al foams at the low frequency range. The cell structure is also important for metallic foams. The Lotus-type porous copper with closed cells showed very poor sound absorption ability at the low frequency range (< 4000Hz).

2.3.5.3 Multi-layer assemblies

Acoustic absorbers composed of multi-layer-assembled porous materials can be applied to absorb broadband noise. The acoustic absorption of these assemblies is dependent very much on their constructions. Acoustic transmission analysis (ATA) methods have been developed for various multi-layer acoustic absorbers. Delany and Bazley (1970) expressed the characteristic impedance, $Z' = R' + jM'$, and complex wave propagation coefficient, $K = \alpha + j\beta$, for porous materials in terms of the flow resistivity r, wave number, air density ρ_0, sound velocity in air c_0 and sound frequency f for each layer as below:

$$R'_n = \rho_0 c_0 \left[1 + C_1 \left(\frac{\rho_0 f}{r_n} \right)^{C_2} \right]$$

$$M'_n = -\rho_0 c_0 \left[C_3 \left(\frac{\rho_0 f}{r_n} \right)^{C_4} \right]$$

$$\alpha_n = \frac{2\pi f}{c_0} \left[C_5 \left(\frac{\rho_0 f}{r_n} \right)^{C_6} \right]$$

$$\beta_n = \frac{2\pi f}{c_0} \left[1 + C_7 \left(\frac{\rho_0 f}{r_n} \right)^{C8} \right] \tag{2.16}$$

where n designates the nth layer, and C_1, C_2, C_3, C_4, C_5, C_6, C_7 and C_8 are constants of the nth layer of a homogeneous porous material, which can be determined by measurements. Empirical relations for the complex wave propagation coefficient K_n and characteristic impedance Z'_n can be expressed as (Huang, 1999):

$$Z'_n = \rho_0 c_0 \left[1 + C_1 \left(\frac{\rho_0 f}{r_n} \right)^{C_2} \right] - j\rho_0 c_0 \left[C_3 \left(\frac{\rho_0 f}{r_n} \right)^{C_4} \right]$$

$$K_n = \frac{\omega}{c_0} \left[C_5 \left(\frac{\rho_0 f}{r_n} \right)^{C_6} \right] + j \frac{\omega}{c_0} \left[1 + C_7 \left(\frac{\rho_0 f}{r_n} \right)^{C_8} \right] \tag{2.17}$$

The acoustic impedance of the nth layer of porous material backed with a rigid wall is:

$$Z_n = Z'_n \coth(K_n t_n), \tag{2.18}$$

where t_n is the thickness of the nth layer. For a multi-layer absorber composed of

porous materials, the normal incidence acoustic impedance at the surface of the multi-layer absorber can be calculated as (Zhu & Huang, 2005):

$$Z_{d+1} = Z'_{d+1} \frac{Z_d \cosh(K_{d+1} t_{d+1}) + Z'_{d+1} \sinh(K_{d+1} t_{d+1})}{Z_d \sinh(K_{d+1} t_{d+1}) + Z'_{d+1} \cosh(K_{d+1} t_{d+1})} \tag{2.19}$$

where d=1, 2, 3...n-1, and the normal incidence acoustic impedance of nth layer assembly is

$$Z_n = R_z + jM_z \tag{2.20}$$

where R_z and M_z are real component and imaginary component of the acoustic impedance, respectively. The ultimate sound absorption coefficient, α, is given by:

$$\alpha = \frac{4R_z}{(1 + R_z / \rho_0 c_0)^2 + (M_z / \rho_0 c_0)^2} \tag{2.21}$$

Beranek and Ver (1992) presented a compact expression for the acoustic impedance of perforated plates. The expression indicated that the influence factors include the thickness, hole radius, hole pitch and porosity of the perforated plates and the gas contained in the holes.

Davern (1977) conducted experiments on a three-layer assembly which contains a perforated plate, airspace and a porous material. The results showed that the porosity

and density of the porous material had a considerable effect on the acoustic impedance and absorption coefficient of the acoustic absorber. High acoustic absorption was only achieved in the frequency bands near the resonance frequency. Wu (1988) confirmed the above empirical expression (Eq. 2.17-2.21) for the porous materials by a large amount of experimental data.

Jinkyo *et al.* (1992) further studied assemblies with two layers of perforated plates backed with an airspace by the EECA approach. The results showed that an assembly would have better acoustic absorption than a single layer. For practical multi-layer-assembled acoustic absorbers, a complex assembly of many layers of perforated plates, airspaces and porous materials is usually employed.

Lee and Chen (2001) demonstrated the applicability and accuracy of the ATA method. This analysis can deal with a multi-layer acoustic absorber containing several components. Each component could include the layers of perforated plates, airspaces and porous materials. They calculated the acoustic impedance and acoustic absorption coefficient of four different types of multi-layer acoustic absorbers. The results showed that a lower porosity of the perforated plate has a lower acoustic resonance frequency and higher acoustic absorption effect. When the incident frequency is equal to the acoustic resonance frequency of the multi-layer acoustic absorber, the medium existing in the acoustic absorber will vibrate with the incident sound and the incident sound energy will be absorbed to a large extent.

Zhang and Chen (2009) studied a sintered fiber porous metal. The sound absorption coefficients and the specific surface acoustic impedances of one-layer porous fiber metal sheets, two-layer assemblies and three-layer assemblies were calculated using the Biot–Allard model and then compared with the corresponding measured values. The theoretical results obtained using the extended model fitted the measured ones well.

Dunn and Davern (1986) carried out an analytical analysis on the outer-layer, middle-layer and inner-layer of assembled porous materials. They suggested that the outer-layer should have a high porosity to encourage the incident sound to enter the composite structure, and the inner-layer should be a porous material with a high sound resistance to attenuate the sound wave energy and to prevent the incident sound from recombining.

2.4 Applications of Porous Metals

A number of variables affect the potential applications of porous metals. These include the base metal, pore type (open or closed cell), porosity, pore size, pore shape and connectivity and pore uniformity. These factors are all dependant on the manufacturing method used for producing the porous metal. Closed-pore structures are favored for applications where high specific strength, stiffness and energy

absorption are required. Open pore structures are more suitable for functional application such as acoustic and thermal management. The typical mechanical and acoustic applications are briefly described in this section.

2.4.1 Structural and mechanical applications

The mechanical properties of porous metals vary extensively, due to the existence of a number of structural variables. For this reason, it is difficult to limit them to certain characteristics and applications. Low density, combined with reasonable shear and fracture strength, makes porous metals ideal for sandwich construction. A sandwich structure consists of two face sheets, usually made from metals or composites, enclosing a sheet of porous metal. It can be used in self-supporting lightweight structures for the building and transport industries (Gibson & Ashby, 1997; Ashby *et al*, 2000; Banhart, 2001; Banhart *et al*, 2003).

The excellent energy absorption characteristics of porous metals, combined with good mechanical strength, make them ideally suited for use as internal and external impact protection in transport applications (Thiele, 1972). Metal foams could exploit their good isotropic properties and replace expensive honeycomb filler materials, which are currently widely used. Similarly, closed-cell porous metals can be used as lightweight decks and bulkheads in the marine industry. Porous metals can also be used as structural parts in aircraft, gearbox housings, motorcycle frames, aircraft crash

recorders, safety pads in systems for lifting and conveying and shock absorbing mounts (Dilley, 1974).

2.4.2 Acoustic applications

Porous metals have been utilized in the operation of high pressure gas-pipe lines for noise reduction. When gas is transported over large distances into local networks, the reduction in pressure produces a high intensity noise. Porous metal arrangements gently diffuse the gas, almost eliminating the noise (Bray, 1972). Porous metals have also been used as exhaust silencers for air tools and automobiles. High porosity porous copper sheet arrangements, with interleaved open-mesh nylon spacers, have been successfully used in noise reduction applications (Dilley, 1974).

Due to the relatively early stages of development, the number of current applications for the use of porous metals in acoustic absorption is low. A limited number of studies have been made regarding the acoustic absorption properties of porous metals; however, early results look promising.

2.5 Objectives of the Research

The early developments of the LCS process (Zhao *et al*, 2005; Tao *et al*, 2007; Zhang & Zhao, 2007) show that it can be used for many metals and it can control the porosity

and pore size of the porous metals accurately. However, the studies up to date are largely confined to porous copper. One objective of this thesis is to manufacture porous steel by LCS and investigate it's mechanical and properties as a function of manufacturing conditions.

The LCS process has two routes to produce porous metals: dissolution and decomposition. This thesis studied the mechanical properties of porous steel manufactured by these two routes, with different porosities, pore sizes, compaction pressures, sintering temperatures and times. The compressive strength, elastic modulus and flexural strength are measured and analyzed using the scaling law.

Thewsey (2009) has showed that porous copper produced by LCS has excellent sound absorption properties. The study, however, did not touch upon the sound absorption mechanisms and no attempt was made to identify the optimum structures for sound absorption. Another objective of this thesis is to study the sound absorption properties of the LCS porous steel. The sound absorption coefficient of a single layer or a multi-layer assembly of the porous steel, with different porosities, pore sizes, pore shapes, thicknesses, metal matrixes and air-gap depths, will be measured and analyzed. The experimental result will be compared with the EECA model.

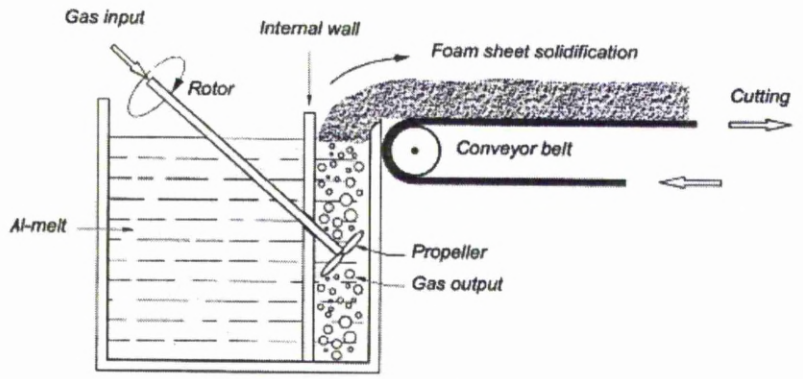

Figure 2.1.1 Melt foaming by gas injection. (Asholt, 1999)

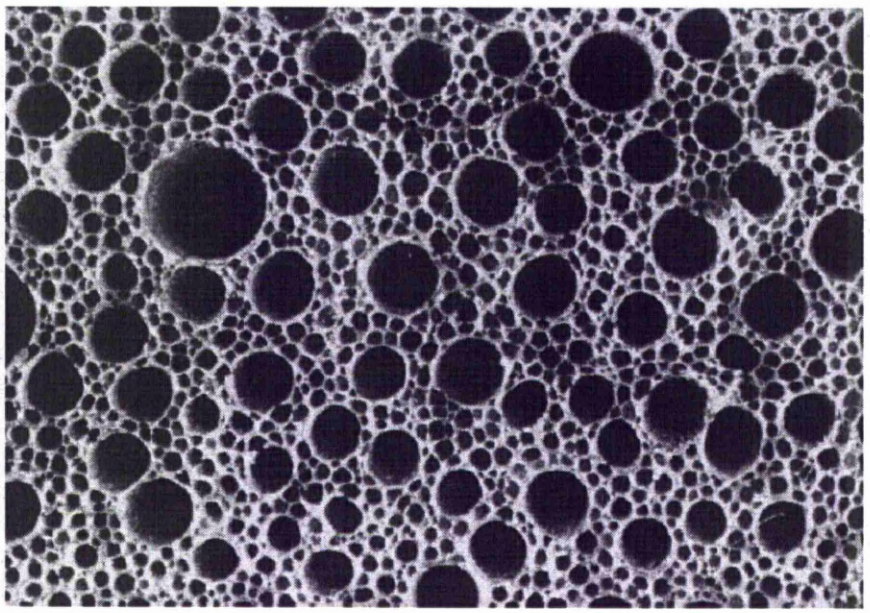

Figure 2.1.2 Porous structure of materials manufactured by Solid-gas eutectic solidification method. (Shapovalov, 1998)

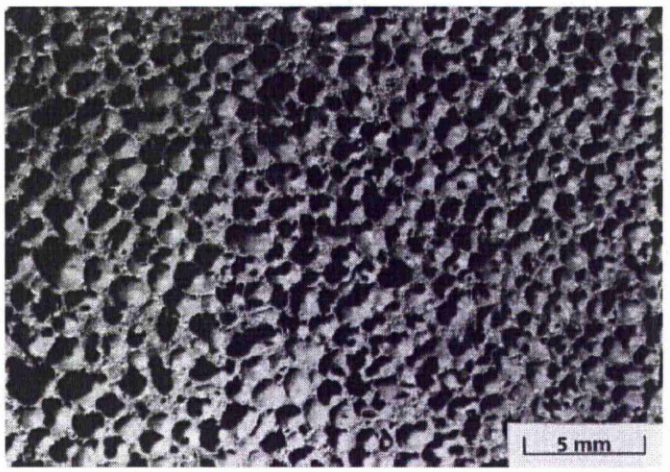

Figure 2.1.3 Porous structure of materials manufactured by powder compact melting method. (Banhart *et al*, 1995)

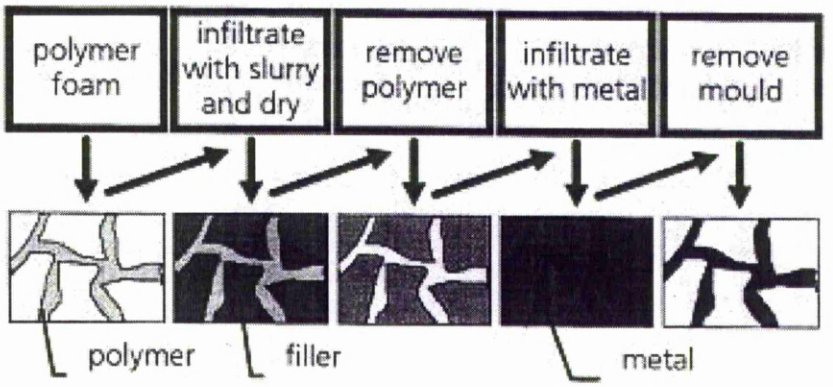

Figure 2.1.4 Production of porous metal by investment casting. (Banhart, 2001)

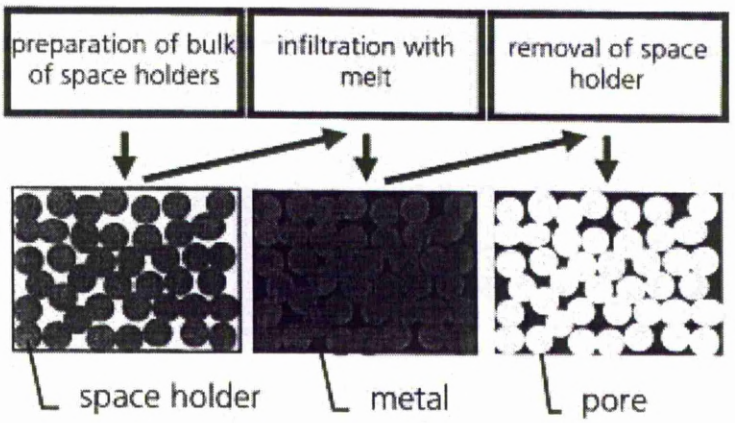

Figure 2.1.5 Production of porous metal by casting around space holder method. (Banhart, 2001)

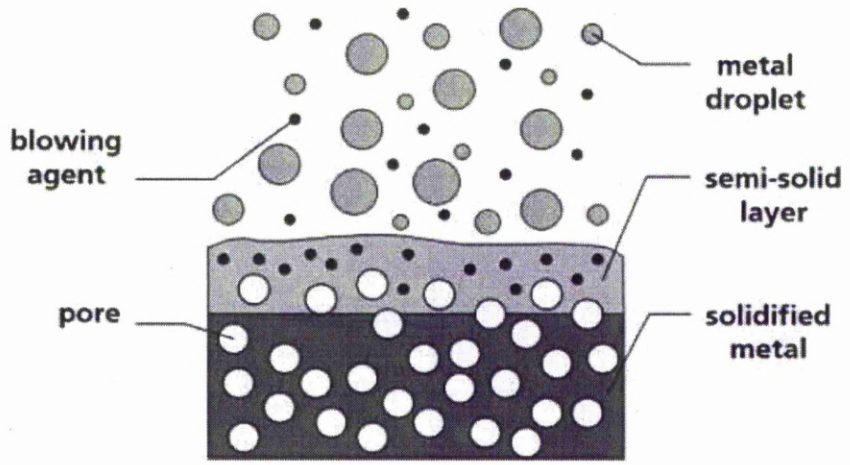

Figure 2.1.6 Production of porous metal by Spray forming method. (Banhart, 2001)

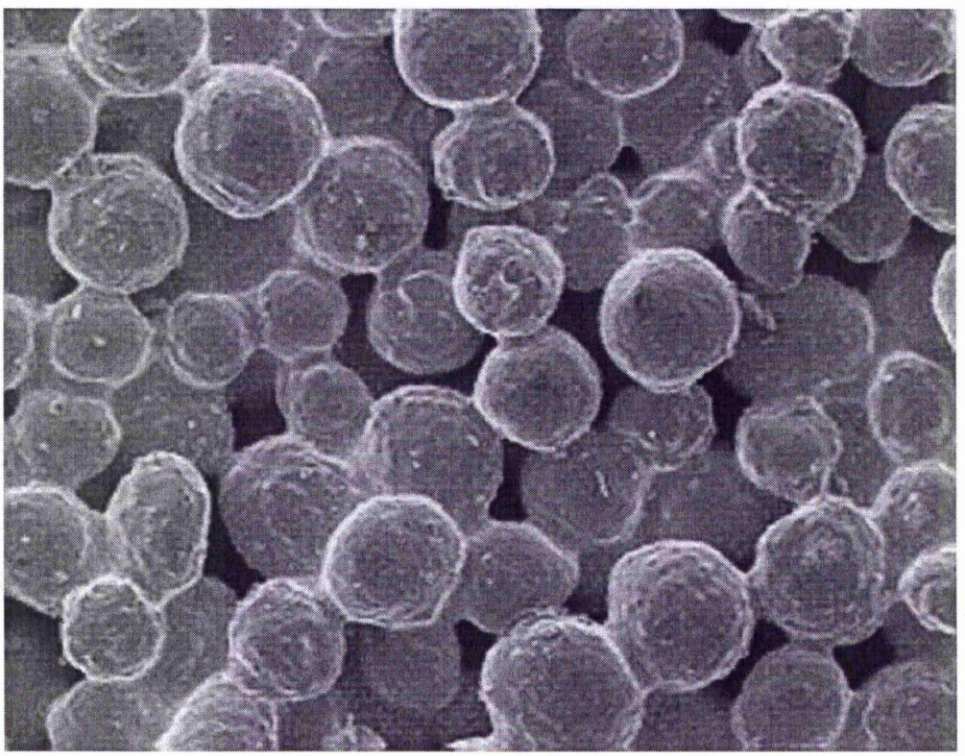

Figure 2.1.7 Porous structure of materials manufactured by powder sintering method. (Eisenmann, 1998)

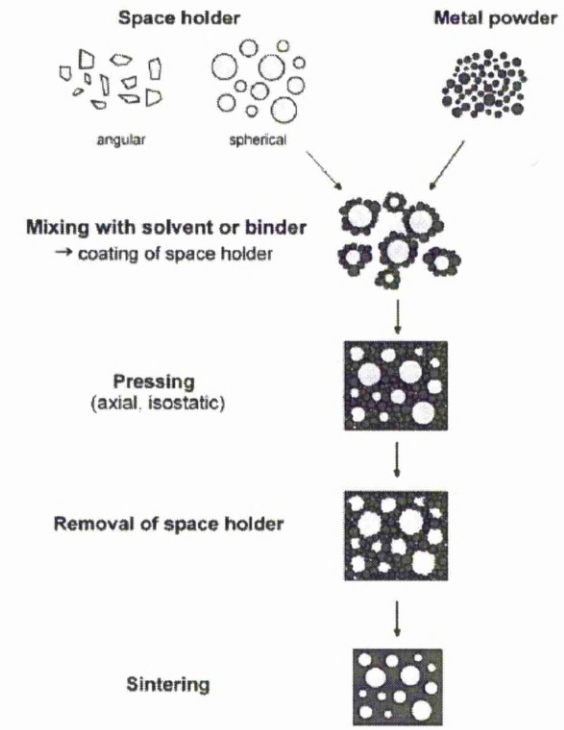

Figure 2.1.8 Production of porous metal by powder sintering around space holder method. (Banhart, 2001)

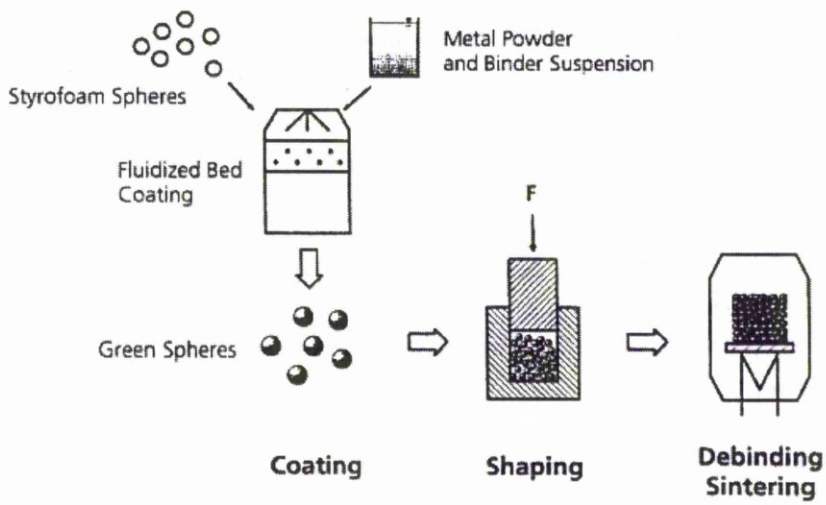

Figure 2.1.9 Production of porous metal by metallic hollow sphere foaming method.

(Andersen *et al*, 2000)

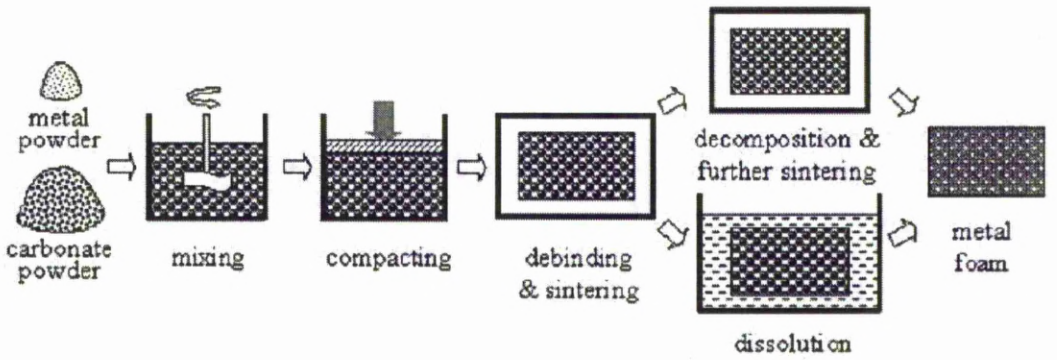

Figure 2.1.10 Schematic of the LCS process for manufacturing porous copper. (Zhao *et al*, 2005).

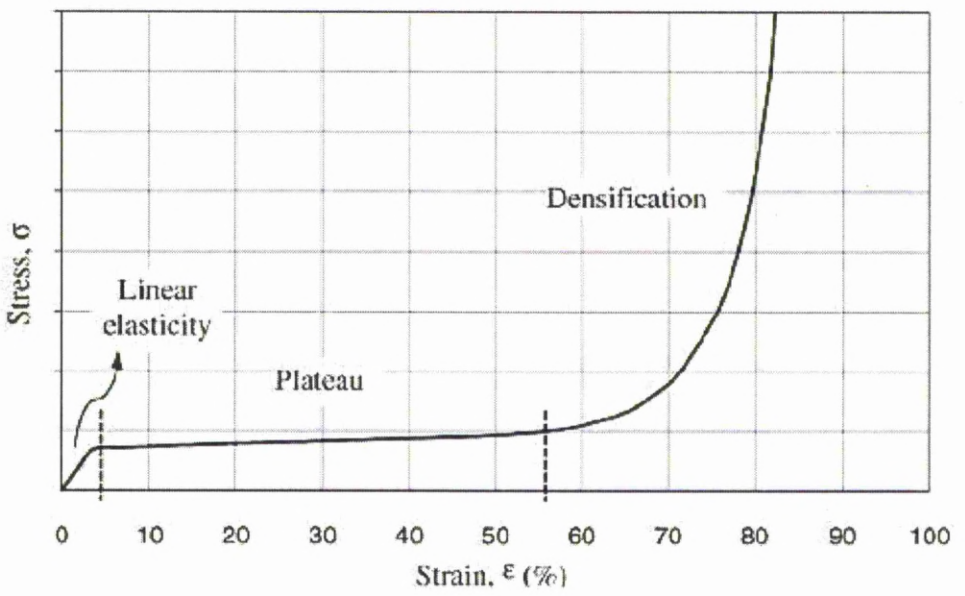

Figure 2.2.1 Typical stress-strain curve of porous metal (Theis, 2002).

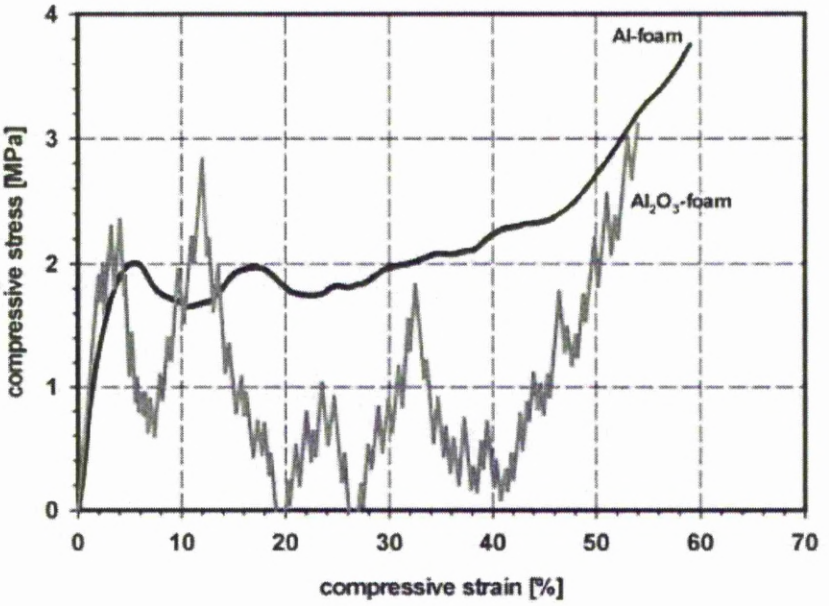

Figure 2.2.2 Stress-strain curves of Al foam and Al_2O_3 foam (Degischer & Kirszt, 2002).

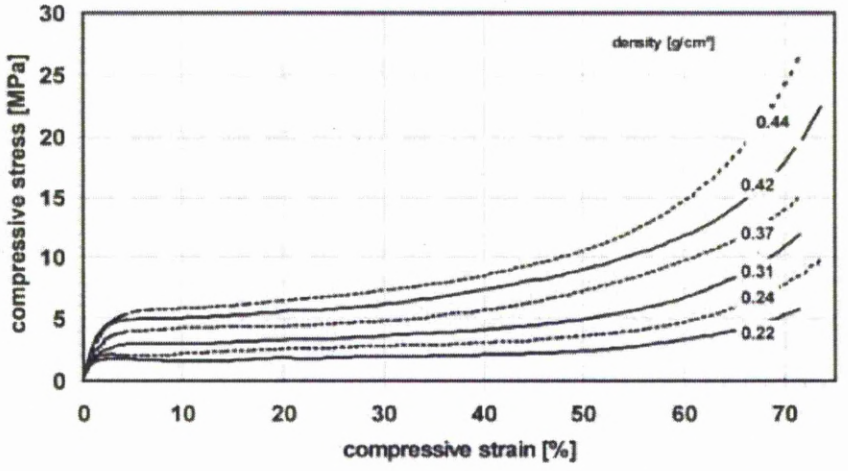

Figure 2.2.3 Stress-strain curves of Al foam with different densities (Degischer & Kirszt, 2002).

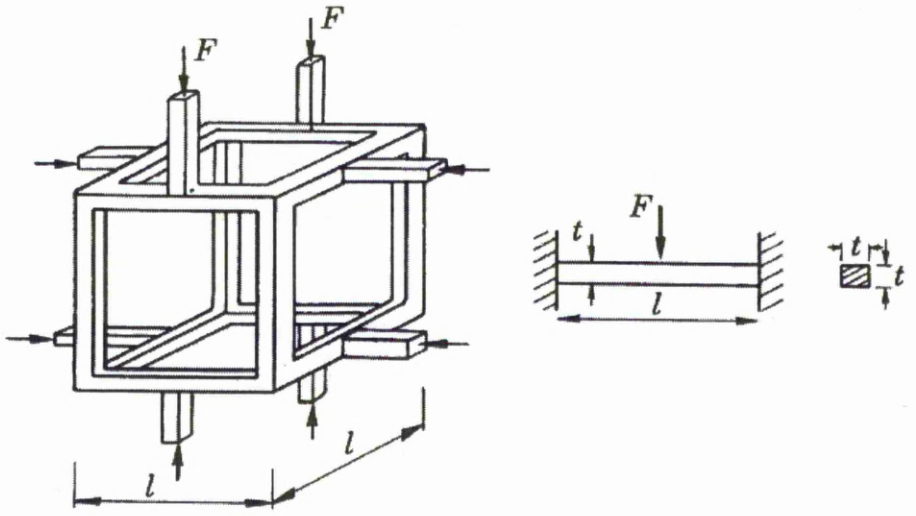

Figure 2.2.4 Cubic model of open-cell cellular material.

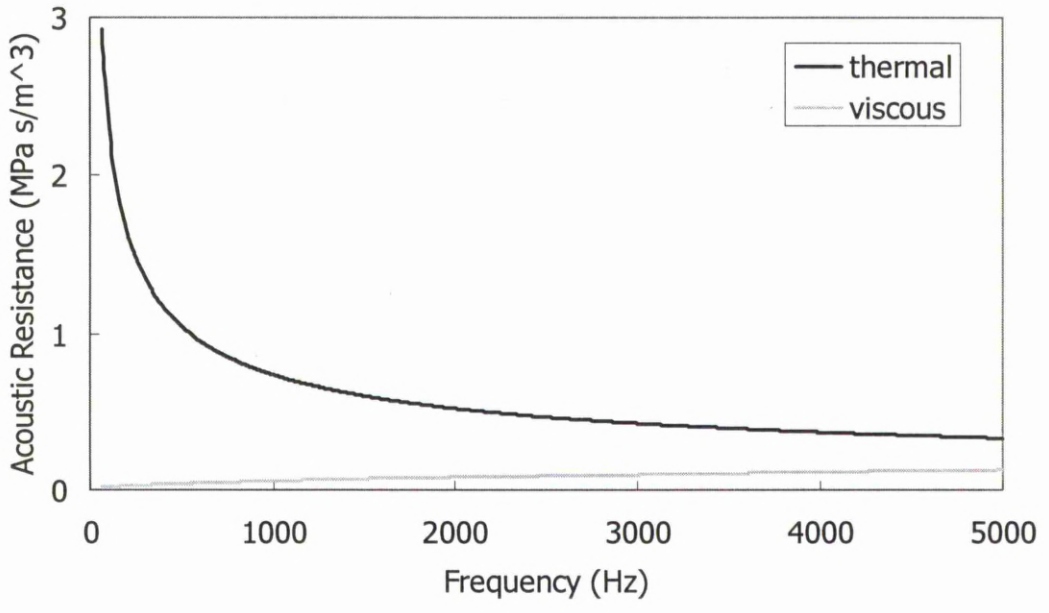

Figure 2.3.1 Thermal resistance and viscous resistance at the surface of a metal foam.

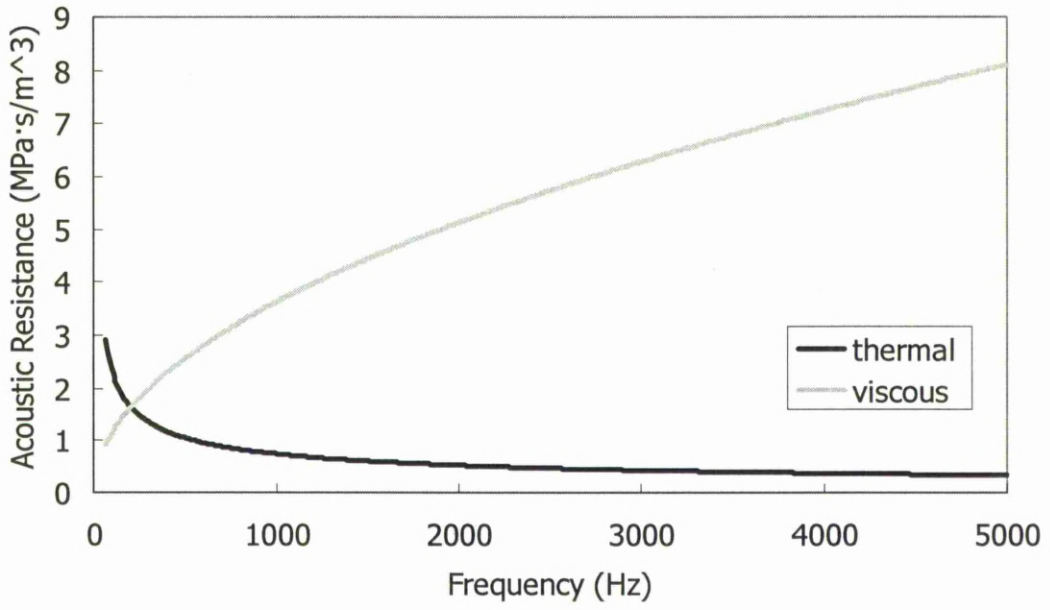

Figure 2.3.2 Thermal resistance and viscous resistance in the neck of a pore of metal foam.

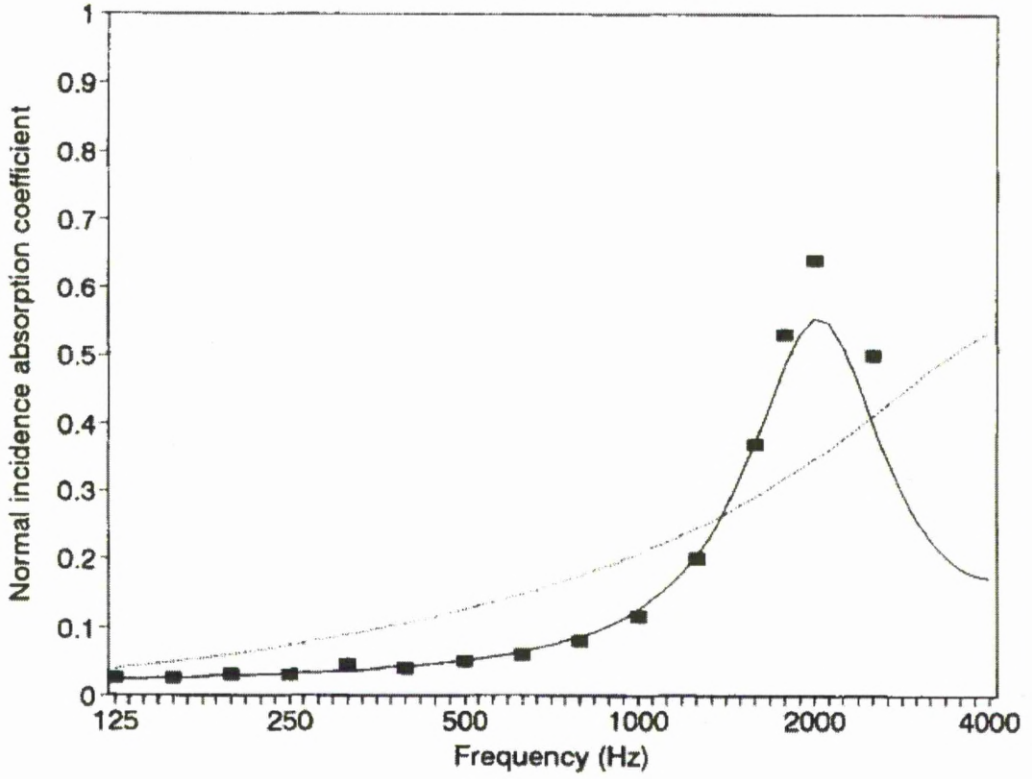

Figure 2.3.3 Sound absorption coefficient of 25 mm thick wood-wool panel bound by cement, tortuosity of 2.8 and porosity of 0.71. The solid curve is predicted from Raylrigh model (Wassilieff, 1996).

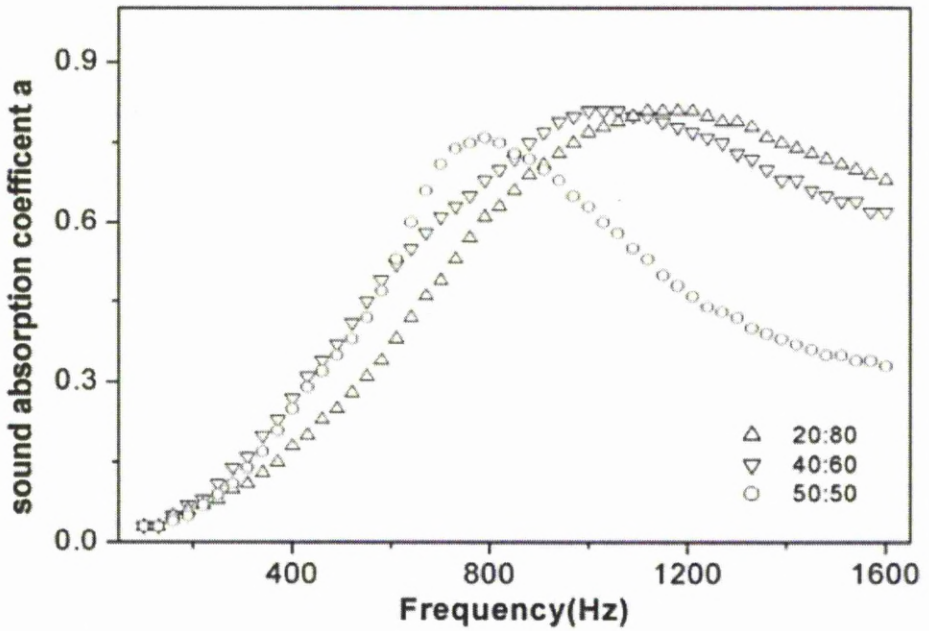

Figure 2.3.4 Sound absorption coefficient of PMMA/BA micro-particles, with a porosity of 80%, 60% or 50%, and a thickness of 20mm (Zhou *et al*, 2006).

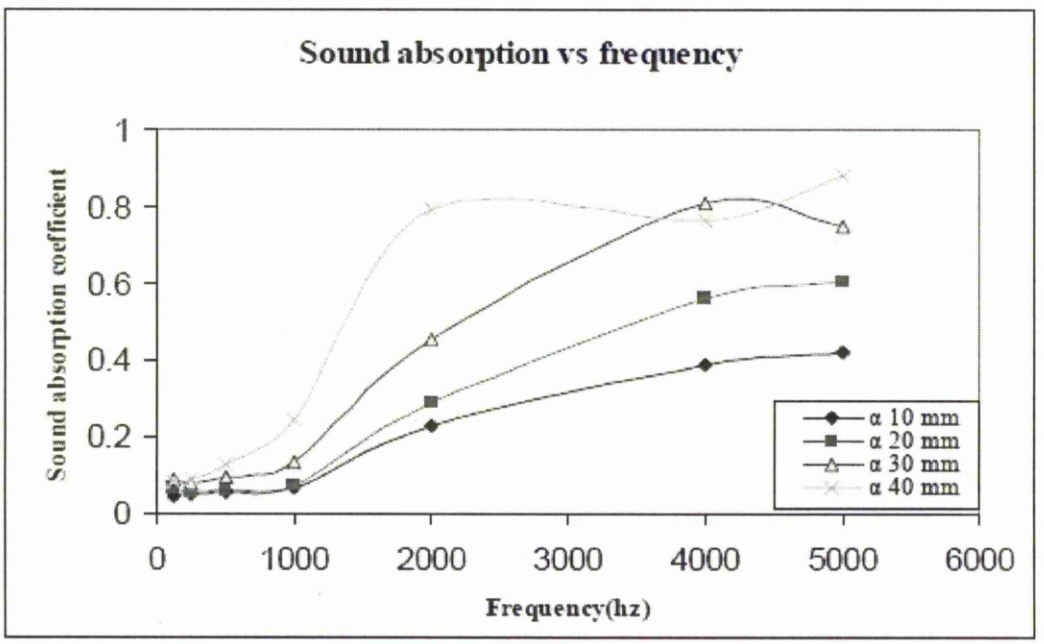

Figure 2.3.5 Sound absorption coefficients of Arenga pinnata fiber with different thicknesses (Ismail *et al*, 2010).

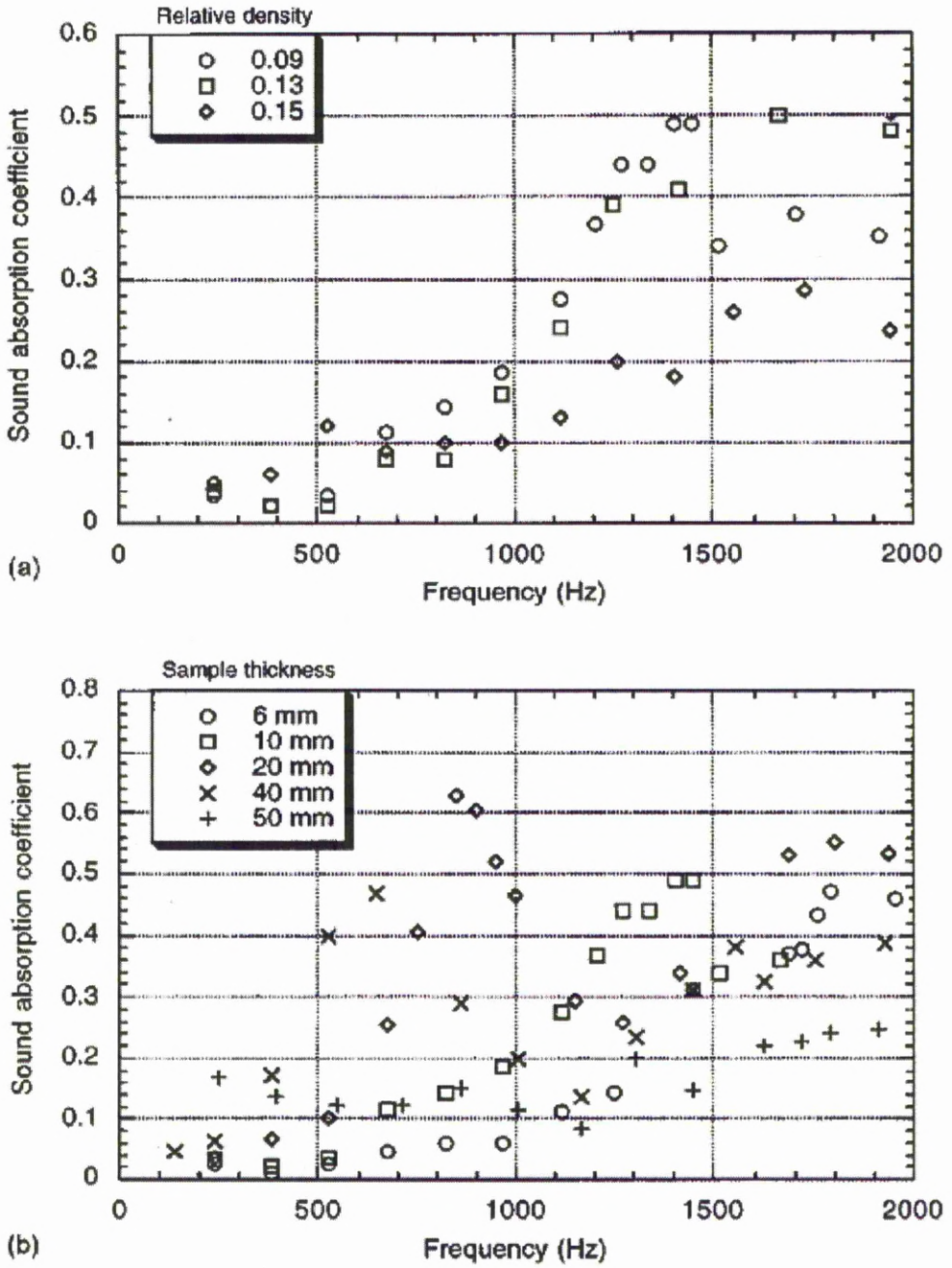

Figure 2.3.6 Sound absorption coefficient of Al alloy (Alporas) foam, with (a) different relative densities and a thickness of 10 mm and (b) different thicknesses and a relative density of 0.09 (Lu *et al*, 1999).

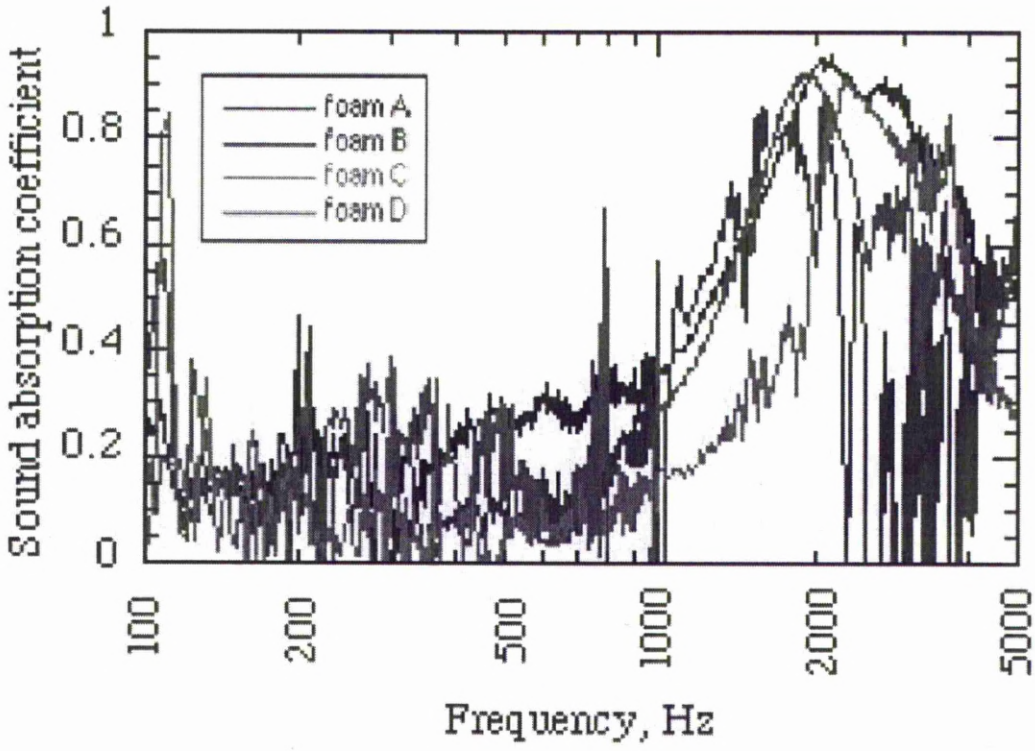

Figure 2.3.7 Sound absorption coefficient of open-cell Al foams with a sample thickness of 20mm. (A) 57% porosity, 0.5mm pore size; (B) 60% porosity, 1.5mm pore size; (C) 59% porosity, 2.5mm pore size; (D) 61% porosity, 3.5mm pore size (Han *et al*, 2003).

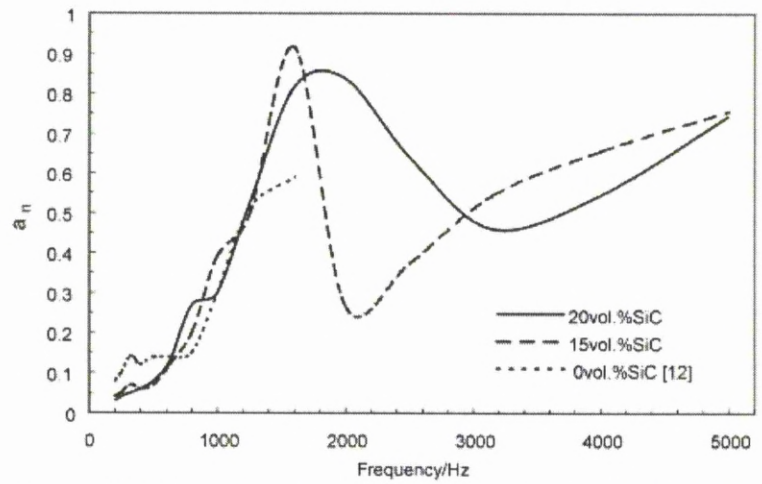

Figure 2.3.8 Sound absorption coefficient (a_n) of Al-SiC foam, with porosity 80% - 85%, thickness 25mm and pore size < 10 μm (Wu *et al*, 2002).

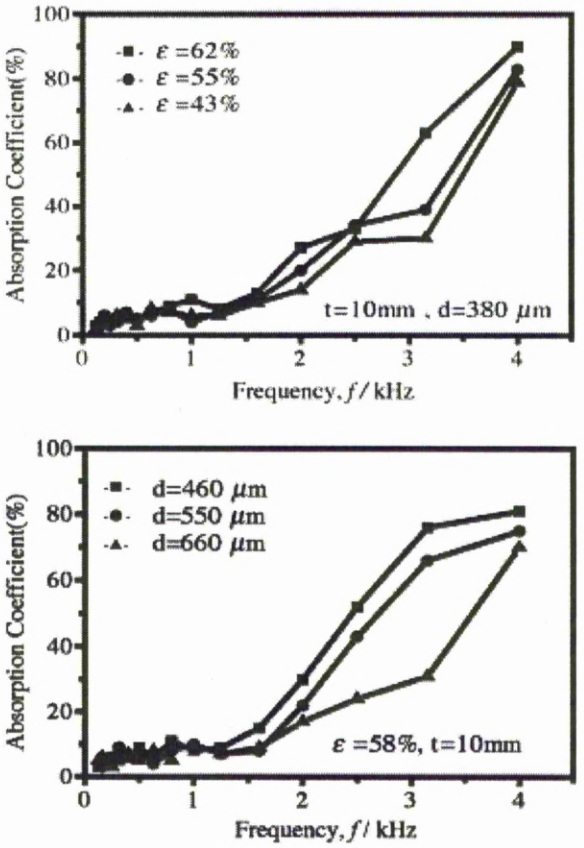

Figure 2.3.9 Sound absorption coefficient of lotus-type porous copper with different porosity ε and pore size d, and a fixed specimen thickness t (Xie *et al*,2004).

CHAPTER 3 EXPERIMENTAL

3.1 Fabrication of Specimens

The porous steel specimens used in this project were manufactured using the Lost Carbonate Sintering (LCS) process developed by Zhao *et al* (2005). As shown in Figures 3.1 and 3.2, the LCS process is a kind of metal powder sintering around space holder method. The potassium carbonate grains are used as the space holder and removed by hot water in the dissolution route and by high temperature in the decomposition route. The experimental procedures are described in detail in the following sections.

3.1.1 Raw materials

The potassium carbonate powder was chosen to be the space holder because of its excellent dissolution and decomposition properties. It was supplied by E&E Ltd and its morphology is shown in Figure 3.3. It has a purity of > 98%. The shape of the potassium carbonate granules is rounded. The particle size range of the carbonate granules was selected according to the required pore size of the final test specimens, as the pore shape and pore size of the specimens would be the same as those of the carbonate granules. The potassium carbonate granulates were sieved and divided into four different size ranges: 250-425μm, 525-710μm, 710-1000μm, and 1000-1500μm.

The Astaloy A steel powder has a high hardness, good corrosion resistance and low cost, and is particularly suitable for sintering. It was supplied by Höganäs (Sweden) and had a composition (wt %) of C (0.02%), Ni (1.88%), Mo (0.54%), Mn (0.20%) and the others (0.10%). The density of solid Astaloy A is 7.8g/cm^3. The powder particles have irregular shapes as shown in Figure 3.3. The particle size distribution is 150-250μm (9.3%), 106-150μm (18.8%), 75-106μm (19.1%), 45-75μm (29.0%) and <45μm (23.8%) by weight. The compressive strength, elastic modulus and flexural strength of the solid Astaloy A steel are 280MPa, 210GPa and 220MPa, respectively (Höganäs Handbook, 2002).

3.1.2 Preparation of containers

Steel cylindrical tubes were used as containers for the mixtures of steel powder and potassium carbonate granules for subsequent compaction and sintering, as shown in Figure 3.1. The sizes of the steel tubes depended on the final specimen sizes required, which were different for different tests. The steel tube wall was selected to be thick enough to withstand the force of the hydraulic press used in compaction. If it were not thick enough, the steel tube would bulge or distort during compaction. When the specimens had a diameter less than 30mm and the compaction pressure was less than 150MPa, the tube wall thickness was greater than 2mm. When the specimen had a diameter from 30mm to 51mm and the compaction pressure was 200MPa, the

thickness of the steel tube wall was greater than 4mm. The largest diameter of the specimens in this project was 100mm. In this case, the thickness of the steel tube wall was greater than 10mm when the compaction pressure was 200MPa.

The steel tubes were cut to lengths of 50-80mm using a hand saw. The internal surface of the tube was then smoothed by 1200 grit sand paper to prevent the final porous steel specimens from contamination of any impurities left on the internal walls. The steel tube was placed on a machined stainless steel plug and an amount of iron (Fe) powder was poured into the tube through a funnel. The amount of iron powder was chosen to achieve a 10mm seal after compaction. The iron powder had irregular particles with size less than 100μm. A stainless steel punch was subsequently inserted into the tube. The diameter of the punch was slightly smaller than the internal diameter of the tube so that the punch could slide in the tube. The iron powder was compacted by a hydraulic press at 100MPa to form a seal. The iron powder layer was used to prevent the mixture of steel powder and potassium carbonate powder from direct contact with air during the sintering process.

3.1.3 Mixing and compaction

According to the required final porosity of the porous steel specimen, the steel powder and potassium carbonate granules were mixed together in a specified ratio. The amount of steel and carbonate mixture was chosen to achieve a thickness of 5mm,

10mm, 20mm or 40mm after compaction. The mixture was poured into a plastic beaker and added with approximately 3-5% volume Ethanol which served as a binder between the steel and carbonate particles. The mixture was manually shaken and the plastic beaker was sealed during the mixing process to prevent the Ethanol from evaporation. The mixing process took approximately 1-2 minutes until no clear separation between the steel and potassium carbonate particles was seen. In order to prevent the seal iron layer and the porous steel specimen from being sintered together, 4-5 layers of paper were added to the top of the seal iron layer before the steel and carbonate mixture was put into the tube. The mixture of the steel and carbonate powders was poured into the tube by a funnel. The steel and carbonate mixture was compacted by a hydraulic press for ten seconds at a pressure of 50, 100, 150, 200, 250 or 300MPa. Three or four layers of mixtures with different volume ratios separated by paper layers were added in one tube. After all mixture layers were added into the steel tube, another layer of iron powder layer was poured on the top, also separated by a paper layer. The hydraulic press was used to compact the iron powder at a pressure of 100MPa to seal the top of the steel tube and to prevent the mixture layers from direct contact with air during sintering.

3.1.4 Dissolution route

Some specimens were manufactured by LCS via the dissolution route. The dissolution route included sintering, shaping and carbonate dissolution stages.

3.1.4.1 Sintering

Sintering took place in an electric furnace. The assembly of preform and tube was placed in the centre of the furnace in order to achieve maximum aeration and even heat distribution. The furnace was heated to the sintering temperature of 850°C, which normally took 2 hours to achieve from room temperature. The temperature was maintained at 850°C for 4 hours when the diameters of the specimen were 21 mm, 30 mm and 51 mm and 8 hours when the diameter of the final specimen was 100mm. This temperature was selected for the dissolution route because the melting point of potassium carbonate is 891°C so potassium carbonate would remain in the solid state. When the sintering process was complete, the assembly was moved from the furnace and cooled in air. It took 20-30 minutes to cool the assembly from 850°C to room temperature.

3.1.4.2 Preform shaping

The steel and carbonate preform was removed from the tube container after the sintering and cooling process using a hydraulic press. The tube was supported on a circular steel ring with an internal diameter of 1 mm greater than the diameter of the specimen and the preform and the sealing iron layers were pushed out from the tube by a punch.

The specimens were machined to the required sizes and shapes using a mechanical lathe and a hand saw. The surfaces of specimens were ground using sandpapers ranging from 400 to 2000 grit. All machining and grinding processes were carried out in dry conditions when the potassium carbonate was still within the preform. This was because potassium carbonate dissolves easily in water. The porous structure of the specimens would be damaged during the machining process if the potassium carbonate was removed.

3.1.4.3 Dissolution of potassium carbonate

The sintered preforms were placed in a running bath of hot water at a temperature of 90°C for a period of 4h to dissolve the potassium carbonate. Hot water was more effective than cold water in dissolving and removing potassium carbonate. The specimens were then dried in an electric furnace at 100°C for 1h. The specimens were finally removed from the furnace and cooled to room temperature.

3.1.4.4 Re-sintering

Some specimens were manufactured by an additional re-sintering step following the dissolution process. The specimens were first sintered by the dissolution route at 850°C for 4hrs. After potassium carbonate was dissolved, the specimens were sintered again at 1000°C for half hour.

3.1.5 Decomposition route

Some specimens were manufactured by LCS via the decomposition route. The decomposition route included sintering and shaping stages.

3.1.5.1 Sintering

The sintering stage took place in an electric furnace. The assembly of preform and tube was placed in the centre of the furnace in order to achieve maximum aeration and even heat distribution. In the decomposition route, the furnace was heated up to the sintering temperature of 1000°C, which normally took 2.5 hrs to achieve from room temperature. The temperature of furnace was maintained at 1000°C for 0.5hrs for specimens with diameters of 21mm, 30mm and 51mm. Because the melting and decomposition point of potassium carbonate is 891°C, the potassium carbonate decomposed to carbon dioxide (CO_2) and potassium oxide (K_2O) at 1000°C. The gaseous carbon dioxide pushed liquid potassium oxide and potassium carbonate out from the tube through the pores of the sealing iron layer. When the sintering process was complete, all the potassium carbonate was decomposed and removed, and a porous steel network was left. The assembly was moved out from the furnace and cooled in air. It just took 20-30 minutes to cool the assembly from 1000°C to room temperature.

In order to study the effects of sintering temperature and time in the LCS process, one group of specimens were sintered at different sintering temperatures of 950°C, 1000°C, 1050°C and 1100°C for a constant time of 0.5 hrs, and another group of specimens were sintered at 1000°C for different times of 0.5, 1, 2 and 3 hrs. These specimens had a relative density of 0.3 and a pore size range of 425-710μm and was compacted at 200 MPa.

3.1.5.2 Preform shaping

The specimens were removed from the tube container after the sintering and cooling process by cutting the tube open longitudinally using a milling machine. The depth of the cut was controlled to be exactly the thickness of the tube wall in order to avoid damaging the porous steel specimens. The specimens were finally machined to the required sizes and shapes using a hand saw. The surfaces of specimens were ground with sandpapers ranging from 400 to 2000 grit.

3.2 Property Tests

3.2.1 Density Measurements

The Archimedes method was used to measure the density of specimens. When the

specimens made by the dissolution route were measured, the specimens were soaked in alcohol before K_2CO_3 is dissolved to measure the volumes. The K_2CO_3 was then dissolved by hot water and the weights of the dried specimens were measured by an electronic balance with a precision of 0.005g. When the specimens made by the decomposition route were measured, the dry specimens were weighed by the electronic balance first. The pores of the specimens were then sealed by Vaseline and soaked into water to measure the volumes. When the dry weights, W, and volumes of the specimens, V, have been measured, the porosities of specimens were finally calculated as W/V.

3.2.2 Compression tests

The compression tests were carried out in an Instron 4505 machine. The specimens were cylindrical with a height of 30 mm and a diameter of 20 mm. The crosshead speed was 1mm/min. The load and displacement data were recorded by computer and the strain and stress values were calculated afterwards.

The elastic modulus (Young's modulus) of the porous material could not be obtained directly from the linear region of the stress-strain curve, because plastic deformation already occurred in the initial linear region. Therefore, loading-unloading have been used to determine the elastic modulus of the elastic-plastic material. The

loading-unloading curve is shown schematically in Figure 3.4. Due to stress concentrations caused by defects in the cellular structure of the porous steels, a small amount of plastic deformation can occur even at a very low stress level of loading and reloading (Simone & Gibson, 1998). The slope of the reloading stress strain curve is therefore not a true representation of the elastic modulus. The unloading slope remains roughly constant until the foam has been loaded to its plastic collapse stress. Therefore, the elastic modulus was taken as the unloading modulus, i.e. the slop of the unloading part of the stress-strain curve.

3.2.3 Flexure tests

Flexural strength measures the ability of a brittle material to resist deformation under bending. The flexural strength was measured using the three-point flexural test. In this method, a prismatic specimen with a rectangular cross section was bent until fracture. The flexural strength represented the highest stress experienced within the material at its moment of rupture.

The specimens used in the flexure test had a width of 10mm, a thickness of 10m and a length of at least 50mm for a span of 40mm, as shown in Figure 3.5. The specimen was placed in the test machine with the ends being supported by two rollers and the loading head at the centre of the beam. The loading head was lowered until a small compressive load was applied to the beam. The load was applied continuously at a

speed of approximately 1mm/min. The load-displacement curve was recorded.

The flexural strength was calculated by:

$$\sigma = \frac{3FL}{2bd^2} \tag{3.1}$$

where F is the load at break or yield, L is the span of specimen between the supports, b is the width and d is the thickness.

3.2.4 Airflow resistance tests

Airflow resistance is an important property of porous materials, related to acoustical properties. The airflow resistance, R, is defined as:

$$\mathrm{R} = \frac{\Delta p}{q_v} \tag{3.2}$$

where Δp (Pa) is the air pressure difference across the test specimen, and q_v (m^3/s) is the volumetric airflow rate passing through the test specimen. The specific airflow resistance, R_s, is defined as:

$$R_s = RA = \frac{\Delta p}{u} \tag{3.3}$$

where A (m^2) is the cross-sectional area of the test specimen perpendicular to the flow direction, and u (m/s) is the linear airflow velocity.

The airflow resistivity, r, which is more useful in theoretical models for the acoustic behaviour of materials, is defined as:

$$r = \frac{R_s}{d} \tag{3.4}$$

where d (m) is the thickness of the test specimen in the flow direction.

The airflow resistance tests were conducted on a purpose built apparatus, following the test procedure described in ISO 29053. A controlled unidirectional airflow was passed through the test specimen with a rectangular cross-section and the resulting pressure drop between the two free faces of the test specimen was measured, as shown in Figure 3.6.

The measurement cell has the same cross-sectioned size as the test specimen with the internal height of 5mm and width of 20 mm. The test specimen, with a length of 30mm was placed in the measurement cell, and the edges were sealed by a petroleum jelly. Compressed air was used to produce the airflow; a flow meter was used to measure the volumetric airflow rate at the exit side of the specimen. Two barometers were used to measure the pressure difference across the test specimen.

3.2.5 Acoustic tests

The standing wave tube method was used for the acoustic test and the transfer-function method was used to calculate the sound absorption coefficient of the porous steel specimens. This method reproduces measurements easily and quickly, and only requires cylindrical specimens with diameters of 30 mm or 100 mm. A comprehensive description of the standing wave tube method and calculation of the transfer-function can be found in EN ISO 10534-2:2001.

The measurement equipment consisted of an impedance tube, a test sample holder, two microphones, a signal generator, a portable two-channel Fast Fourier Transform (FFT) analyser, a power amplifier, a loudspeaker and a sound level detector, as shown in Figure 3.7. Two microphones were used to ensure that no phase mismatch between the two measurement places were present between the sample and the sound source. Different diameters of samples and tubes were used for different frequency ranges. The samples with a diameter of 30mm were used for the frequency range from 100Hz to1000Hz, and 100mm diameter samples were used for the range from 500Hz to 5000Hz. The samples either touched the back-plate at the end of impedance tube or had a 20mm or 50mm air-gap between the sample and back-plate. Vaseline was used to daub around the perimeter of samples to ensure that no gap was left between the

tube and the samples.

The test sample was mounted at one end of the impedance tube, and a sound source was mounted at another end. Plane waves were generated in the tube, and the sound pressures are measured at two locations near the sample by two microphones.

The measurement method is based on the principle that the sound reflection at normal incidence can be determined from the measured transfer function H_{12} between two microphone positions (x_1 and x_2) along the impedance tube. The transfer-function for the incident wave is given by:

$$H_I = \frac{P_{2I}}{P_{1I}} = e^{-jk_0(x_1-x_2)} = e^{-jk_0 s} \tag{3.5}$$

where $s = x_1 - x_2$. In the same way, the transfer-function for the reflected wave is given by:

$$H_R = \frac{P_{2R}}{P_{1R}} = e^{jk_0(x_1-x_2)} = e^{jk_0 s} \tag{3.6}$$

Combining H_I and H_R, the transfer-function for the complete sound field can be expressed as:

$$H_{12} = \frac{P_2}{P_1} = \frac{e^{jk_0x_2} + re^{-jk_0x_2}}{e^{jk_0x_1} + re^{-jk_0x_1}} \tag{3.7}$$

The sound reflection factor, r, can be written as:

$$r = \frac{H_{12} - H_1}{H_R - H_{12}} e^{2jk_0 x_1} \tag{3.8}$$

The sound absorption coefficient can be determined, in terms of the real and imaginary terms of r, r_r and r_i:

$$\alpha = 1 - |r|^2 = 1 - r_r^2 - r_i^2 \tag{3.9}$$

Five groups of specimens were used to study the effects of porosity, pore size, pore shape, thickness and metal matrix on the sound absorption of LCS porous steel. The first group of specimens had different nominal porosities of 60%, 65%, 70% and 75%, designated as X, L, M and H, respectively. The second group had different pore sizes of 250-425μm, 425-710μm, 710-1000μm and 1000-1500μm, designated as S, M, B and V, respectively. The third group had different pore shapes: sphere and rhombus. The fourth group had different thicknesses of 5mm, 10mm, 20mm and 40mm. The fifth group had different metal matrices of steel, copper and aluminium. Each type of specimens had two diameters of 30mm and 100mm for short and long sound wave lengths. The specimens in the first, second and fourth groups were added with different air-gaps of 20 and 50mm to study the effect of air-gap depth.

In order to study the sound absorption behaviour of LCS specimens with multi-layer assembled porous structures, various orders of assembly were tested. Each assembly is represented by a series of designation letters. For example, XH indicated that the first

(front) layer has a porosity of 60% and the second layer (rear) has a porosity of 75%. SMBV indicates that the first (front) layer has a pore size of 250-425μm, the second 425-710μm, the third 710-1000μm and the fourth (rear) 1000-1500μm.

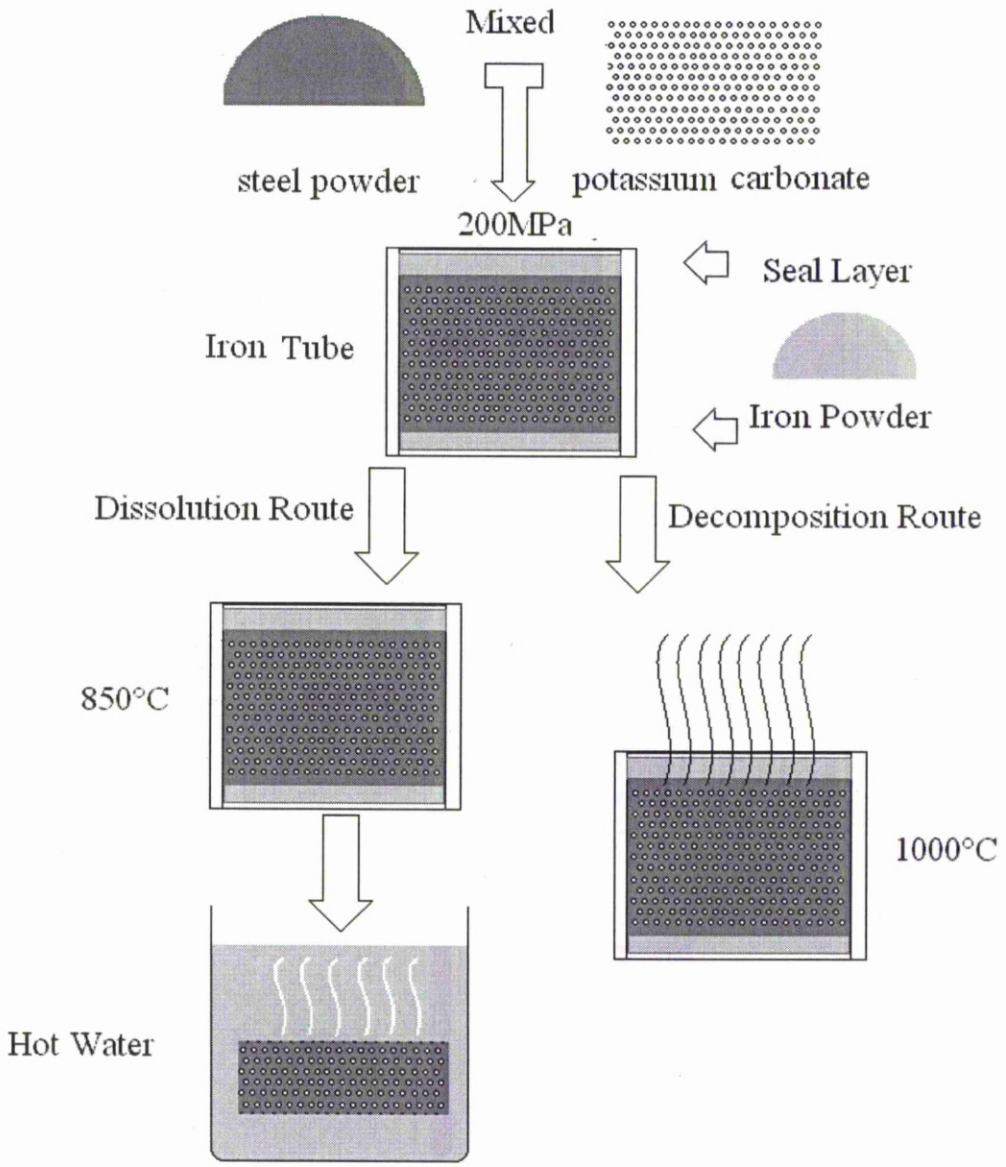

Figure 3.1 Schematic diagrams of the two routes of the LCS process.

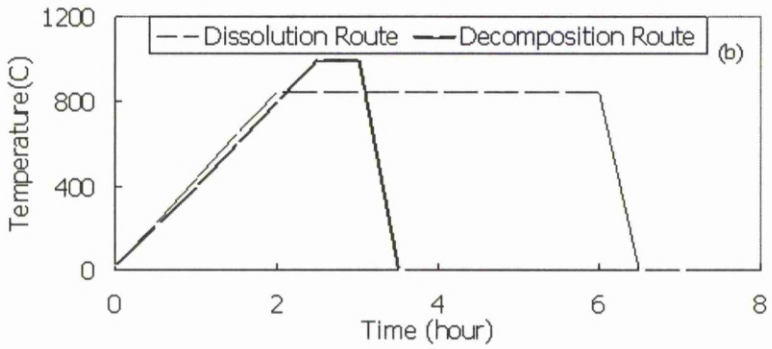

Figure 3.2 Sintering procedures of the two routes of the LCS process

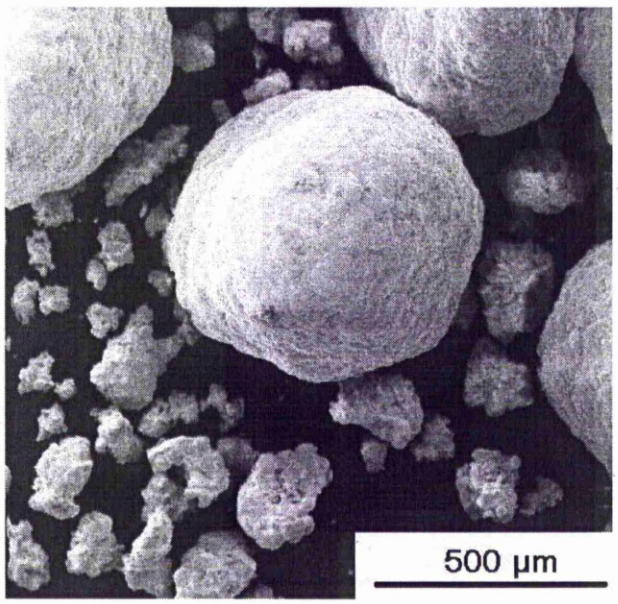

Figure 3.3: SEM micrograph showing potassium carbonate (large particles) and Astaloy A steel powders (small particles).

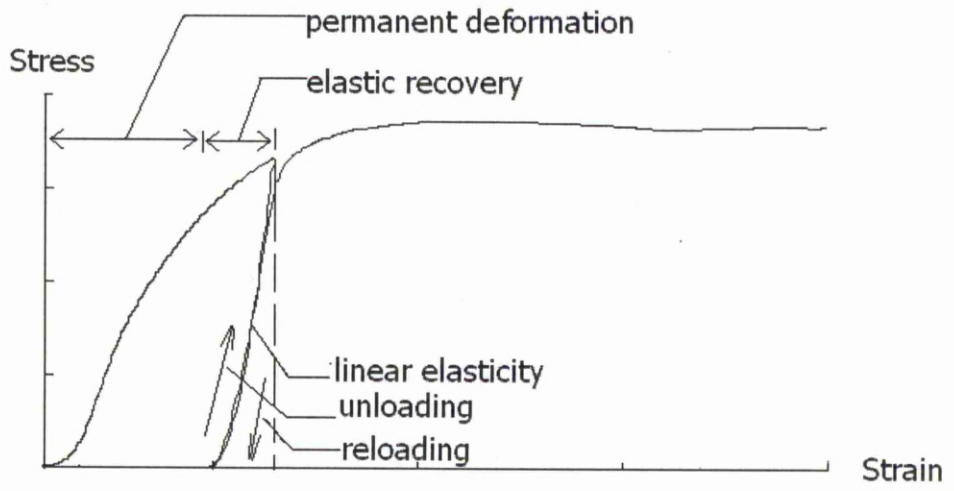

Figure 3.4 Typical loading-unloading curve.

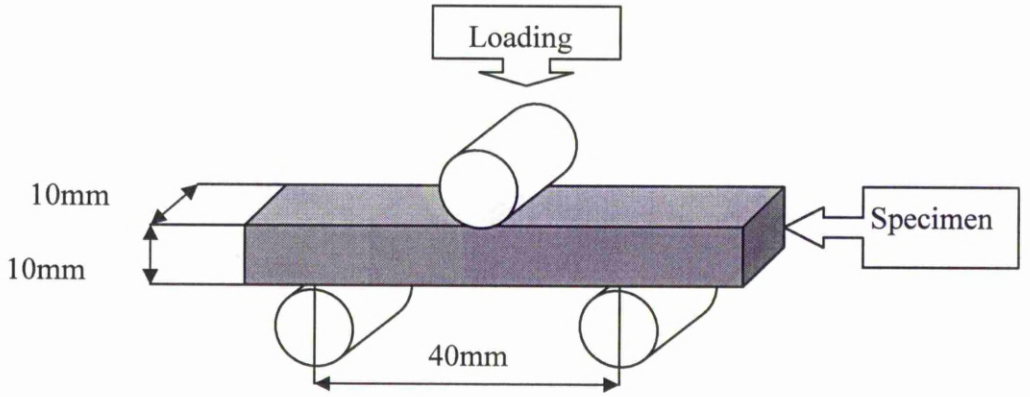

Figure 3.5 Schematic diagram of three-point bending flexure test.

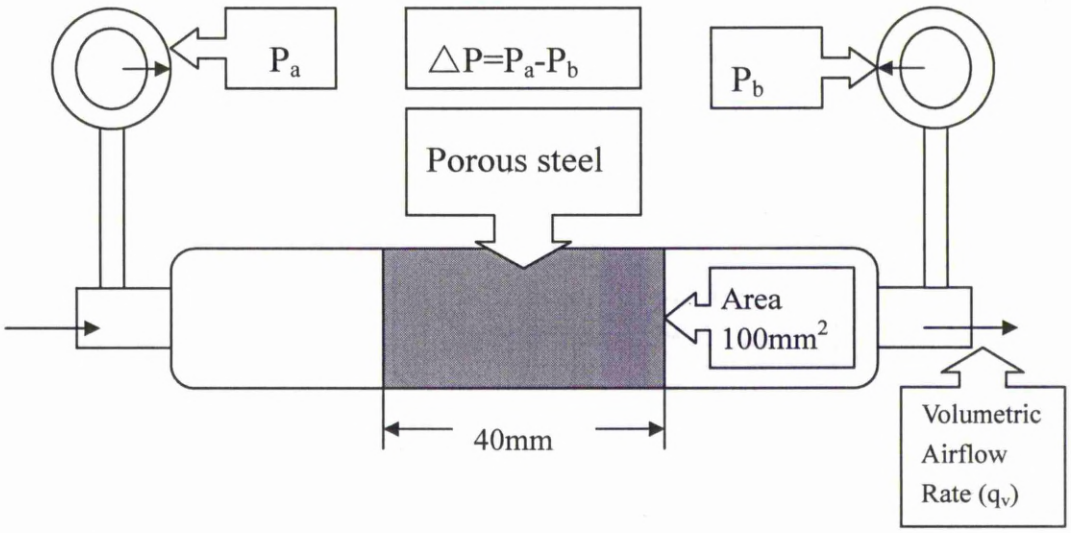

Figure 3.6: Schematic diagram of the direct airflow method for airflow resistance measurements.

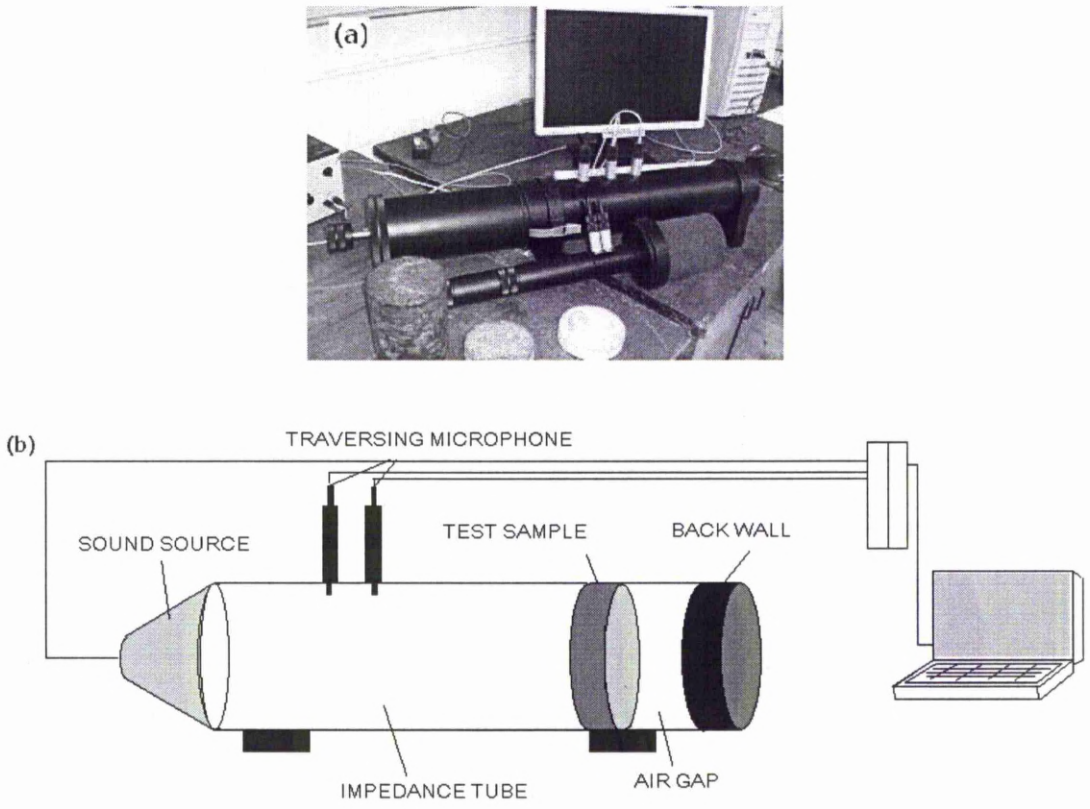

Figure 3.7 (a) Photograph of the test equipment and (b) schematic diagram of the standing wave tube method.

CHAPTER 4 MECHANICAL PROPERTIES OF POROUS STEEL

4.1 Porous Steel Manufactured by Dissolution Route

Mechanical tests were carried out on a series of porous steel specimens with pore size of 425-710μm and nominal relative densities of 0.25, 0.3, 0.35 and 0.4, manufactured by LCS via the dissolution route. The conditions used in manufacturing the specimens described in this section are: compaction pressure 200MPa, sintering temperature 850°C and sintering time 4hrs.

4.1.1 Effects of relative density

Figure 4.1.1 shows the stress-strain curves of four typical steel specimens with different relative densities under compression tests. Like other cellular solids, porous steel has a stress-strain curve with the three distinct regions mentioned previously. From the stress-strain curves, it can be directly observed that linear elasticity can only appear at very low strain (0-0.06). Lowering the relative density of the porous steel gives rise to a lower slope of the linear portion of the curve because the structure affords more cell space to deform during the compression process. Each stress-strain curve has a plateau region after the peak of elasticity region. Complete collapse of some cells has occurred in this region while the rest is still elastic. Therefore, elastic and plastic deformations coexist at almost the same loading. The curves are smooth

throughout the entire flow range, indicating a progressive deformation process characteristic of a plastic foam. As the compression proceeds, the collapse region increases in size with increasing strain until the structure is totally collapsed. The broken structure is squeezed together and therefore the stress rises, entering the densification region (Gibson and Ashby, 1997).

The compressive strength of the porous steels increases rapidly with relative density. The compressive strength of the specimens increases from 2.5MPa to 15MPa when the relative density of the porous steel increases from 0.22 to 0.38.

Previous work on the compressive properties of open-cell porous material has shown that the plastic collapse stress (equal to compressive strength in elastic-plastic porous materials), σ_c, of such a structure follows the scaling law, equation (2.4) (Gibson & Ashby, 1997).

Figure 4.1.2 shows the variation of the relative compressive strength (σ_c/σ_s) with relative density (ρ/ρ_s) for the porous steel samples with a pore size of 425-710μm plotted in logarithmic scales. The data in Figure 4.1.2 were fit to equation (2.4), yielding a C value of 0.31 and n value of 2.3 with the correlation coefficient R^2 equal to 0.94. The results showed that the scaling law is applicable to the compressive strength of the porous steel. The C value is about the same as that given by Gibson and Ashby (1997) for Al and Al alloy foams, but the n value is higher than that given

by Gibson and Asnby (1997) for Al and Al alloy foam.

The elastic modulus of the porous steel specimens was obtained from the loading-unloading curve during the compression test. It increases readily from 0.23GPa to 1.15GPa when the relative density of porous steel increases from 0.22 to 0.38. Figure 4.1.3 shows the relationship between relative elastic modulus (E/E_S) and relative density. The data were fitted to equation (2.5), yielding a C' value of 0.04 and n' value of 2.1, with the correlation coefficient R^2 equal to 0.89. The value of n' for the LCS porous steel is approximately the same as that for Al foam, but the geometric constant C' for the porous steel is much lower than those in the previous works shown in Table 2.3 (0.67-0.92). This is probably because C' is very sensitive to the microstructure and macrostructure, especially porosity, within the cell struts or cell walls. Most of the porous metals shown in Table 2.3 (Hagiwara & Green, 1987; Simone & Gibson, 1998; Zhang & Wang, 2004; Friedl *et al*, 2007) were produced either by melt foaming or by hollow sphere sintering. The cell walls of the porous metals produced by these two methods are solid and have mechanical properties very similar to those of their solid counterparts. It maybe because there were significant amount of small pores and defects in the cell walls of LCS porous steel and these defects buckled with the compaction pressure before the buckling of large pores appeared. Therefore, the small pores and defects in cell wall not affect the compressive strength but affect the elastic modulus at the unloading process very much.

Figures 4.1.4 (a) and (b) show the specific energy absorption of the LCS porous steel with increasing relative density. The energy absorption property is used to evaluate the performance of absorbing materials; it is a very important parameter for engineering design (Gibson & Ashby, 1997). For the LCS porous steel, the absorbed energy per unit volume increases with relative density up to 0.4, as shown in Figure 4.1.4 (a). However, the effect of relative density becomes gradually small. This is because the absorbed energy depends not only on plateau stress but also densification strain. While the plateau stress increases with relative density, the densification strain region decreases with relative density. For example, the plateau stress of the specimen with a relative density of 0.22 is 3.9MPa and the densification strain is 0.67, the plateau stress of the specimen with a relative density of 0.37 is 11.4MPa and the densification strain is 0.44.

Figure 4.1.4 (b) shows that the absorbed energy per unit mass increases with increasing relative density from 0.22 to 0.29, but decreases with increasing relative density further to 0.37. The maximum energy absorption per unit mass appeared at the range between 0.29 and 0.33.

Figure 4.1.5 shows typical load-displacement traces of the porous steel specimens in the three-point bending tests. The load increases smoothly with displacement up to the peak. The peaks of the curves appear at displacement in the range of 0.15-0.3mm for

the specimens. The curve of specimen with relative density of 0.37 was lower than specimens with relative density of 0.33 at initial slope because the top and bottom surface of the specimen with relative density of 0.37 was not very parallel. The loads for the specimens drop very fast afterwards, as fracture happened at the bottom of the specimens and the cracks extended by increasing load. Increasing the relative density of the porous steel results in a higher slope of the linear portion of the curve and a higher peak load of the porous steel.

Figure 4.1.6 shows that the flexural strength increases with relative density. The data from the three-point bending tests were fitted to the scaling law equation, yielding a geometric constant of 2.5 and exponent constant of 3.1. A geometric constant value greater than unity means that the scaling law is not appropriate to describe the relationship between the flexural strength and relative density for the LCS porous steel. It maybe because the tensile strength of porous steel were affected by the defect much higher than the compressive strength of LCS porous steel.

4.1.2 Effects of pore size

Mechanical tests were carried out on a series of porous steel specimens with a pore size of 250-425, 425-710, 710-1000 or 1000-1500μm, and a nominal relative density of 0.25, 0.3, 0.35 or 0.4, manufactured by LCS via the dissolution route. The conditions used in manufacturing the specimens described in this section are:

compaction pressure 200MPa, sintering temperature 850°C and sintering time 4 hrs.

Figure 4.1.7 shows the relationship between the average compressive strength and pore size for the porous steel specimens with a nominal relative density of 0.25, 0.3, 0.35 and 0.4. The standard error of the compressive strength values are indicated by the error bar. Increasing the pore size of porous steel specimens generally serves to increase the compressive strength, because the cell walls of larger pore size specimens are thicker and less sensitive to sintering defeats and have less opportunity to deform at the loading process. The effect of pore size on the compressive strength is particularly high when the specimens have lower relative densities because of the low thickness of cell walls.

Figure 4.1.8 shows the data of relative compressive strength (σ_c/σ_s) versus the relative density of porous steel specimens with different pore sizes. The data were fitted to equation (2.4), yielding the geometric constant C values and density exponent n values. It is shown that the value of C for LCS porous steel is not affected by the pore size, but the density exponent n decreases with increasing pore size. The C values are very close to the value of 0.3 given by Gibson and Ashby (1997), but they are higher than those for Fe and Cu specimens list in Table 2.2 (0.2-0.24). The n values are higher than the value of 1.5 given by Gibson and Ashby (1997). They are similar to the values for Al and Al alloy foams in previous works (1.5-2.6), and have a narrower range than those for the Cu and Fe specimens (1-4.9) shown in Table 2.2. The

difference may be because the Cu and Fe specimens listed in Table 2.2 have higher relative densities (0.45-1) and have different microstructures.

Figure 4.1.9 shows the relationship between the average elastic modulus and pore size for the porous steel specimens with different relative densities. The elastic modulus increases with increasing pore size of porous steel. Figure 4.1.10 shows the data of relative elastic modulus (E/E_s) versus the relative density of porous steel specimens with different pore sizes. The data from the compression tests were fitted to equation (2.5), yielding the geometric constant C' values and density exponent n' values. The experimentally determined values of C' for LCS porous steel increase with increasing pore size. The trend is different from that of the compressive strength. The density exponent n' also decreases slightly with increasing pore size. This C' values are much lower than those shown in Table 2.2 (0.73-0.92). The range of n' values is similar to that of the porous metals in Table 2.2 (2.1-4.2).

Figure 4.1.11 shows the effect of pore sizes on the flexural strength of porous steel specimens. 4.1.12 shows the relationship between the average flexural strength and pore size for the porous steel specimens with different relative densities. A greater pore size improves the flexural strength of porous steel.

4.1.3 Effects of compaction pressure

Mechanical tests were carried out on a series of porous steel specimens with a pore size of 425-710μm and nominal relative densities of 0.25, 0.3, 0.35 and 0.4, manufactured by LCS via the dissolution route. The conditions used in manufacturing the specimens described in this section are: compaction pressure 100, 150, 200, 250 and 300MPa, sintering temperature 850°C and sintering time 4 hrs.

Figure 4.1.13 shows the relationship between the compressive strength and the relative density of porous steel specimens manufactured with different compaction pressures. Figure 4.1.14 shows the relationship between the average compressive strength and compaction pressure for the porous steel specimens with a nominal relative density of 0.3. Increasing the compaction pressure generally serves to increase the compressive strength because the contact area of the metal particles increases with increasing pressure, which enhances sintering and increases the strength of the neck between particles.

Figure 4.1.15 shows the variation of the elastic modulus with relative density for the porous steel specimens manufactured with different compaction pressures. Figure 4.1.16 shows the relationship between the average elastic modulus and compaction pressure for the porous steel specimens with a nominal relative density of 0.3.The elastic modulus increases with increasing compaction pressure.

Figure 4.1.17 shows the effect of compaction pressure on the flexural strength of porous steel specimens. Figure 4.1.18 shows the relationship between the average flexural strength and compaction pressure for porous steel specimens with a nominal relative density of 0.3. A higher compaction pressure improves the flexural strength of porous steel.

4.2 Porous Steel Manufactured by Decomposition Route

4.2.1 Effects of relative density

Mechanical tests were carried out on a series of porous steel specimens with a pore size of 425-710μm and nominal relative densities of 0.25, 0.3, 0.35 and 0.4, manufactured by LCS via the decomposition route. The conditions used in manufacturing the specimens described in this section are: compaction pressure 200MPa, sintering temperature 1000°C and sintering time 0.5 hr.

The compressive strength of LCS porous steels increases rapidly from 3MPa to 19MPa when the relative density of porous steel increases from 0.22 to 0.38. Figure 4.2.1 shows the relationship between the relative compressive strength (σ_c/σ_s) and the relative density (ρ/ρ_s). The data were fitted to equation (2.4), yielding a C value of 0.3 and n of 1.7. The results showed that the scaling law is applicable to the compressive

strength of the porous steel. C and n values of porous steel are similar to the values given by Gibson and Ashby (1997).

The Young's modulus of the specimens increases readily from 0.2 to 1.8 GPa when the relative density increases from 0.22 to 0.38. Figure 4.2.2 shows the relationship between the relative elastic modulus and the relative density. The data were fitted to equation (2.5), yielding a C' value of 0.043 and n' value of 1.7. The n' values for the LCS porous steel was lower than that for previous works shown in Table 2.3 (2.1-4.3). The geometric constant C' for the porous steel is much lower than previous suggested and works' result (0.67-0.92).

Figures 4.2.3 (a) and (b) shows the specific energy absorption of the porous steel specimens with different relative densities manufactured by the decomposition route. The absorbed energy per unit volume of LCS porous steel increases with increasing relative density from 0.22 to 0.33, but decreases with increasing relative density from 0.33 to 0.37, as shown in Figure 4.1.4 (a). The maximum value of absorbed energy per unit volume appeared at the relative density of 0.31-0.34. The absorbed energy per unit mass of LCS porous steel increases with increasing relative density from 0.22 to 0.27, but decreases with increasing relative density from 0.27 to 0.37, as shown in Figure 4.1.4 (b). The maximum value of energy absorption per unit mass appeared at the relative density of 0.29-0.33.

Figure 4.2.4 shows the flexural strength of porous steel manufactured by the decomposition route increase when the relative density of porous steel increases from 0.21 to 0.37. A higher relative density improves the flexural strength of porous steel.

4.2.2 Effects of pore size

Mechanical tests were carried out on a series of porous steel specimens with a pore size of 250-425, 425-710, 710-1000 or 1000-1500μm, at different nominal relative densities of 0.25, 0.3, 0.35 and 0.4, manufactured by LCS via the decomposition route. The conditions used in manufacturing the specimens described in this section are: compaction pressure 200MPa, sintering temperature 1000°C and sintering time 0.5hr.

Figure 4.2.5 shows the relationship between the average compressive strength and pore size for the porous steel specimens with nominal relative densities of 0.25, 0.3, 0.35 and 0.4. Increasing the pore size generally serves to increase the compressive strength. Figure 4.2.6 shows the variations of the relative compressive strength (σ_c/σ_s) with the relative density of porous steel specimens with different pore sizes. The data were fitted to equation (2.4), yielding the geometric constant C values and density exponent n values. It is shown that the value of C of LCS porous steel manufactured by decomposition route is not affected by the pore size.

Figure 4.2.7 shows the relationship between the average elastic modulus and pore size for the porous steel specimens with different nominal relative densities of 0.25, 0.3,

0.35 and 0.4. The elastic modulus increases readily with the increase of pore size. Figure 4.2.8 shows the variations of the relative elastic modulus with the relative density of porous steel specimens with different pore sizes. The data were fitted to Equation (2.5), yielding the geometric constant C' values and density exponent n' values. The C' values for LCS porous steel increase and the n' values decreases slightly with increasing pore size. This C' values are much lower than those shown in Table 2.2 (0.73-0.92). The n' values range (1.4-1.8) is smaller that of the porous metals in Table 2.2 (2.1-4.2).

Figure 4.2.9 shows the flexural strength versus relative densities of the porous steel specimens with different pore size. Figure 4.2.10 shows the relationship between the average flexural strength and pore size for the porous steel specimens with different nominal relative densities of 0.25, 0.3, 0.35 and 0.4. A greater pore size improves the flexural strength of porous steel.

4.2.3 Effects of compaction pressure

Mechanical tests were carried out on a series of porous steel specimens with a pore size of 425-710μm and nominal relative density of 0.3, manufactured by LCS via the decomposition route, with different compaction pressure. The conditions used in manufacturing the specimens described in this section are: compaction pressure 100, 150, 200, 250 or 300MPa, sintering temperature 1000°C and sintering time 0.5 hr.

Figure 4.2.11 shows the compressive strength of porous steel specimens with a nominal relative density of 0.3 manufactured with different compaction pressures. The compressive strength data for the specimens with other relative densities, compacted under 100MPa, are also shown. Increasing the compaction pressure generally serves to increase the compressive strength because the contact area between the metal powder particles increases with increasing pressure, resulting in higher strength of the neck after sintering. Figure 4.2.12 shows the relationship between the average compressive strength and compaction pressure for the porous steel specimens with a nominal relative density of 0.3. It is shown more clearly that the compressive strength increases significantly with increasing compaction pressure.

Figure 4.2.13 shows the elastic modulus values for the porous steel specimens with a nominal relative density of 0.3 manufactured with different compaction pressures. The elastic modulus values for the specimens with other nominal relative densities manufactured with a compaction pressure of 100MPa are also shown. Figure 4.2.14 shows the relationship between the average elastic modulus and compaction pressure for the porous steel specimens with a nominal relative density of 0.3. The elastic modulus increases readily with the increase of compaction pressure.

Figure 4.2.15 shows the flexural strength values for the porous steel specimens with a nominal relative density of 0.3 manufactured with different compaction pressures.

Figure 4.2.16 shows the relationship between the average flexural strength and compaction pressure for porous steel specimens with a nominal relative density of 0.3. A higher compaction pressure improves the flexural strength of porous steel.

4.2.4 Effects of sintering temperature

Mechanical tests were carried out on a series of porous steel specimens with a pore size of 425-710μm and different nominal relative densities, manufactured by LCS via the decomposition route with different sintering temperature. The conditions used in manufacturing the specimens described in this section are: compaction pressure 200MPa, sintering temperature 950, 1000, 1050 or 1100°C, and sintering time 0.5 hr.

Figure 4.2.17 shows the relationship between the average compressive strength and sintering temperature for the porous steel specimens with nominal relative densities of 0.25, 0.3 and 0.35. Increasing the sintering temperature generally serves to increase the compressive strength. Figure 4.2.18 shows the data of relative compressive strength versus the relative density of porous steel specimens manufactured with different sintering temperatures. The data were fitted to equation (2.4), yielding the geometric constant C values and density exponent n values. The C values do not change much (≈0.3) with sintering temperatures of and the density exponent n increase with increasing sintering temperature.

Figure 4.2.19 shows the relationship between the average elastic modulus and

sintering temperature for the porous steel specimens with nominal relative densities of 0.25, 0.3 and 035. It is shown that the elastic modulus increases with increasing sintering temperature. Figure 4.2.20 shows the data of relative elastic modulus versus the relative density of porous steel specimens manufactured with different sintering temperatures. The data were fitted to equation (2.5), yielding the geometric constant C' values and density exponent n' values. The C' values do not change much (0.041-0.045) with sintering temperature and the n' values decrease with increasing sintering temperature.

Figure 4.2.21 shows the effect of sintering temperature on the flexural strength of porous steel specimens. Figure 4.2.22 shows the relationship between the average flexural strength and sintering temperature. A higher sintering temperature improves the flexural strength of porous steel.

4.2.5 Effects of sintering time

Mechanical tests were carried out on a series of porous steel specimens with a pore size of 425-710μm and nominal relative densities of 0.25, 0.3, 0.35 and 0.4, manufactured by LCS via the decomposition route with different sintering times. The conditions used in manufacturing the specimens described in this section are: compaction pressure 200MPa, sintering temperature 1000°C and sintering times 0.5, 1, 2 or 3 hrs.

Figure 4.2.23 shows the variation of the compressive strength with the relative density of porous steel specimens manufactured with different sintering times. Increasing the sintering time generally serves to increase the compressive strength. Figure 4.2.24 shows the relationships between the average compressive strength and sintering time for the porous steel specimens with nominal relative densities of 0.25 and 0.35. It is shown more clearly that the compressive strength increases with increasing sintering time. However, the effect of sintering time becomes small when it is longer than 2 hours.

Figure 4.2.25 shows the variation of the elastic modulus with relative density for the porous steel specimens manufactured with different sintering times. The elastic modulus increases steadily with the increase of sintering time. Figure 4.2.26 shows the relationships between the average elastic modulus and sintering time for the porous steel specimens with nominal relative densities of 0.25and 0.35. It is shown more clearly that the elastic modulus increases with increasing sintering time. The effect of sintering time is more pronounced for the higher relative density but it becomes small when the sintering time is longer than two hours.

Figure 4.2.27 shows the effect of sintering time on the flexural strength of porous steel specimens. A higher sintering time improves the flexural strength of porous steel. Figure 4.2.28 shows the relationship between the average flexural strength and

sintering time for porous steel specimens with nominal relative density of 0.25 and 0.35. It is shown more clearly that the flexural strength increases with increasing sintering time. Again, the effect of sintering time is more marked for the specimens with a higher relative density but it becomes small when the sintering time is longer than two hours.

4.3 Comparison of Two Routes

4.3.1 Mechanical properties

Figure 4.3.1 shows the ratios of average compressive strength between the porous steel specimens manufactured by LCS via the decomposition and dissolution routes with different porosities and pore sizes. The average compressive strength of the porous steel manufactured by the decomposition route is always higher than that of the porous steel with the same porosity and pore size manufactured by the dissolution route. At a small pore size of 250-425μm, the ratio increases with decreasing relative density, or increasing porosity. At other pore sizes, the ratio does not change much with relative density. The specimens manufactured by decomposition route are normally 15-30% stronger than those manufactured by the dissolution route.

Figure 4.3.2 shows the ratios of average elastic modulus between the porous steel specimens manufactured by the decomposition and dissolution routes with different

porosities and pore sizes. The average elastic modulus of the porous steel manufactured by the decomposition route is always higher than that of the porous steel manufactured by the dissolution route with the same porosity and pore size. The specimens manufactured by the decomposition route are normally 50-100% stiffer than those manufactured by the dissolution route. The ratio increases with decreasing relative density at a small pore size of 250-425μm, and increases with increasing relative density at a large pore size of 1000-1500μm. At other pore sizes, the ratio does not change much with relative density.

Figure 4.3.3 shows the ratios of average flexural strength between the porous steel specimens manufactured via the decomposition and dissolution routes with different porosities and pore sizes. The average flexural strength of the porous steel manufactured by the decomposition route is always higher than that of the porous steel manufactured by the dissolution route. The ratio is high at a low relative density of 0.25 for all pore size. For higher relative densities of 0.3, 0.35 and 0.4, the ratio depends on the pore sizes. It is low for pore sizes between 250 and 710μm but high for pore sizes between 710 and 1500μm.

Figure 4.3.4 shows the variation of the ratio of average specific energy absorption between porous steel specimens manufactured by the decomposition and dissolution routes as a function of relative density with a pore size of 425-710μm. For the same porosity and pore size, the average energy absorption of the porous steel manufactured

by the decomposition route is always higher than that of the porous steel specimens manufactured by the dissolution route. The specimens manufactured by the decomposition route are normal absorb 30-80% more energy than those manufactured by the dissolution route. The ratio decreases with increasing relative density.

Figures 4.3.5 (a), (b) and (c) show the ratios of average compressive strength, elastic modulus and flexural strength between the porous steel specimens manufactured by LCS via the decomposition and dissolution routes with different compaction pressures. There is no clear trend in the effect of compaction pressure on the ratio of flexural strength. However, a compaction pressure higher than 200MPa leads to higher ratios of compressive strength and elastic modulus than lower compaction pressures.

4.3.2 Re-sintered specimens

In the re-sintering process, the specimens with a pore size of 425-710μm and nominal relative densities of 0.25, 0.3, 0.35 and 0.4 were first manufactured by the dissolution route and then sintered again at 1000°C for 0.5 hr, in a vacuum furnace.

Figures 4.3.6 (a), (b) and (c) show the compressive strength, elastic modulus and flexural strength versus the relative density of porous steel specimens manufactured by the dissolution, decomposition and re-sintering routes. The compressive strength of porous steel manufactured by the re-sintering route is often lower than that of the

porous steel specimens manufactured by either the decomposition or the dissolution route. The elastic modulus of porous steel manufactured by the re-sintering route is always lower than that of the porous steel specimens manufactured by the decomposition and dissolution routes. The flexural strength of porous steel manufactured by the re-sintering route is often higher than those of the porous steel specimens manufactured by the dissolution route, but lower than that of the porous steel specimens manufactured by the decomposition route.

The specimens manufactured by the re-sintering route do not show improvement in the compression and flexural strengths in comparison with the specimens manufactured by the decomposition route. The elastic modulus of specimens manufactured by the re-sintering route is lower than that of the specimens manufactured by the other two routes. The reason for this anomaly is not clear. It is likely because the potassium carbonate is not fully cleaned by hot water in the dissolution process and the remaining potassium carbonate stay at defects of cell wall. These remain potassium carbonate corroded the metal during the re-sintering process. When the size of defects increasing, the elastic modulus of porous steel decreases clearly because the solid part of cell wall decreased. The flexural strength of re-sintering specimens was not changed clearly because the cleaning of potassium carbonate was better at the surface of porous steel and these parts affect the flexural strength very much. The compressive strength of the LCS porous steel not was affected by the small defects but maybe was affected by the large defects. Therefore,

some of the results of compressive strength of re-sintering specimens were lower than that of the specimens manufactured by the dissolution route, and compressive strength of some other re-sintering specimens were higher than that of the dissolution route specimens.

4.3.3 Advantages and disadvantages of decomposition route

The porous steel specimens manufactured by the decomposition route have higher mechanical properties, including compressive strength, elastic modulus and flexural strength, than those manufactured by the dissolution route. In the decomposition route, the specimens can be sintered at a temperature ranging from 890°C to 1500°C. In the dissolution route, the specimens can only be sintered at a temperature below 890°C. A higher sintering temperature can improve the mechanical properties significantly, as discussed in section 4.2.4. The sintering time can also be reduced accordingly. The decomposition route involves only two steps while the dissolution route has one more step to dissolve the potassium carbonate. Therefore, the decomposition route is simpler and benefits productivity.

In the decomposition route, however, the potassium carbonate is decomposed to K_2O and CO_2. The liquid K_2O may not be fully pushed out from the porous steel specimens by the gaseous CO_2. The remaining K_2O is corrosive and can damage the specimens. The liquid K_2O can also damage the sintering furnace.

4.4 Scaling Law Parameters

Table 4.1 Geometric constant and density exponent of porous steel manufactured by decomposition and dissolution routes with different pore sizes and sintering temperatures.

Pore size (μm)	Sintering Temperature	C	n	C'	n'
Dissolution route					
250-425	850°C	0.31	2.6	0.035	2.3
425-710	850°C	0.31	2.2	0.040	2.1
710-1000	850°C	0.29	2.0	0.051	2.0
1000-1500	850°C	0.32	1.9	0.061	1.9
Decomposition route					
250-425	1000°C	0.30	1.9	0.034	1.8
425-710	1000°C	0.30	1.7	0.043	1.7
710-1000	1000°C	0.30	1.6	0.052	1.5
1000-1500	1000°C	0.31	1.5	0.061	1.4
425-710	950°C	0.29	2.1	0.041	2.0
425-710	1000°C	0.30	1.7	0.043	1.6
425-710	1050°C	0.29	1.5	0.044	1.4
425-710	1100°C	0.31	1.2	0.045	1.2

Table 4.1 shows the geometric constant (C and C') and density exponent (n and n') values of porous steel specimens manufactured under different conditions including manufacturing route, relative density, pore size and sintering temperature. The C values of the specimens are all close to 0.3, not affected by pore size or sintering temperature. It is reasonable to assume that C is a constant independent of processing

conditions. The density exponent n decreases with pore size or sintering temperature. The n values for the LCS porous steel manufactured by the decomposition route are generally lower than those of porous steel manufactured by the dissolution route mainly due to the effect of sintering temperature.

The C' value increases with increasing pore size but is independent of sintering temperature. Similar to n, the density exponent n' values decrease with pore size or sintering temperature.

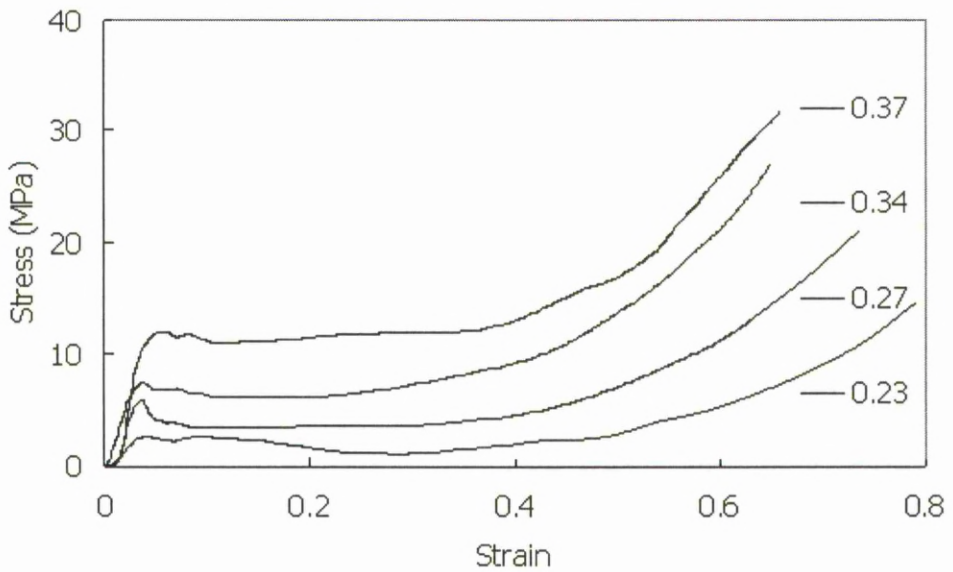

Figure 4.1.1 Typical compressive stress-strain curves of porous steel specimens with relative densities of 0.23, 0.27, 0.34 and 0.37. The pore size of the specimens is 425-710μm.

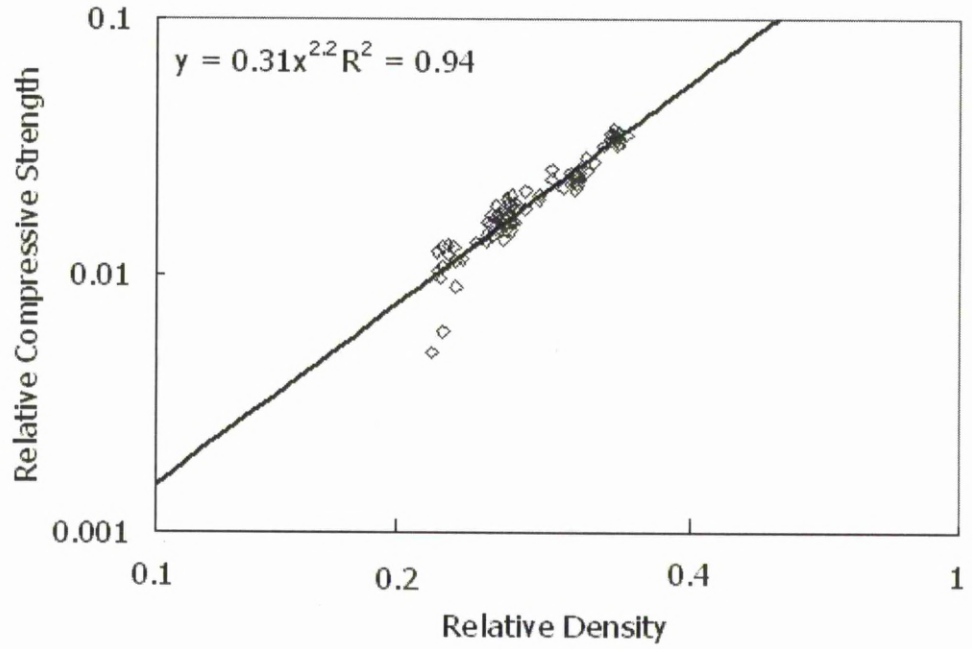

Figure 4.1.2 Relative compressive strength versus relative density of porous steel specimens. The pore size of the specimens is 425-710μm.

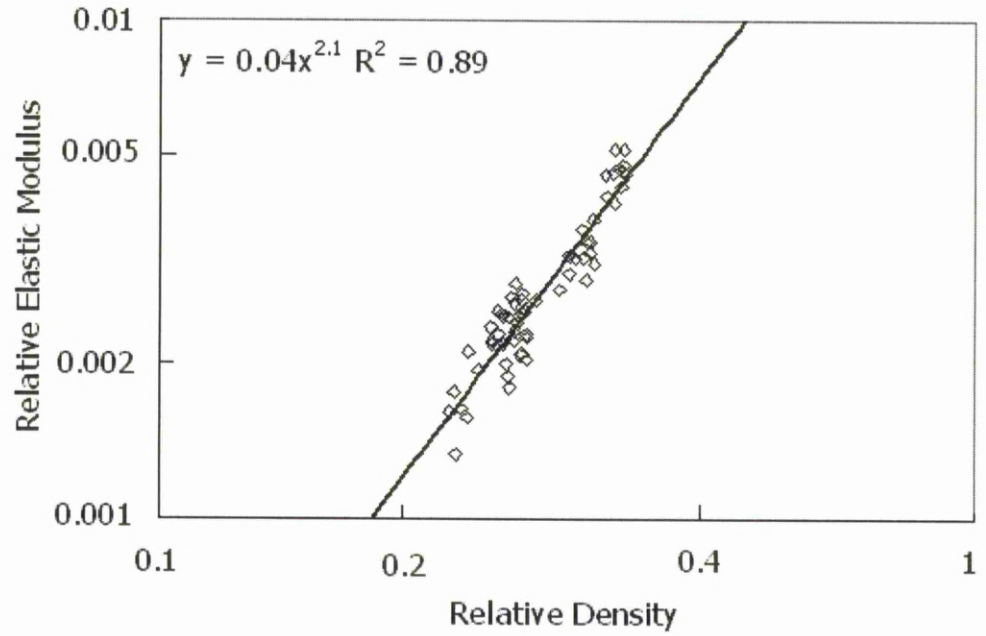

Figure 4.1.3 Relative elastic modulus versus relative density of porous steel specimens. The pore size of the specimens is 425-710μm.

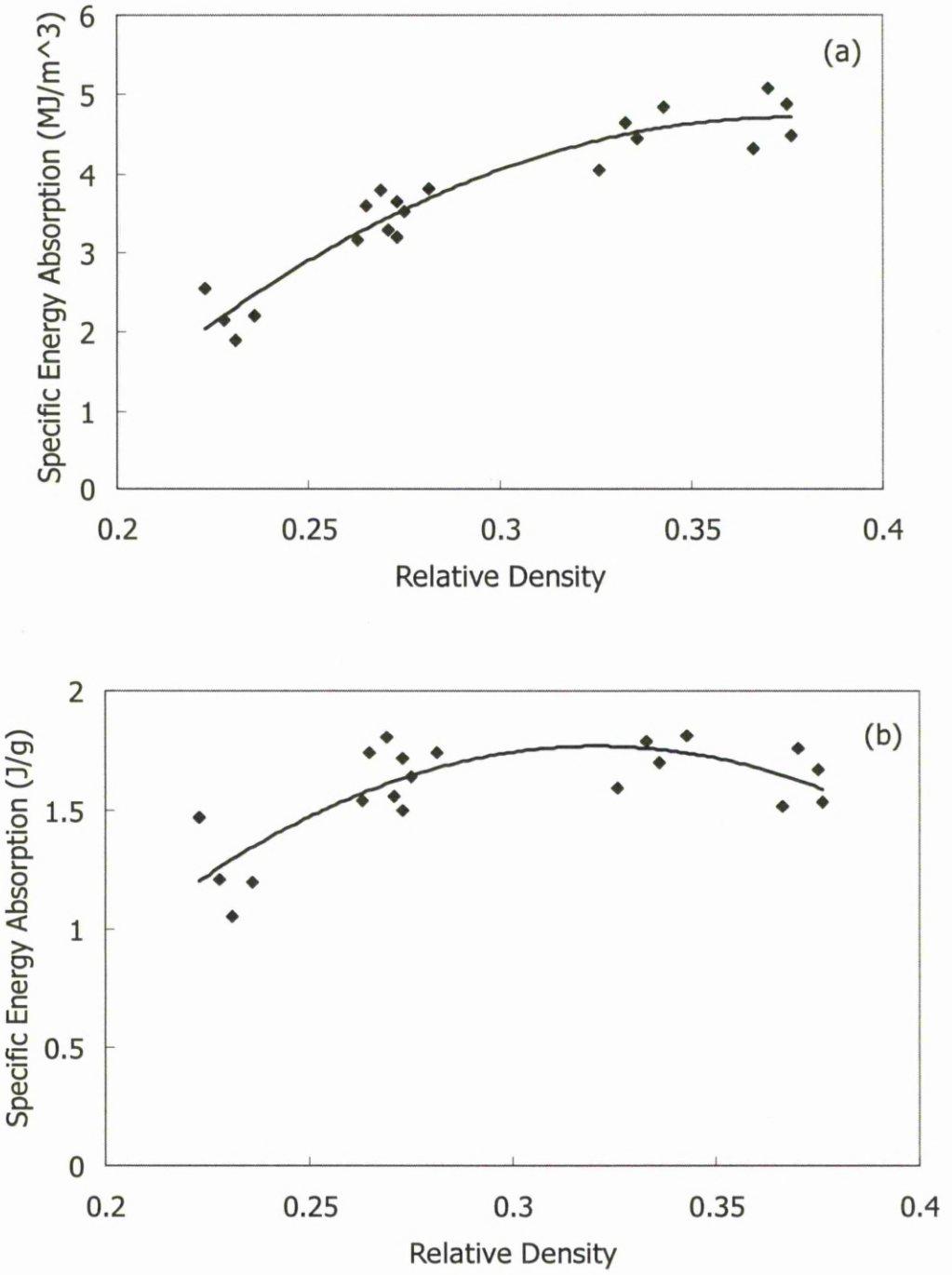

Figure 4.1.4 Energy absorption (a) per unit volume and (b) per unit mass versus relative density of porous steel specimens manufactured by the dissolution route. The pore size of the specimens is 425-710μm.

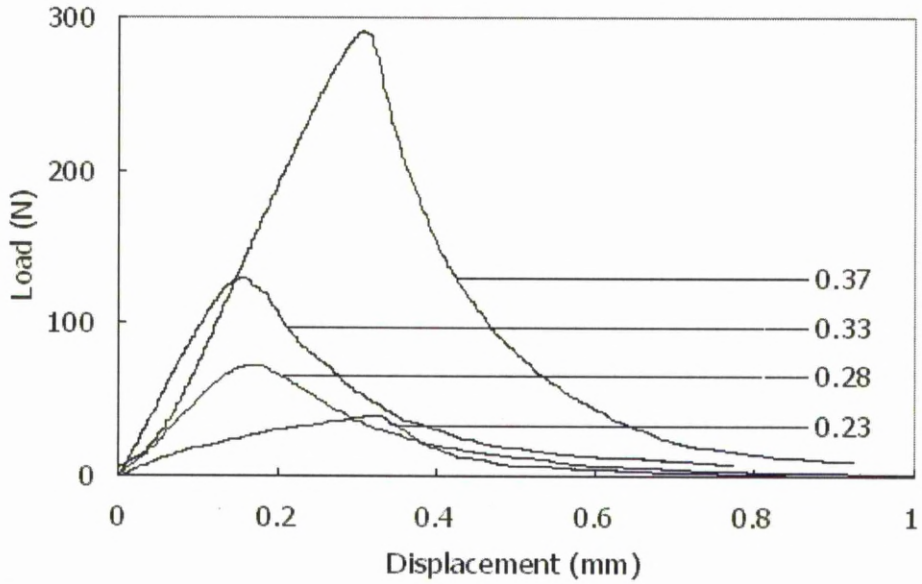

Figure 4.1.5 Typical flexural load-displacement curves in three point bending test on specimens with relative densities of 0.23, 0.27, 0.33 and 0.37. The pore size of the specimens is 425-710μm.

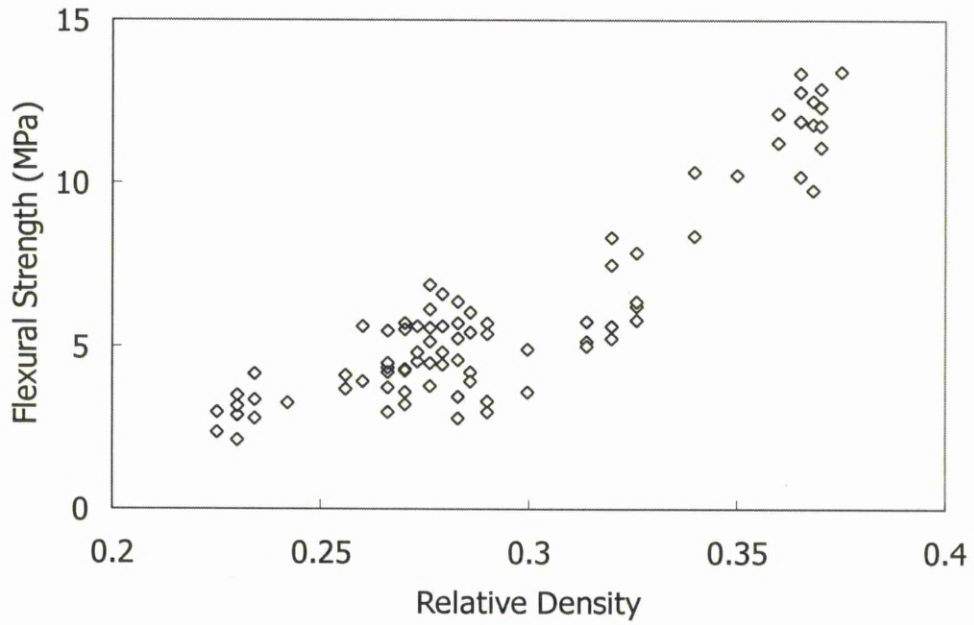

Figure 4.1.6 Variation of relative flexural strength with relative density for the porous steel manufactured by the dissolution route. The pore size of the specimens is 425-710μm.

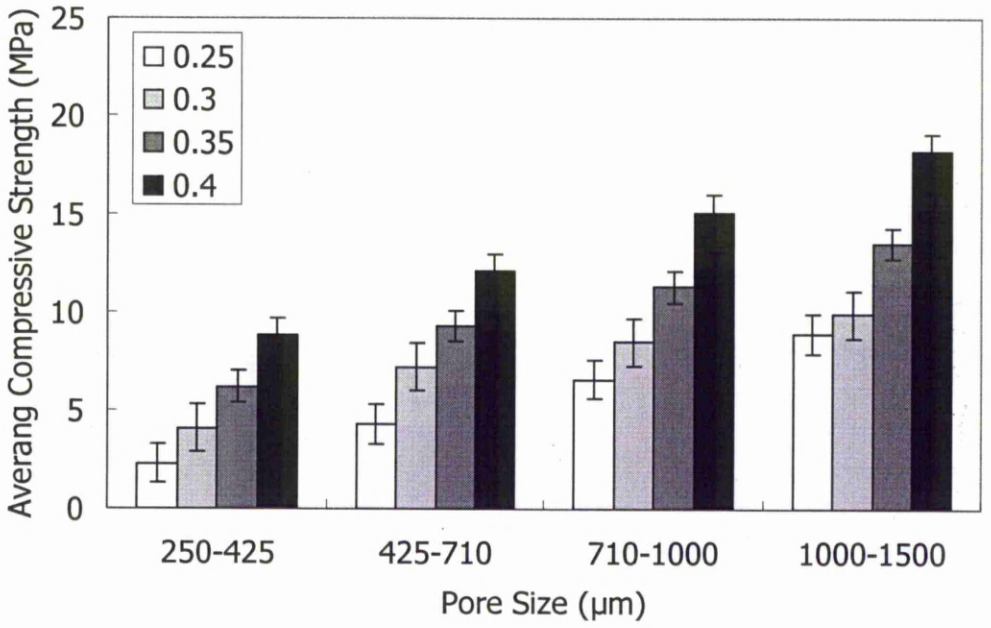

Figure 4.1.7 Average compressive strength versus the nominal relative density for the porous steel specimens with different pore sizes, manufactured by the dissolution route.

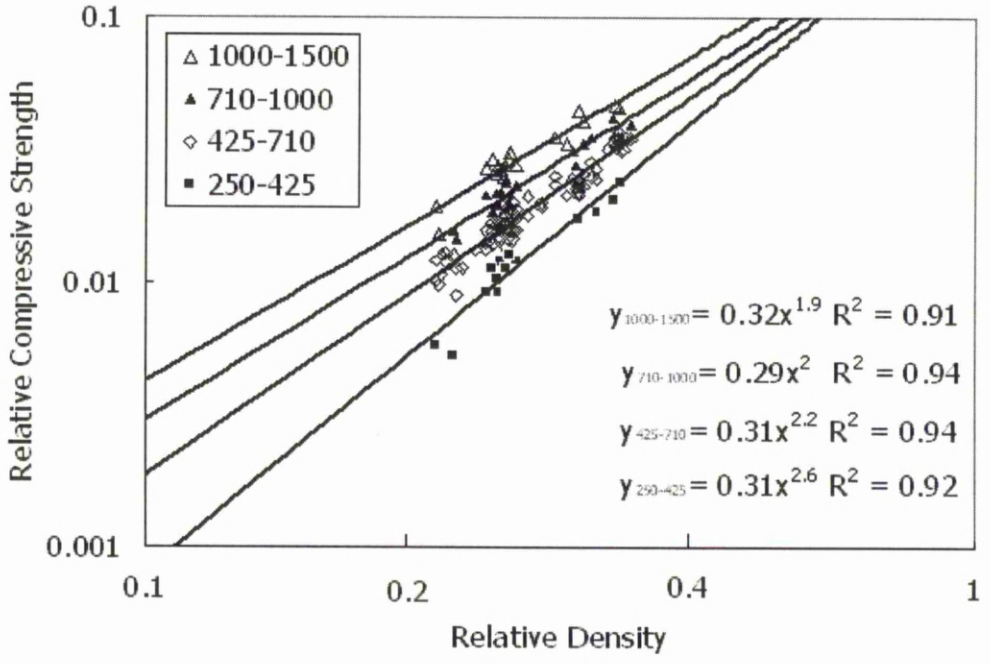

Figure 4.1.8 Relative compressive strength versus the relative density of porous steel specimens with different pore sizes, manufactured by the dissolution route.

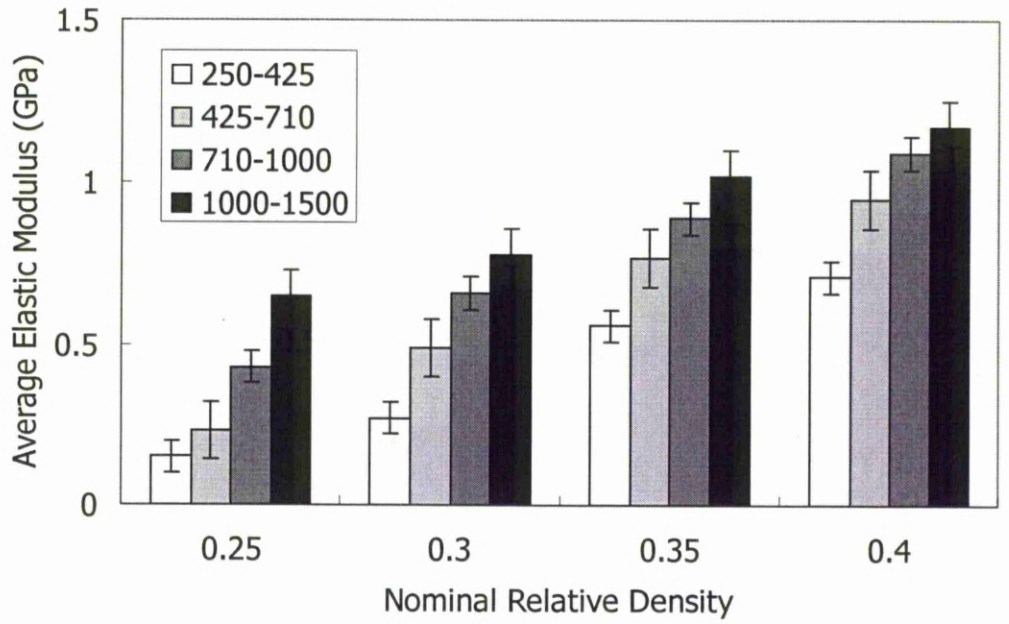

Figure 4.1.9 Average elastic modulus versus the nominal relative density for the porous steel specimens with different pore sizes, manufactured by the dissolution route.

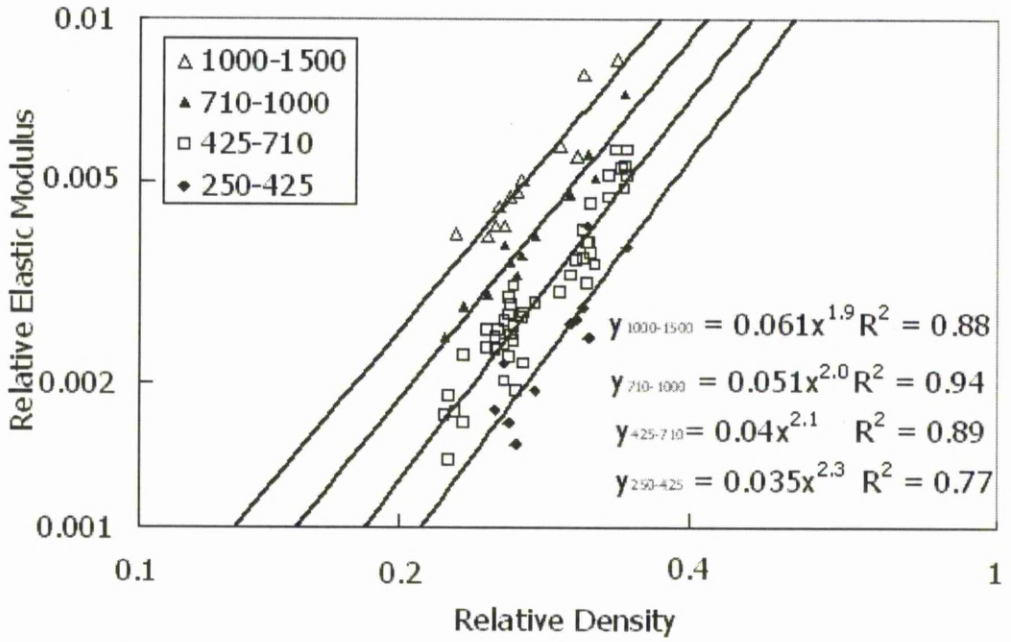

Figure 4.1.10 Relative elastic modulus versus the relative density of porous steel specimens with different pore sizes, manufactured by the dissolution route.

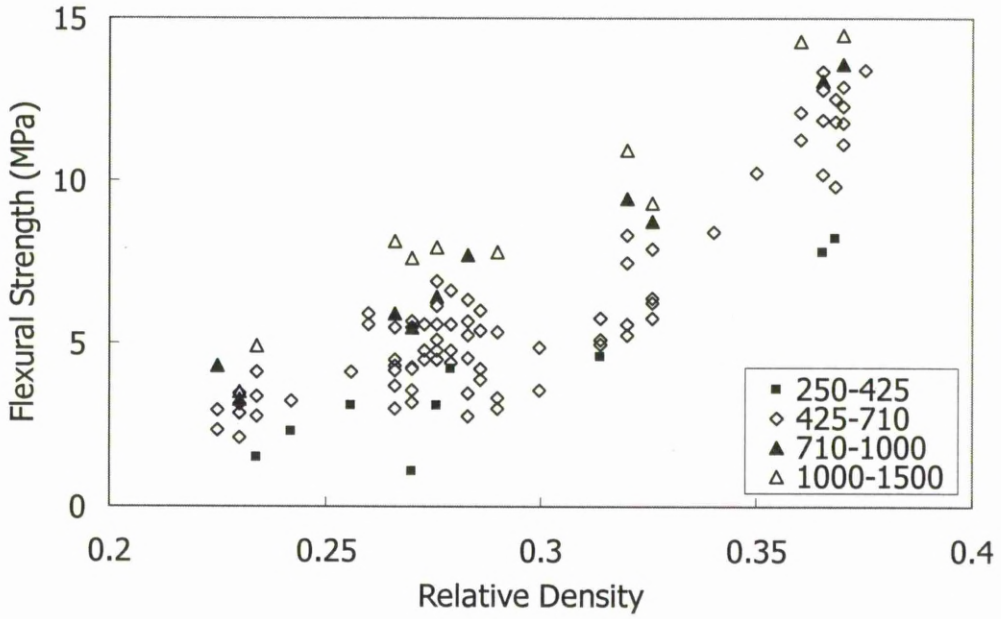

Figure 4.1.11 Flexural strength versus the relative density of porous steel specimens with different pore sizes, manufactured by the dissolution route.

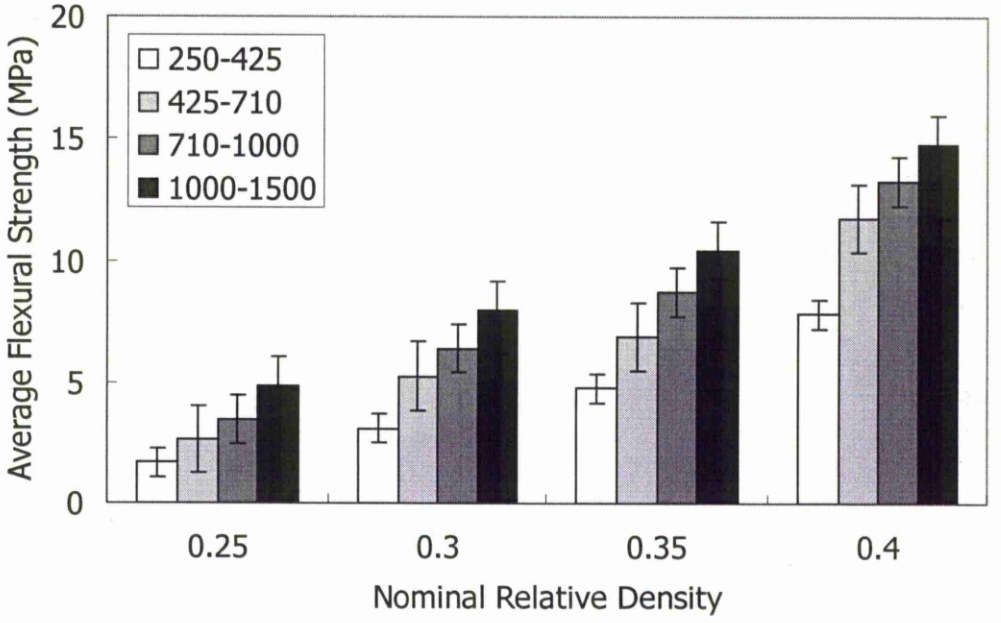

Figure 4.1.12 Flexural strength versus the nominal relative density for the porous steel specimens with different pore sizes, manufactured by the dissolution route.

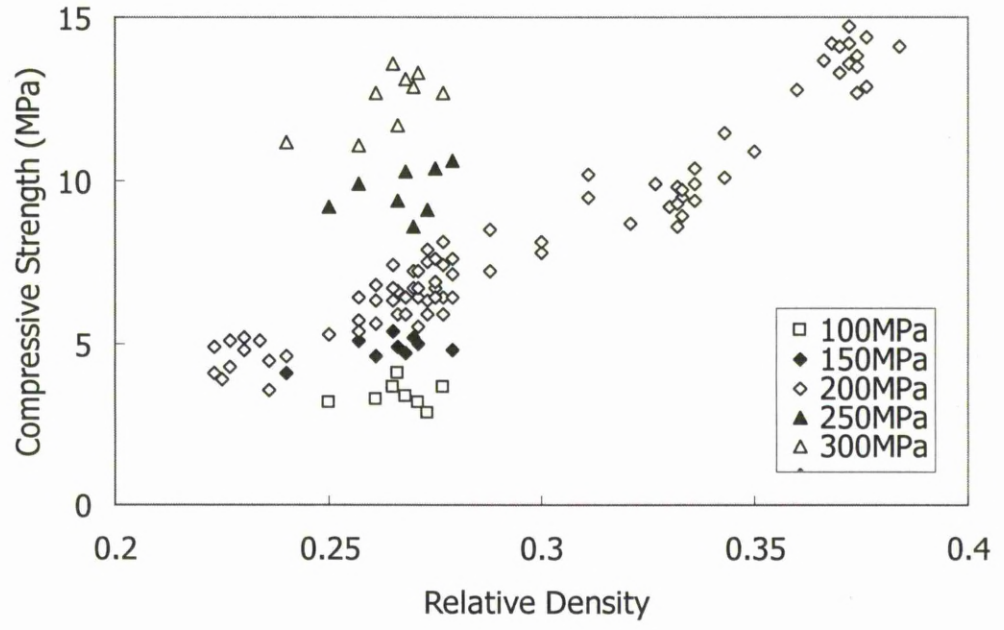

Figure 4.1.13 Variation of compressive strength with relative density for the porous steel specimens manufactured by the dissolution route, with different compaction pressures.

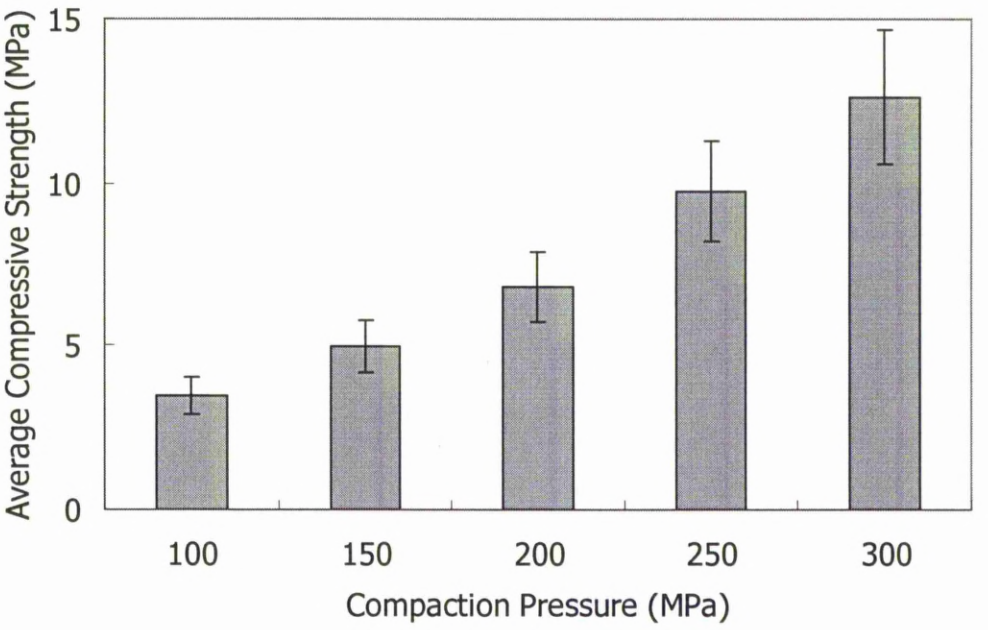

Figure 4.1.14 Compressive strength versus compaction pressure for the porous steel specimens with a nominal relative density of 0.3, manufactured by the dissolution route.

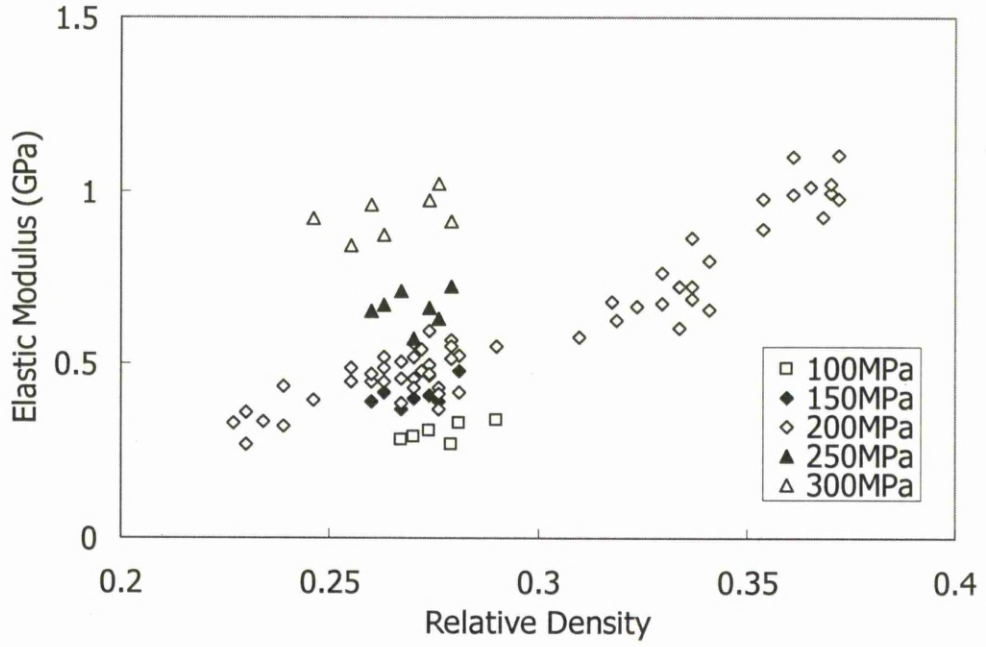

Figure 4.1.15 Variation of elastic modulus with relative density for the porous steel specimens manufactured by the dissolution route, with different compaction pressures.

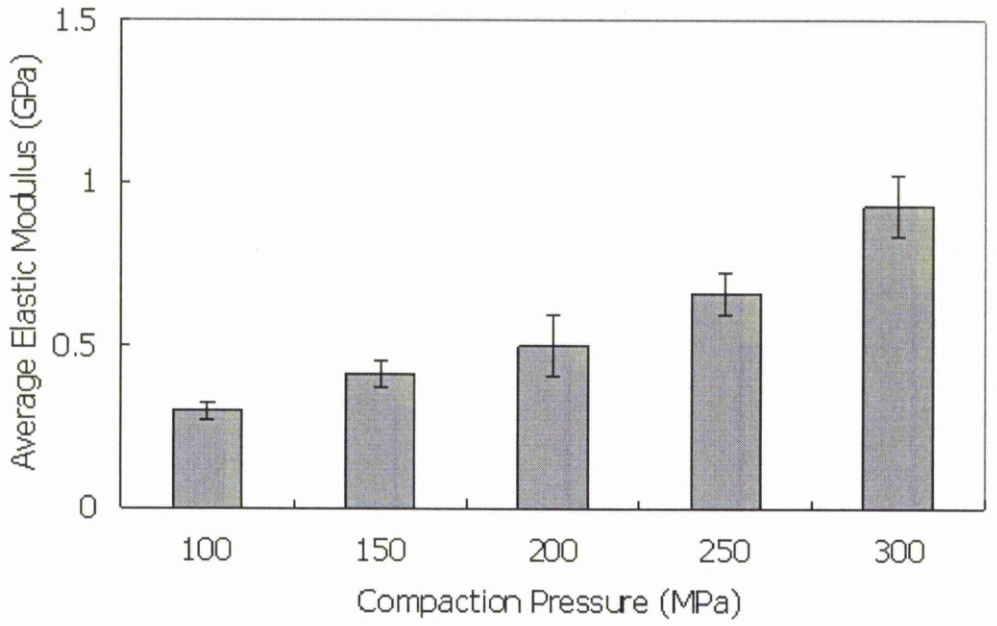

Figure 4.1.16 Elastic modulus versus compaction pressure for the porous steel specimens with a nominal relative density of 0.3, manufactured by the dissolution route.

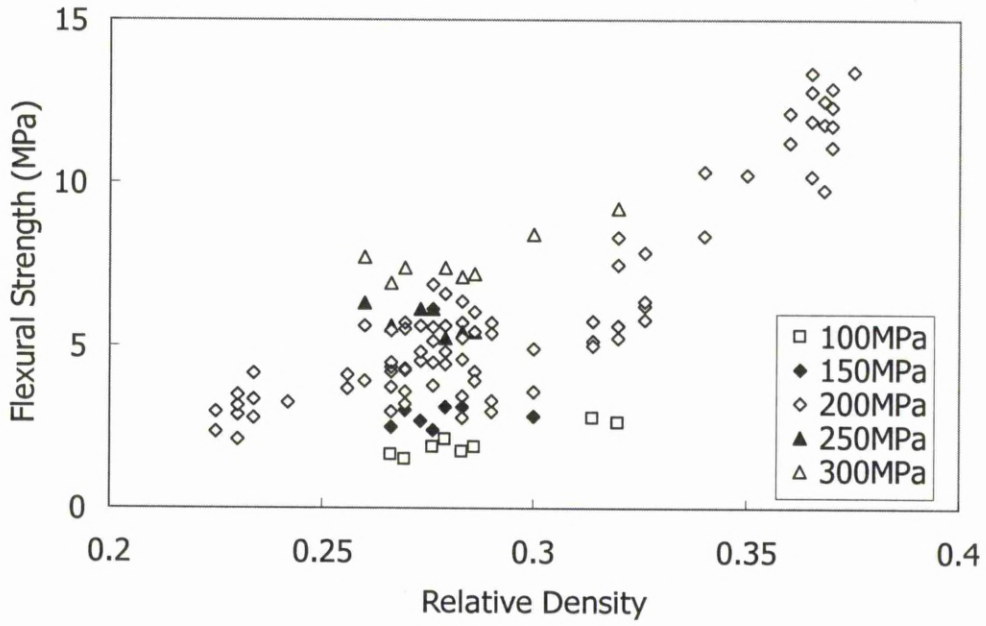

Figure 4.1.17 Variation of flexural strength with relative density for the porous steel specimens manufactured by the dissolution route, with different compaction pressures.

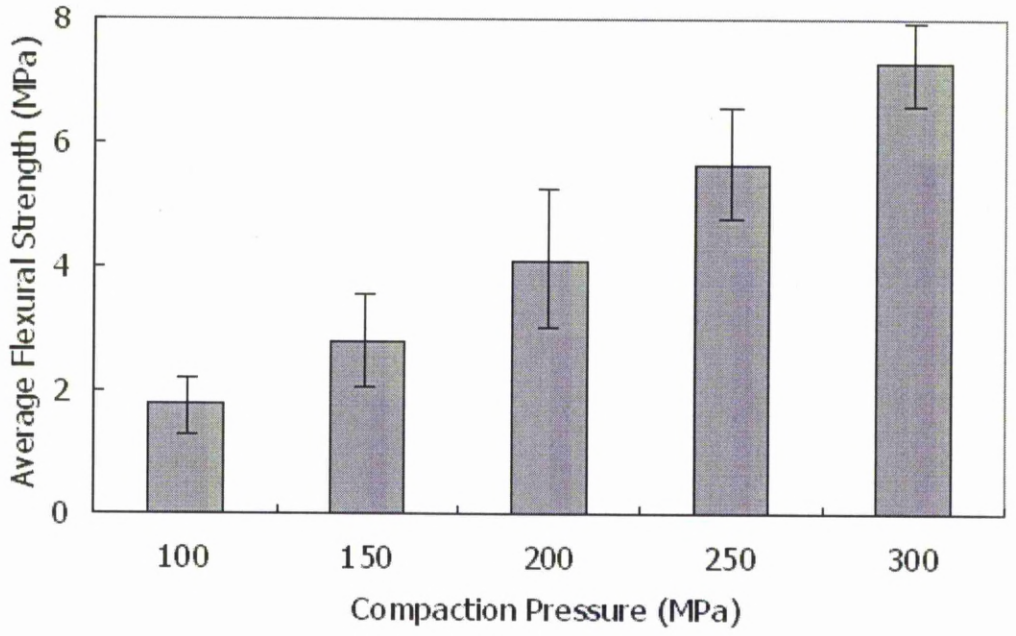

Figure 4.1.18 Flexural strength versus compaction pressure for the porous steel specimens with a nominal relative density of 0.3, manufactured by the dissolution route.

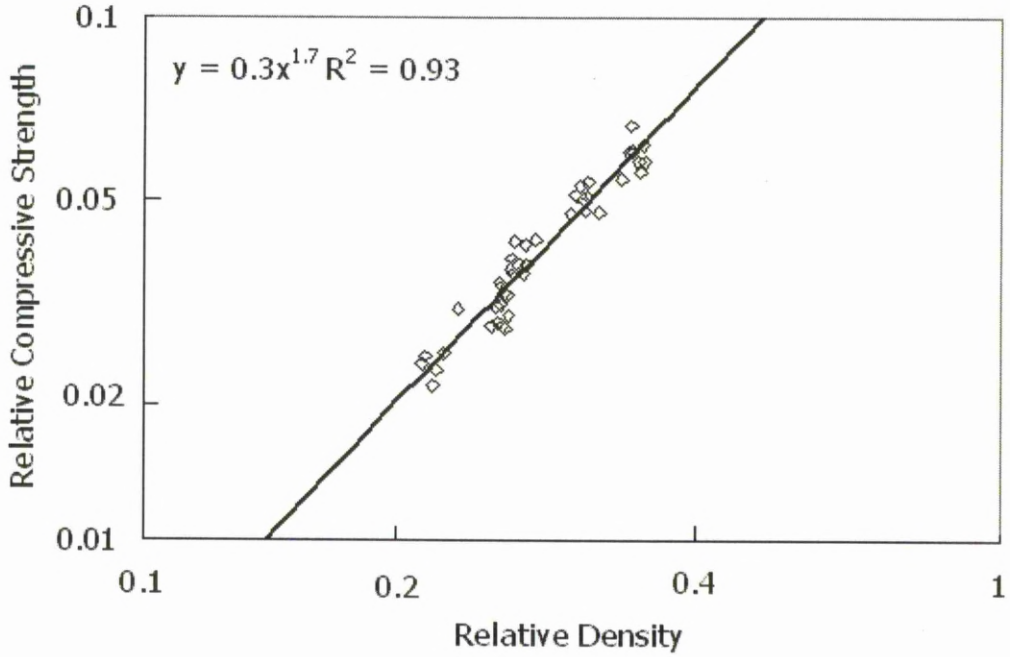

Figure 4.2.1 Relative compressive strength versus the relative density of porous steel specimens manufactured by the decomposition route. The pore size of the specimens is 425-710μm.

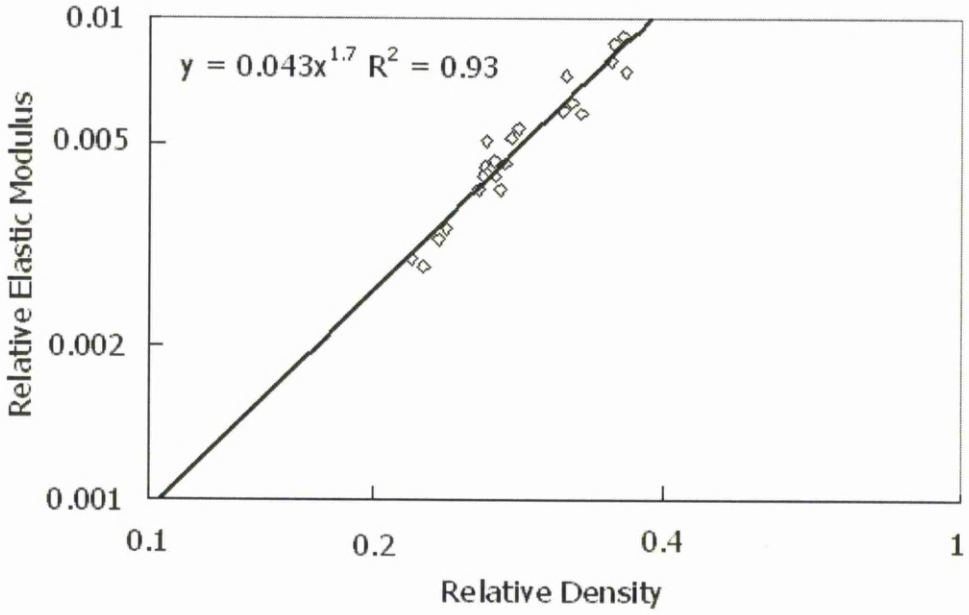

Figure 4.2.2 Relative elastic modulus versus the relative density of porous steel specimens manufactured by the decomposition route. The pore size of the specimens is 425-710μm.

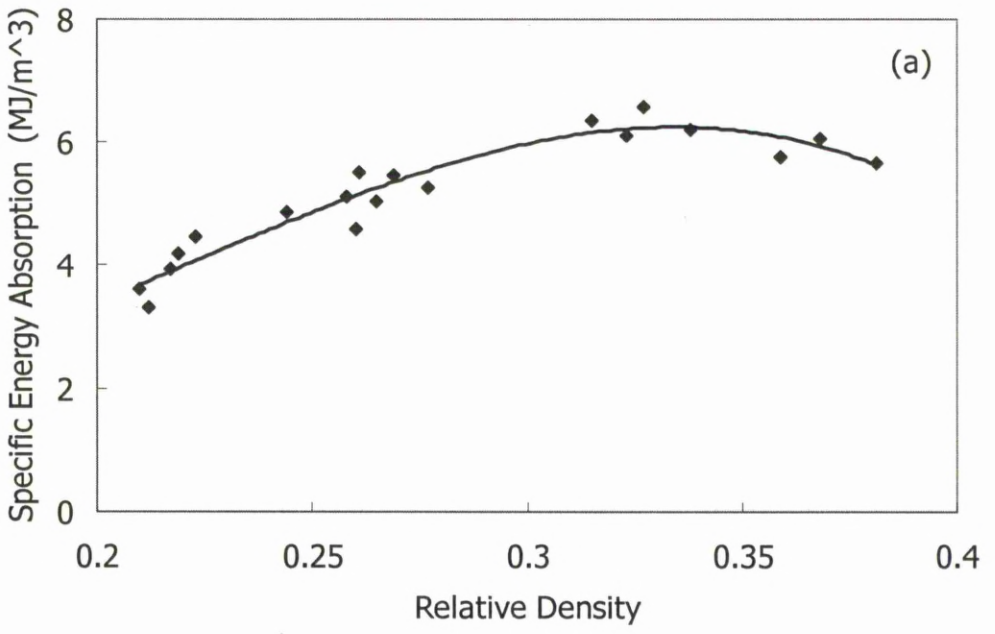

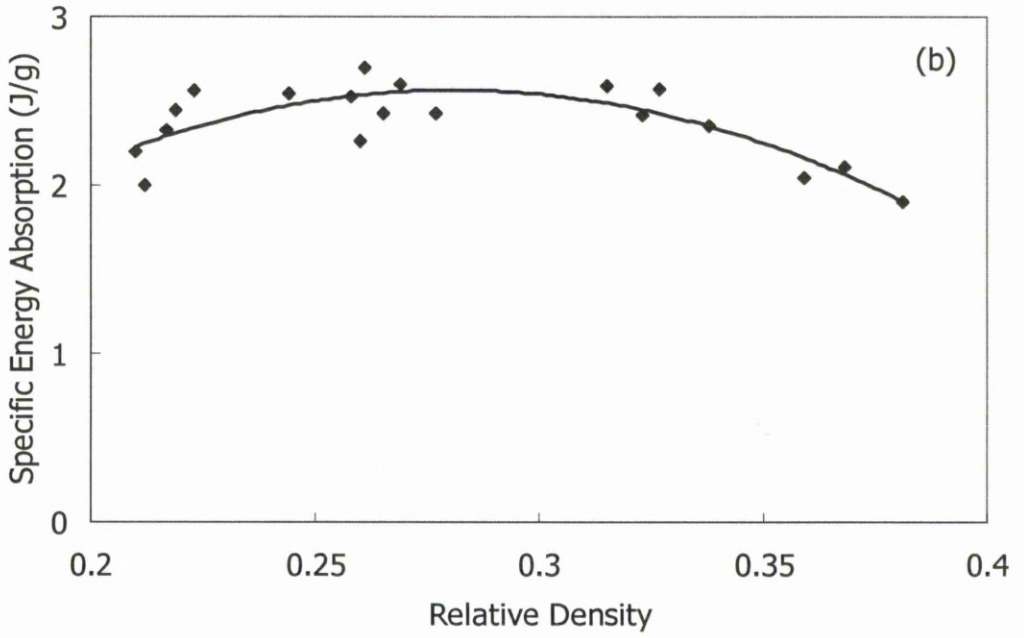

Figure 4.2.3 Specific energy absorption (a) per unit volume and (b) per unit mass versus relative density of porous steel specimens manufactured by the decomposition route. The pore size of the specimens is 425-710μm.

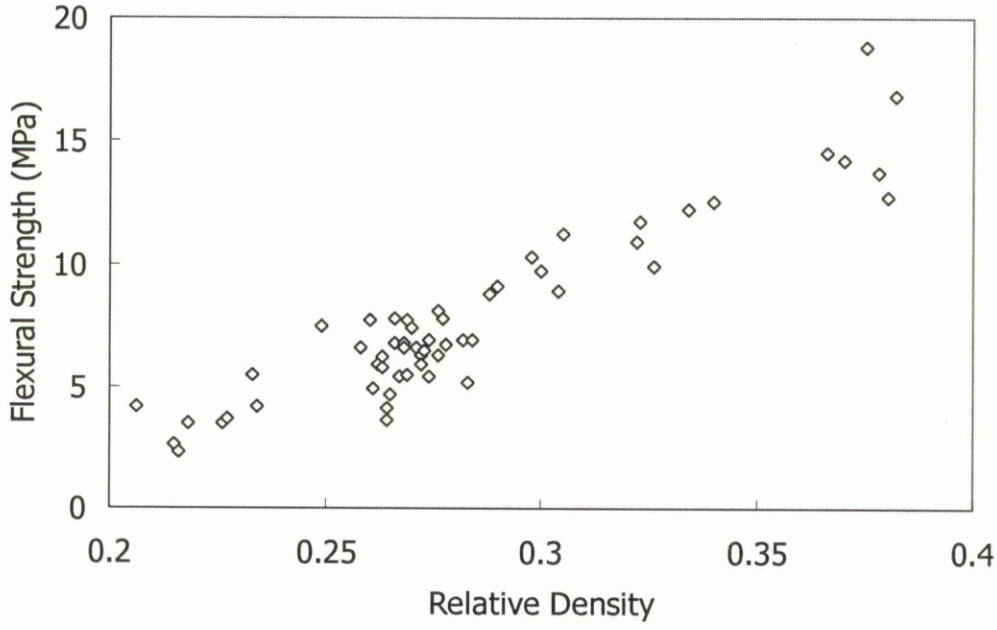

Figure 4.2.4 Variation of flexural strength with relative density for the porous steel manufactured by the decomposition route. The pore size of the specimens is 425-710μm.

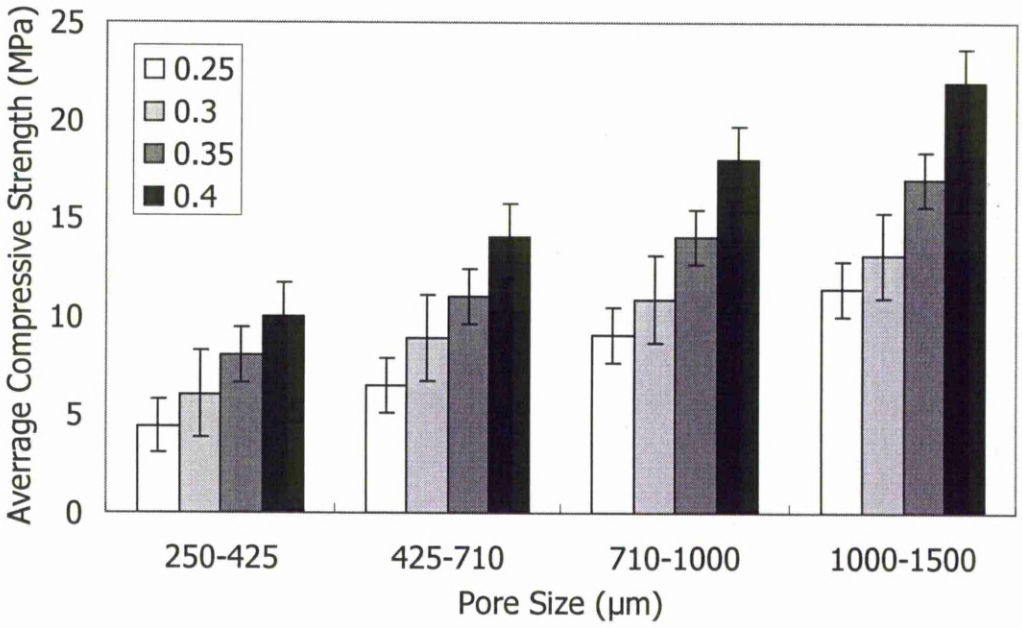

Figure 4.2.5 Average compressive strength versus the pore size of porous steel specimens with different relative densities, manufactured by the decomposition route.

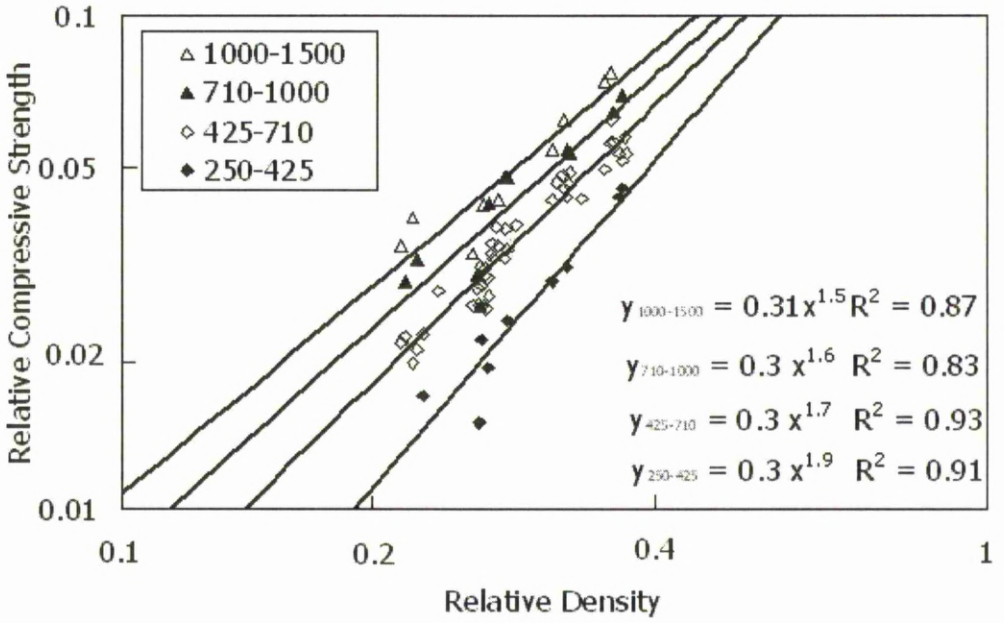

Figure 4.2.6 Relative compressive strength versus the relative density of porous steel specimens with different pore sizes, manufactured by the decomposition route.

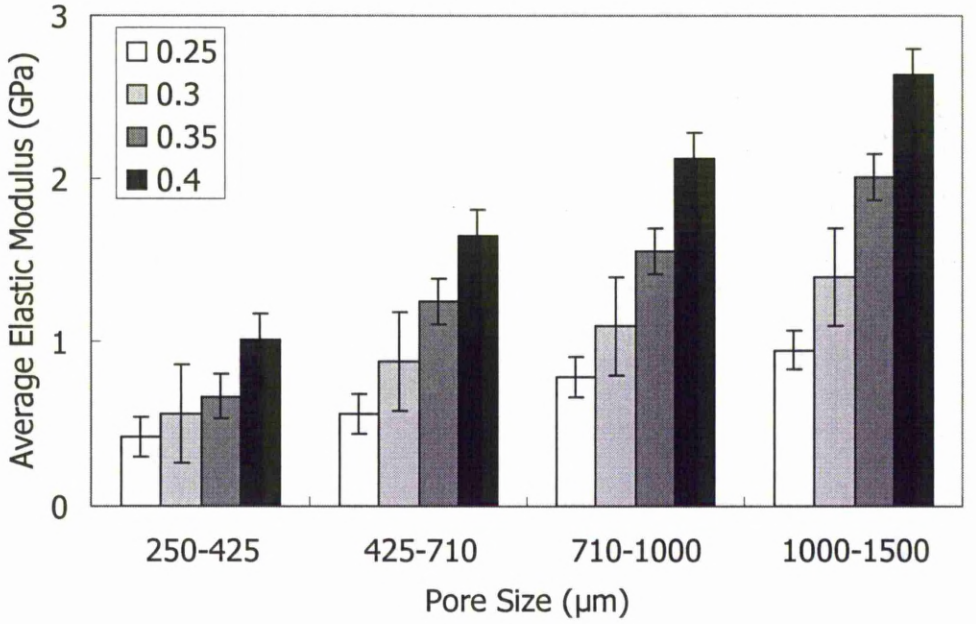

Figure 4.2.7 Average elastic modulus versus the pore size of porous steel specimens, manufactured by the decomposition route.

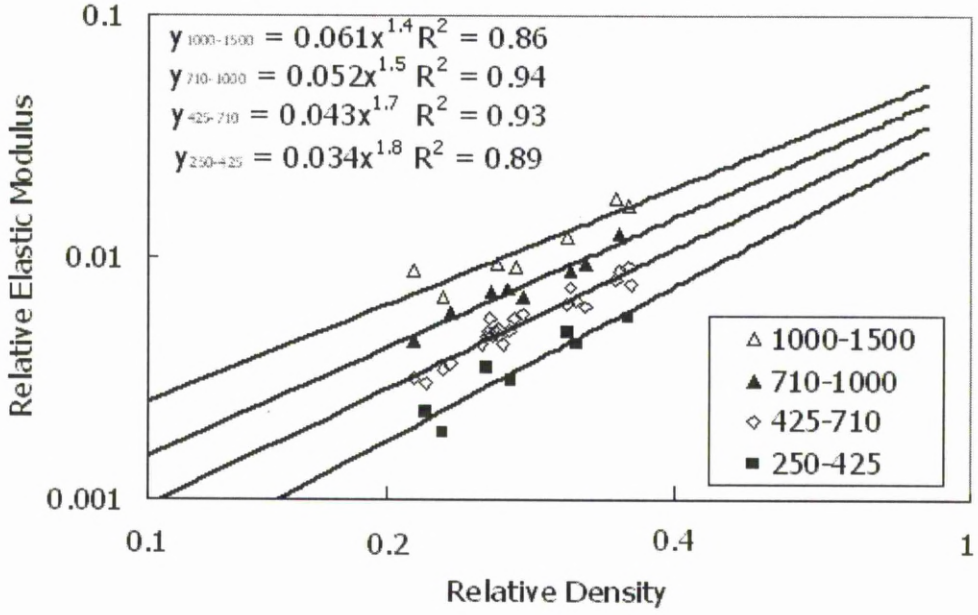

Figure 4.2.8 Relative elastic modulus versus the relative density of porous steel specimens with different pore sizes, manufactured by the decomposition route.

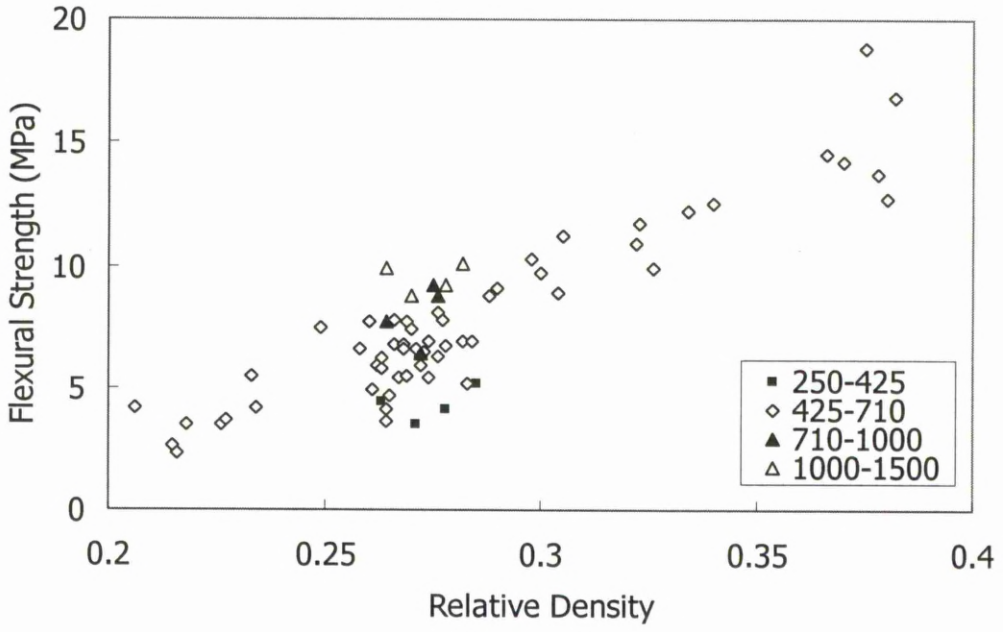

Figure 4.2.9 Flexural strength versus the relative density of porous steel specimens with different pore sizes, manufactured by the decomposition route.

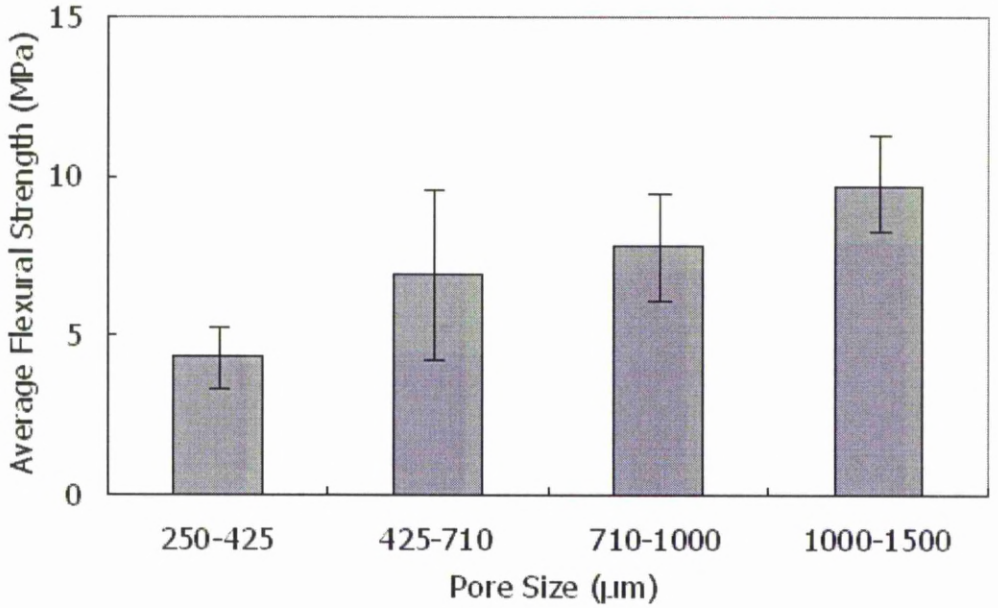

Figure 4.2.10 Average flexural strength versus the pore size of porous steel specimens with nominal relative density of 0.3, manufactured by the decomposition route.

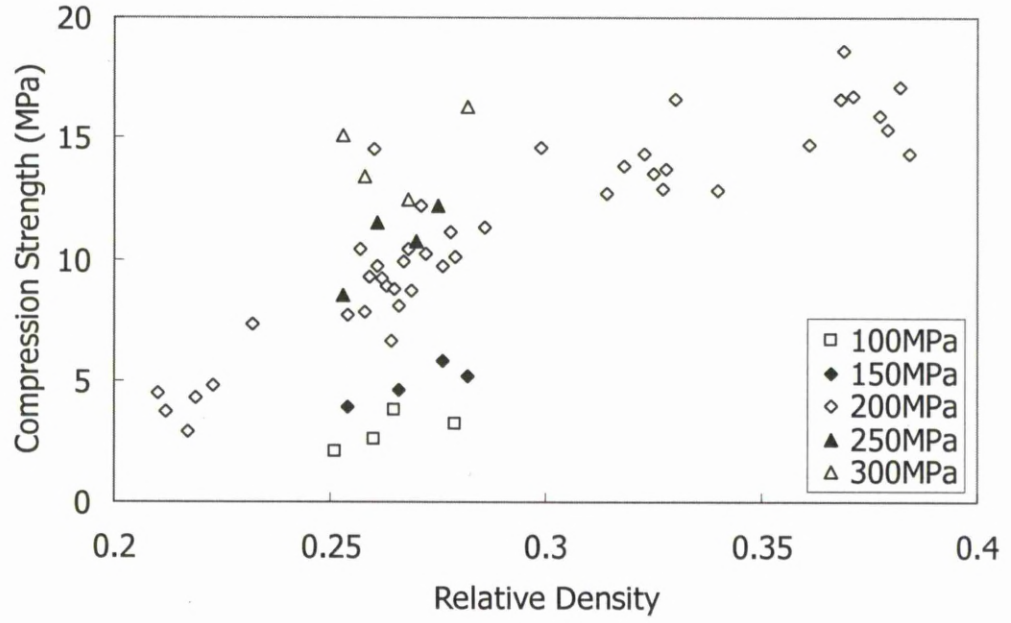

Figure 4.2.11 Variation of compressive strength with relative density for the porous steel specimens manufactured by the decomposition route with different compaction pressures.

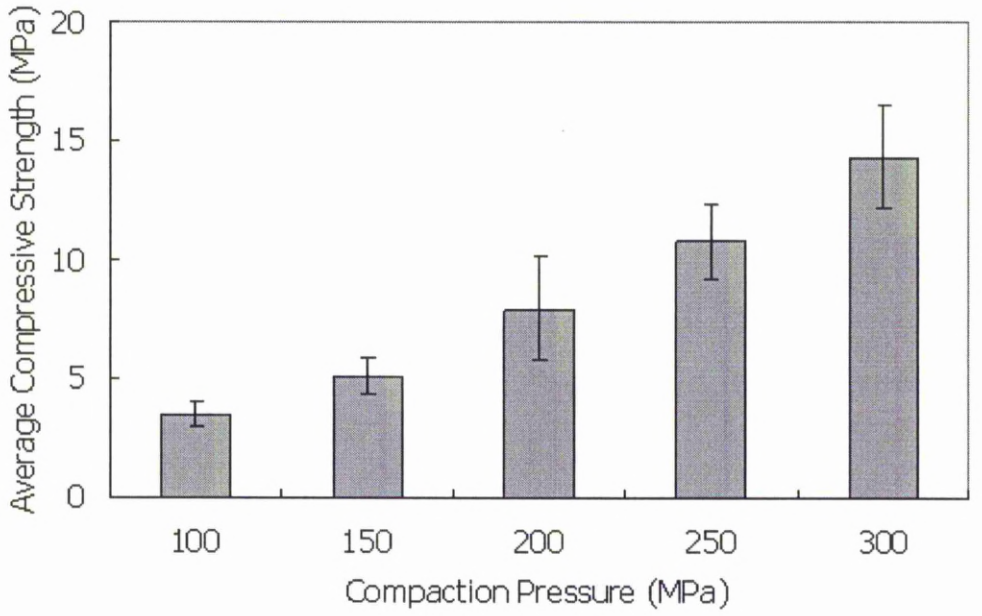

Figure 4.2.12 Average compressive strength versus compaction pressure for the porous steel specimens with a nominal relative density of 0.3, manufactured by the decomposition route.

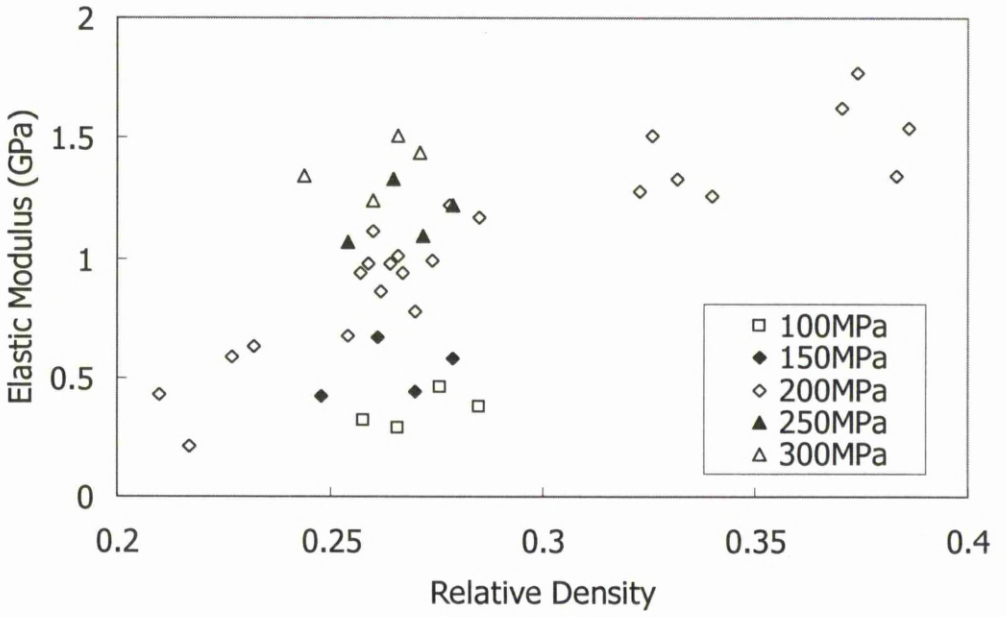

Figure 4.2.13 Variation of elastic modulus with relative density for the porous steel specimens manufactured by the decomposition route with different compaction pressures.

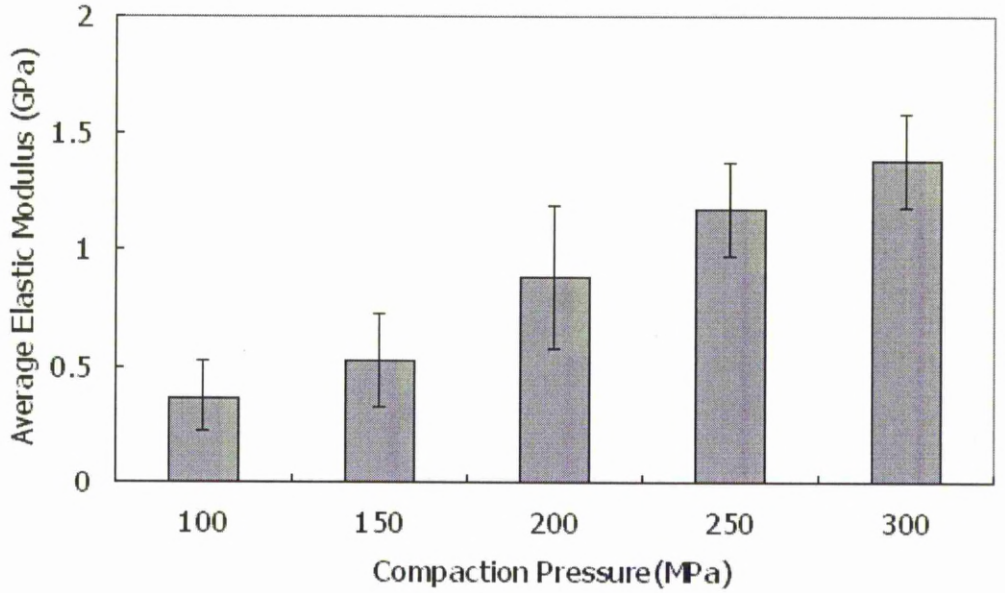

Figure 4.2.14 Average elastic modulus versus compaction pressure for the porous steel specimens with a nominal relative density of 0.3, manufactured by the decomposition route.

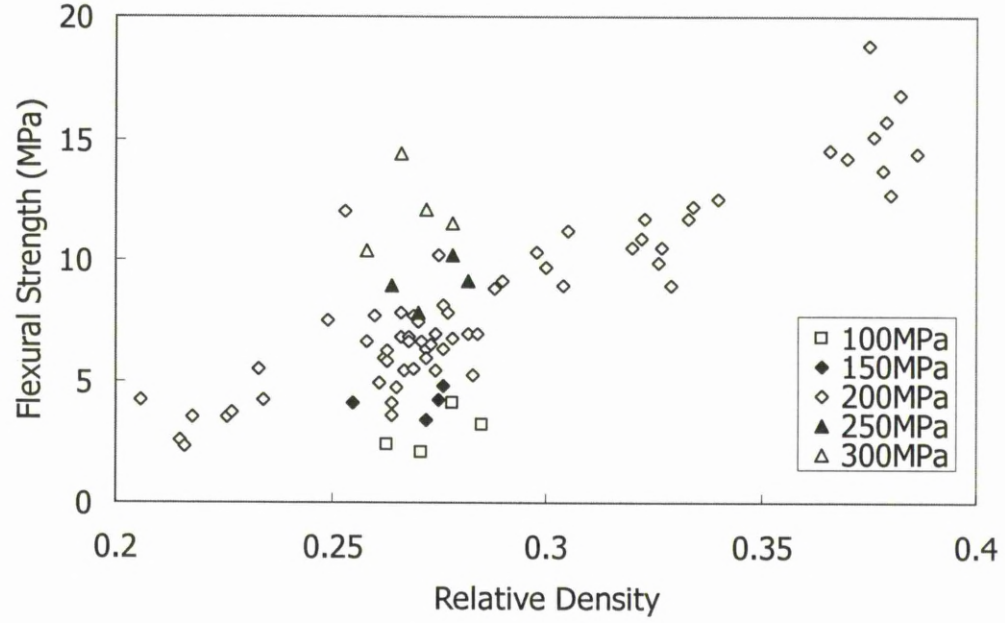

Figure 4.2.15 Variation of flexural strength with relative density for the porous steel specimens manufactured by the decomposition route with different compaction pressures.

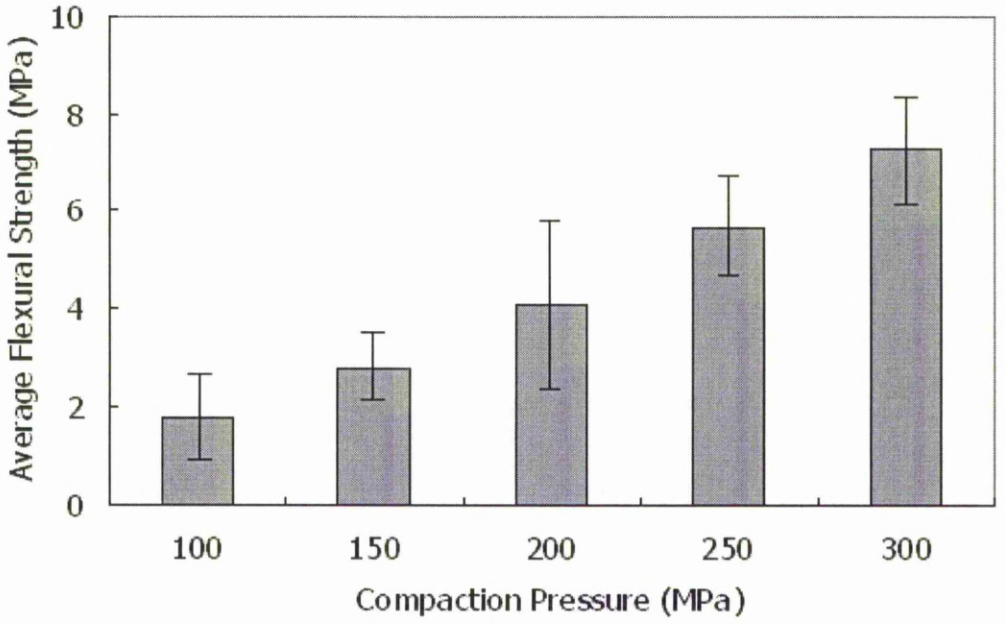

Figure 4.2.16 Average flexural strength versus compaction pressure for the porous steel specimens with a nominal relative density of 0.3, manufactured by the decomposition route.

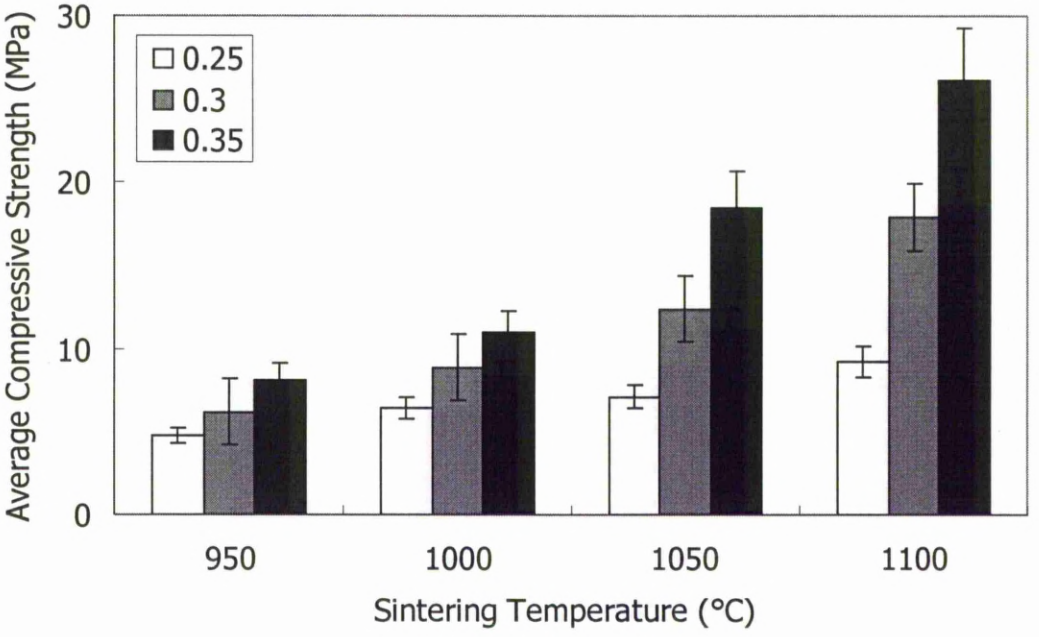

Figure 4.2.17 Average compressive strength versus sintering temperature for the porous steel specimens with different nominal relative densities manufactured by the decomposition route.

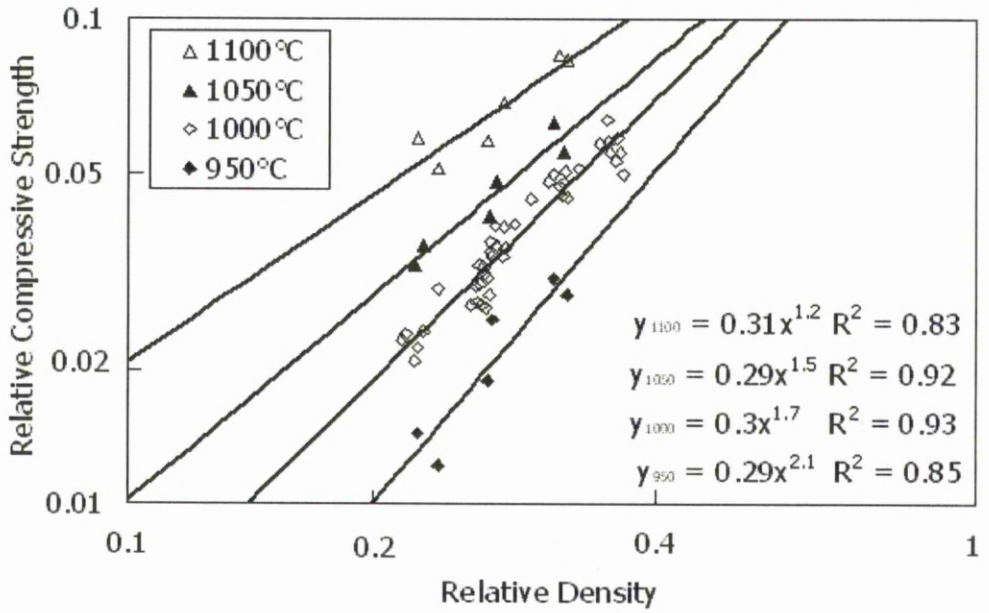

Figure 4.2.18 Relative compressive strength versus the relative density of porous steel specimens manufactured by the decomposition route with different sintering temperatures. The pore size of the specimens is 425-710μm.

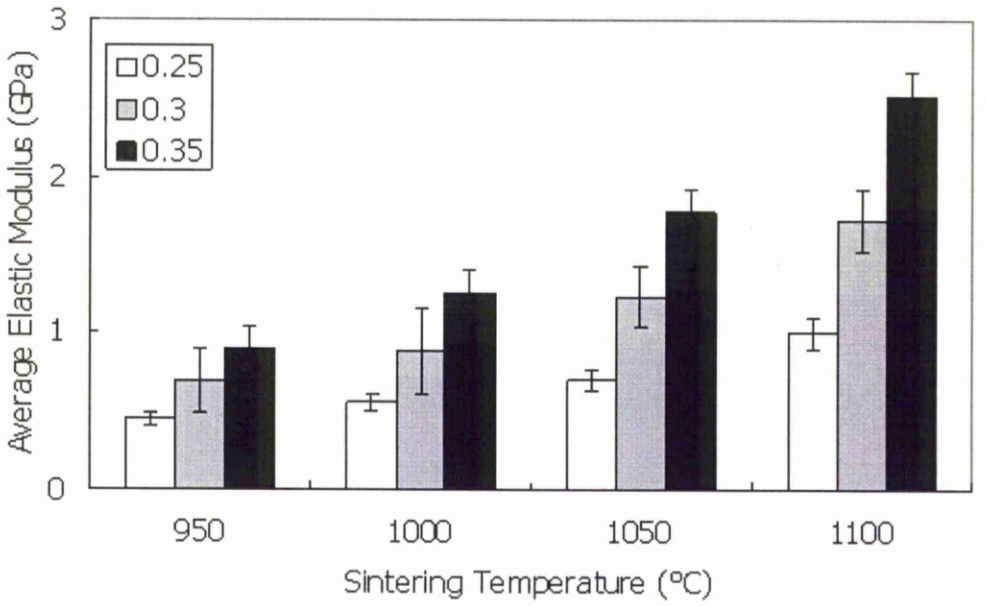

Figure 4.2.19 Average elastic modulus versus sintering temperature for the porous steel specimens with different nominal relative densities manufactured by the decomposition route.

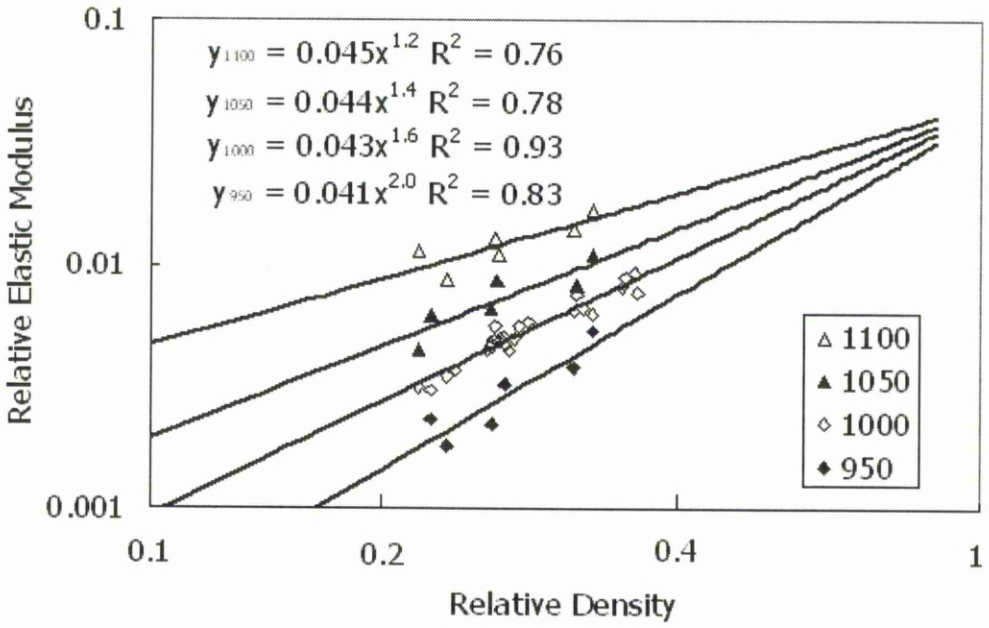

Figure 4.2.20 Relative elastic modulus versus the relative density of porous steel specimens, manufactured by the decomposition route with different sintering temperatures. The pore size of the specimens is 425-710μm.

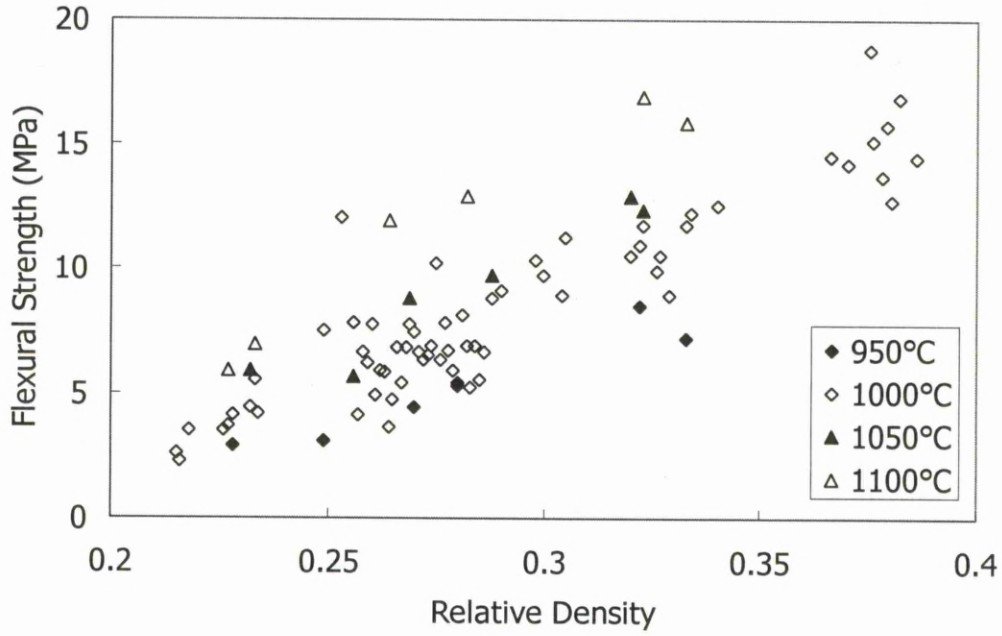

Figure 4.2.21 Flexural strength versus the relative density of porous steel specimens, manufactured by the decomposition route with different sintering temperatures. The pore size of the specimens is 425-710μm.

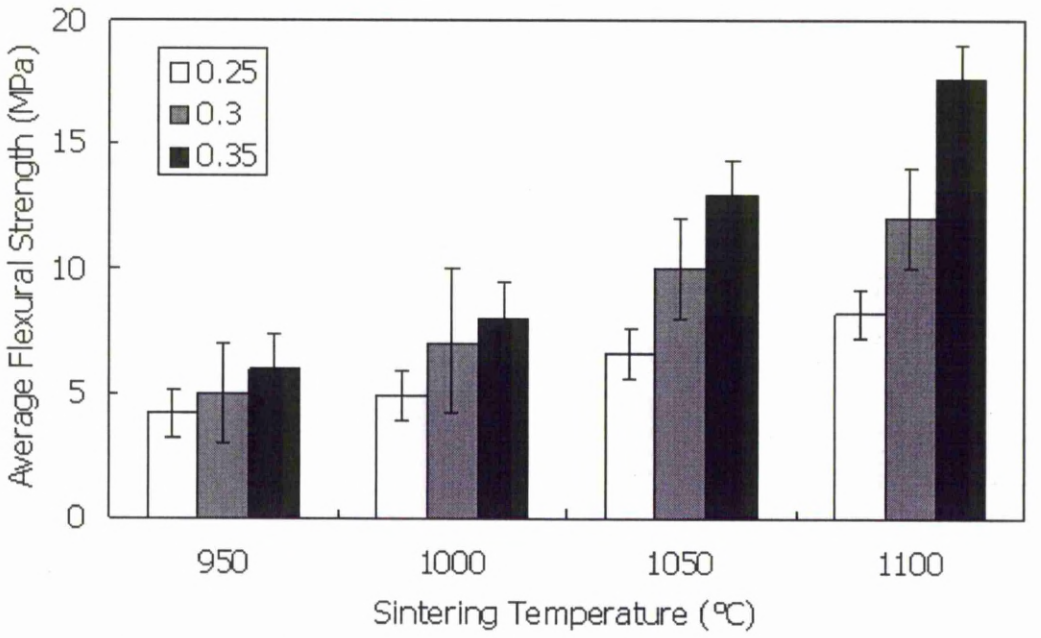

Figure 4.2.22 Average flexural strength versus sintering temperature of porous steel specimens with different nominal relative densities manufactured by the decomposition route.

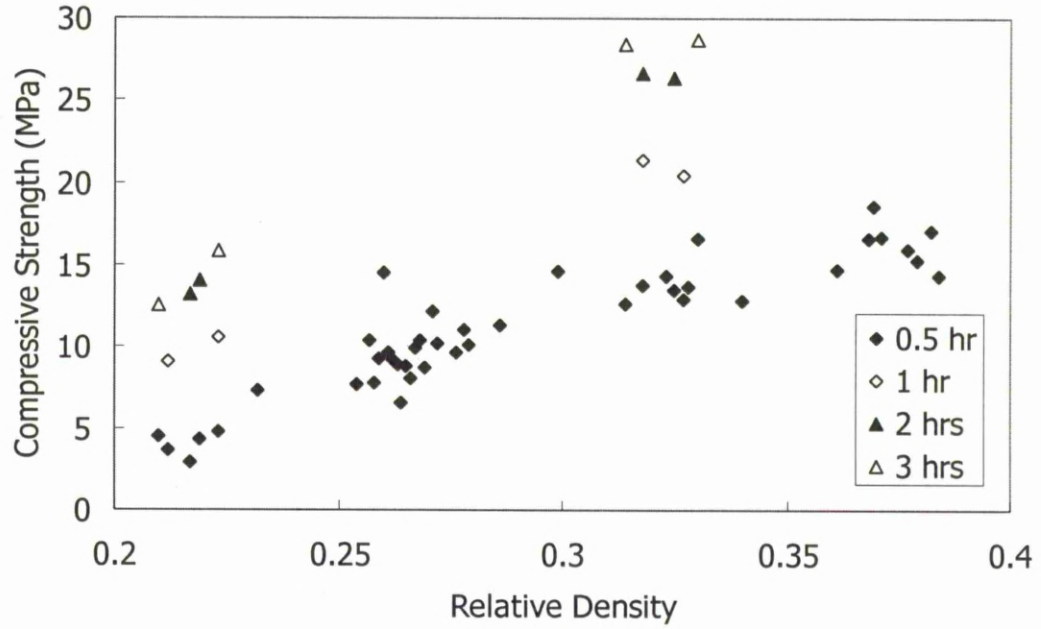

Figure 4.2.23 Variation of compressive strength with relative density for the porous steel specimens manufactured by the decomposition route with different sintering times.

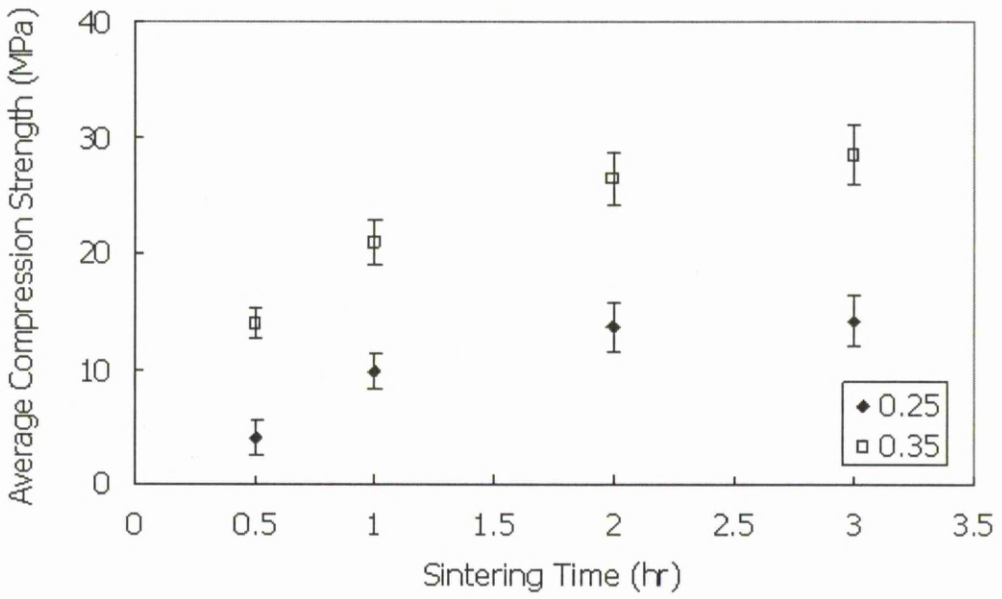

Figure 4.2.24 Average compressive strength versus the sintering time for the porous steel specimens with a nominal relative densities of 0.25 0r 0.35, manufactured by the decomposition route.

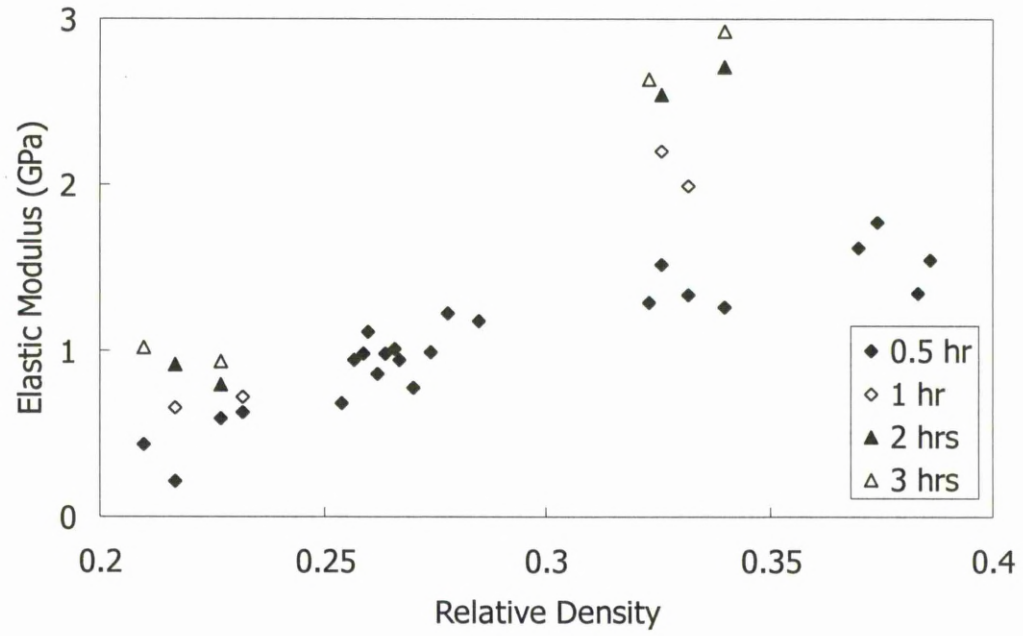

Figure 4.2.25 Variation of elastic modulus with relative density for the porous steel specimens manufactured by the decomposition route with different sintering times.

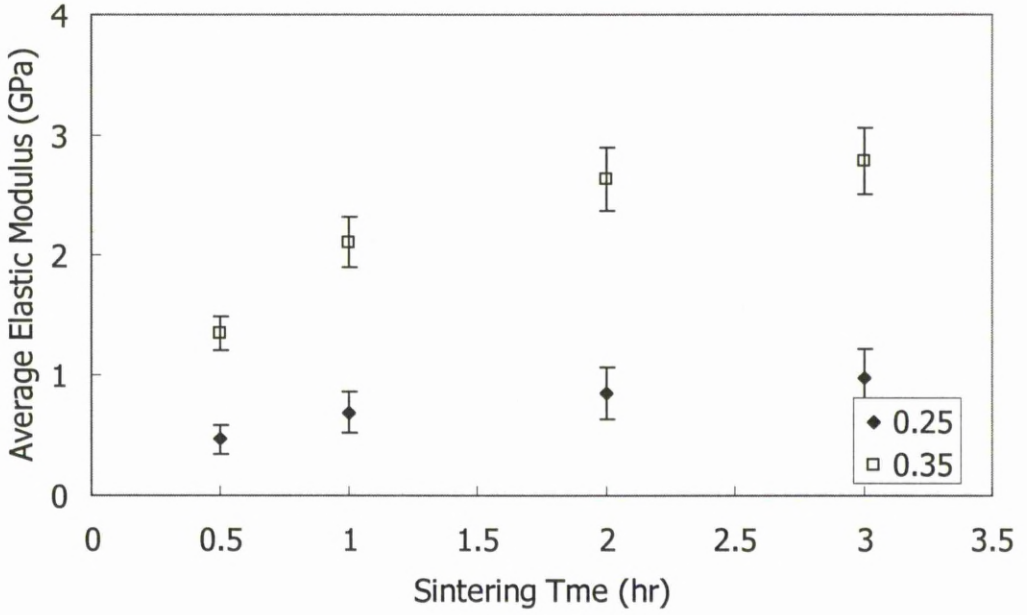

Figure 4.2.26 Average elastic modulus versus the sintering time for the porous steel specimens with a nominal relative densities of 0.25 0r 0.35, manufactured by the decomposition route.

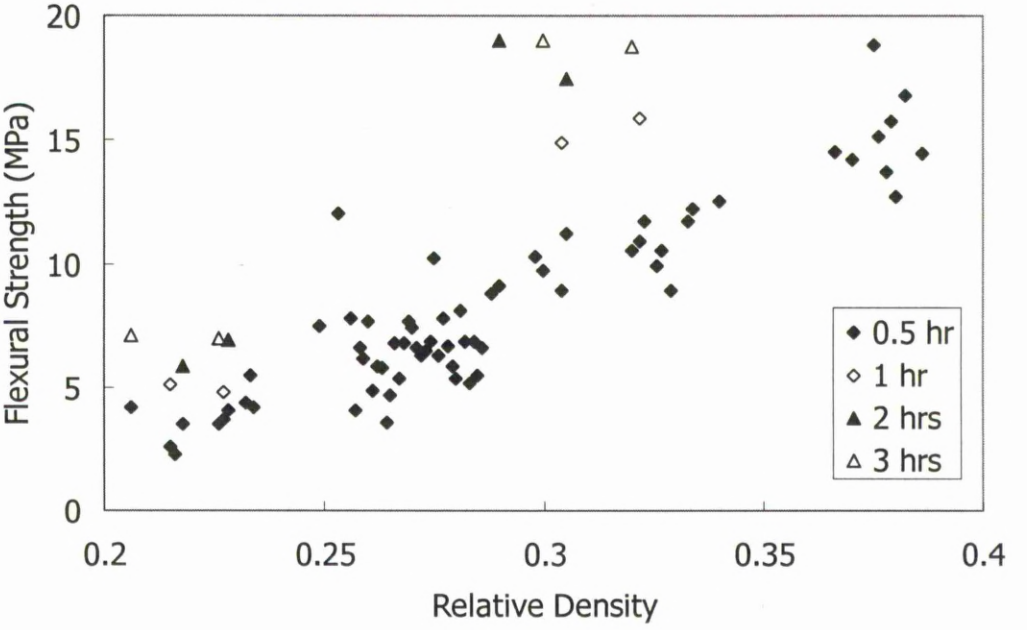

Figure 4.2.27 Variation of flexural strength with relative density for the porous steel specimens manufactured by the decomposition route with different sintering times.

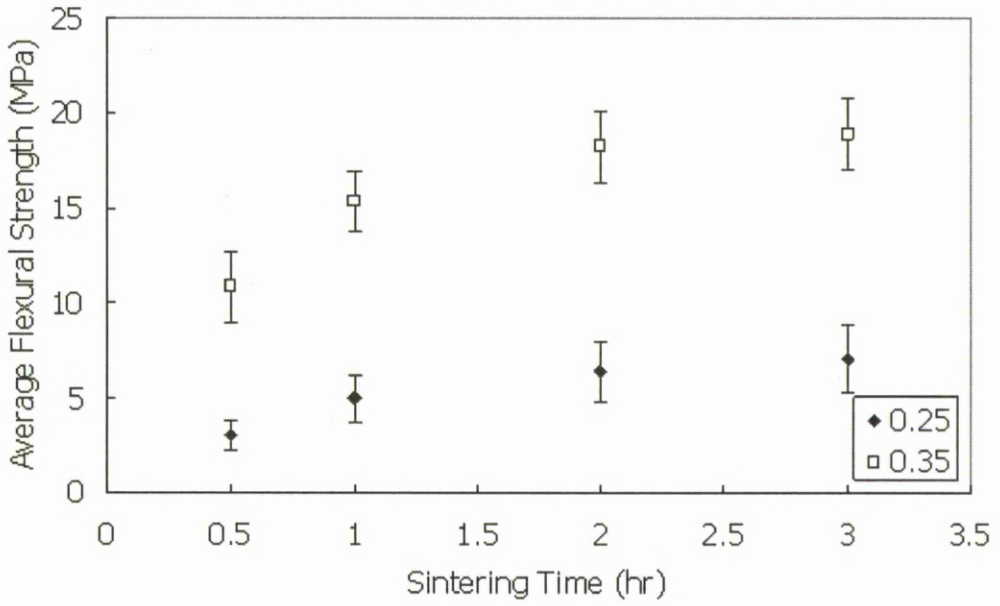

Figure 4.2.28 Average flexural strength versus the sintering time for the porous steel specimens with a nominal relative densities of 0.25 0r 0.35, manufactured by the decomposition route.

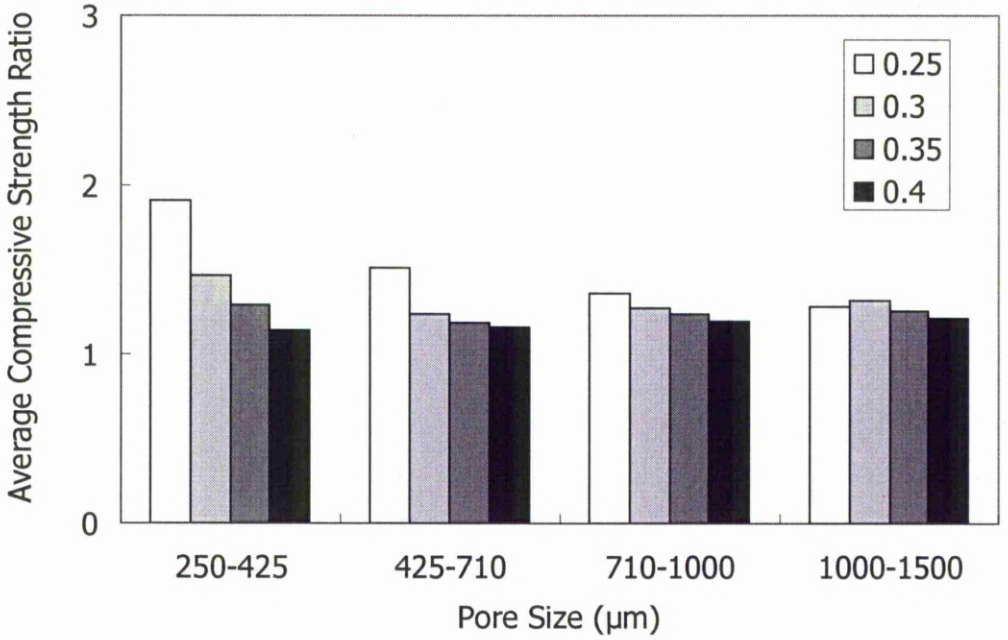

Figure 4.3.1 The ratios of average compressive strength between the porous steel specimens manufactured by the decomposition and dissolution routes, with different pore sizes and relative densities. The compaction pressure is 200MPa.

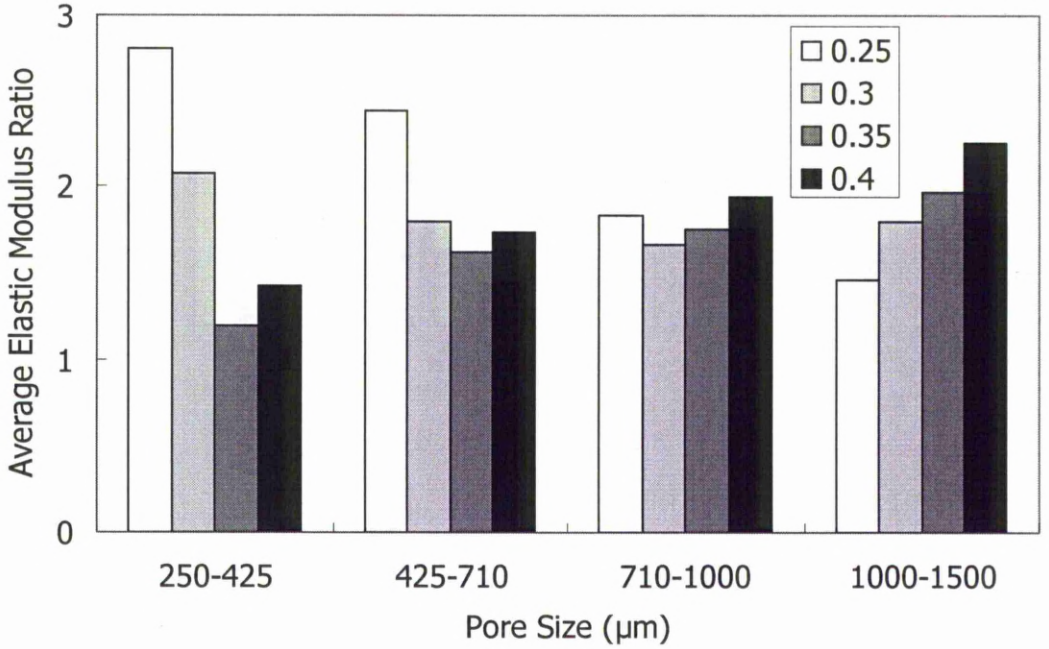

Figure 4.3.2 The ratios of average elastic modulus between the porous steel specimens manufactured by the decomposition and dissolution routes, with different pore sizes and relative densities. The compaction pressure is 200MPa.

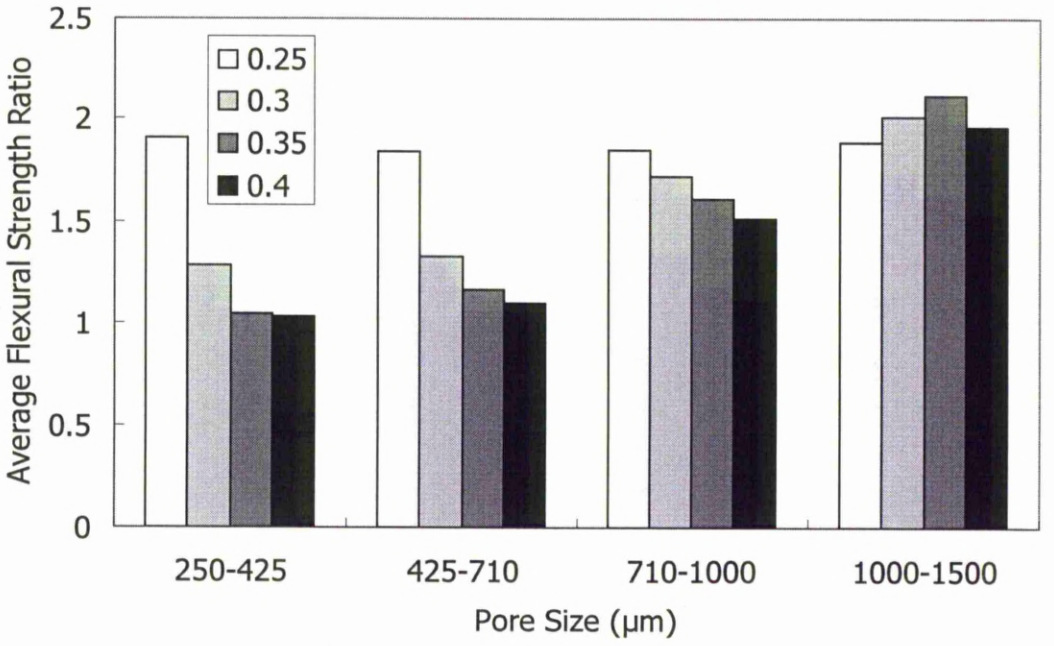

Figure 4.3.3 The ratios of average flexural strength between the porous steel specimens manufactured by the decomposition and dissolution routes, with different pore sizes and relative densities. The compaction pressure is 200MPa.

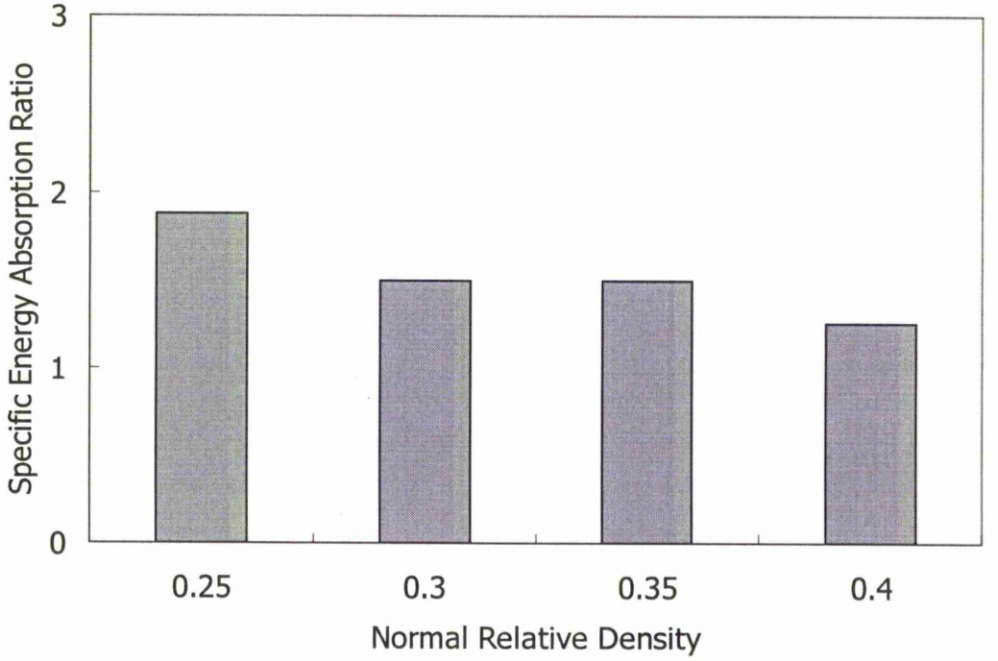

Figure 4.3.4 The ratios of average energy absorption per unit mass between the porous steel specimens manufactured by the decomposition and dissolution routes, with different relative densities. The pore size of the specimens is 425-710μm and the compaction pressure is 200MPa.

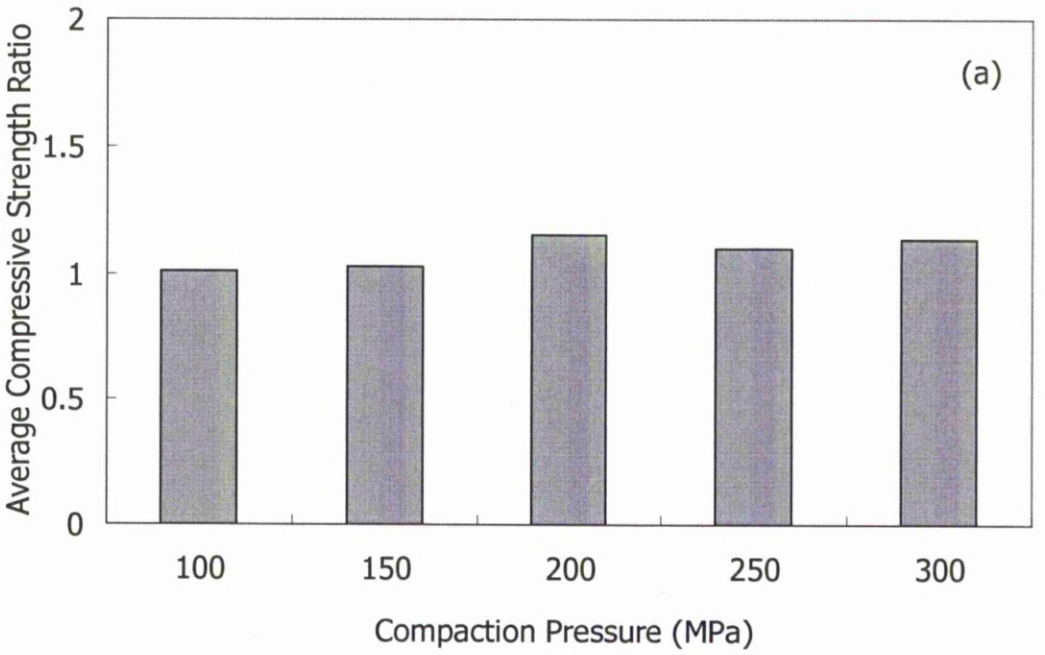

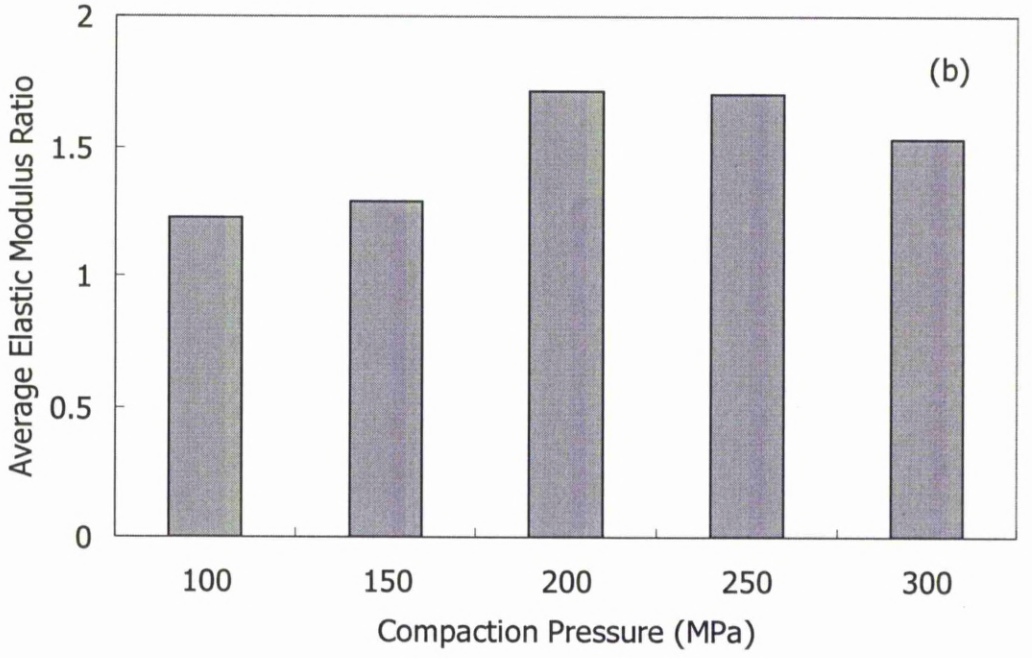

Figure 4.3.5 The ratios of (a) average compressive strength, (b) average elastic modulus and (c) average flexural strength between the porous steel specimens manufactured by the decomposition and dissolution routes, with different compaction pressures. The pore size of the specimens is 425-710μm and the nominal relative density is 0.3. (to be continued)

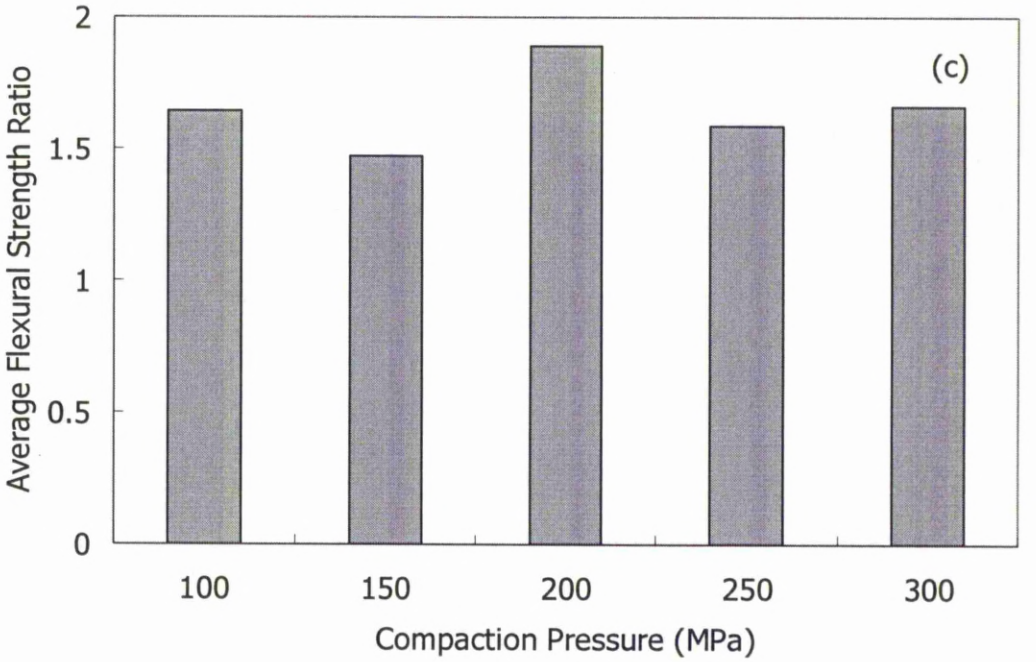

Figure 4.3.5 The ratios of (a) average compressive strength, (b) average elastic modulus and (c) average flexural strength between the porous steel specimens manufactured by the decomposition and dissolution routes, with different compaction pressures. The pore size of the specimens is 425-710μm and the nominal relative density is 0.3.

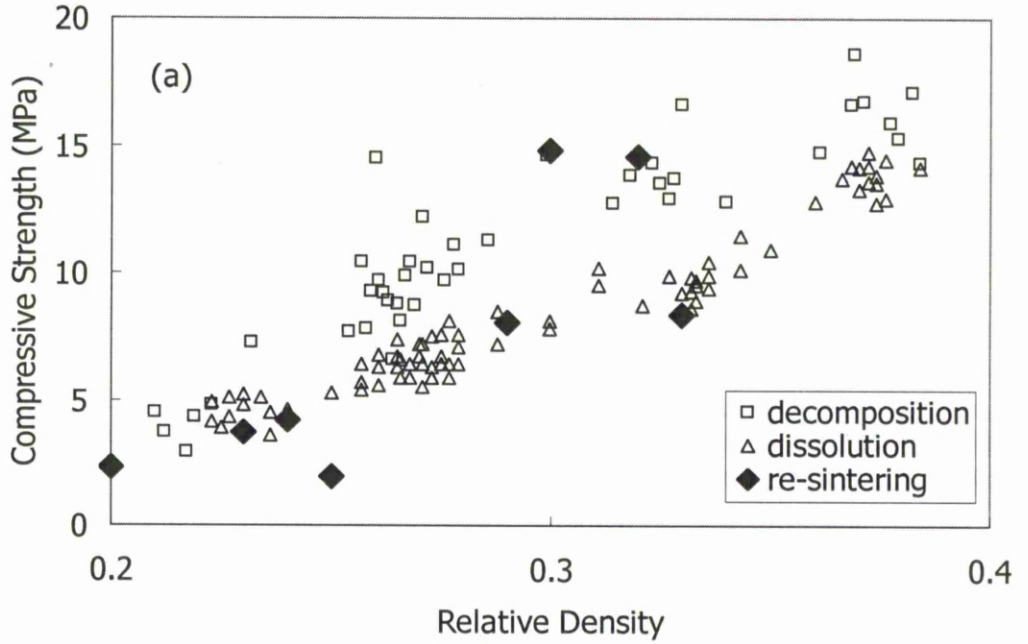

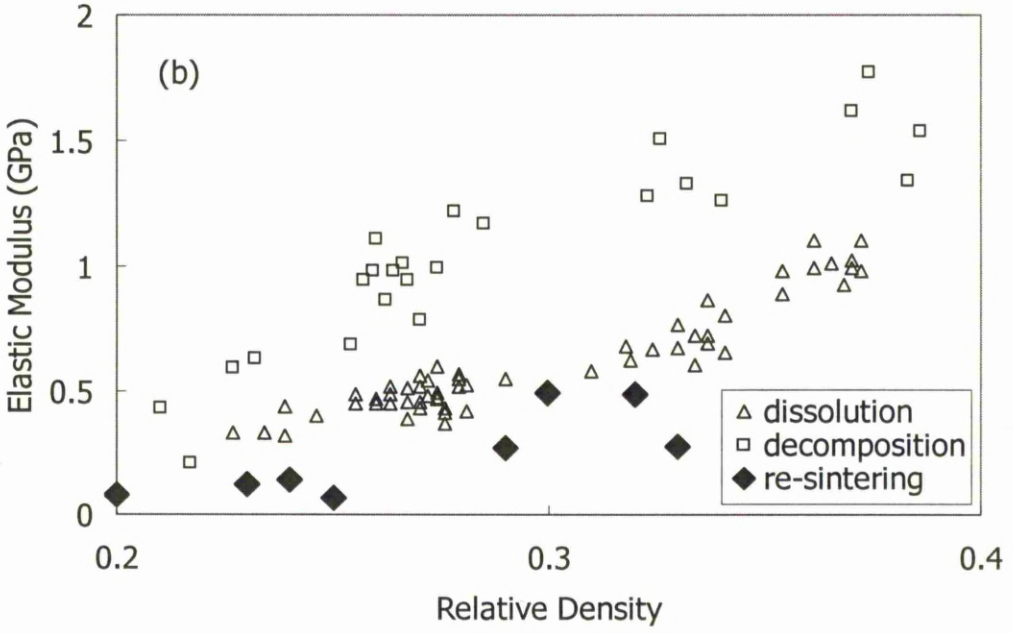

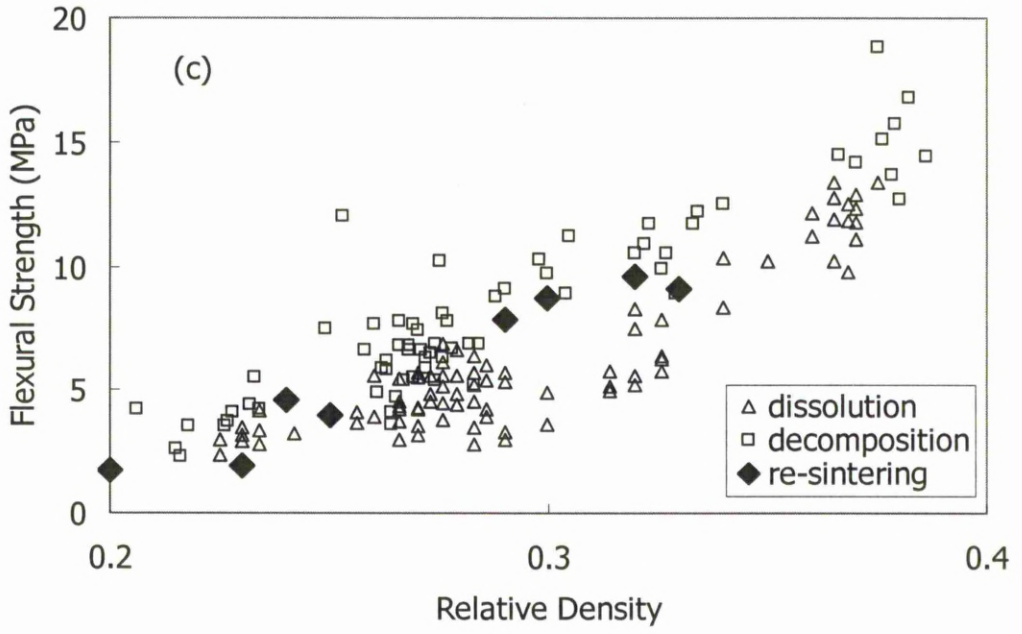

Figure 4.3.6 (a) compressive strength, (b) elastic modulus and (c) flexural strength of the porous steel specimens manufactured by the dissolution decomposition and re-sintering routes, as a function of relative density. The pore size of the specimens is 425-710μm and the compaction pressure is 200MPa.

CHAPTER 5 ACOUSTIC PROPERTIES OF POROUS STEEL

5.1 Homogeneous Single-layer Specimens

The sound absorption properties of the LCS porous steel specimens manufactured by the dissolution route with a homogeneous structure and different porosities, pore sizes, pore shapes, thicknesses, air-gap depths and metal metrics are presented in this section. In order to make quantitative comparisons among the samples, the characteristic parameters of the sound absorption coefficient curves, including peak half-width of the curve and Noise Reduction Coefficient (NRC), are presented and compared. The peak half-width is defined as the width of the frequency band of the sound absorption curve above an absorption coefficient of 0.5. NRC is the mean or arithmetic average of the absorption coefficients at the frequencies of 250, 500, 1000 and 2000 Hz (Bell, 1982). These parameters serve as a convenient set of values for the assessment of the acoustic performance of the materials.

5.1.1 Air flow resistance

It is well known that air flow resistance can be used to predict the acoustical properties of acoustical absorbers. The effects of porosity, pore size and thickness of the porous steel specimens on the air-flow resistance are shown in Figures 5.1.1-5.1.3, respectively. Figure 5.1.1 shows that with a fixed pore size and specimen thickness

the air-flow resistance of porous steel specimens decrease as porosity increases. Figure 5.1.2 shows that pore size of the specimens in the range of 250-1500 μm does not affect the air-flow resistance significantly. Figure 5.1.3 shows that with a fixed pore size and porosity the air-flow resistance of the specimens increase with increasing thickness.

5.1.2 Effects of porosity

Figure 5.1.4 shows the sound absorption coefficient as a function of frequency for the porous steel specimens with four different nominal porosities of 60%, 65%, 70% and 75%. The specimens have the same pore size of 425-710μm, thickness of 10 mm and no air gap.

The peaks of the sound absorption coefficient curves are well above 0.5 in all cases. All these sound absorption curves exhibit strong and broad absorption peaks. The higher porosity specimens have better sound absorption coefficients as shown in Figure 5.1.4. The NRC, peak absorption coefficient, peak frequency and peak half-width of the curves are shown in Table 5.1.1.

The NRC decreases when the porosity increases, as shown in Figure 5.1.5. The specimen with 60% porosity shows the greatest NRC of 0.269, while the specimen with 75% porosity has a NRC of 0.137.

Table 5.1.1 NRC, peak absorption coefficient, peak frequency and peak half-width of specimens with different porosities.

Porosity (%)	NRC	Peak Absorption Coefficient	Peak Frequency (Hz)	Peak Half-Width (Hz)
60	0.269	0.668	2120	3008
65	0.258	0.899	2680	3160
70	0.204	0.965	3192	3336
75	0.137	0.985	4080	3528

The porosity affects both the peak sound absorption coefficient and the frequency of the peak of the sound absorption curve. For nominal porosities of 60%, 65%, 70% and 75%, the peak absorption coefficients are 0.674, 0.896, 0.963 and 0.992, as shown in Figure 5.1.6, and the frequencies of the peaks are 2120HZ, 2680Hz, 3192Hz and 4080Hz, as shown in Figure 5.1.7. Both the frequency and absorption coefficient of the peak increase as porosity increases.

Figure 5.1.8 shows the peak half-width of the sound absorption coefficient curves as a function of porosity. The specimen with 75% porosity shows the greatest peak half-width of 3528Hz, while the specimen with 60% porosity shows a peak half-width of 2568Hz. It is clear that the peak half-width decreases as porosity increases.

In general, a low porosity leads to good sound absorption at low frequencies, and a high porosity leads to good absorption at high frequencies.

The sound absorption behaviour of porous steel is affected by air-flow resistance, which in turn is determined by the complex channel structure and the rough internal pore surface of the porous steel specimens. Figure 5.1.9 shows the microstructure of the porous steel specimens with nominal porosities of 60% and 75%. The number of pores in the specimen with a nominal porosity of 60% is lower than that in the specimen with a nominal porosity of 75%. The area of channels in the specimen with a nominal porosity of 60% is smaller than that of the specimen with a nominal porosity of 75%, and the number of channels in the specimen with a nominal porosity of 60% is less than that in the specimen with a nominal porosity of 75%.

The effect of the size of the small channels to the sound dissipation by viscous losses and thermo-elastic damping is much higher than that of the large pores (Lu, 1999). When air moves from the large pores into the much smaller channels, its velocity increases significantly because of the changing volume. This process leads to massive sound wave dissipation via friction. The porous steel produced by the LCS process has a great number of smaller channels as connective channels of large pores. The number of small channels increases when the nominal porosity of porous steel increases and the size of small channels also increase. As shown in Figure 5.1.1, the air-flow resistance of specimens decreases when the nominal porosity of specimens increases because the size of small channels and air transmission rate increase. When the size of channels increases, the sound dissipation via friction in each channel decreases. As a consequence the NRC decreases with porosity, as shown in Figure

5.1.5. The sound dissipation via friction in the channels at the resonance frequency is much higher than that at other frequencies (Wang and Lu, 1999). The sound absorption coefficient of the peak increases because the number of channels increases, as shown in Figure 5.1.6. The frequency of the peak increases because the resonance frequency of each channel increases when the size of the channel increases, as shown in Figure 5.1.7. The increasing number of channels also increases the range of peak of the curve, i.e., peak half-width, as shown in Figure 5.1.8.

5.1.3 Effects of pore size

Figure 5.1.10 shows the sound absorption coefficients as a function of frequency for the porous steel specimens with four different pore sizes of 250-425μm, 425-710μm, 710-1000μm and 1000-1500μm. The specimens have a nominal porosity of 70%, a specimen thickness of 10 mm and no air gap. The NRC, peak absorption coefficient, peak frequency and peak half-width of the curves are shown in Table 5.1.2.

The NRC decreases with increasing pore size, but the changes are not significant, as shown in Figure 5.1.11. The specimens with the pore size of 250-425μm shows the greatest NRC of 0.217, and that with the pore size of 1000-1500μm shows the lowest NRC of 0.180.

Table 5.1.2 NRC, peak absorption coefficient, peak frequency and peak half-width of specimens with different pore sizes.

Pore Size (μm)	NRC	Peak Absorption Coefficient	Peak Frequency (Hz)	Peak Half-Width (Hz)
250-425	0.217	0.957	3336	3288
425-710	0.204	0.963	3192	3056
710-1000	0.182	0.977	3032	3160
1000-1500	0.180	0.992	2984	3120

The specimen with the smallest pore size of 250-425μm has the lowest and broadest peak in the sound absorption coefficient curve. The specimen with the largest pore size of 1000-1500μm has the highest and narrowest peak in the sound absorption coefficient curve. The specimens with pore sizes of 250-425μm, 425-710μm, 710-1000μm and 1000-1500μm have the peak absorption coefficients of 0.957, 0.963, 0.977 and 0.992, as shown in Figure 5.1.12, and peak frequencies of 3336HZ, 3192Hz, 3032Hz and 2984Hz, as shown in Figure 5.1.13. The absorption coefficient of peak increases and the peak frequency decreases as the pore size increases.

Figure 5.1.14 shows the peak half-width of the sound absorption coefficient curves as a function of pore size. The peak half-width does not change very much with pore size. The specimen with 250-425μm pore size shows the greatest peak half-width of 3288Hz, while the specimen with 425-710μm pore size shows the lowest peak half-width of 3056Hz.

As Figure 5.1.2 shows, there is not much difference between the air-flow resistances

of the specimens with different pore sizes. The sound absorption coefficient curves of the specimens with different pore sizes are also very similar, as shown in Figure 5.1.10.

5.1.4 Effects of cell shape

The shape of the potassium carbonate particles used in the LCS process determines the pore shape of the porous steel specimens. Figure 5.1.15 shows two kinds of potassium carbonate grains with different shapes: (a) angular and (b) spherical. The effect of cell shape on the sound absorption coefficient is shown in Figure 5.1.16. The open-celled porous steel specimens have a pore size of 425-710μm, thickness of 10 mm, and no air gap. The NRC, peak absorption coefficient, peak frequency and peak half-width of the curves are shown in Table 5.1.3.

Table 5.1.3 NRC, peak absorption coefficient, peak frequency and peak half-width of specimens with different cell shapes.

Nominal porosity	NRC		Peak Absorption Coefficient		Peak Frequency (Hz)		Peak Half-Width (Hz)	
	angular	spherical	angular	spherical	angular	spherical	angular	spherical
65%	0.306	0.258	0.894	0.896	2448	2680	2568	2568
70%	0.235	0.204	0.962	0.963	3200	3168	3200	3056
75%	0.133	0.137	0.98	0.992	4040	3720	3464	3336

The NRC of specimens with angular cells decreases with increasing porosity slightly more than that of specimens with spherical cells, as shown in Figure 5.1.17. The NRC

values of the specimens with angular and spherical cells are 0.306 and 0.258 at a nominal porosity of 65% and 0.133 and 0.137 at a nominal porosity of 75%.

Figure 5.1.18 shows that the angular cell specimens and spherical cell specimens have a similar peak sound absorption coefficient when they have the same porosity and pore size. The peak sound absorption coefficients of the angular cell specimens are 0.894, 0.962, and 0.980, and those of the spherical cell specimens are 0.896, 0.963 and 0.992, when the nominal porosities of the specimens are 65%, 70% and 75%, respectively. The differences of peak coefficients between the two types of specimens are very small.

Figure 5.1.19 shows that the peak frequency of angular cell specimens increases slightly more than that of spherical cell specimens when the porosity increases. The peak frequencies of the angular cell specimens are 2448Hz, 3200Hz, and 4040HZ and those of the spherical cell specimens are 2680Hz, 3168Hz, and 3720Hz, when the nominal porosities of the specimens are 65%, 70% and 75%, respectively. The differences of frequencies between the two types of specimens are -232Hz, 32Hz and 320Hz, respectively.

Figure 5.1.20 shows that the peak half-width of specimens with angular cells increases slightly more than that of specimens with spherical cells with increasing porosity. The peak half-width of the spherical cell specimen with a nominal porosity

of 65% is 3336Hz, while that of the angular cell specimen with a nominal porosity of 65% is 3468Hz. The specimens with angular and spherical cells with a nominal porosity of 75% show the same peak half-width of 2568Hz.

Rezanezhad *et al* (2009) suggested that airflow resistivity of a porous material is controlled by a pore shape coefficient, which in turn is controlled by the factors such as path tortuosity, pore size distribution, the sphericity and roundness of the pores. Hubbert (1956) expressed the relationship between air-flow resistivity, r, and permeability, K_p, by:

$$r = \frac{\rho_0}{K_p} \tag{5.1.1}$$

where ρ_0 is the air density. Carman (1937) gave the relationship between permeability and pore shape coefficient, c_{ps}, as:

$$K_p = c_{ps} \frac{a^2 \phi^3}{(1-\phi)^2} \tag{5.1.2}$$

where ϕ is porosity and a is pore size. The pore shape coefficient, c_{ps}, is:

$$c_{ps} = \frac{S_p}{N_p{}^2 \tau_p}, \tag{5.1.3}$$

where S_p is sphericity of pores (fully spherical pores have sphericity = 1, and other shapes have sphericity < 1), N_p is number of pores and τ_p is pore path tortuosity.

According to equations (5.1.1), (5.1.2) and (5.1.3), with a fixed porosity, pore size, and thickness, a spherical pore specimen has a higher pore shape coefficient, lower air-flow resistivity, because of the higher sphericity.

The measured results show the same trend as forecast by this theory, where the sound absorption coefficient of specimen decreases with increasing sphericity.

5.1.5 Effects of specimen thickness

Figure 5.1.21 shows the effect of thickness of specimens on the sound absorption coefficient with a nominal porosity of 60%. The porous steel specimens have thicknesses of 5mm, 10mm, 20mm, or 40mm, a pore size of 425-710μm, and no air gap. The NRC, peak absorption coefficient, peak frequency and peak half-width of the curves are shown in Table 5.1.4.

Figure 5.1.22 shows that the NRC increases with increasing specimen thickness. The specimen with 5mm thickness shows the lowest NRC of 0.162, while the specimen with 40mm thickness shows the highest NRC of 0.442.

The peak frequency and absorption coefficient increase when the thickness decreases. When the thicknesses of specimens are 5mm, 10mm, 20mm and 40mm, the peak absorption coefficients are 0.707, 0.664, 0.531 and 0.506, as shown in Figure 5.1.23,

and the peak frequencies are 3184HZ, 2120Hz, 1096Hz and 440Hz, as shown in Figure 5.1.24, respectively. Thicker specimens have lower peak sound absorption coefficients but broader resonant absorption peaks.

Table 5.1.4 NRC, nominal peak absorption coefficient, peak frequency and peak half-width of specimens with a nominal porosity of 60% and different thicknesses.

Specimen Thickness	NRC	Peak Absorption Coefficient	Peak Frequency (Hz)	Peak Half-Width (Hz)
5 mm	0.162	0.707	3184	3168
10 mm	0.269	0.664	2120	2816
20 mm	0.355	0.531	1096	1504
40 mm	0.442	0.506	440	776

Figure 5.1.25 shows that the peak half-width of sound absorption coefficient curve decreases with increasing thickness. The specimen with 10mm thickness shows the greatest peak half-width of 3168Hz, while the specimen with 40mm thickness shows the lowest peak half-width of 776Hz.

Figure 5.1.26 shows the effect of thickness on the sound absorption coefficient curve of specimens with a nominal porosity of 75%. The NRC, peak absorption coefficient, peak frequency and peak half-width of the curves are shown in Table 5.1.5.

Figure 5.1.27 shows that the NRC increases with increasing thickness. The specimen with a thickness of 5mm shows the lowest NRC of 0.063, while the specimen with a thickness of 40mm shows the highest NRC of 0.569. This is because the sound

absorption coefficient of specimens at low frequencies increases significantly with increasing thickness.

Table 5.1.5 NRC, nominal peak absorption coefficient, peak frequency and peak half-width of specimens with a nominal porosity of 75% and different thicknesses.

Specimen Thickness	NRC	Peak Absorption Coefficient	Peak Frequency (Hz)	Peak Half-Width (Hz)
5 mm	0.063	-	-	-
10 mm	0.137	0.992	4080	2400
20 mm	0.397	0.994	2200	3824
40 mm	0.569	0.906	944	1256

The peak frequency and absorption coefficient increase when the thickness decreases. Thicker specimens have lower peak sound absorption coefficients. When the thicknesses of the specimens are 10mm, 20mm and 40mm, the peak sound absorption coefficients are 0.992, 0.994 and 0.906, as shown in Figure 5.1.28, and the peak frequencies are 4080HZ, 2200Hz and 944Hz, as shown in Figure 5.1.29. The sound absorption curve of the specimen with 40mm thickness has a second peak, with its sound absorption coefficient being 0.881 and the frequency being 3188Hz.

Figure 5.1.30 shows that the peak half-width of the porous steel specimens does not show a clear trend with increasing thickness. The specimen with 20mm thickness shows the greatest peak half-width of 3824Hz, while the specimen with 40mm thickness shows the lowest peak half-width of 1256Hz.

Figure 5.1.3 shows that the air-flow resistance increases with increasing thickness of specimens. Figures 5.1.22 and 5.1.27 show that the NRC increases with increasing thickness of specimens in the same trend as air-flow resistance, as shown in Figure 5.1.3. In other word, the effect of thickness on the overall sound absorption is mainly due to its effect on airflow resistance.

5.1.6 Effects of air-gap depth

The porous steel specimens have poor sound absorption capacities at low frequencies when they are secured directly to a rigid backing. Introducing an air gap between the porous structure and the back plate shifts the sound absorption peak towards a lower frequency. Figures 5.1.31 (a) and (b) show the effects of 20mm and 50mm air-gap depth on the sound absorption coefficient curves of specimens with nominal properties of 60%, 65% 70% and 75%. The NRC, peak absorption coefficient, peak frequency and peak half-width of the curves are shown in Table 5.1.6.

Figure 5.1.32 shows that the NRC increases with increasing air-gap depth. The NRC of the specimen with a normal porosity of 60% increases from 0.269 to 0.586 and NRC of the specimen with a normal porosity of 75% increases from 0.137 to 0.555 when the air-gap depth increases from 0mm to 50mm. NRC decreases with increasing porosity when there is no air-gap. It does not change much with porosity when the air-gap depths are 20mm and 50mm.

Table 5.1.6 NRC, peak absorption coefficient, peak frequency and peak half-width of specimens with different porosities and air-gap depths.

Nominal Porosity	NRC		Peak Absorption Coefficient		Peak Frequency (Hz)		Peak Half-Width (Hz)	
	20mm	50mm	20mm	50mm	20mm	50mm	20mm	50mm
60%	0.458	0.586	0.805	0.953	864	378	2040	1792
65%	0.493	0.626	0.855	0.957	968	386	2392	2008
70%	0.503	0.616	0.997	0.998	1288	784	2344	1968
75%	0.456	0.558	0.998	0.999	1576	960	2552	1656

Figures 5.1.33 and 5.1.34 show that the peak sound absorption coefficient increases and the peak frequency decreases with increasing air-gap depth. Figure 5.1.33 shows that the effect of air-gap depth on peak sound absorption coefficient decreases with increasing porosity. When the air-gap depth increases from 0mm to 50mm, the peak sound absorption coefficient of the specimen with a nominal porosity of 60% increases from 0.674 to 0.953, and the peak sound absorption coefficient of the specimen with a nominal porosity of 75% increases from 0.992 to 0.999. Figure 5.1.34 shows that the effect of air-gap depth on peak frequency increases with increasing porosity. When the air-gap depth increases from 0mm to 50mm, the peak frequency of the specimen with a nominal porosity of 60% decreases from 2120Hz to 378Hz and the peak frequency of the specimen with a nominal porosity of 75% decreases from 4080Hz to 960Hz.

Figure 5.1.35 shows that the peak half-width decreases with increasing air-gap depth. The peak half-width of the specimen with a nominal porosity of 60% decreases from 3008Hz to 1792Hz and the peak half-width of the specimen with a nominal porosity of the 75% decreases from 3528Hz to 1656Hz when the air-gap depth increases from 0mm to 50mm. Peak half-width increases with increasing porosity when there is no air-gap depth, but it does not change much with porosity when the air-gap depths are 20mm and 50mm.

Introducing an air-gap between the specimen and the back plate increases the sound absorption coefficient at low frequencies. The effect of air-gap depth is much higher than the nominal porosity of specimens. As shown in Figures 5.1.32 and 5.1.35, the NRC decreases and the peak half-width increases with increasing porosity when the air-gap depth is 0mm, but they do not change much with porosity when the air-gap depths are 20mm and 50mm. As shown in Figures 5.1.33 and 5.1.34, the peak absorption coefficient and the peak frequency increase with increasing porosity but the effect of porosity decreases with increasing air-gap depth.

Figures 5.1.36 (a) and (b) show the sound absorption coefficient curves of the porous steel specimens with nominal porosities of 60%, 65%, 70% and 75%, pore sizes of 250-425μm, 425-710μm, 710-1000μm and 1000-1500μm with air-gap depths of 20mm and 50mm respectively. The NRC, peak absorption coefficient, peak frequency and peak half-width of the curves are shown in Table 5.1.7.

Table 5.1.7 NRC, peak absorption coefficient, peak frequency and peak half-width of specimens with different pore sizes and air-gap depths.

Pore Size (μm)	NRC		Peak Absorption Coefficient		Peak Frequency (Hz)		Peak Half-Width (Hz)	
	20mm	50mm	20mm	50mm	20mm	50mm	20mm	50mm
250-425	0.564	0.660	0.999	0.999	1352	826	3432	2504
425-710	0.501	0.582	0.997	0.998	1288	784	2200	1928
710-1000	0.497	0.602	0.957	0.998	1104	632	1664	1800
1000-1500	0.489	0.601	0.984	0.996	1072	560	1648	1784

Figure 5.1.37 shows that the NRC increases with increasing air-gap depth. The NRC of the specimen with a pore size of 250-425μm increases from 0.217 to 0.660 and the NRC of the specimen with a pore size of 1000-1500μm increases from 0.180 to 0.601 when the air-gap depth increases from 0mm to 50mm. However, the NRC does not change very much when the air-gap depth is increased from 20mm to 50mm.

Figures 5.1.38 and 5.1.39 show that the peak sound absorption coefficient increases and the peak frequency decreases with increasing air-gap depth. However, the peak sound absorption coefficients in all cases are close to one and the variations are small. Figure 5.1.39 shows that when the air-gap depth increases from 0mm to 50mm, the peak frequency of the specimen with a pore size of 250-425μm decreases from 3336Hz to 826Hz, and the peak frequency of the specimen with a pore size of 1000-1500μm decreases from 2984Hz to 560Hz.

Figure 5.1.40 shows that the peak half-width generally decreases with increasing air-gap depth for the specimens with a fixed pore size. The peak half-width of the specimen with a pore size of 250-425μm decreases from 3288Hz to 2504Hz and the peak half-width of the specimens with a pore size of 1000-1500μm decreases from 3120Hz to 1784Hz when the air-gap depth increases from 0mm to 50mm.

Figures 5.1.41 (a), (b) and (c) show the sound absorption coefficient curves for the specimens with a nominal porosity of 70%, a pore size of 425-710μm, and thicknesses of 5mm, 10mm and 20mm and with air-gap depths of 0, 20 and 50mm respectively. The NRC, peak absorption coefficient, peak frequency and peak half-width of the curves are shown in Table 5.1.8.

Figure 5.1.42 shows that the NRC increases with increasing air-gap depth, and the effect of air-gap depth decreases with increasing the thickness of specimens. The NRC of the specimen with a thickness of 5mm increases from 0.079 to 0.508 and the NRC of the specimen with a thickness of 20mm increases from 0.417 to 0.600 when the air-gap depth increases from 0mm to 50mm. The NRC decreases with increasing specimens' thickness when the air-gap depths are 0mm and 20mm, but it does not change very much with specimens' thickness when the air-gap depth is 50mm.

Table 5.1.8 NRC, peak absorption coefficient, peak frequency and peak half-width of specimens with different thicknesses and air-gap depths.

Specimen	NRC			Peak Absorption Coefficient		
Thickness	0mm	20mm	50mm	0mm	20mm	50mm
5 mm	0.079	0.454	0.578	-	0.997	0.991
10 mm	0.204	0.521	0.620	0.963	0.996	0.998
20 mm	0.417	0.569	0.600	0.897	0.831	0.796
	Peak Frequency (Hz)			Peak Half-Width (Hz)		
	0mm	20mm	50mm	0mm	20mm	50mm
5 mm	-	1720	1008	-	3272	1768
10 mm	3192	1288	784	3056	2136	1472
20 mm	1792	576	520	2580	1256	1344

Figure 5.1.43 shows the effect of air-gap depth on peak sound absorption coefficient. There is not much change in peak sound absorption coefficient with increasing air-gap depth and thickness, as it is close to unity in all cares. Figure 5.1.44 shows that the effect of air-gap depth on peak frequency decreases with increasing thickness. When the air-gap depth increases from 0mm to 50mm, the peak frequency of the specimen with a thickness of 10mm decreases from 3192Hz to 784Hz, and the peak frequency of the specimen with a thickness of 20mm decreases from 1792Hz to 520Hz.

Figure 5.1.45 shows that the peak half-width decreases with increasing air-gap depth. The peak half-width of the specimen with a thickness of 10mm decreases from 3056Hz to 1472Hz and the peak half-width of the specimen with a thickness of

20mm decreases from 2580Hz to 1344Hz when the air-gap depth increases from 0mm to 50mm. Peak half-width increases with increasing thickness but the effect of thickness decreases with increasing air-gap depth.

A greater air-gap depth leads to a lower peak frequency. As a consequence, the absorption performance is considerably enhanced at the low frequency range (Wang and Lu, 1999; Lu *et al*, 1999; Lu *et al*, 2000; Xie *et al*, 2004), and the NRC increases accordingly. However, the effects of air-gap depth on the peak sound absorption coefficient and the effective frequency band width of the absorption peak are not significant.

All rigid-framed porous materials backed with a rigid surface have low absorption at low frequencies. When there is an air-gap between the face of the porous material and the rigid backing surface, the sound absorption coefficient in the low frequency range can be enhanced, and the Helmholtz resonator (cavity resonator) mechanism becomes effective and predominant. Helmholtz resonator is composed of a cavity with small neck. The resonator has a definite sound absorption peak at the resonant frequency of the mass of the enclosed air in the resonator. The resonant frequency, f_r, can be calculated by (Irwin, 1979)

$$f_r = \frac{C}{2\pi}\sqrt{\frac{A}{LV}} \tag{5.1.4}$$

where C is the velocity of sound, A the cross-sectional area of the neck, L the neck length plus $0.8\sqrt{A}$ and V the volume of the cavity.

In the porous steel specimens, the combination of each pore channel with the backing air-gap can be regarded as a Helmholtz resonator. The channel can be seen as the neck and the air gap can be seen as the cavity. It can be seen from equation (5.1.4) that A/L increases when the size of small holes increases. Therefore, the resonant frequency, f_r, increases when the porosity and pore size increase. Consider a cylinder specimen with a pore size of 425-710μm, thickness of 10mm, diameter of 100mm and an air-gap behind it of 30mm, as a Helmholtz resonator system. It can be assumed that the neck of the resonator is a straight tube across the specimen. When the diameter of neck equals to an internal diameter of 500μm, the dimensional parameters of this resonator are: $A = 0.2 \times 10^{-6}$ m^2, $L \approx 9 \times 10^{-4}$ m and $V = 1.57 \times 10^{-4}$ m^3. Using these values in equation (5.1.4), the first-order estimation of the resonant frequency is 40 Hz. When the diameter of neck equals to an internal diameter of 700μm, the dimensional parameters of this resonator are: $A = 0.4 \times 10^{-6}$ m^2, $L \approx 1.2 \times 10^{-3}$ m and $V = 1.57 \times 10^{-4}$ m^3. According to equation (5.1.4), the first-order estimation of the resonant frequency is 70 Hz. The whole system has a large number of such resonators because there are numerous air channels in the rigid-framed porous materials with different lengths and cross- sectional areas. Each resonator has a peak at the selective resonator frequency and over a narrow frequency band. The whole system can accomplish the attenuation at a wide range of frequencies because each resonator has a different frequency range of peak.

When the volume of the cavity, V, increases by increasing the air-gap depth, the resonator frequency of each small hole, f_r, decreases. It is consistent with the results of the standing wave tube test in this study. Figures 5.1.4 show that the peak sound absorption coefficients appear at high frequencies of above 2000 Hz for the open-cell porous steel specimens with 0mm air-gap. The peak frequencies move towards frequencies near 1000 Hz when the specimens are backed by a 20mm air-gap and frequencies near 500Hz when they are backed by a 50mm air-gap. The results are consistent with the above analysis.

The foam samples, if backed with an air gap, with medium pore sizes perform better than that with the smallest pore size. This can be understood by examining the sound absorption mechanisms. As has been mentioned above, the sound dissipation in these conditions is principally attributed to the Helmholtz resonator effects whilst viscous losses and thermo-elastic damping become insignificant, particularly in the low frequency range.

5.1.7 Effects of matrix

Figure 5.1.46 shows the sound absorption coefficient curves of porous steel and copper (Cu), both manufactured by the LCS process. The porous Cu specimen was manufactured by Zhang and Zhao (2007). The porous steel and porous Cu specimens have the same nominal porosity of 70%, pore size of 425-710μm and thickness of

10mm. Their sound absorption coefficient curves are very similar. The peak absorption coefficient of the porous Cu specimen is 0.961 and that of the steel specimen is 0.964. The peak frequencies are 3280HZ (Cu) and 3192Hz (Steel). The peak frequency of porous steel specimen is slightly lower than that of porous Cu specimen. The porous Cu specimen shows peak half-width of 3168Hz, while the porous steel specimen shows peak half-width of 3056Hz. Overall, there is little difference in sound absorption coefficient behaviour between the porous steel and copper.

Figure 5.1.47 shows the sound absorption coefficient curves of porous steel and porous Al. The porous Al specimen was manufactured by Han *et al* (2003) using a semi-liquid sintering method. The porous steel and Al specimens have the same nominal porosity of 60%, pore size of 425-710μm, and thickness of 20mm. The porous steel specimen has a lower peak sound absorption coefficient and a narrower peak half-width than those of the porous Al specimen. The peak sound absorption coefficient of porous Al specimen is 0.945 and that of steel specimen is only 0.532. The peak frequencies are 2168HZ (Al) and 1120Hz (Steel). The peak frequency of porous steel specimen is much lower than that of the porous Al specimen. The porous Al specimen shows a peak half-width of 3168Hz, while the porous steel specimen shows a peak half-width of 3056Hz. There is a significant difference in sound absorption coefficient between the porous steel and Al specimens.

Figures 5.1.48 (a), (b) and (c) show the microstructures of the porous steel, Cu and Al, respectively. The porous steel and porous Cu specimens were produced by LCS and have the same type of porous structure, with many channels between the large pores. The porous Al specimen was manufactured by the semi-liquid sintering method and has a very different pore structure. There are fewer channels between the large pores and pore surface is less rough. The difference between porous steel and porous Al is therefore mainly due to pore structure instead of metal matrix.

Table 2.5 showed the sound absorption coefficients and NRC of a few other porous metals. The highest NRC of the closed-cell Alporas Al foam, which has a porosity of 91% and a thickness of 40mm, is 0.24 (Lu *et al*, 1999). The LCS porous steel with a nominal porosity of 75% and a thickness of 40mm has a NRC value of 0.57 (Table 5.1.5), which is much higher than the NRC of Alporas Al foam. The NRC of the lotus-type Cu with porosities of 58% and a thickness of 10mm are 0.1-0.13 (Bell, 1982). They are much lower than the NRC of the LCS porous steel with a similar porosity and thickness, which is 0.27 as shown in Table 5.1.4. The open-cell Al foam with porosities of 57-61% and thickness of 20mm have NRC values of 0.3-0.5 (Han *et al*, 2003). They are close to the NRC of 0.355 of LCS porous steel with a nominal porosity of 60% and a thickness of 20mm as shown in Table 5.1.4.

The sound absorption properties of rigid framed porous materials are mainly affected by the porous structure. The effect of metal matrix is not significant. The NRC values

of porous metals with a closed-cell (including lotus-type cell) structure are lower than that of the LCS porous steel. However, the NRC values of open-cell porous metals with different metal matrices are similar to that of the LCS porous steel.

Table 2.4 showed the sound absorption coefficients of several typical non-rigid materials. The non-rigid materials have different structures from porous metals. The sound absorption properties of non-rigid materials are affected by the porosity and flexibility of the materials. Wood fiber and three-ply board with low porosities (<20%) and flexibility have very low NRC values of 0.05 and 0.12 (Ma, 1983). The NRC values of non-rigid materials with low porosity and high flexibility, such as carpet (20mm, NRC = 0.19) and arenga pinnata (40mm, NRC = 0.33) are better than those of wood fiber and three-ply board, but lower than that of the LCS porous steel with a porosity of 60% and thickness of 20mm (NRC = 0.36) or 40mm (NRC = 0.44). The non-rigid materials with high porosities and flexibility, such as sugarcane fiber (30mm, NRC = 0.42), Bakelite (30mm, NRC = 0.48), polyurethane (50mm, NRC = 0.67) and velour (5mm, NRC = 0.33) (Ma, 1983), have higher NRC values than those of the LCS porous steel specimens with similar thicknesses. In summary, the sound absorption properties of non-rigid materials are mainly affected by their porosities and the flexibility. Non-rigid materials with high porosities and flexibility have very good sound absorption properties. The sound absorption properties of open-cell porous metals could approach those that of non-rigid materials in certain conditions.

5.2 Multi-layer assemblies

The sound absorption properties of porous steel specimens with multi-layer assembled structure with different porosities, pore sizes, thicknesses and air-gap depths are presented in this section.

5.2.1 Assemblies with different porosities

5.2.1.1 Two-layer-assemblies

Figure 5.2.1 shows the sound absorption coefficient curves of two-layer-assembled specimens. The first layers have nominal porosities of (a) 60% (X) and (b) 75% (H). The second layers have nominal porosities of 60% (X), 65% (L), 70% (M) or 75% (H). All layers have a pore size of 425-710μm and a thickness of 10 mm, with a total thickness of 20 mm. The NRC, peak absorption coefficient, peak frequency and peak half-width of the curves are shown in Table 5.2.1.

Figure 5.2.1 (a) shows that there is a large difference between the sound absorption curves of specimens XX and XL, but the sound absorption curves of specimens XM and XH are similar. When the nominal porosity of the second layer increases from 60% to 65%, the peak sound absorption coefficient increases from 0.932 to 0.977 and the peak frequency increases from 1368Hz to 2080Hz. When the nominal porosity of

the second layer increases further to 75%, the peak frequency does not increase very much. Figure 5.2.1 (b) shows that there is a large difference in peak frequency between specimens XX and XL, but the peak frequencies of XM and XH are similar. Figures 5.2.1 (a) and (b) also show that the sound absorption coefficients of two-layer-assembled specimens beyond the peaks increase when the nominal porosity of the first layer increases from 60% to 75%.

Table 5.2.1 NRC, peak absorption coefficient, peak frequency and peak half-width of two-layer assemblies with different nominal porosity orders

Order	Porosity	NRC	Peak Absorption Coefficient	Peak Frequency (Hz)	Peak Half-Width (Hz)
XX	60%-60%	0.364	0.533	888	1432
XL	60%-65%	0.432	0.788	1072	1864
XM	60%-70%	0.433	0.86	1256	2200
XH	60%-75%	0.433	0.867	1328	2632
HX	75%-60%	0.470	0.932	1368	1624
HL	75%-65%	0.429	0.977	2080	1896
HM	75%-70%	0.398	0.997	2176	3248
HH	75%-75%	0.365	0.989	2192	3184

Figure 5.2.2 shows the NRC values of the two-layer assemblies with different nominal porosity orders. The first layer of the assembly does not affect the NRC very much. However, the NRC of the two-layer assemblies increases with increasing nominal porosity of the second layer when the nominal porosity of the first layer is 60% and decreases with increasing nominal porosity of the second layer when the

nominal porosity of the first layer is 75%. When the nominal porosity of the first layer is 60%, increasing the nominal porosity of second layer from 60% to 65%, the NRC of assemblies increases from 0.364 to 0.432. When nominal porosity of the second layer increases further to 75%, the NRC does not change much. When the nominal porosity of the first layer of the two-layer assemblies is 75%, increasing the nominal porosity of the second layer from 60% to 75% decreases the NRC of assemblies from 0.471 to 0.399.

Figures 5.2.3 and 5.2.4 show the peak absorption coefficients and peak frequencies of two-layer assemblies with different nominal porosity orders. The peak sound absorption coefficient of the assembly increases with increasing the nominal porosity of the first layer. When the nominal porosity of the first layer is fixed at 60%, the peak sound absorption coefficient and peak frequency increase with increasing the nominal porosity of the second layer. When the nominal porosity of the second layer increasing from 60% to 65%, the peak sound absorption coefficient increases from 0.533 to 0.788 and the peak frequency increases from 888Hz to 1072Hz. When the nominal porosity of the second layer increases further to 75%, the peak sound absorption coefficient and frequency do not change very much.

Figure 5.2.5 shows the peak half-widths of two-layer assemblies with different nominal porosity orders. The peak half-width of the assemblies with a first layer porosity of 60% is lower than that with a first layer porosity of 75%. The peak

half-width of the assemblies increases with increasing the nominal porosity of the second layer. When the nominal porosity of the first layer is 60%, increasing the nominal porosity of the second layer from 60% to 75% increases peak half-width from 1432Hz to 2632Hz. When the nominal porosity of the first layer is 75%, increasing the nominal porosity of the second layer from 60% to 75% increases the peak half-width from 1624Hz to 3184Hz. Comparing XX and HX, which have the same second layer, the peak half-width decreases from 1432Hz to 1624Hz when the nominal porosity of the first layer increases from 60% to 75%.

In general, the nominal porosity of the first layer of the two-layer-assembled specimens has a significant effect on the sound absorption coefficient and peak frequency. Increasing first-layer porosity increases the sound absorption coefficient at all frequencies after the peak of the sound absorption curve. The effects of the second-layer porosity are smaller than the first layer. When the nominal porosity of the first layer is high, increasing the nominal porosity of the second layer increases the peak frequency but does not affect the peak sound absorption coefficient. When the nominal porosity of the first layer is low, increasing the nominal porosity of the second layer increases the peak sound absorption coefficient but does not affect the peak frequency very much.

Assembly order has an important effect on the total sound absorption characteristics. For instance, the sound absorption characteristic of XH is better than that of HX. This

phenomenon shows that the front layer of the multi-layer-assembled specimens must be selected properly. A high porosity layer at the front is normally better. When the front layer has a low porosity, the incidence sound energy will largely be reflected back from the surface. The function of the second layer is only to increase the assembly's total thickness. A front layer with a high porosity has a low primary reflection by encouraging the incoming wave to enter the next layer. The inner layer with a lower porosity can be selected to attenuate the wave energy within the absorbing material as much as possible, without causing any substantial interlayer reflections.

5.2.1.2 Four-layer assemblies

Figure 5.2.6 shows sound absorption coefficient curves of the assemblies with porosity orders of XXXX, XXXH, XXHH and XHHH. Figure 5.2.7 shows sound absorption coefficient curves of the assemblies with porosity orders of HHHH, HHHX, HHXX and HXXX. The NRC, peak absorption coefficient, peak frequency and peak half-width of the curves are shown in Table 5.2.2.

Table 5.2.2 NRC, peak absorption coefficient, peak frequency and peak half-width of four-layer assemblies with different nominal porosity orders.

Order	Porosity (%)	NRC	Peak Absorption Coefficient	Peak Frequency (Hz)	Peak Half-Width (Hz)
XXXX	60-60-60-60	0.445	0.511	472	600
XXXH	60-60-60-75	0.572	0.682	432	696
XXHH	60-60-75-75	0.586	0.697	504	840
XHHH	60-75-75-75	0.571	0.756	569	1136
HHHH	75-75-75-75	0.683	0.973	688	1288
HHHX	75-75-75-60	0.776	0.946	672	1016
HHXX	75-75-60-60	0.714	0.832	624	704
HXXX	75-60-60-60	0.626	0.698	560	592

Figures 5.2.8 and 5.2.9 show the NRC values of the assemblies corresponding to Figures 5.2.6 and 5.2.7. When the nominal porosity of the first layer is 60%, the NRC increases with increasing the nominal porosity of the second, third and fourth layers. When the nominal porosity of the first layer is 75%, the NRC increases with increasing the nominal porosity of the second, third and fourth layers, except when all layers have high porosities.

Figure 5.2.10 shows that for the assemblies with a low-porosity first layer the peak sound absorption coefficient of the assembly increases with increasing the nominal porosity of the rear layers. When the nominal porosities of the second, third and fourth layers increase from 60% to 75%, the peak absorption coefficient increases from 0.511 to 0.756, as shown in Figure 5.2.10, and the peak frequency increases

from 472HZ to 592Hz, as shown in Figure 5.2.11.

Figure 5.2.12 shows that for the assemblies with a high-porosity first layer the peak sound absorption coefficient of the assembly decreases with decreasing the nominal porosity of the rear layers. When the nominal porosities of the second, third and fourth layers increase from 60% to 75%, the peak absorption coefficient increases from 0.698 to 0.973, as shown in Figure 5.2.12, and the peak frequency increases from 560Hz to 688Hz, as shown in Figure 5.2.13.

Figure 5.2.14 shows that for the assemblies with a low-porosity first layer the peak half-width of the assembly increases with increasing the nominal porosity of the rear layers. Figure 5.2.15 shows that for assemblies with a high-porosity first layer the peak half-width of the assembly decreases with decreasing the nominal porosity of the rear layers.

Overall the effect of porosity of fourth layer is lower than that of the third layer. The effect of porosity of the third layer is lower than that of the second layer. The nominal porosity of the first layer shows the highest effect. The difference of sound absorption coefficient between assembled and homogeneous specimens with the same porosities is not big. Furthermore, the fluctuation of the sound absorption coefficient curves of four-layer-assembled porous steel structures becomes less remarkable in comparison with one-layer and two-layer-assembled porous steel structures.

Figures 5.2.16 (a) and (b) show the acoustic absorption behaviour of assemblies with gradient porosities. The orders of the specimens are XXHH and XLMH in (a) and HHXX and HMLX in (b). Each layer has the same pore size of 425-710μm, thickness of 10 mm. The total thickness of the assemblies is 40mm, with no air gap. The NRC, peak absorption coefficient, peak frequency and peak half-width of the curves are shown in Table 5.2.3.

Table 5.2.3 NRC, peak absorption coefficient, peak frequency and peak half-width of four-layer assemblies with gradient porosity orders.

Order	Porosity (%)	NRC	Peak Absorption Coefficient	Peak Frequency (Hz)	Peak Half-Width (Hz)
XXHH	60-60-75-75	0.586	0.697	504	920
XLMH	60-65-70-75	0.58	0.774	480	928
HHXX	75-75-60-60	0.714	0.832	642	904
HMLX	75-70-65-60	0.683	0.882	768	912

Table 5.2.3 shows that the assemblies with nominal porosities of XXHH and XLMH have similar NRC and peak half-width values. The peak sound absorption coefficient of the XXHH assembly is lower than that of the XLMH assembly. The peak frequency of the XXHH assembly is higher than that of the XLMH assembly. The NRC of the assembly with porosity order of HHXX is higher than that of the assembly with porosity order of HMLX. The peak sound absorption coefficient of the HHXX assembly is lower than that of the HMLX assembly. The peak frequency of

the HHXX assembly is higher than the HMLX assembly. The peak half-widths of the two assemblies are similar.

In summary, the XLMH assembly has better sound absorption behavior than the XXHH assembly, and the HMLX assembly has better sound absorption behavior than the HHXX assembly at high frequencies. The sound absorption capacity of the HMLX assembly is much higher than that of the XLMH assembly. The fluctuation of the sound absorption curve of the HMLX structure is less remarkable than that of the XLMH structure. The multi-layer-assembled structure has good sound absorption ability in a wide frequency range. The structures with decreasing gradient porosity have higher sound absorption ability than the structures with increasing gradient porosities in a wide frequency range.

5.2.1.3 Five-layer assemblies

Figure 5.2.17 shows the sound absorption coefficient curves of the five-layer assembled specimens with different orders of porosities. The nominal porosity of the first layer is either 60% or 75%, and the porosity orders of the rear layers are XLMH and HMLX. The NRC, peak absorption coefficient, peak frequency and peak half-width of the curves are shown in Table 5.2.4.

Table 5.2.4 NRC, peak absorption coefficient, peak frequency and peak half-width of five-layer assemblies with different nominal porosity orders.

Order	Porosity (%)	NRC	Peak Absorption Coefficient	Peak Frequency (Hz)	Peak Half-Width (Hz)
XXLMH	60-60-65-70-75	0.578	0.67	384	680
XHMLX	60-75-70-65-60	0.623	0.795	448	696
HXLMH	75-60-65-70-75	0.659	0.775	400	736
HHMLX	75-75-70-65-60	0.701	0.874	576	680

As Table 5.2.4 shows, the sound absorption coefficient of an assembly increases with increasing the nominal porosity of the first layer. The assembled structure with decreasing porosities in the rear layers has a higher peak sound absorption coefficient.

It is evident that the sound absorption coefficient of the XXLMH assembly is lower at low frequencies (<1500Hz) and higher at high frequencies (>1500Hz) than that of the XHMLX assembly. The sound absorption coefficient of the HXLMH assembly is lower at low frequencies (<1500Hz) and higher at high frequencies (>1500Hz) than that of the HHMLX assembly. When the difference in porosity between the first layer and the second layer increases, the effect of the front layer increases at high frequencies.

5.2.2 Assemblies with different pore sizes

Figure 5.2.18 shows the sound absorption coefficient curves of four-layer assemblies of open-cell porous steel specimens with pore sizes of 250-425μm, 425-710μm, 710-1000μm (B) and 1000-1500μm (V). Each layer has a nominal porosity of 70% and a thickness of 10 mm. The total thickness of the assembly is 40mm and has no air gap. The order of the assembly is either SMBV or VBMS. The NRC, peak absorption coefficient, peak frequency and peak half-width of the curves are shown in Table 5.2.5.

Table 5.2.5 NRC, peak absorption coefficient, peak frequency and peak half-width of four-layer assemblies with different pore size orders. (S: 250-425μm, M: 425-710μm, L: 710-1000μm and V: 1000-1500μm)

Order	NRC	Peak Absorption Coefficient	Peak Frequency (Hz)	Peak Half-Width (Hz)
SMBV	0.620	0.851	680	864
VBSM	0.652	0.842	768	856

The difference of the sound absorption coefficient between the assembly with increasing gradient pore sizes and the assembly with decreasing gradient pore sizes is not as much as the assemblies with gradient porosities. The sound absorption coefficient curves of the two assemblies are very similar at low frequencies, and slightly different at frequencies above 800Hz.

5.2.3 Assemblies with different thicknesses

Figures 5.2.19 (a) and (b) show the sound absorption coefficient curves of four-layer-assembled porous steel specimens with different thicknesses and porosity orders. The open-cell porous steel specimens have four nominal porosities of 60%, 65%, 70% and 75%. All specimens have a pore size of 425-710μm and a thickness of 5mm, 10mm, 15mm or 20mm. The total thickness of assembly is 20mm, 40mm, 60mm or 80mm, with no air gap. The NRC, peak absorption coefficient, peak frequency and peak half-width of the curves are shown in Table 5.2.6.

Table 5.2.6 NRC, peak absorption coefficient, peak frequency and peak half-width of four-layer assemblies with different thicknesses and porosity orders. (a) XLMH, (b)HMLX.

Thickness (mm)	NRC	Peak Absorption Coefficient	Peak Frequency (Hz)	Peak Half-Width (Hz)
XLMH				
20	0.479	0.792	1120	2336
40	0.580	0.774	480	928
60	0.606	0.586	320	632
80	0.563	-	-	-
HMLX				
20	0.444	0.964	1688	2096
40	0.683	0.822	768	912
60	0.712	0.704	600	520
80	0.708	-	-	-

The total thickness of the four-layer-assembled specimens determines the peak frequency and peak sound absorption coefficient in sound absorption curves. The sound absorption coefficient at low frequencies is poor with a total thickness of 20mm and improves with increasing thickness of specimens. The curves become flatter when the total thickness of the assembly is higher than 60 mm.

Figure 5.2.20 shows that the NRC of the assemblies increases with increasing the thickness of assembly. The effect of thickness of the XLMH assembly is lower than that of the HMLX assembly. When the thickness of the assembly is 20mm, the NRC of the XLMH assembly is higher than that of the HMLX assembly. When the thickness of the assembly is 80mm, the NRC of the XLMH assembly is much lower than that of the HMLX assembly.

Figure 5.2.21 shows that the peak absorption coefficient decreases with increasing the thickness of the assembly and the effect of thickness of the XLMH assembly is lower than that of the HMLX assembly. The sound absorption coefficient of assembly at low frequencies increases when the thickness increases. The assemblies with a total thickness of 80mm have flat curves.

Figure 5.2.22 shows that the peak frequency decreases with increasing the thickness of the assembly and the effect of thickness of the XLMH assembly is lower than that of the HMLX assembly. When the thickness increases from 20mm to 60mm, the peak absorption coefficient decreases from 1120HZ to 320Hz. Figure 5.2.23 shows that the

peak half-width decreases with increasing thickness. There is not much difference between the assemblies with different orders.

5.2.4 Assemblies with different air-gap depths

Table 5.2.7 NRC, peak absorption coefficient, peak frequency and peak half-width of four-layer assemblies with different air-gap depths and porosity orders.

Thickness (mm)	NRC	Peak Absorption Coefficient	Peak Frequency (Hz)	Peak Half-Width (Hz)
XLMH				
0	0.580	0.774	480	928
10	0.576	0.773	360	744
20	0.578	0.778	328	704
30	0.579	0.743	280	688
40	0.574	0.743	256	664
50	0.574	0.743	240	632
HMLX				
0	0.683	0.882	768	912
10	0.703	0.831	528	664
20	0.725	0.803	400	648
30	0.741	0.784	336	592
40	0.743	0.77	296	536
50	0.740	0.776	228	504

Figures 5.2.24 (a) and (b) show the effect of air-gap depth on the sound absorption coefficient curves of assemblies with porosity orders of (a) XLMH and (b) HMLX. Each layer has a pore size of 425-710μm and a thickness of 10mm. The total

thickness of the assemblies is 40mm. The air-gap depths for the assemblies are 0mm, 10mm, 20mm, 30mm, 40mm and 50mm. The NRC, peak absorption coefficient, peak frequency and peak half-width of the curves are shown in Table 5.2.7.

Figures 5.2.24 (a) and (b) show that the sound absorption coefficient curves of the multi-layer assemblies with different air-gap depths are very close to each other. When the air-gap depth increases, the sound absorption coefficient of the assembly at low frequencies increases, the frequency of the peak decreases, and the effect of air-gap depth decreases.

Figure 5.2.25 shows that the NRC values of the XLMH assembly with different air-gap depths are similar and that the NRC of the HMLX assembly increases with increasing air-gap depth. The NRC of the XLMH assembly is lower than that of the HMLX assembly.

Figures 5.2.26 and 5.2.27 show that the peak sound absorption coefficient and frequency decrease with increasing air-gap depth. The effects of air-gap depth on peak sound absorption coefficient and peak frequency for the XLMH assembly are lower than those for the HMLX assembly. When the air-gap depth is increased from 0 to 50 mm, the peak sound absorption coefficient of the XLMH assembly decreases from 0.774 to 0.743, and the peak frequency decreases from 480HZ to 240Hz. The peak sound absorption coefficient of the HMLX assembly decreases from 0.882 to

0.776, and the peak frequency decreases from 768HZ to 228Hz.

Figure 5.2.28 shows that the peak half-width of assemblies decreases with increasing air-gap depth. The effects of air-gap depth on peak half-width for the XLMH and HMLX assemblies are similar.

5.2.5 Equivalent Electrical Circuit Approach analysis

The Equivalent Electrical Circuit Approach (EECA) is one of the most popular approaches in acoustic system analysis (Munjal, 1987; Jinkyo *et al,* 1992). In this approach, the sound pressure, particle velocity and acoustic impedance are analogous to the voltage, electrical current and electrical impedance, respectively. Du *et al.* (2001) regarded the acoustic vibration system combined by multiple resonant absorbers as a filter circuit by analogy.

Figure 5.2.29 is a schematic diagram showing the EECS method. The subscript number indicates the layer number and the innermost layer of the porous materials is defined as the first layer of the porous materials. For the nth layer, empirical relations for the complex wave propagation coefficient k_n and characteristic impedance Z'_n can be expressed as (Huang, 1999):

$$Z'_n = \rho_0 c_0 \left[1 + C_1 \left(\frac{\rho_0 f}{r_n}\right)^{C_2}\right] - j\rho_0 c_0 \left[C_3 \left(\frac{\rho_0 f}{r_n}\right)^{C_4}\right],$$

$$k_n = \frac{\omega}{c_0}\left[C_5 \left(\frac{\rho_0 f}{r_n}\right)^{C_6}\right] + j\frac{\omega}{c_0}\left[1 + C_7 \left(\frac{\rho_0 f}{r_n}\right)^{C_8}\right], \qquad (5.2.1)$$

The acoustic impedance of the nth layer of porous material backed with a rigid wall is:

$$Z_n = Z'_n \coth(k_n t_n), \qquad (5.2.2)$$

where ρ_0 is the air density (=1.213kgm^{-3}), c_0 is the sound speed in the air, ω is the angular frequency (ω=2πf), f is the frequency of the sound wave, t_n is the thickness of the nth porous layer and r_n is the flow resistivity. C_1, C_2, C_3, C_4, C_5, C_6, C_7, C_8 are materials constants. For porous metal structures, $C_1 \approx 0.114$, $C_2 \approx -0.369$, $C_3 \approx 0.0985$, $C_4 \approx -0.758$, $C_5 \approx 0.168$, $C_6 \approx -0.715$, $C_7 \approx 0.136$, $C_8 \approx -0.41$ (Huang, 1999). The flow resistivity of a specimen, r, is calculated from the airflow resistance, R, by $r=RA/t$, where A is cross sectional area and t is thickness of the specimen used in the airflow resistance test. Table 5.2.8 shows the flow resistance and resistivity of the porous steel samples used in the assemblies.

The characteristic impedance Z_c of the air-gap backed with a rigid wall in the multi-layer material can be expressed as:

$$Z_c = -j\rho_0 c_0 \coth(kt_c), \qquad (5.2.3)$$

where t_c is the depth of the airspace, and K is the wave propagation constant of air

($=\omega/c_0$).

Zwicker and Kosten (1949) have shown that the normal incidence acoustic impedance, Z_1, at the front of a layer of homogeneous material of thickness t is given by:

$$Z_1 = Z'_1 \frac{Z_0 \cosh k_1 t_1 + Z'_1 \sinh k_1 t_1}{Z_0 \sinh k_1 t_1 + Z'_1 \cosh k_1 t_1} \tag{5.2.4}$$

where Z_0 is the backing impedance of the layer, Z'_1 is the characteristic impedance of the layer and k_1 is its propagation coefficient which can be calculated by equation (5.2.1) , when the specimens are backed with a rigid wall, $Z_1 \approx Z'_1$.

Table 5.2.8 Airflow resistance and resistivity of specimens with different porosities or pore sizes.

Nomimal Porosity	Pore size (μm)	Airflow resistance, R (MPa s/m^3)	Flow resistivity, r (MPa s/m^2)
60%	425-710	145.6	0.49
65%	425-710	128.5	0.43
70%	425-710	112.5	0.38
75%	425-710	93.9	0.31
70%	250-425	113.6	0.38
70%	710-1000	114.8	0.38
70%	1000-1500	110.9	0.37

For multi-layer absorbers composed of porous materials, the normal incidence

acoustic impedance at the surface of the multi-layer absorber can be calculated by equation (5.2.4) as (Zhu and Huang, 2005):

$$Z_{d+1} = Z'_{d+1}\frac{Z_d \cosh(k_{d+1}t_{d+1}) + Z'_{d+1}\sinh(k_{d+1}t_{d+1})}{Z_d \sinh(k_{d+1}t_{d+1}) + Z'_{d+1}\cosh(k_{d+1}t_{d+1})}, \tag{5.2.5}$$

where d=1,2,3...n-1.

The normal incidence acoustic impedance of the nth layer, Z_n, calculated by equation (5.2.5), is the acoustic impedance of the assembly:

$$Z_n = R_z + jM_z \tag{5.2.6}$$

where R_z and M_z are real and imaginary components of the acoustic impedance, respectively. The ultimate sound absorption coefficient, α, is given by:

$$\alpha = \frac{4R_z}{(1 + R_z/\rho_0 c_0)^2 + (M_z/\rho_0 c_0)^2}, \tag{5.2.7}$$

For example, the flow resistivity of specimen M (porosity: 70%, Pore size: 425-710μm) is 0.49 MPa s/m^2. At a frequency of 1000Hz, according to equation (5.2.1), the characteristic impedance Z'_M= 595.2-775.5i, k_M= 29.7+28.1i. As the thickness of the specimen is 0.01m, according to equation (5.2.2), the acoustic

impedance of specimen M is Z_M= 1014.1+1477.3i. From equations (5.2.6) and (5.2.7), the sound absorption coefficient of specimen M at 1000Hz is α = 0.159. It is very close to the measured value of 0.160 as shown in Figure 5.1.4. Using the same method, the acoustic impedances of specimens X (60%), L (65%) and H (75%) at the frequency of 1000Hz are calculated to be Z_X = 954.5 + 1203.7i, Z_L = 1025.2 + 1333.3i, and Z_H = 1146.5 + 1498.8i. According to equation (5.2.5), the acoustic impedance of assembly XLMH at 1000Hz is Z_{XLMH}= 732.4+904.5i. According to equation (5.2.7), the sound absorption coefficient, α, of assembly XLMH at 1000Hz is 0.486, which is close to the measured value of 0.479 as shown in Figure 5.2.16 (a).

According to equation (5.2.1), the characteristic impedance, Z'_n, and propagation coefficient, k, decrease with decreasing airflow resistivity, r, which decreases with increasing porosity of the specimen. According to equations (5.2.5) and (5.2.6), the specific acoustic resistivity, R_z, and reactance of porous material, M_z, decrease with the increasing porosity. According to equation (5.2.7), the sound absorption coefficient of the multi-layer-assembled structure, α, increases with increasing the nominal porosity of each layer. The pore size of the porous steel specimens does not affect the air-flow resistivity markedly. Therefore, the sound absorption coefficients of the multi-layer-assembled structures with different pore sizes do not show much difference. Equation (5.2.2) shows that the thickness of nth layer, t_{an}, affects the acoustic impedance, Z_n, by a trigonometric function. The sound absorption coefficient of the multi-layer-assembled structure increases with increasing the nominal porosity

of each layer, but not in proportionality. According to equation (5.2.3), the acoustic impedance of an air-gap can be calculated by $Z_c = -j\rho_0 c_0 \coth(k_c t_c)$. From equations (5.2.5) and (5.2.6), it is clear that the depth of air-gap affects the sound absorption coefficient of the multi-layer-assembled structure.

Figures 5.2.30-34 show the calculated and measured sound absorption coefficient curves of (a) two-layer assemblies with different porosities, (b) four-layer assemblies with different porosities, (c) four-layer assemblies with different pore sizes, (d) four-layer assemblies with different specimen thicknesses, and (e) four-layer assemblies with different air-gap depths, respectively. The calculated values fit the measured ones well on the whole, which indicates that EECA approach is suitable for calculating the sound absorption properties of multi-layer-assembled porous metals. There is a particularly good agreement between the calculated and measured values at frequencies below 2000Hz. At frequencies between 2000 and 5000 Hz, the calculated results are slightly higher than the measured results.

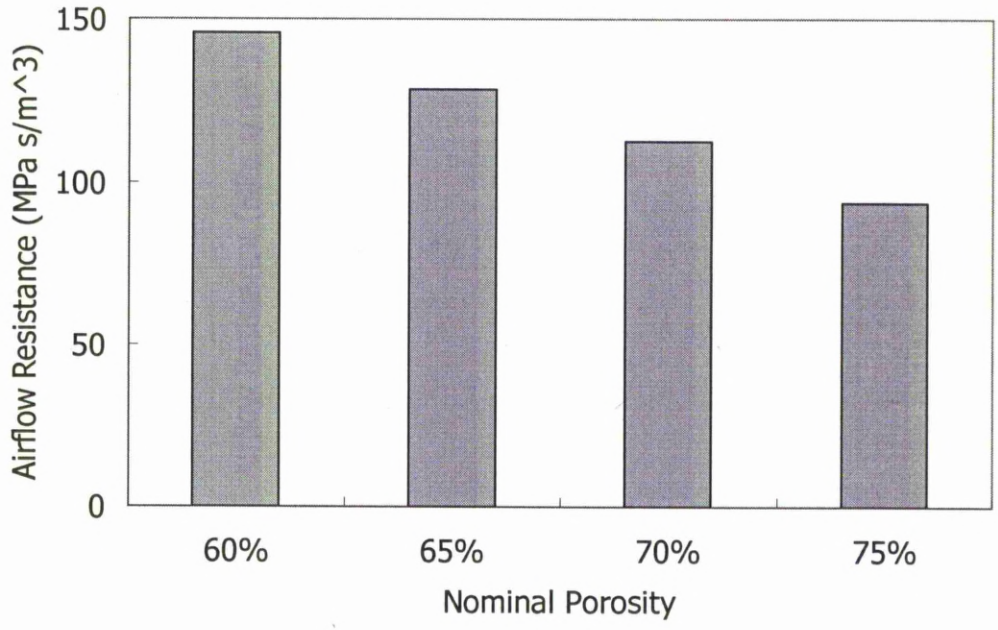

Figure 5.1.1 Variation of airflow resistance with porosity of porous steel specimens with pore size of 425-710μm and thickness of 30mm.

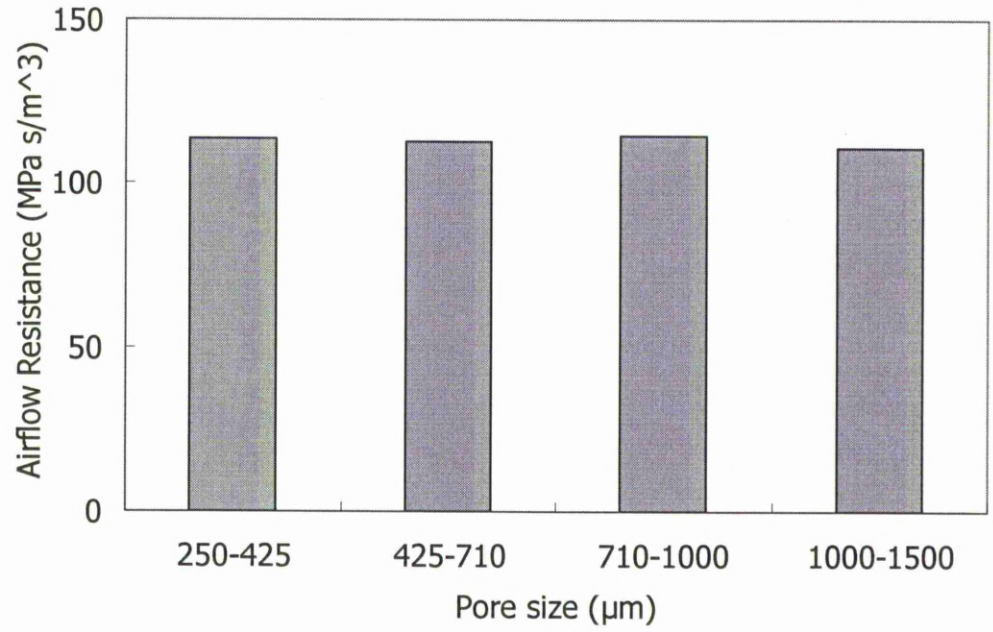

Figure 5.1.2 Variation of airflow resistance with pore size of porous steel specimens with nominal porosity of 70% and thickness of 30mm.

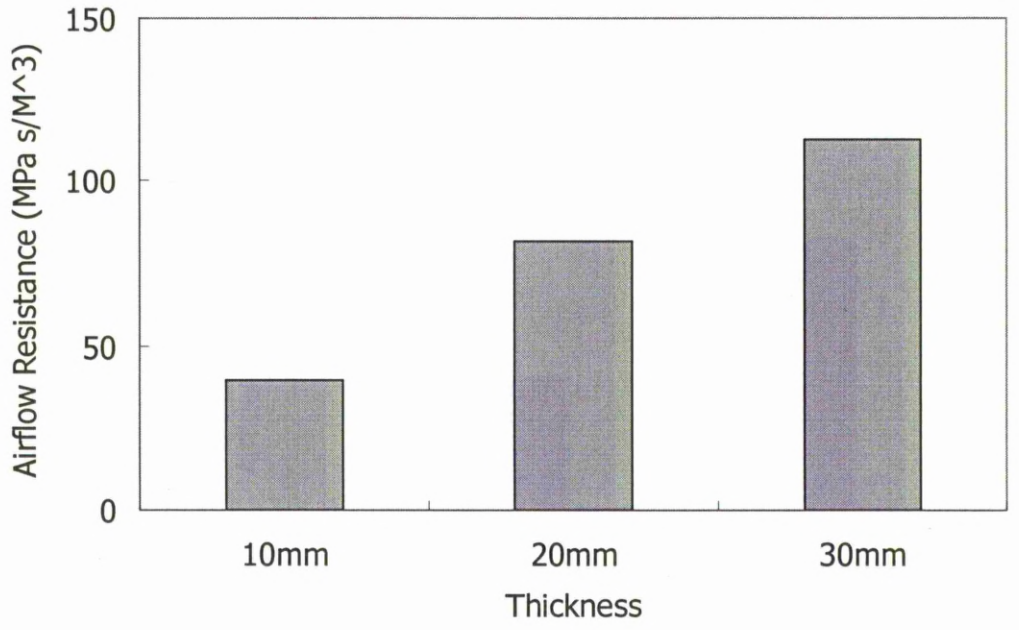

Figure 5.1.3 Variation of airflow resistance with specimen thickness of porous steel specimens with nominal porosity of 70% pore size of 425-710μm.

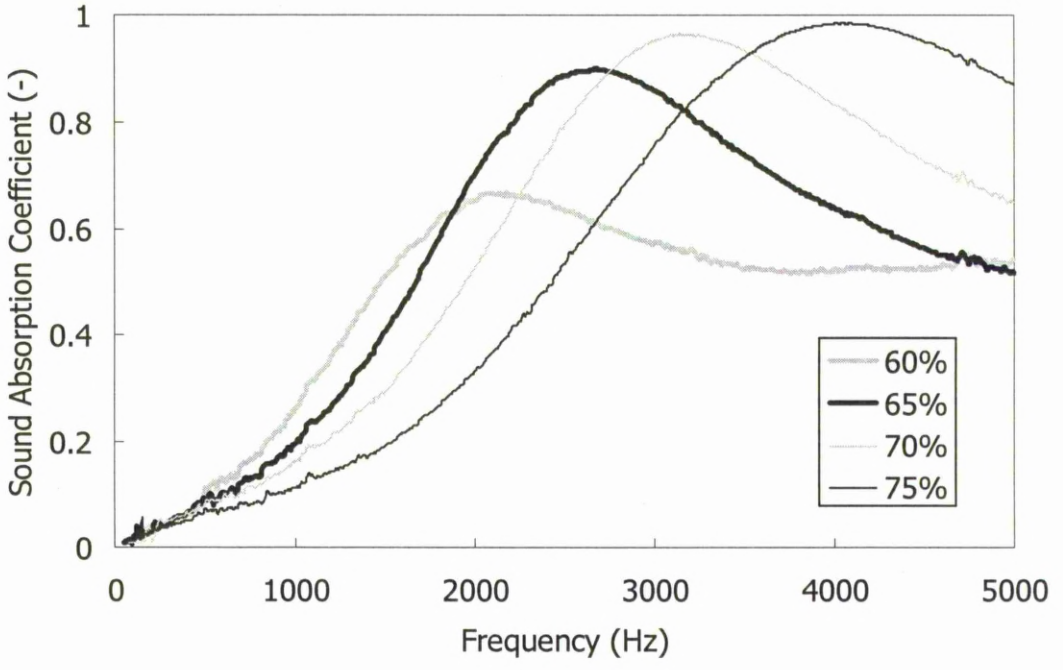

Figure 5.1.4 Sound absorption coefficient curves of open cell porous steel showing the effect of porosity. Pore size is 425-710μm, thickness is 10mm.

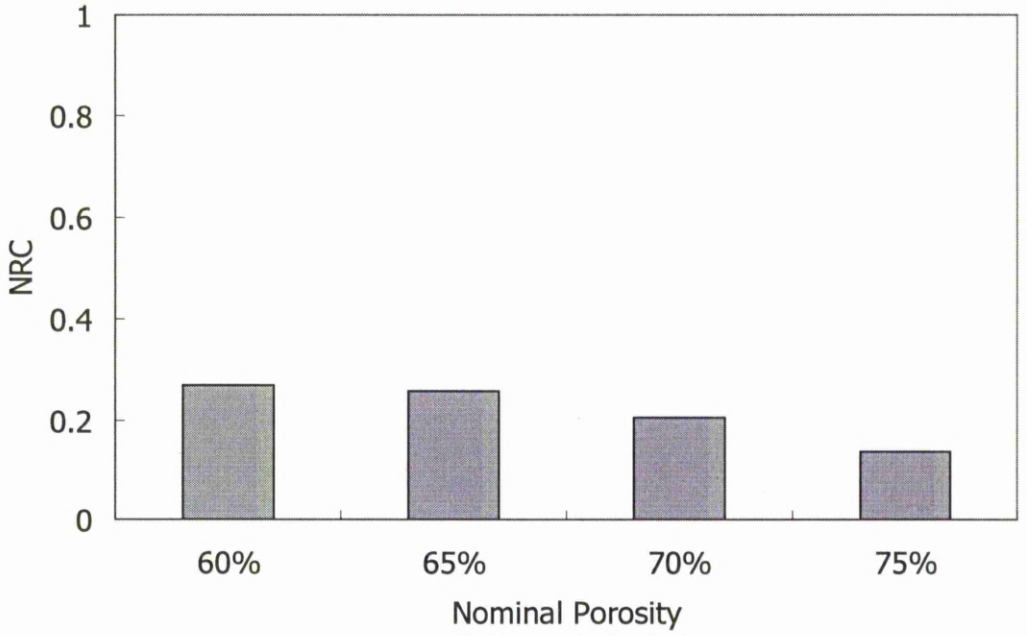

Figure 5.1.5 Variation of NRC with nominal porosity of porous steel specimens. Pore size is 425-710μm, thickness is 10mm. Pore size is 425-710μm, thickness is 10mm.

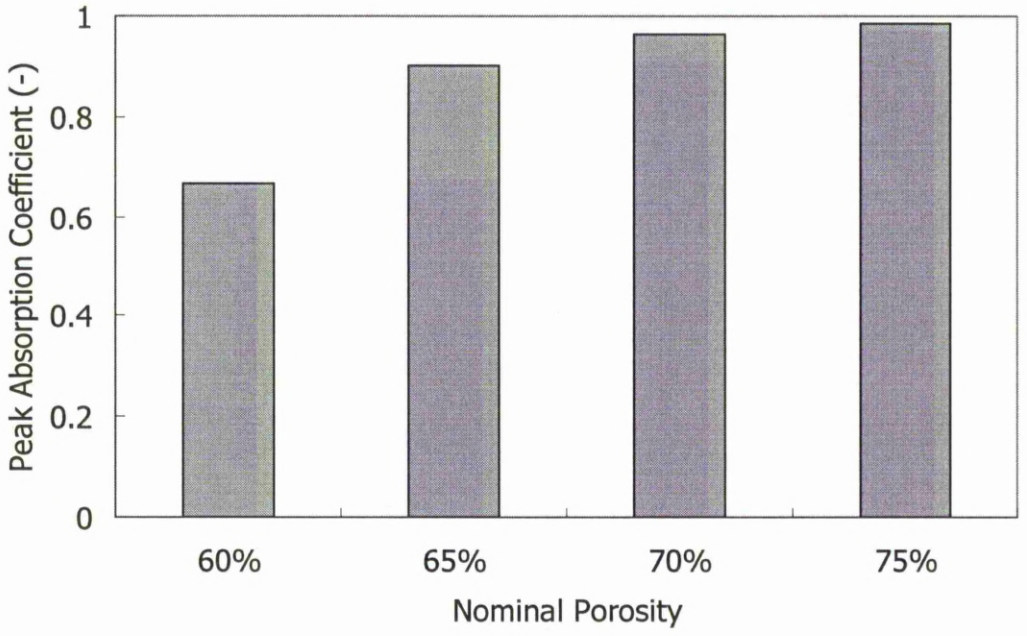

Figure 5.1.6 Variation of peak absorption coefficient with nominal porosity of porous steel specimens. Pore size is 425-710μm, thickness is 10mm.

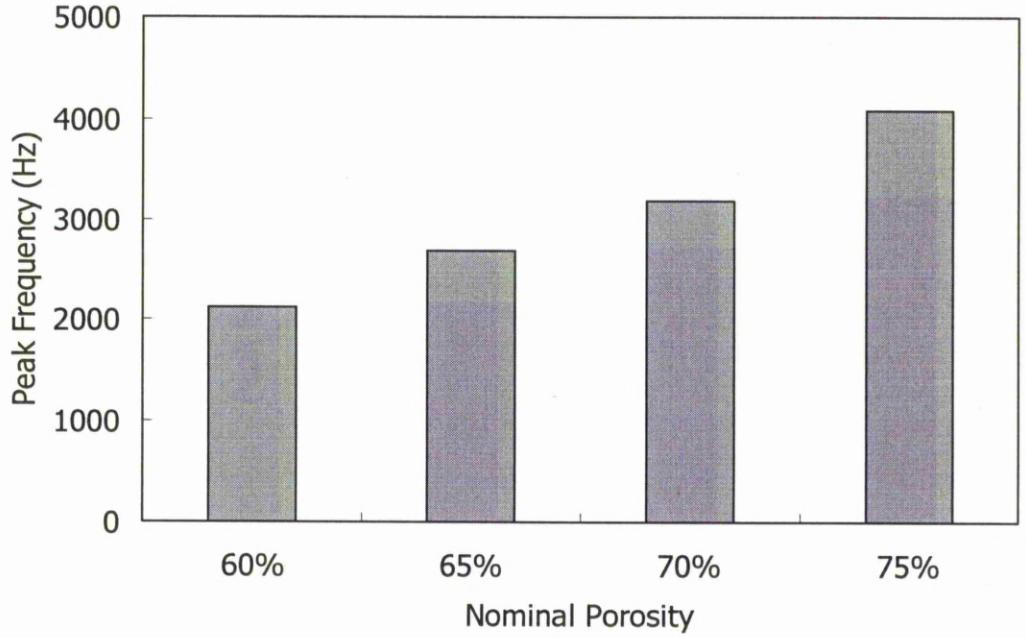

Figure 5.1.7 Variation of peak frequency with nominal porosity of porous steel specimens. Pore size is 425-710μm, thickness is 10mm.

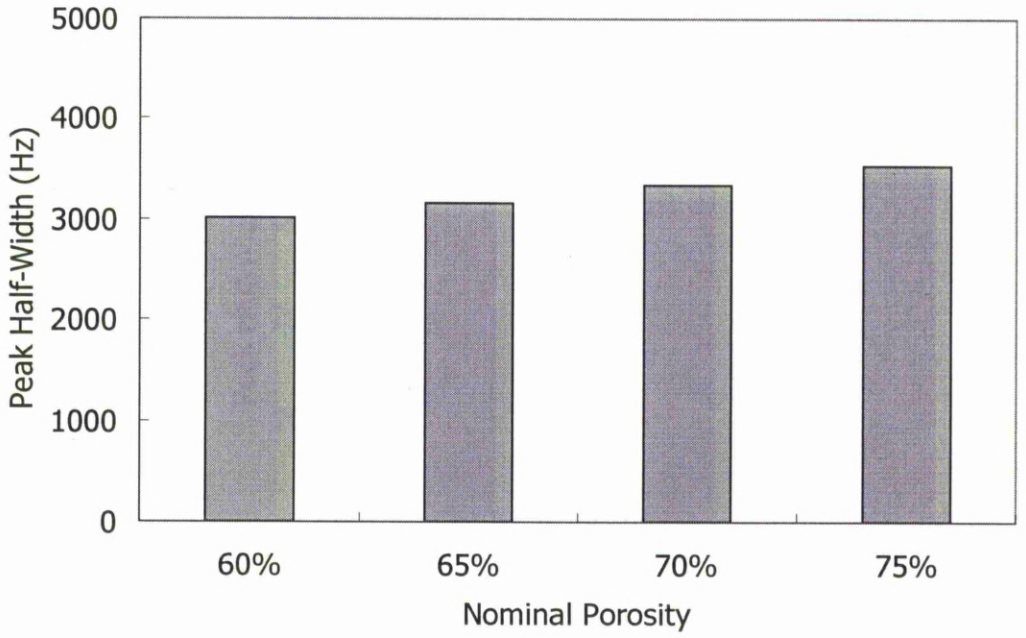

Figure 5.1.8 Variation of peak half-width with porosity of porous steel specimens. Pore size is 425-710μm, thickness is 10mm.

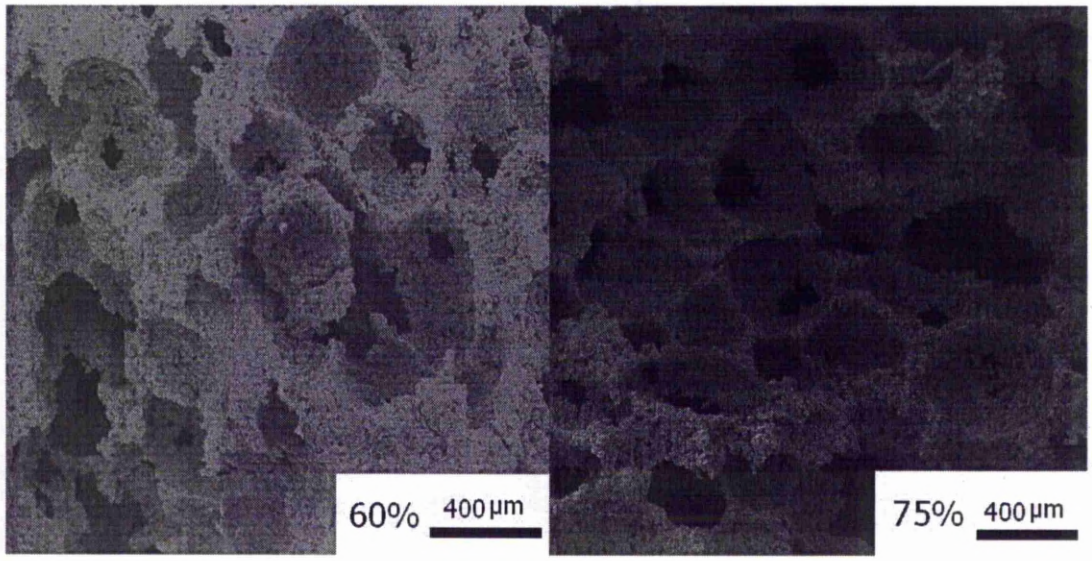

Figure 5.1.9 Microstructures of porous steel specimens with nominal porosities of 60% and 75%, showing the interconnecting channels. Pore size is 425-710µm,

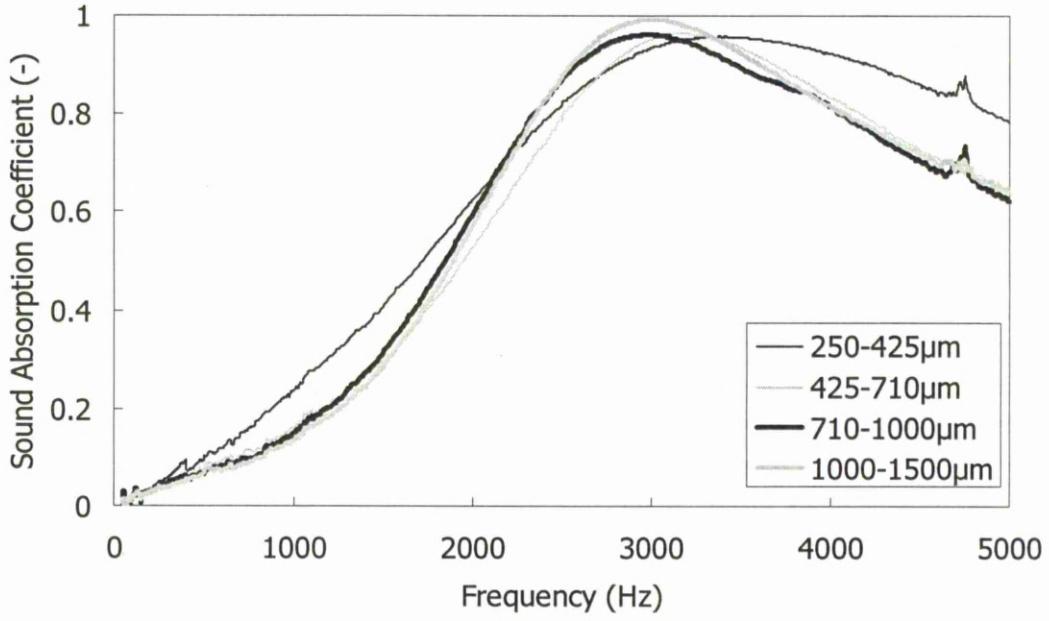

Figure 5.1.10 Sound absorption coefficient curves of open cell porous steel specimens with a nominal porosity of 70% and different pore sizes.

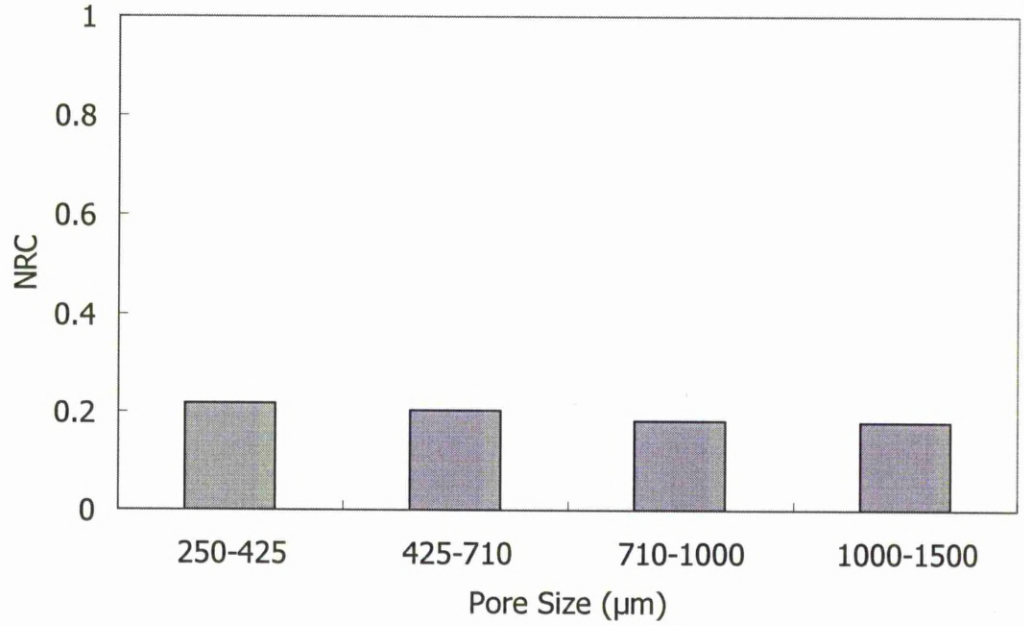

Figure5.1.11 Variation of NRC with pore size of porous steel specimens. Nominal porosity is 70%, thickness is 10mm.

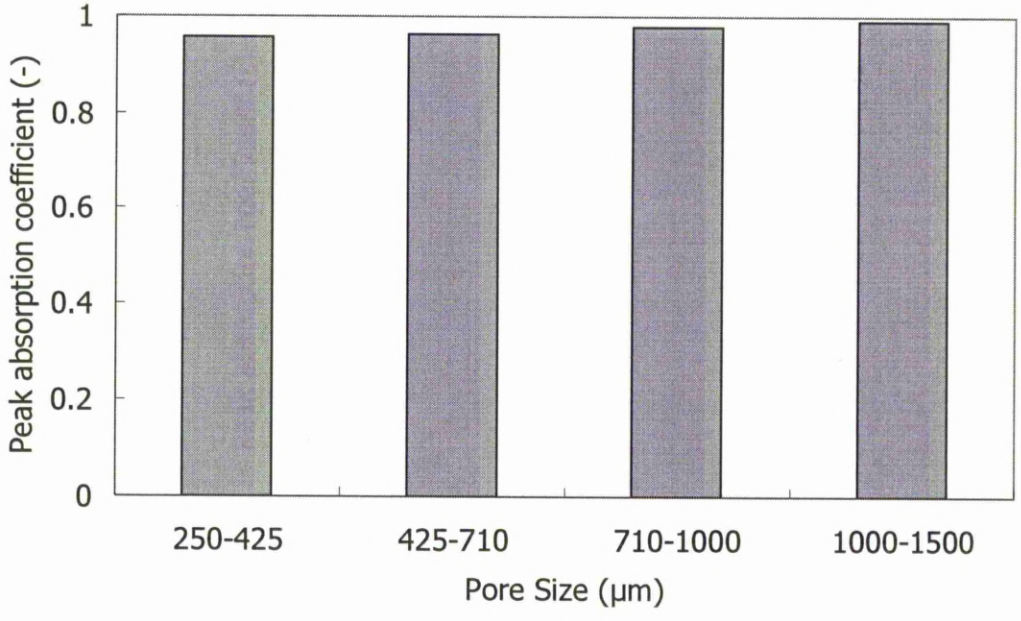

Figure 5.1.12 Variation of peak absorption coefficient with pore size of porous steel specimens. Nominal porosity is 70%, thickness is 10mm.

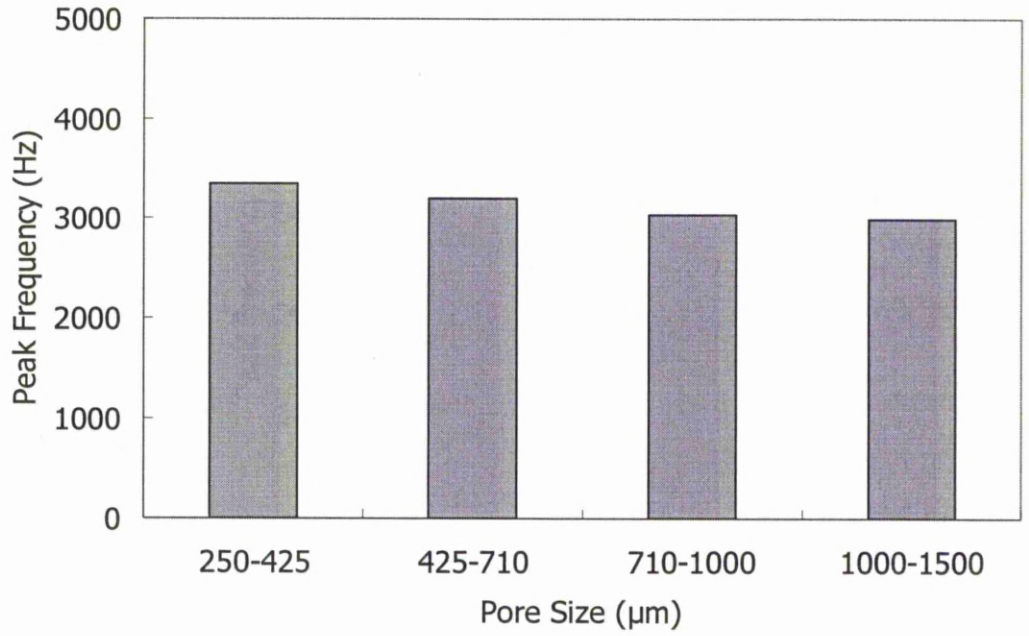

Figure 5.1.13 Variation of peak frequency with pore size of porous steel specimens. Nominal porosity is 70%, thickness is 10mm.

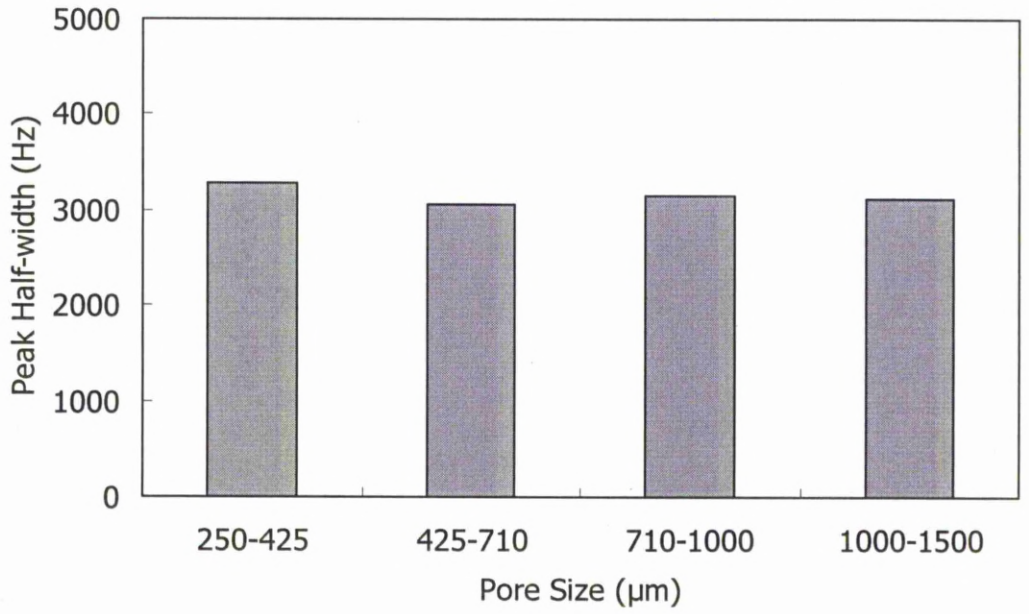

Figure 5.1.14 Variation of peak half-width with pore size of porous steel specimens. Nominal porosity is 70%, thickness is 10mm.

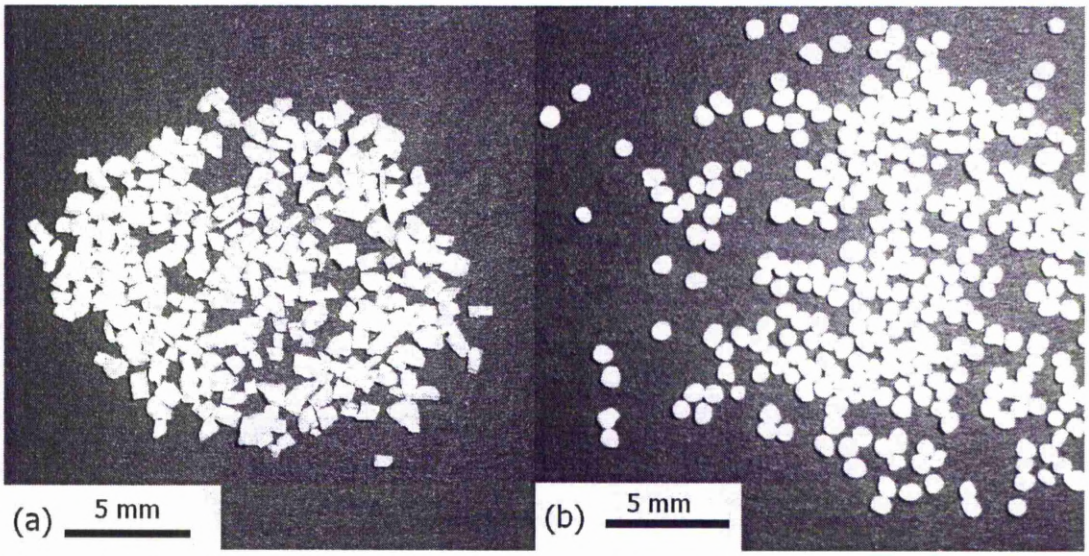

Figure 5.1.15 Photos of potassium carbonate grains with a diameter of 425-710μm used in the LCS process, showing different shapes: (a) angular and (b) spherical.

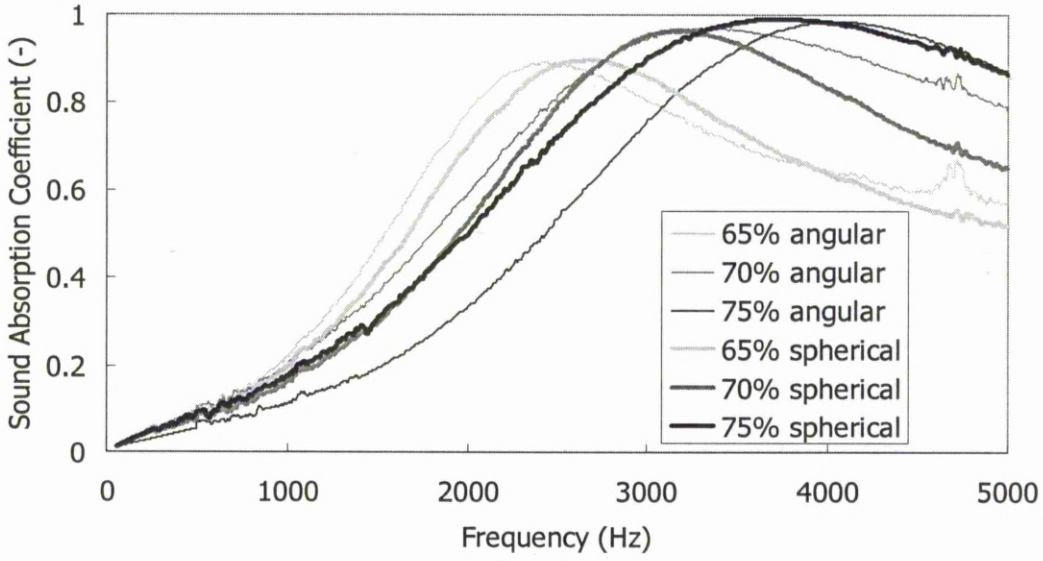

Figure 5.1.16 Sound absorption coefficient curves of open cell porous steel, showing the effect of pore shape. Pore size is 425-710μm, thickness is 10mm.

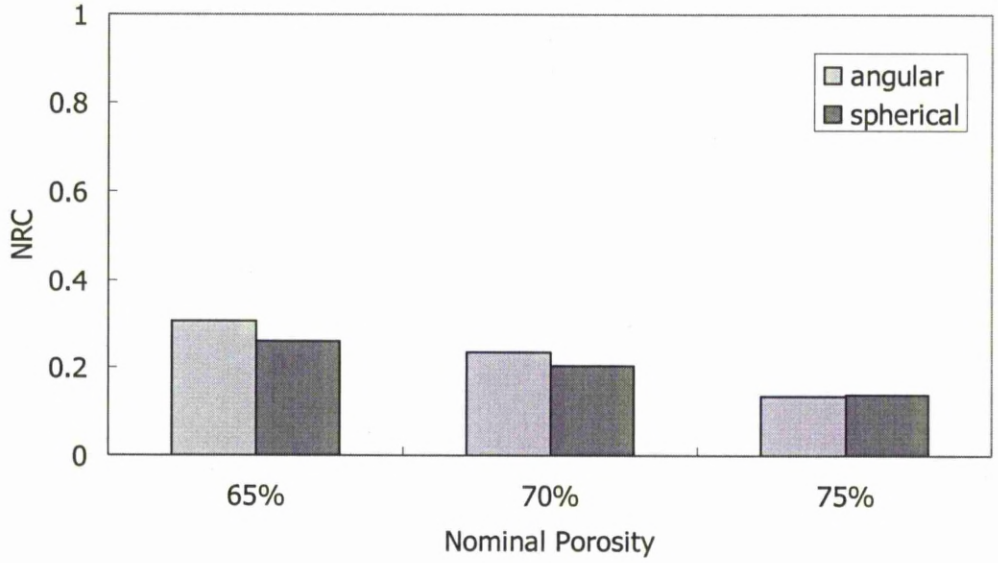

Figure 5.1.17 Variation of NRC with nominal porosity of porous steel specimens, showing the effect of pore shape. Pore size is 425-710μm, thickness is 10mm.

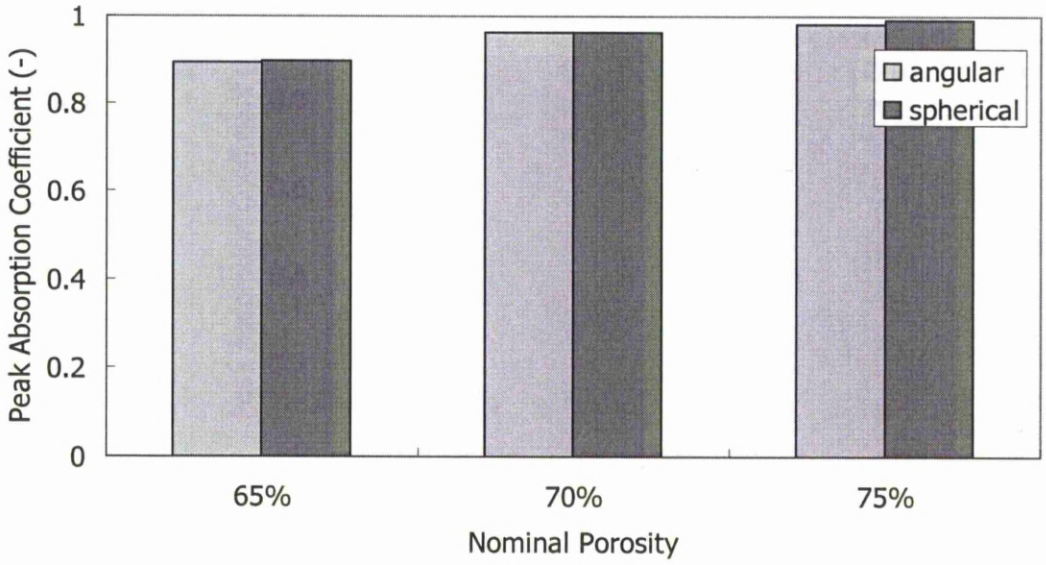

Figure 5.1.18 Variation of peak absorption coefficient with nominal porosity of porous steel specimens, showing the effect of pore shape. Pore size is 425-710μm, thickness is 10mm.

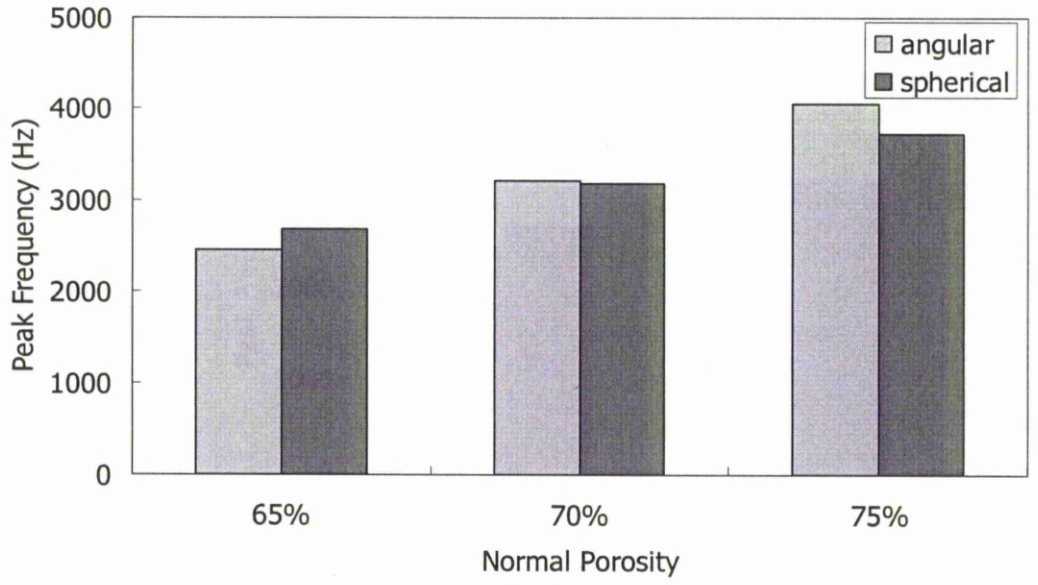

Figure 5.1.19 Variation of peak frequency with nominal porosity of porous steel specimens, showing the effect of pore shape. Pore size is 425-710μm, thickness is 10mm.

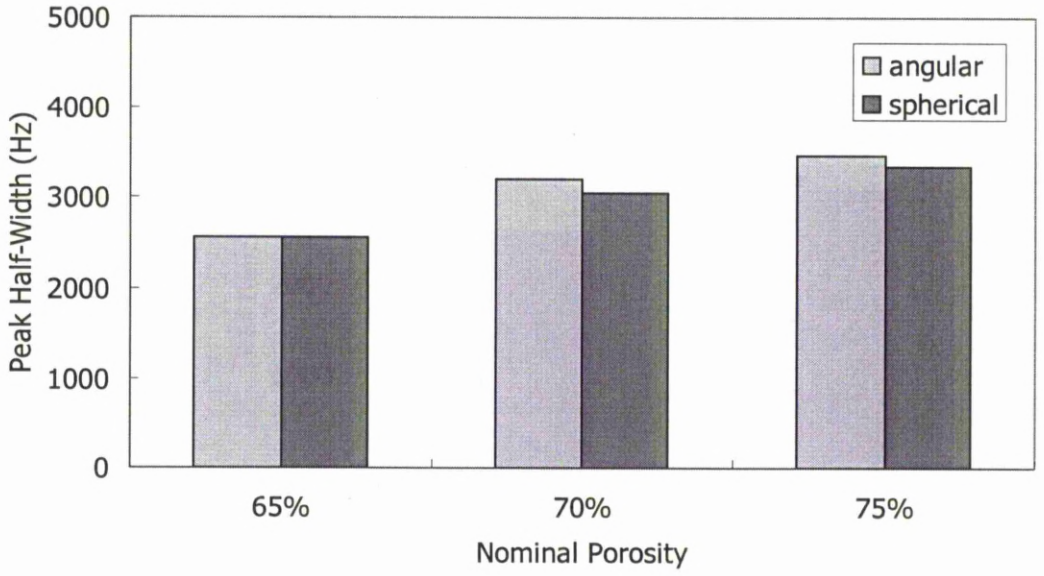

Figure 5.1.20 Variation of peak half-width with nominal porosity of porous steel specimens, showing the effect of pore shape. Pore size is 425-710μm, thickness is 10mm.

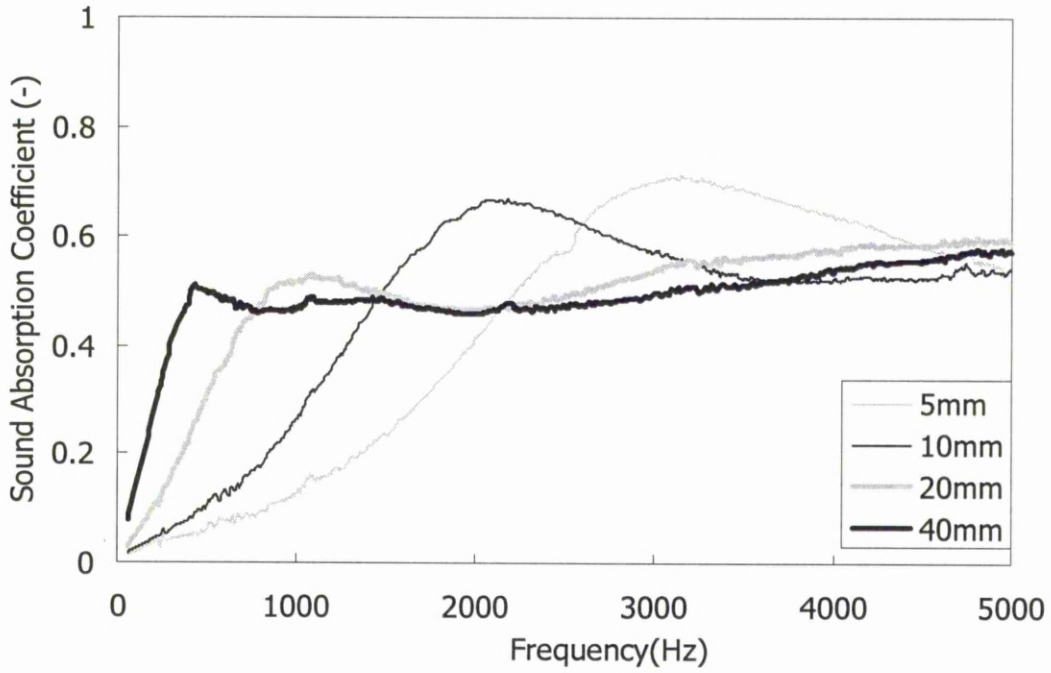

Figure 5.1.21 Sound absorption coefficient curves of open cell porous steel specimens with a nominal porosity of 60% and pore size of 425-710μm, showing the effect of thickness.

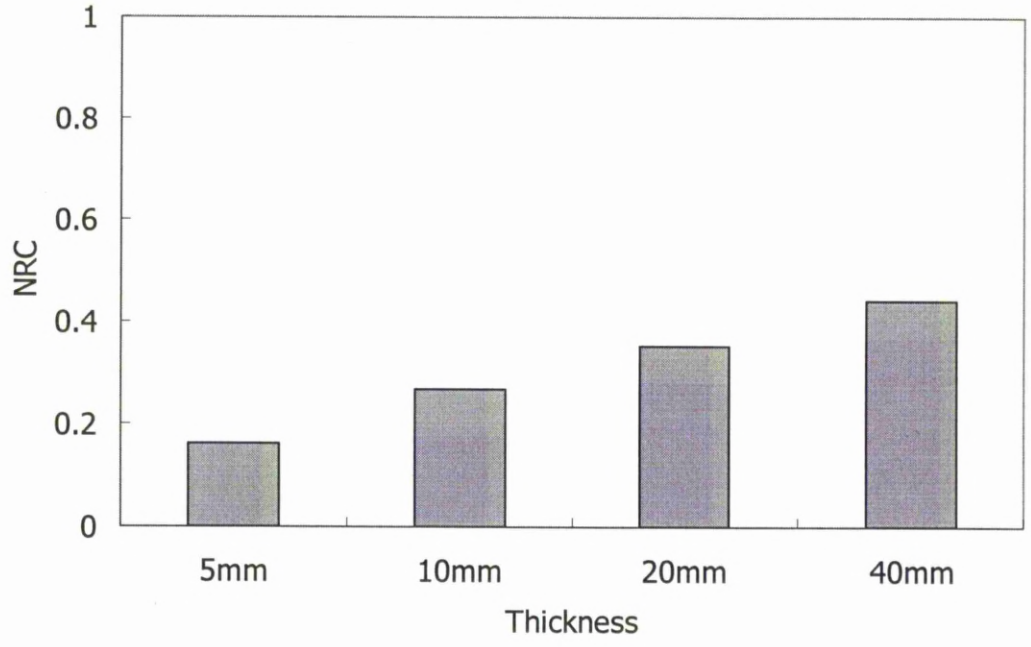

Figure 5.1.22 Variation of NRC with specimen thickness of porous steel specimens with a nominal porosity of 60% and pore size of 425-710μm.

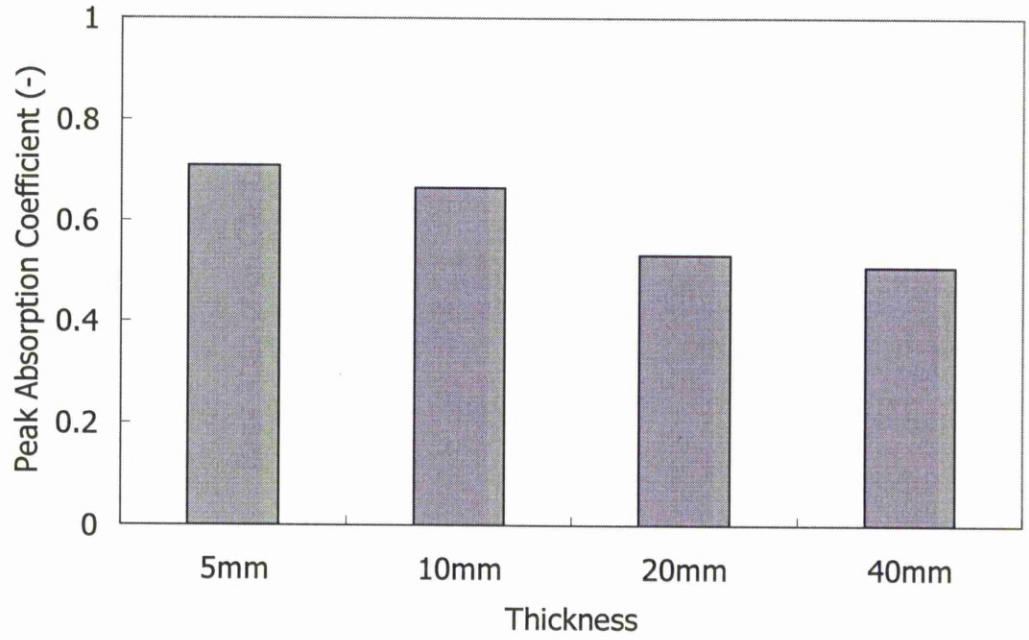

Figure 5.1.23 Variation of peak absorption coefficient with specimen thickness of porous steel specimens with a nominal porosity of 60% and pore size of 425-710μm.

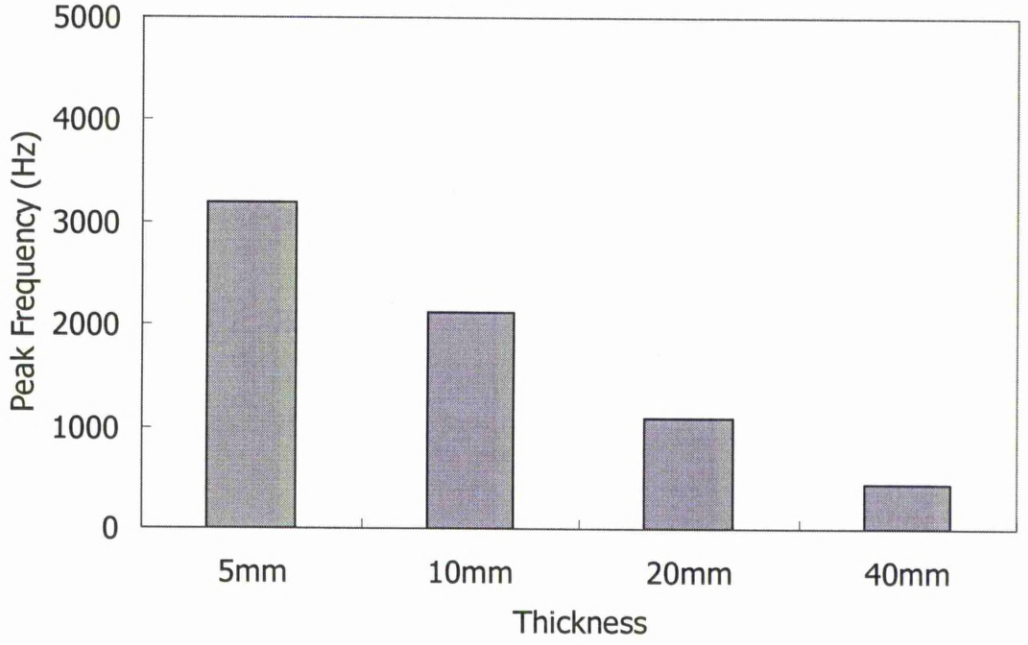

Figure 5.1.24 Variation of peak frequency with specimen thickness of porous steel specimens with a nominal porosity of 60% and pore size of 425-710μm.

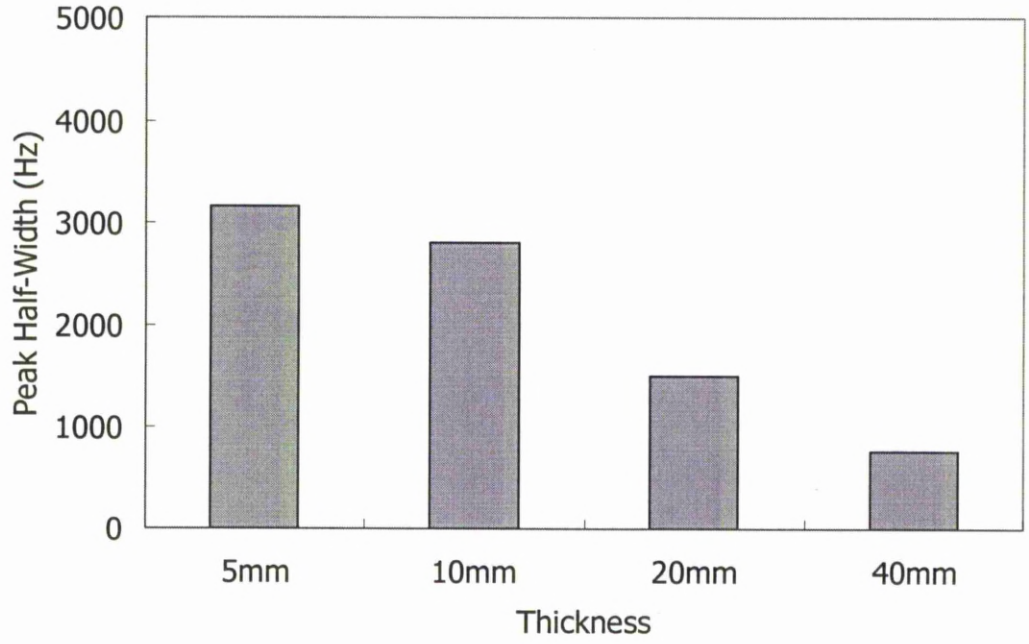

Figure 5.1.25 Variation of peak half-width with specimen thickness of porous steel specimens with a nominal porosity of 60% and pore size of 425-710μm.

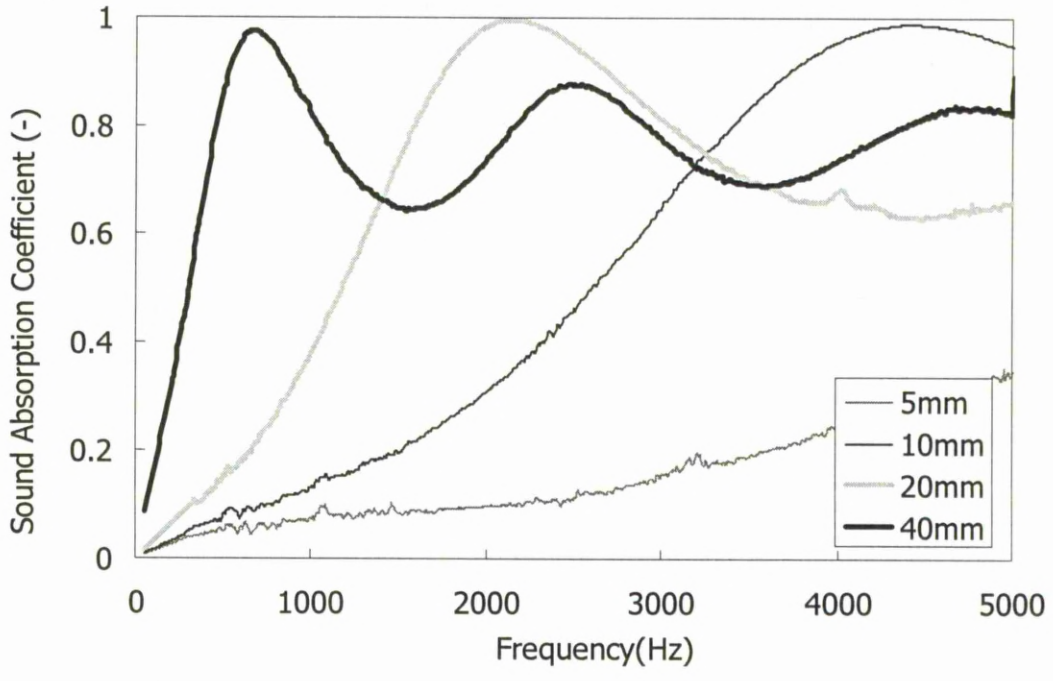

Figure 5.1.26 Sound absorption coefficient curves of open cell porous steel specimens with a nominal porosity of 75% and pore size of 425-710μm, showing the effect of thickness.

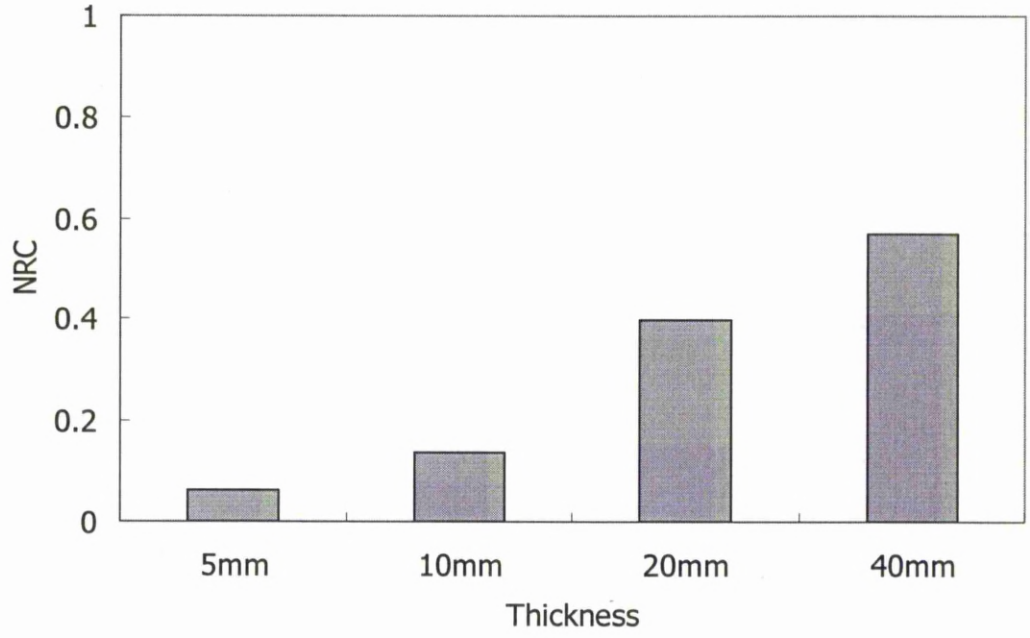

Figure 5.1.27 Variation of NRC with specimen thickness of porous steel specimens with a nominal porosity of 75% and pore size of 425-710μm.

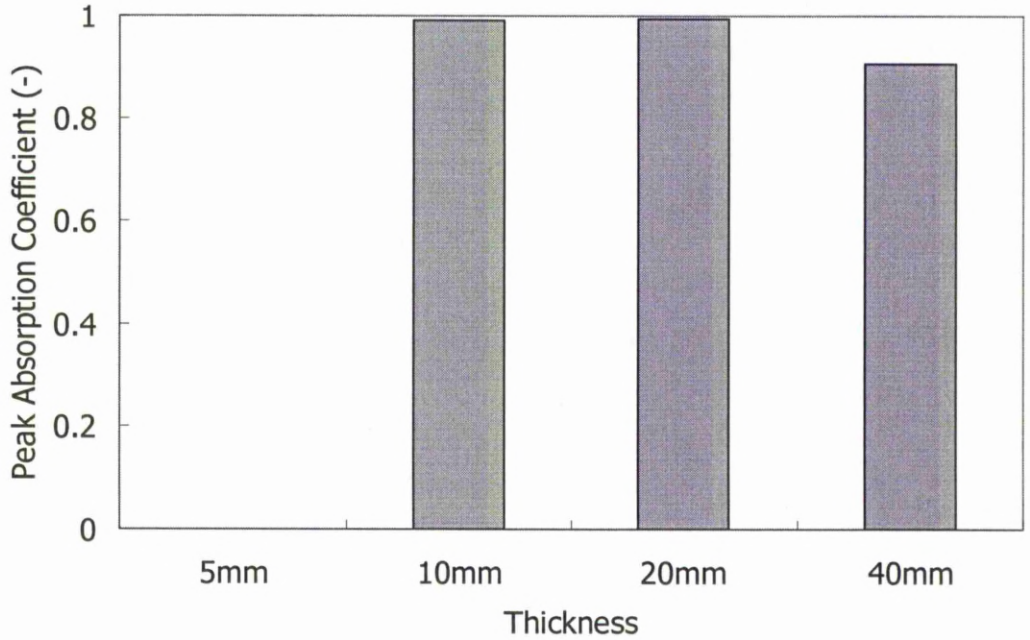

Figure 5.1.28 Variation of peak absorption coefficient with specimen thickness of porous steel specimens with a nominal porosity of 75% and pore size of 425-710μm.

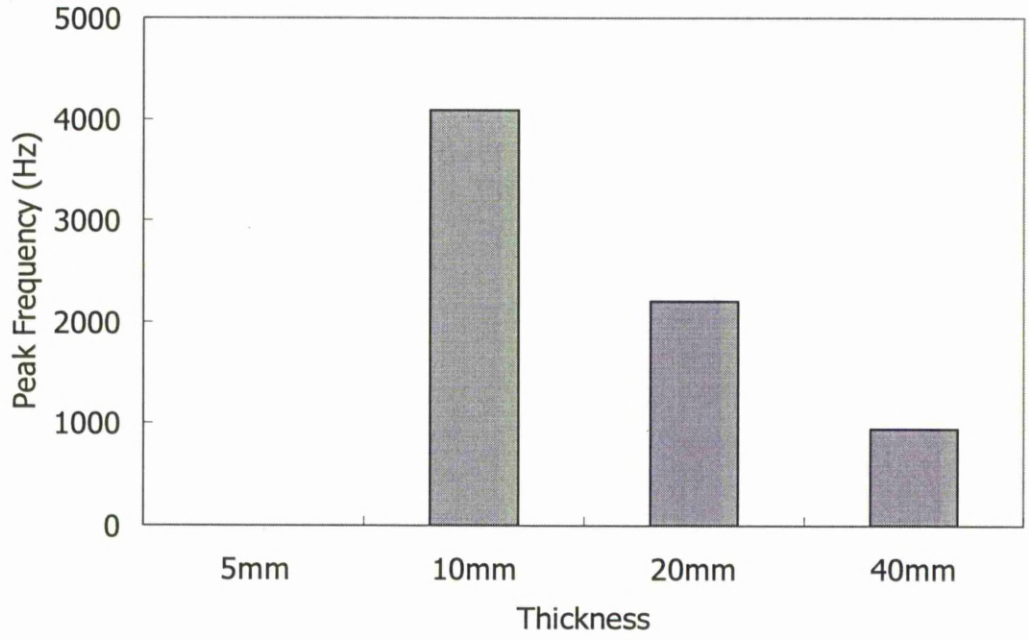

Figure 5.1.29 Variation of peak frequency with specimen thickness of porous steel specimens with a nominal porosity of 75% and pore size of 425-710μm.

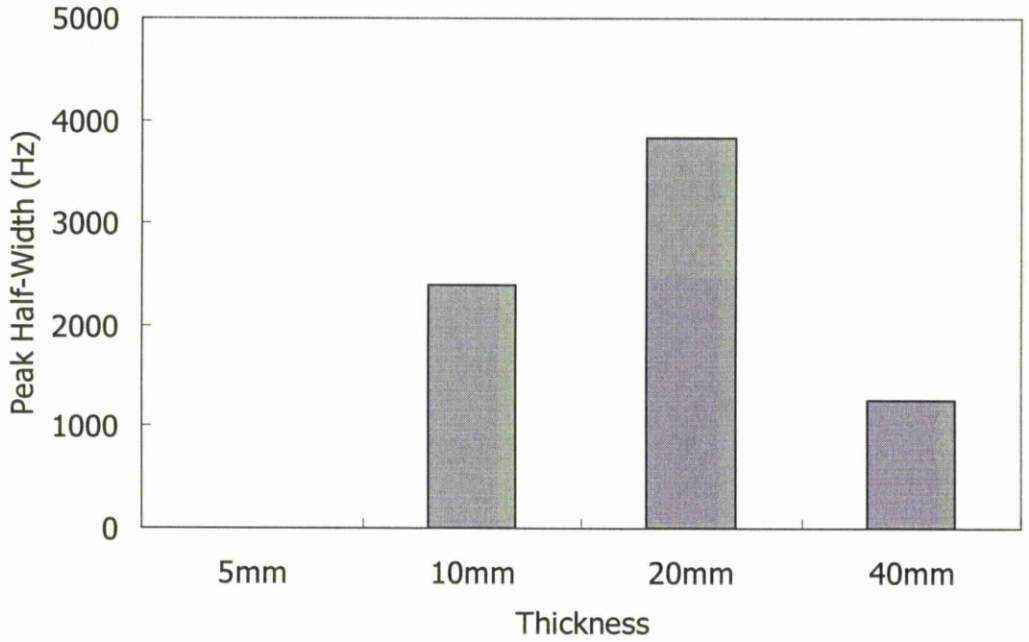

Figure 5.1.30 Variation of peak half-width with specimen thickness of porous steel specimens with a nominal porosity of 75% and pore size of 425-710μm.

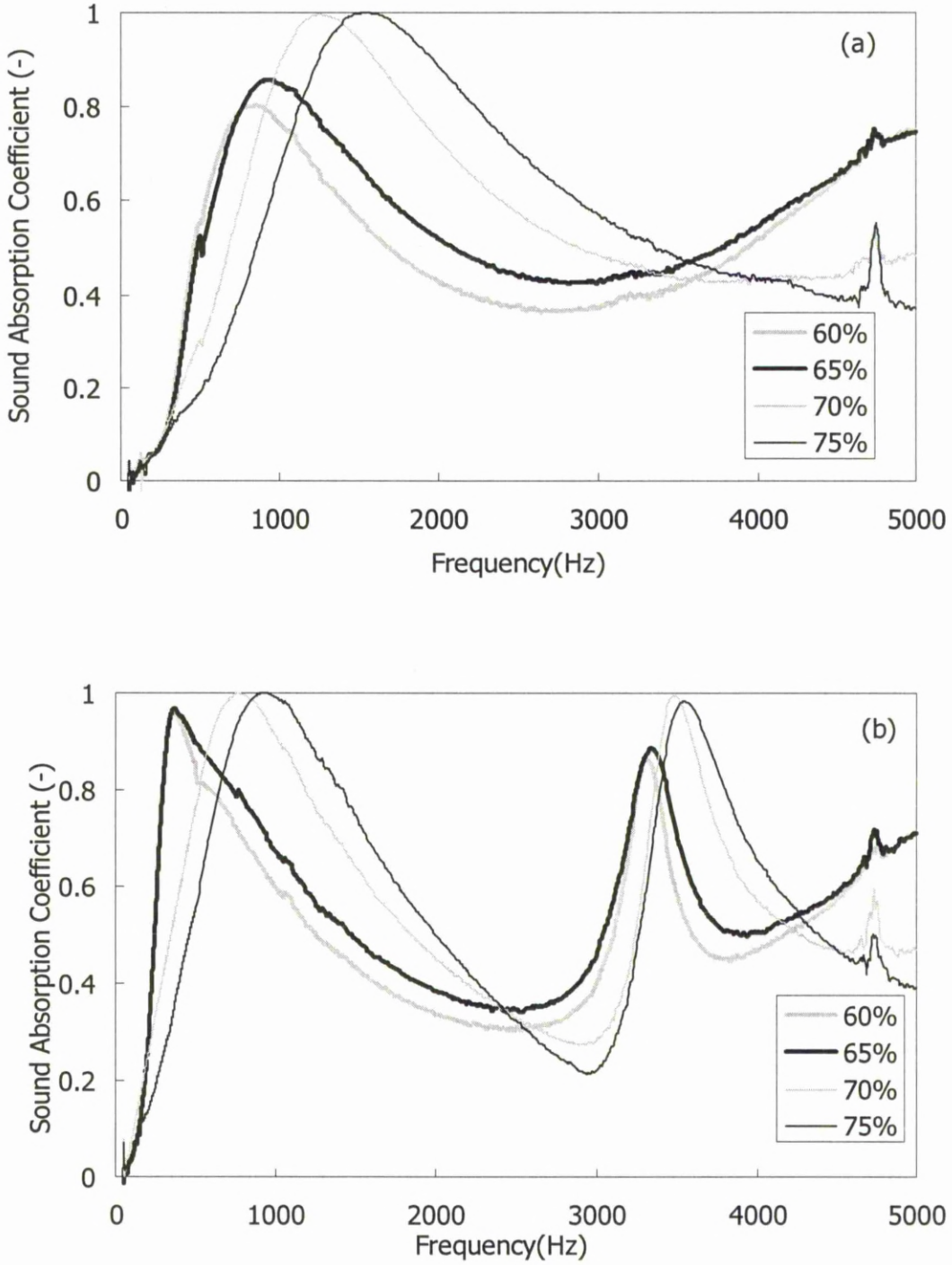

Figure 5.1.31 Sound absorption coefficient curves of open cell porous steel specimens with air-gap depths of (a) 20mm and (b) 50mm, with a pore size of 425-710μm and different porosities.

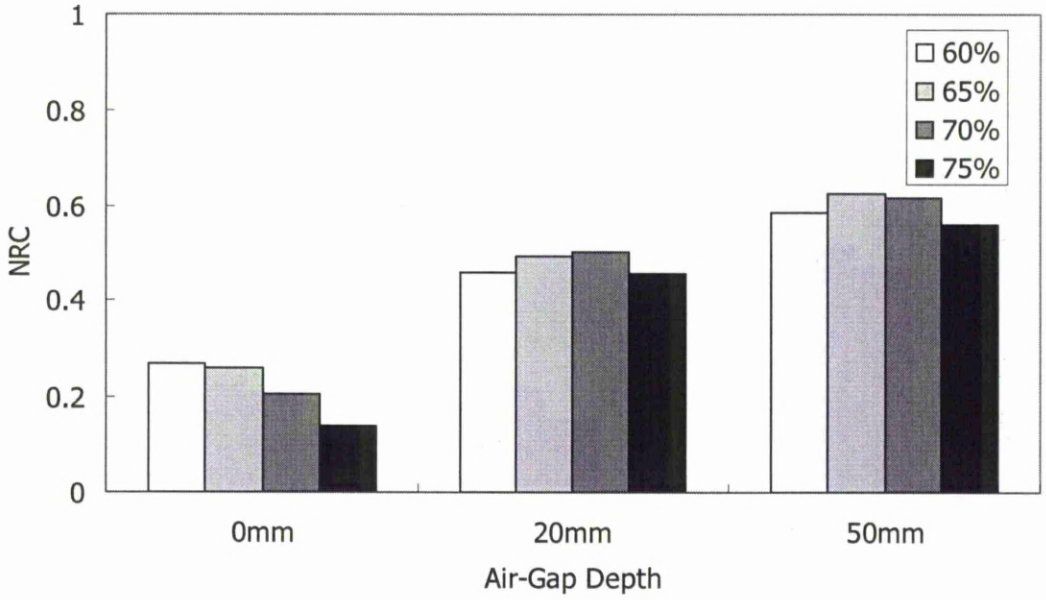

Figure 5.1.32 Variation of NRC with air-gap depth of porous steel specimens with different porosities.

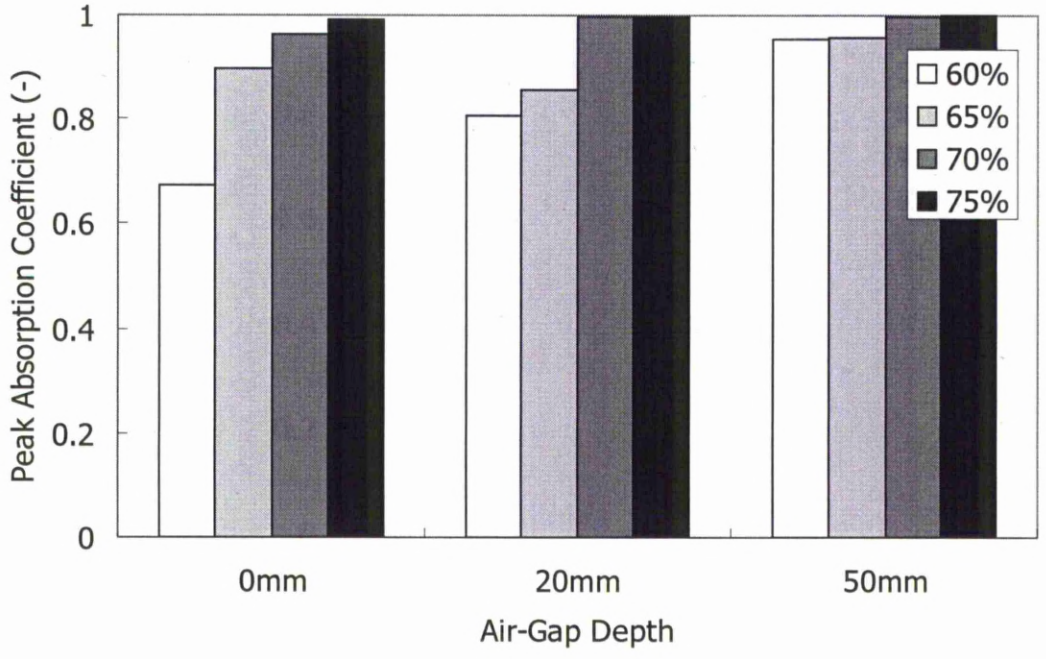

Figure 5.1.33 Variation of peak absorption coefficient with air-gap depth of porous steel specimens with different porosities.

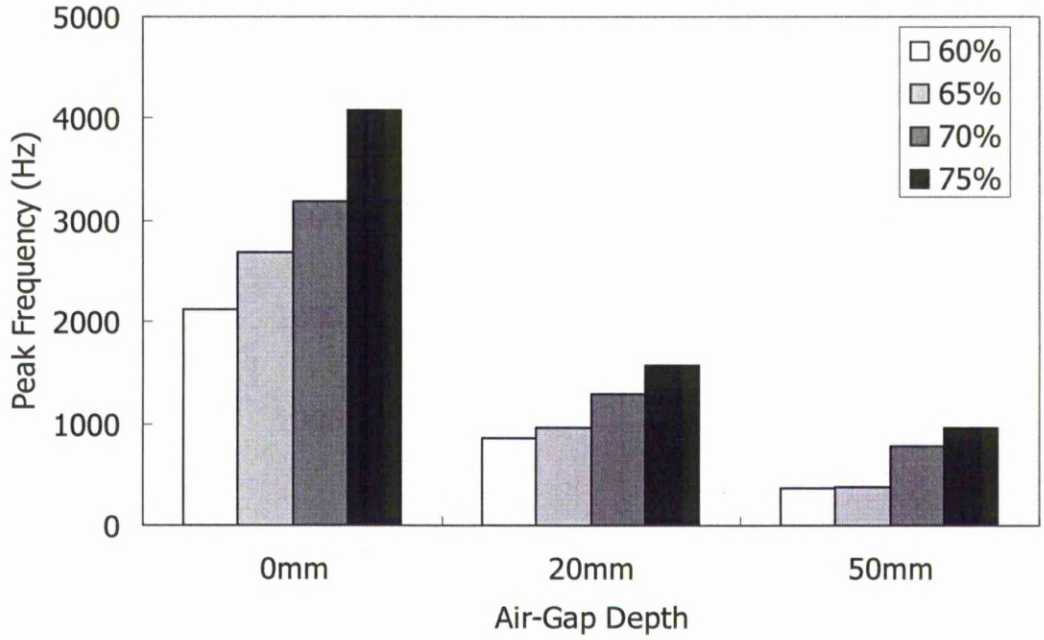

Figure 5.1.34 Variation of peak frequency with air-gap depth of porous steel specimens with different porosities.

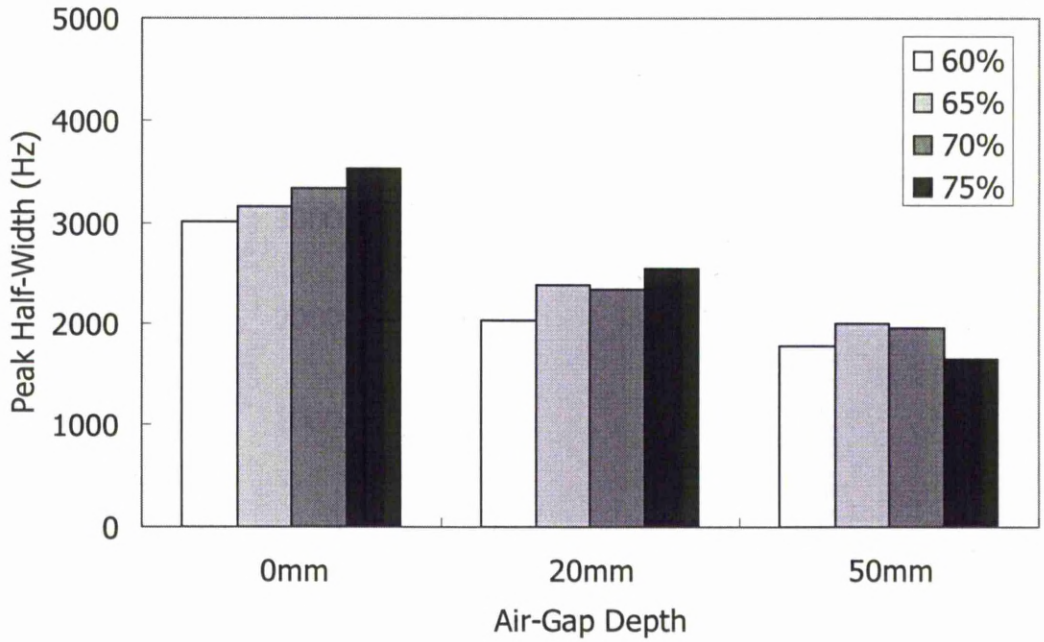

Figure 5.1.35 Variation of peak half-width with air-gap depth of porous steel specimens with different porosities.

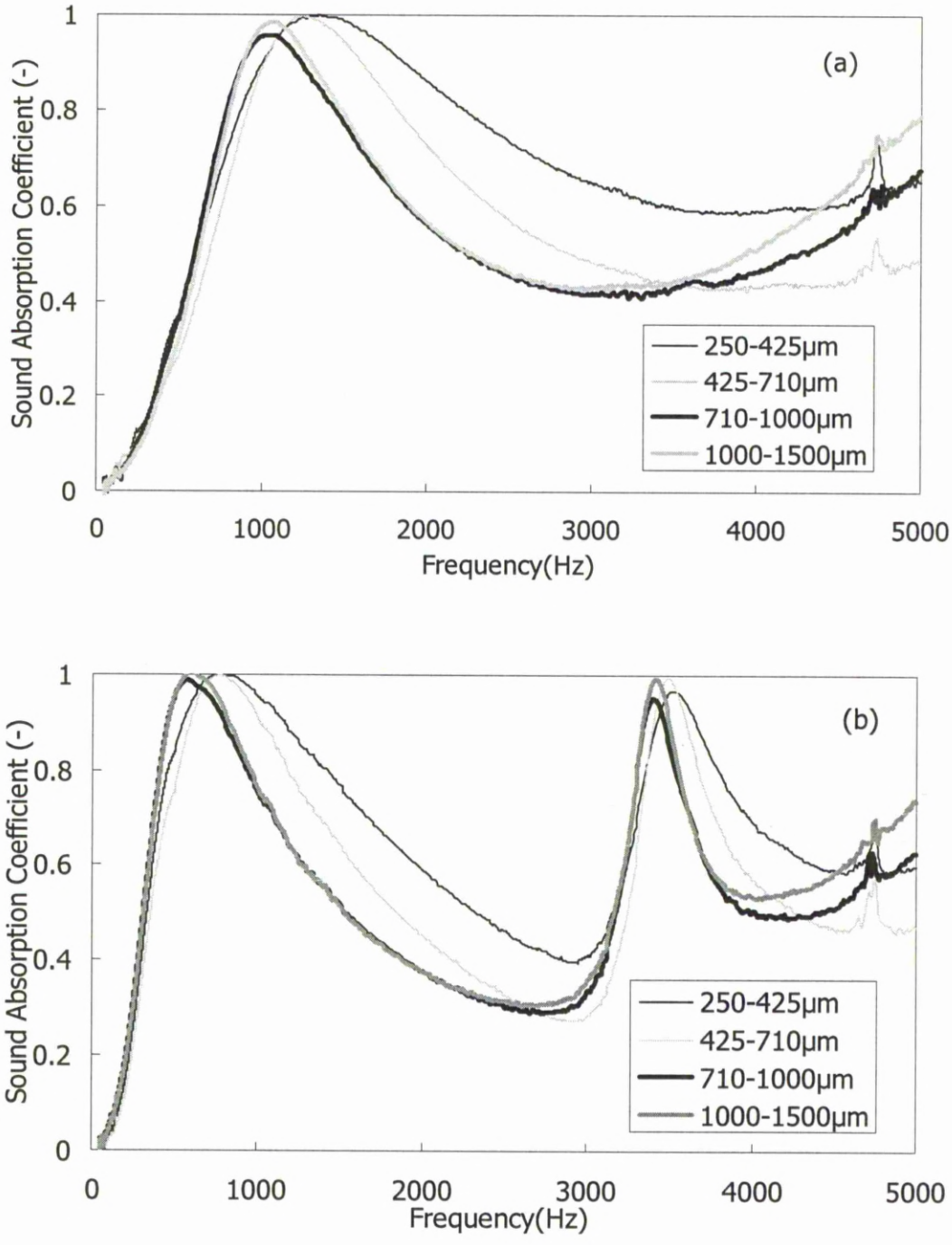

Figure 5.1.36 Sound absorption coefficient curves of open cell porous steel specimens with air-gap depths of (a) 20mm and (b) 50mm, with a nominal porosity of 70% and different pore sizes.

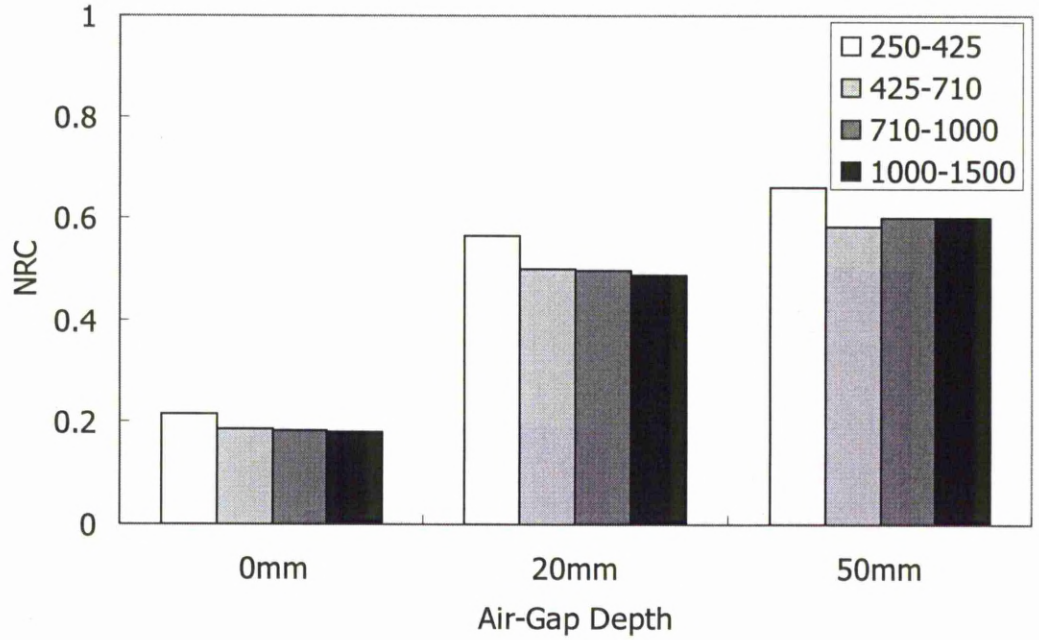

Figure 5.1.37 Variation of NRC with air-gap depth of porous steel specimens with different pore sizes.

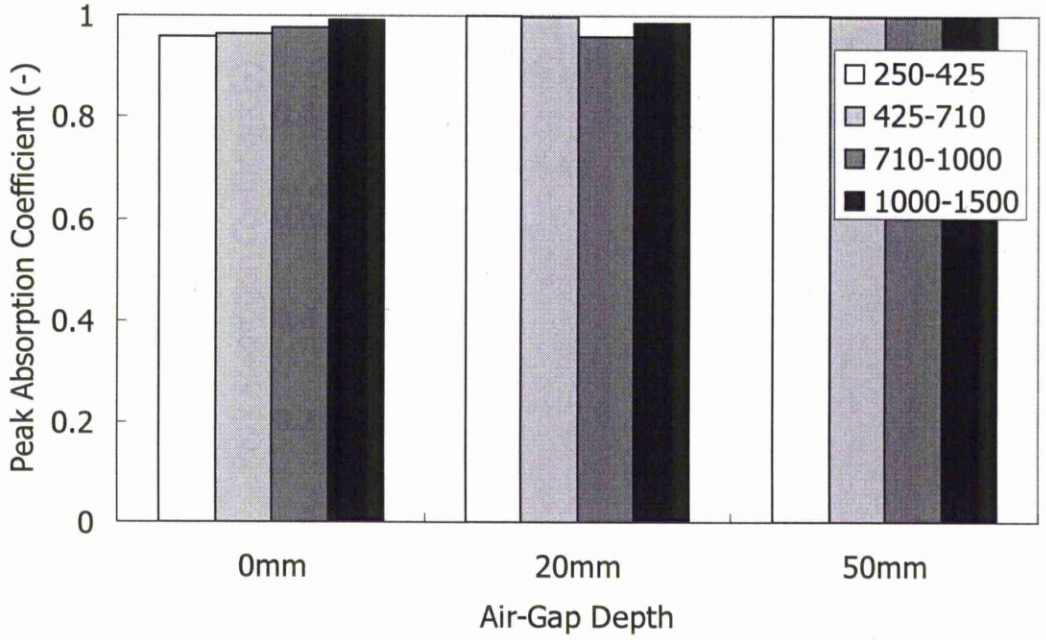

Figure 5.1.38 Variation of peak absorption coefficient with air-gap depth of porous steel specimens with different pore sizes.

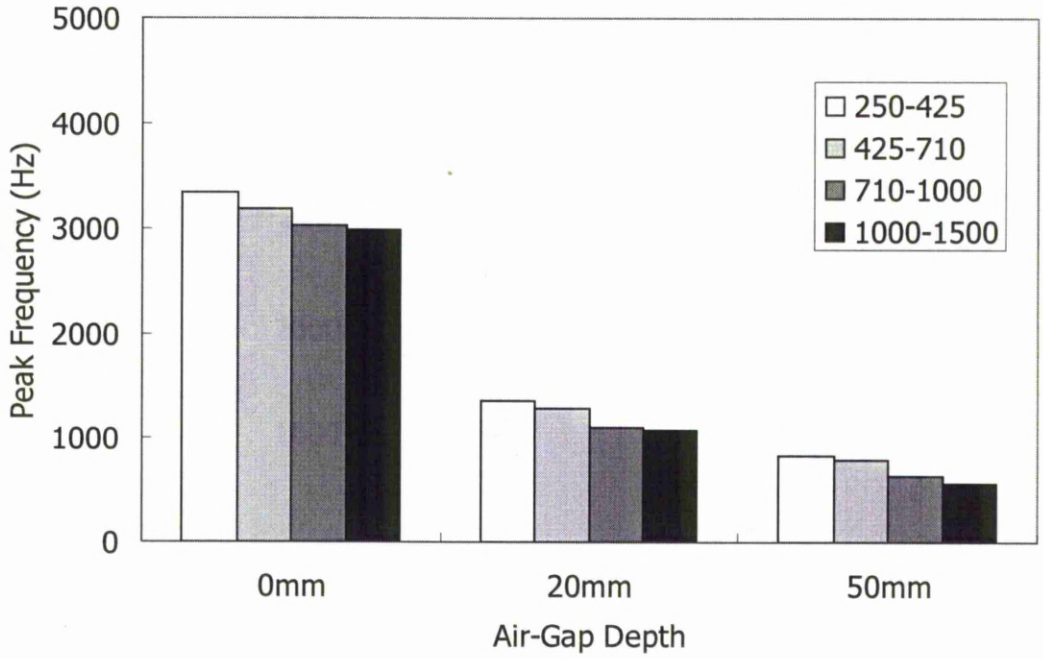

Figure 5.1.39 Variation of peak frequency with air-gap depth of porous steel specimens with different pore sizes.

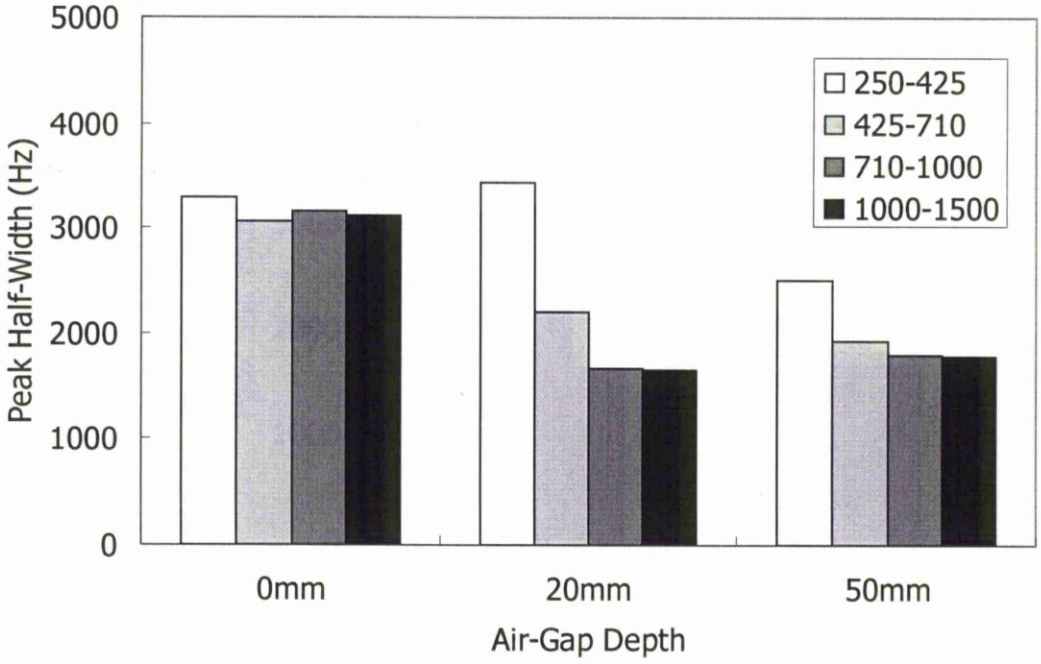

Figure 5.1.40 Variation of peak half-width with air-gap depth of porous steel specimens with different pore sizes.

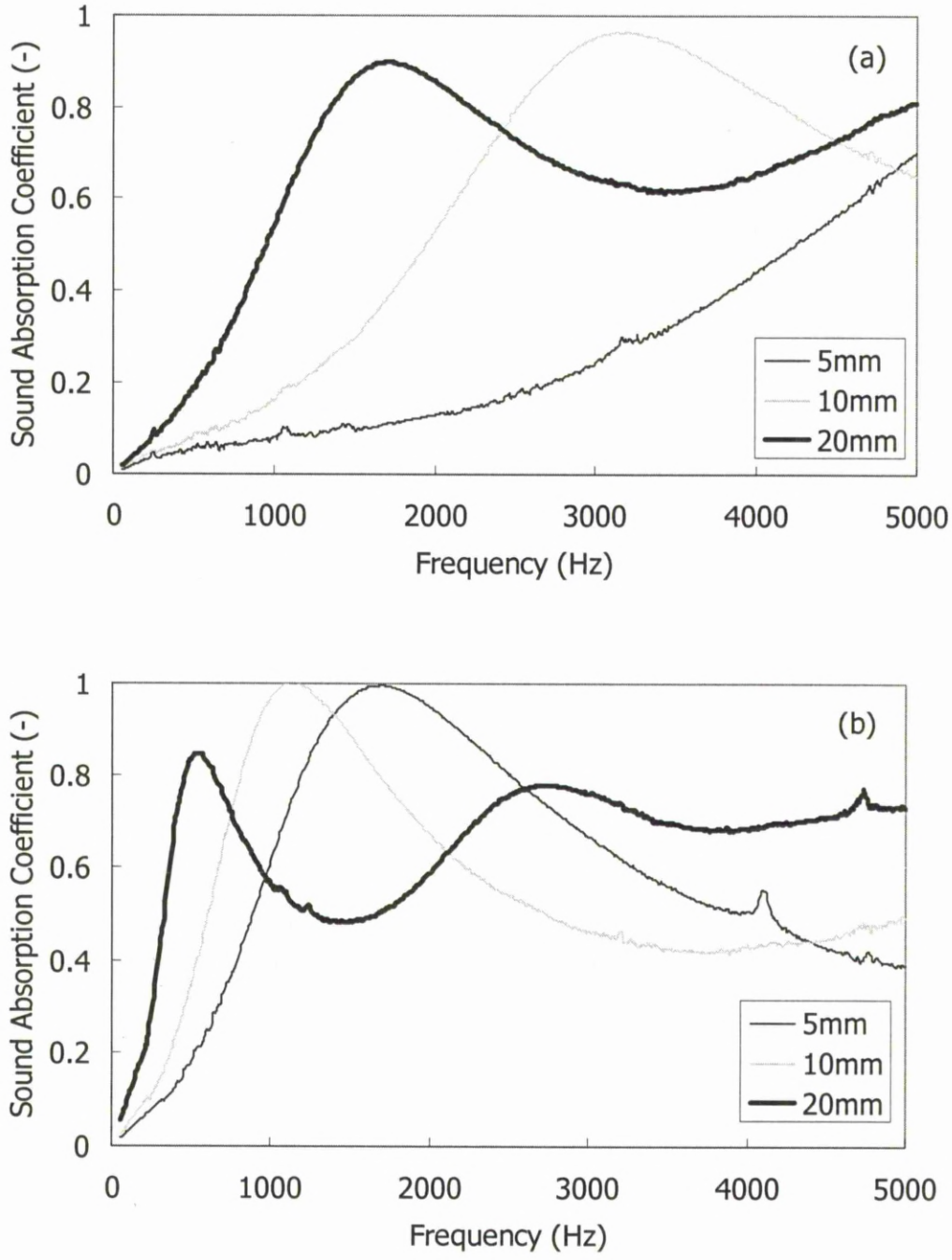

Figure 5.1.41 Sound absorption coefficient curves of open cell porous steel specimens with air-gap depths of (a) 0mm, (b) 20mm and (c) 50mm, with a nominal porosity of 70%, a pore size of 425-710μm and different thicknesses. (To be continued)

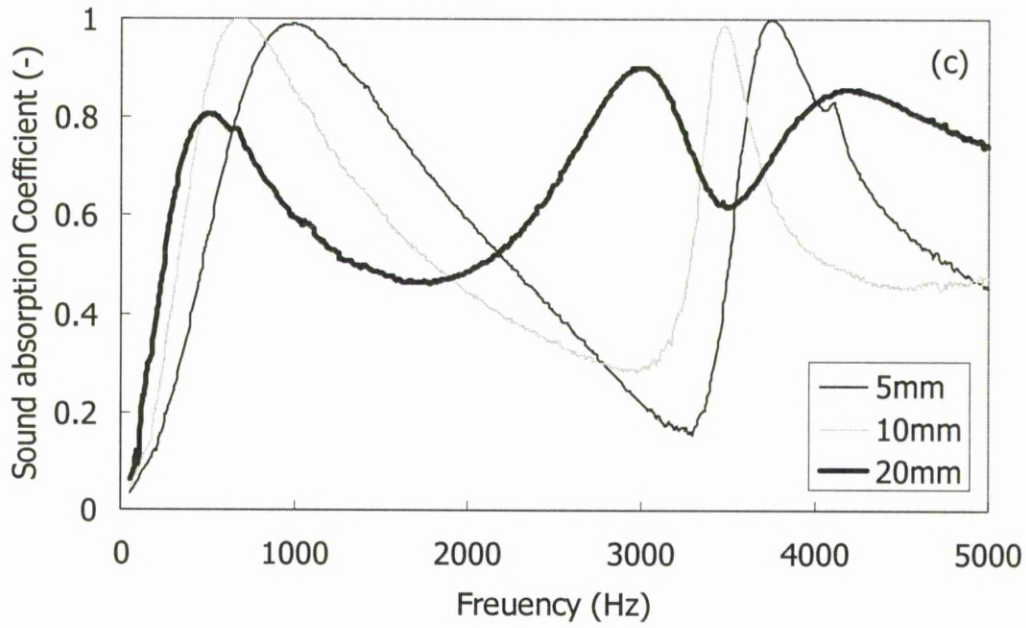

Figure 5.1.41 Sound absorption coefficient curves of open cell porous steel specimens with air-gap depths of (a) 0mm, (b) 20mm and (c) 50mm, with a nominal porosity of 70%, a pore size of 425-710μm and different thicknesses.

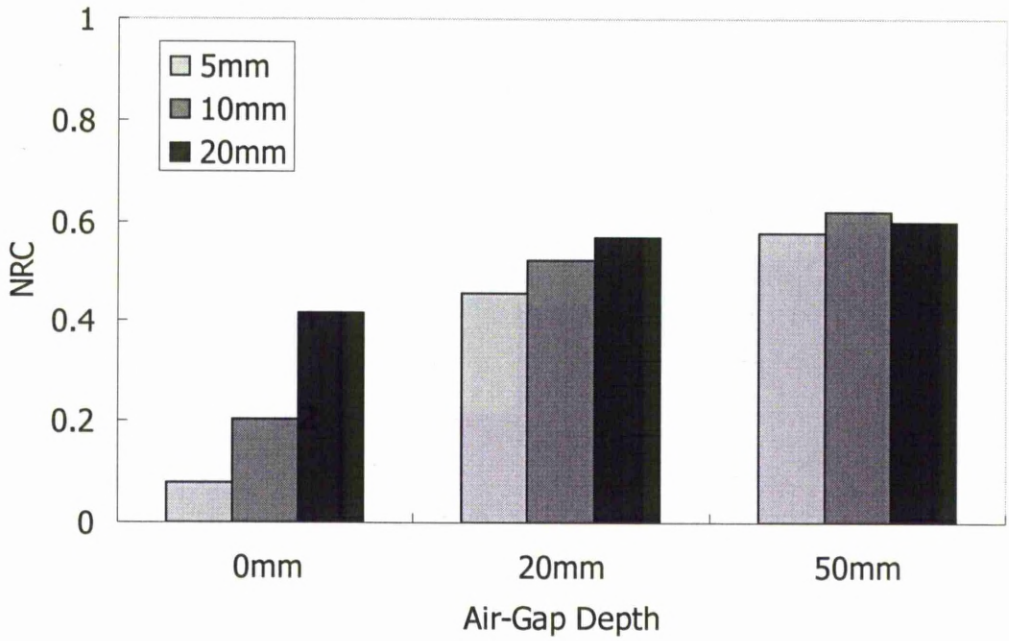

Figure 5.1.42 Variation of NRC with air-gap depth of porous steel specimens with different thicknesses.

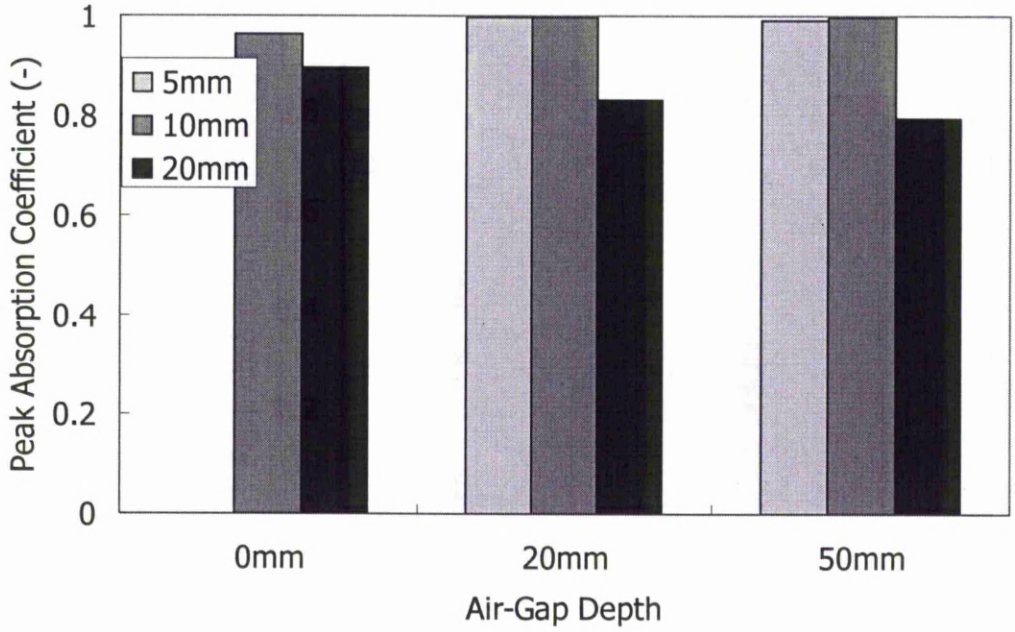

Figure 5.1.43 Variation of peak absorption coefficient with air-gap depth of porous steel specimens with different thicknesses.

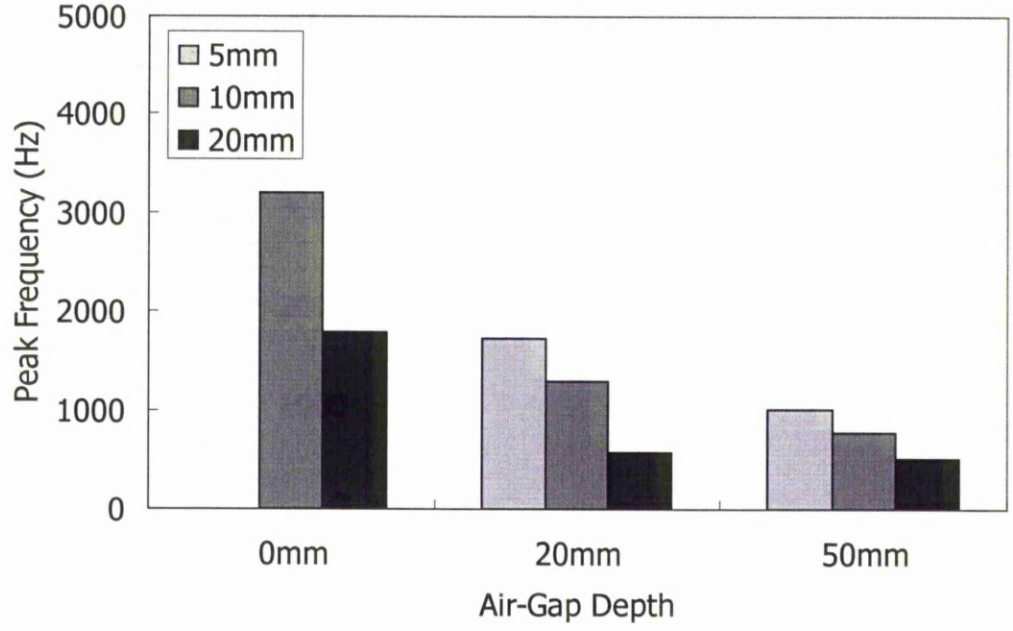

Figure 5.1.44 Variation of peak frequency with air-gap depth of porous steel specimens with different thicknesses.

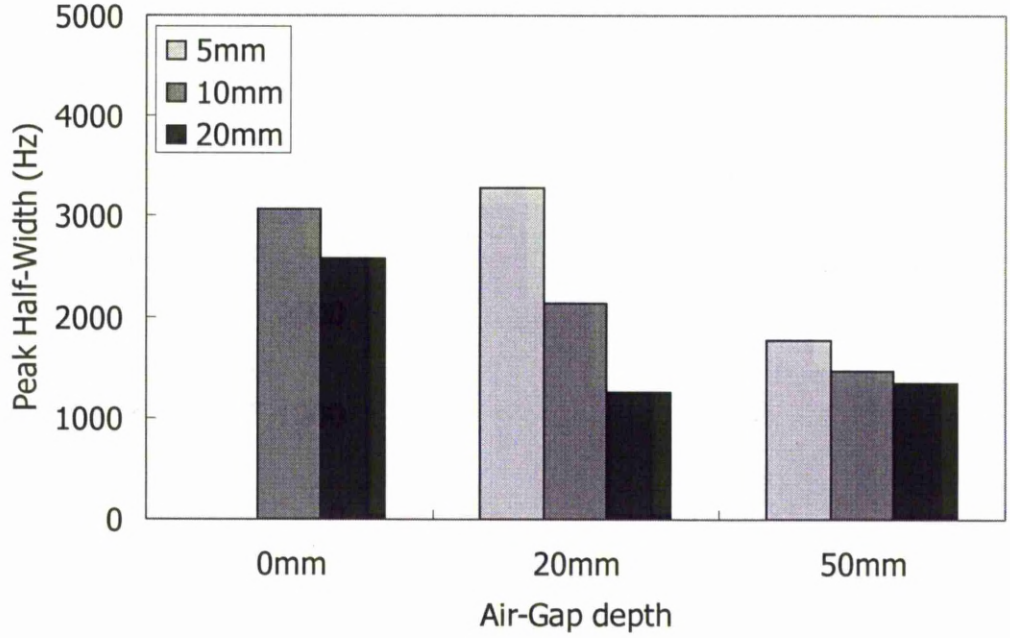

Figure 5.1.45 Variation of peak half-width with air-gap depth of porous steel specimens with different thicknesses.

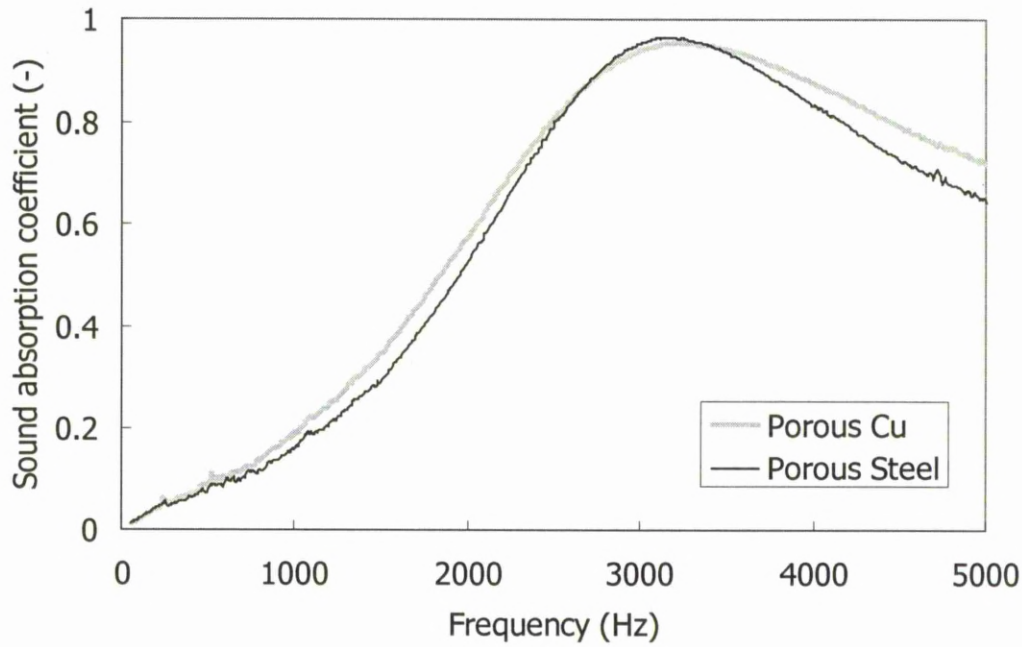

Figure 5.1.46 Sound absorption coefficient curves of open cell porous steel and porous copper, both manufacture by LCS, with the same nominal porosity of 70%, pore size of 425-710μm and specimen thickness of 10mm.

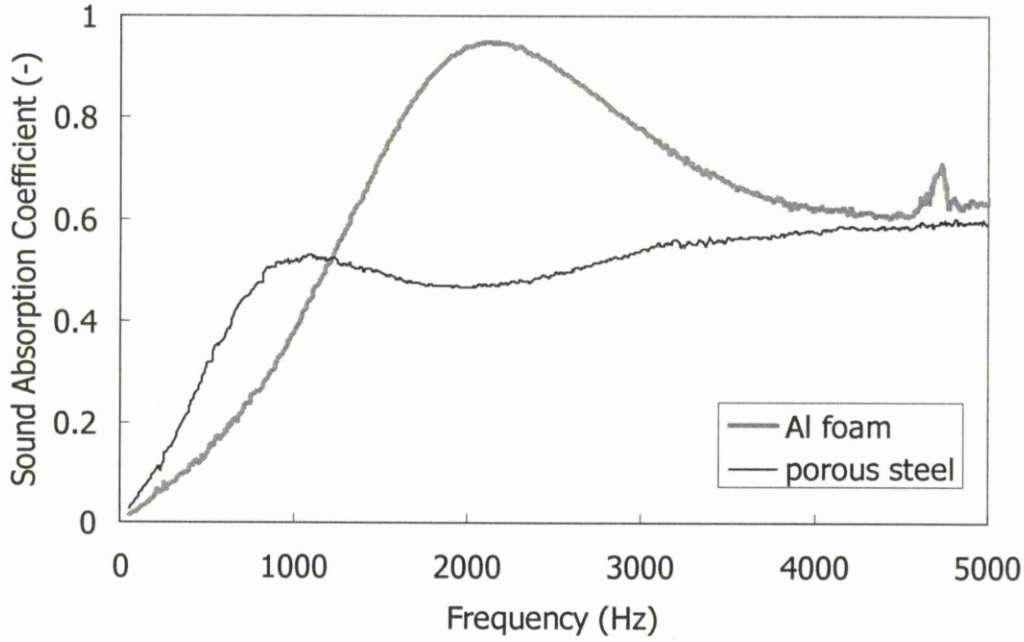

Figure 5.1.47 Sound absorption coefficient curves of open cell porous steel, manufactured by LCS, and porous Al, manufactured by melt infiltration, with the same nominal porosity of 60%, pore size of 425-710μm and specimen thickness of 20mm.

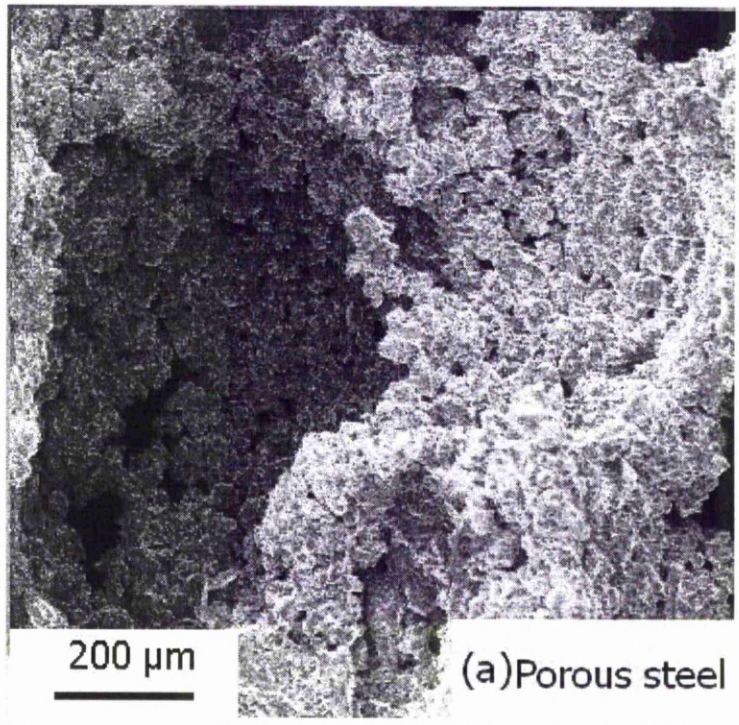

Figure 5.1.48 Microstructure of (a) porous steel (b) porous Cu (Zhang and Zhao, 2007) and (c) porous Al (Han, *et al*, 2003). (To be continued)

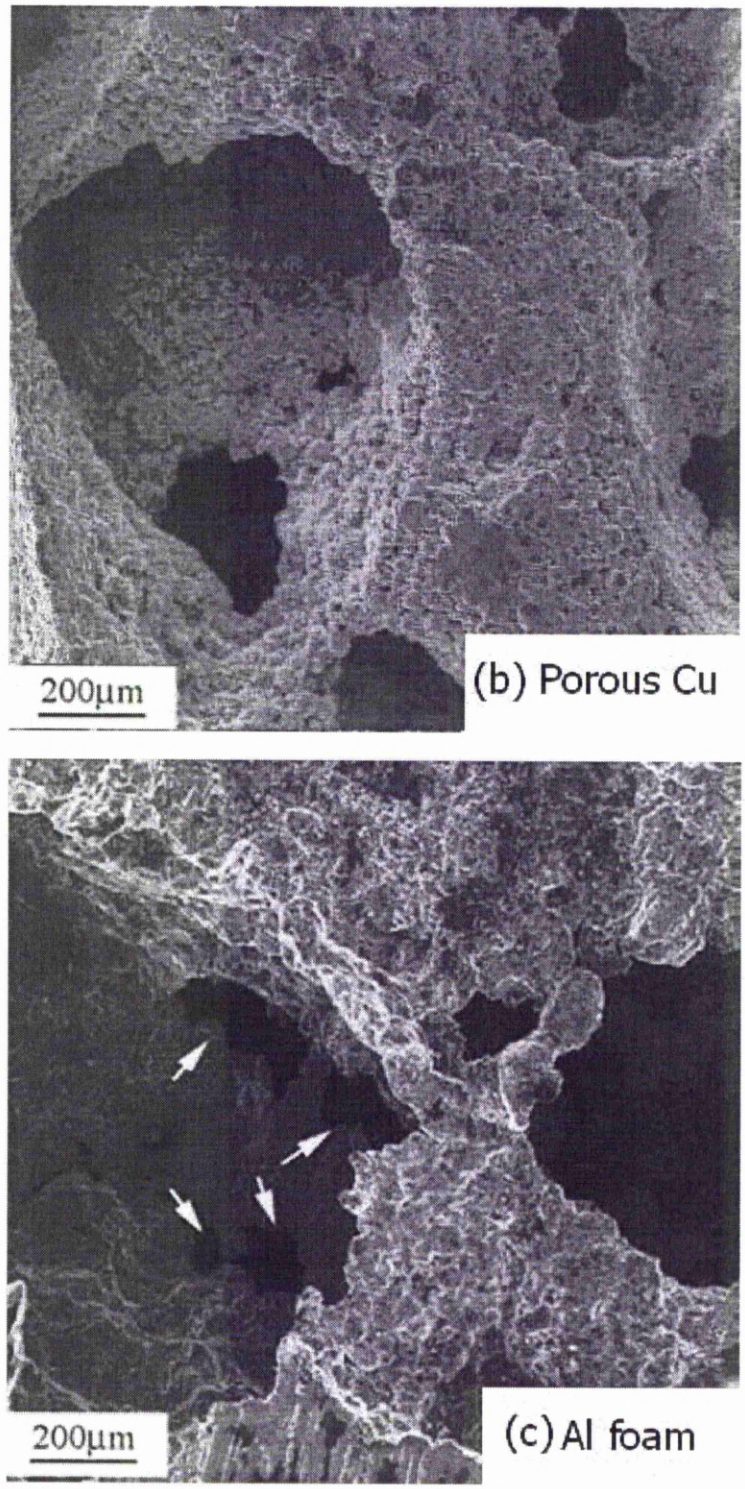

Figure 5.1.48 Microstructure of (a) porous steel (b) porous Cu (Zhang and Zhao, 2007) and (c) porous Al (Han, *et al*, 2003).

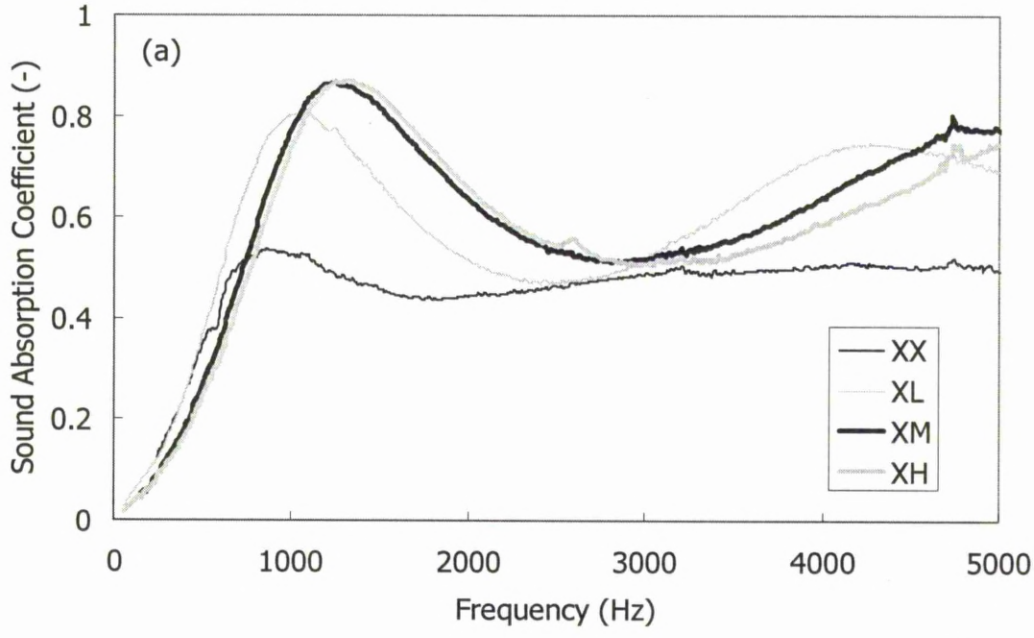

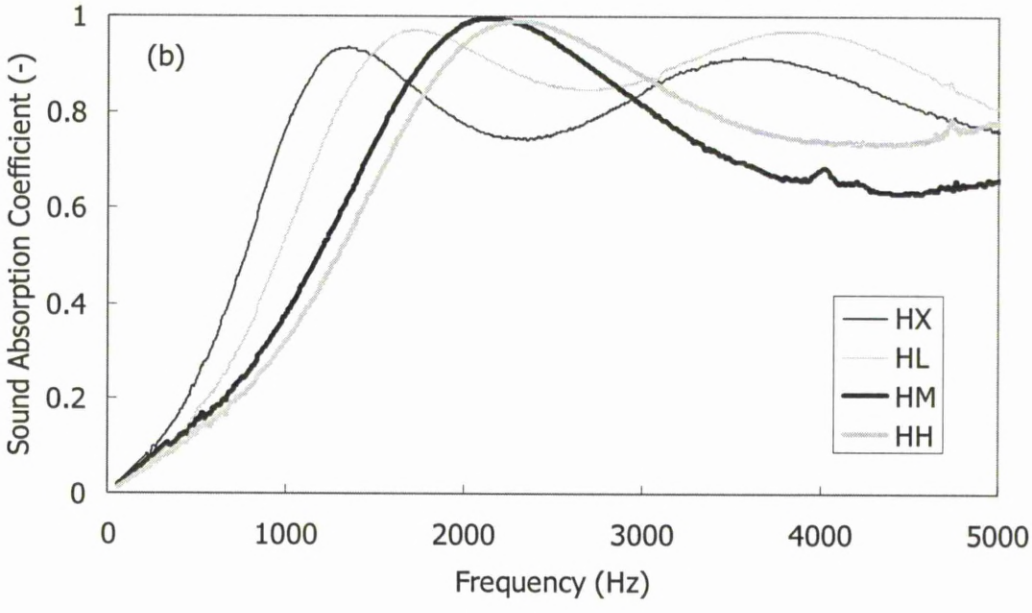

Figure 5.2.1 Sound absorption coefficient curves of two-layer assemblies with different porosities and different orders: (a) low-high and (b) high-low. X-60%, L-65%, M-70%, H-75%.

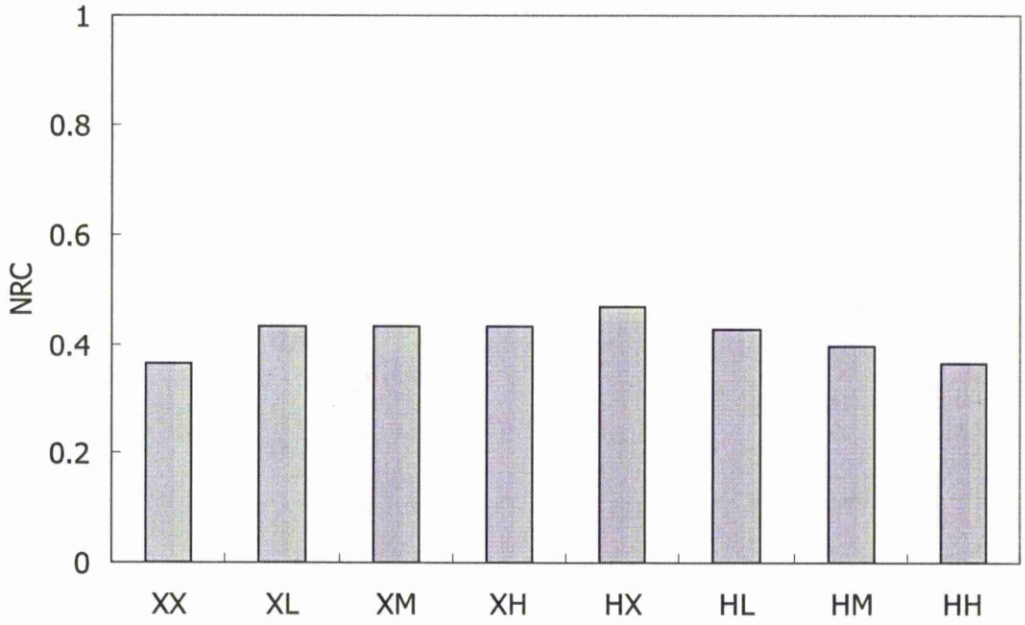

Figure 5.2.2 NRC of two-layer assemblies with different nominal porosity orders. X-60%, L-65%, M-70%, H-75%.

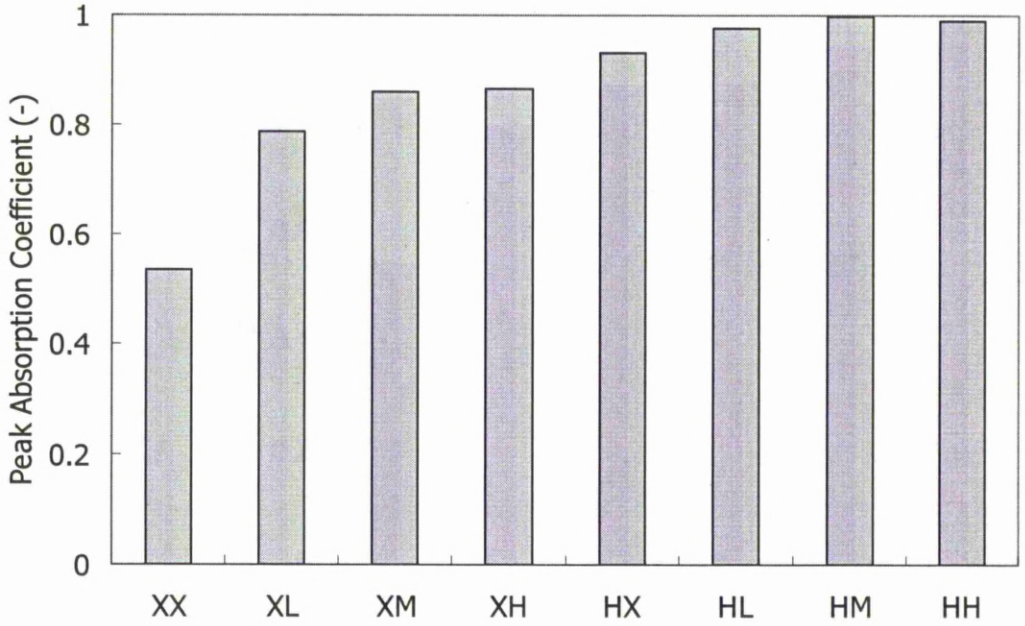

Figure 5.2.3 Peak absorption coefficients of two-layer assemblies with different nominal porosity orders. X-60%, L-65%, M-70%, H-75%.

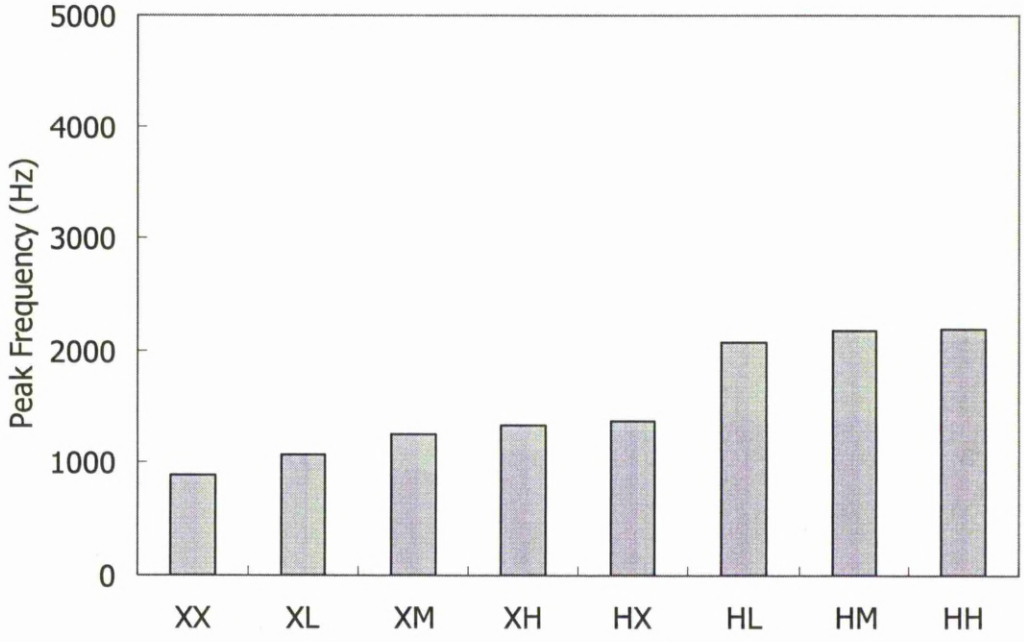

Figure 5.2.4 Peak frequencies of two-layer assemblies with different nominal porosity orders. X-60%, L-65%, M-70%, H-75%.

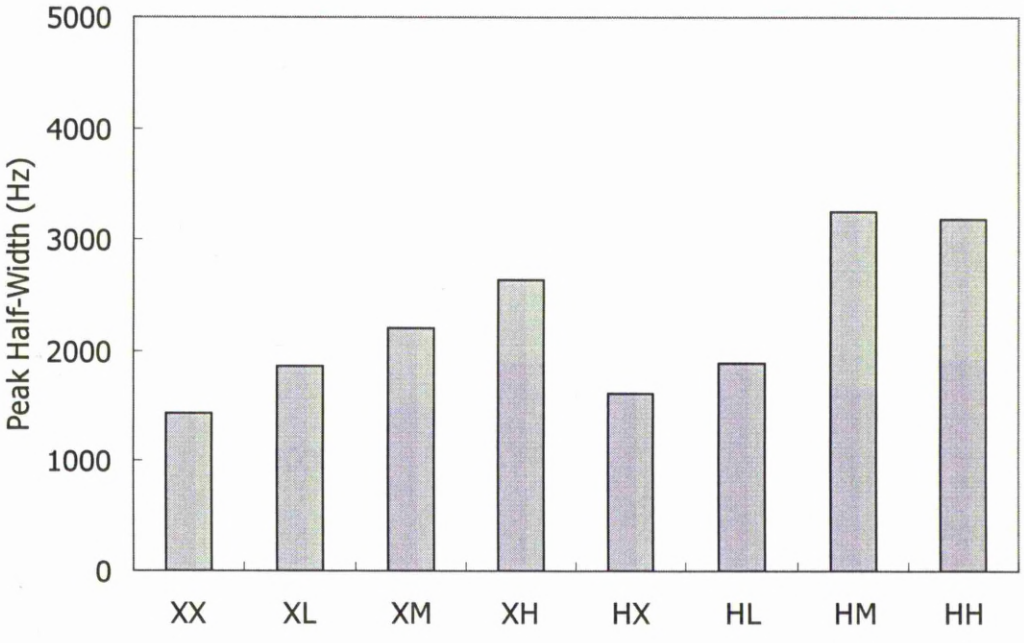

Figure 5.2.5 Peak half-widths of two-layer assemblies with different nominal porosity orders. X-60%, L-65%, M-70%, H-75%.

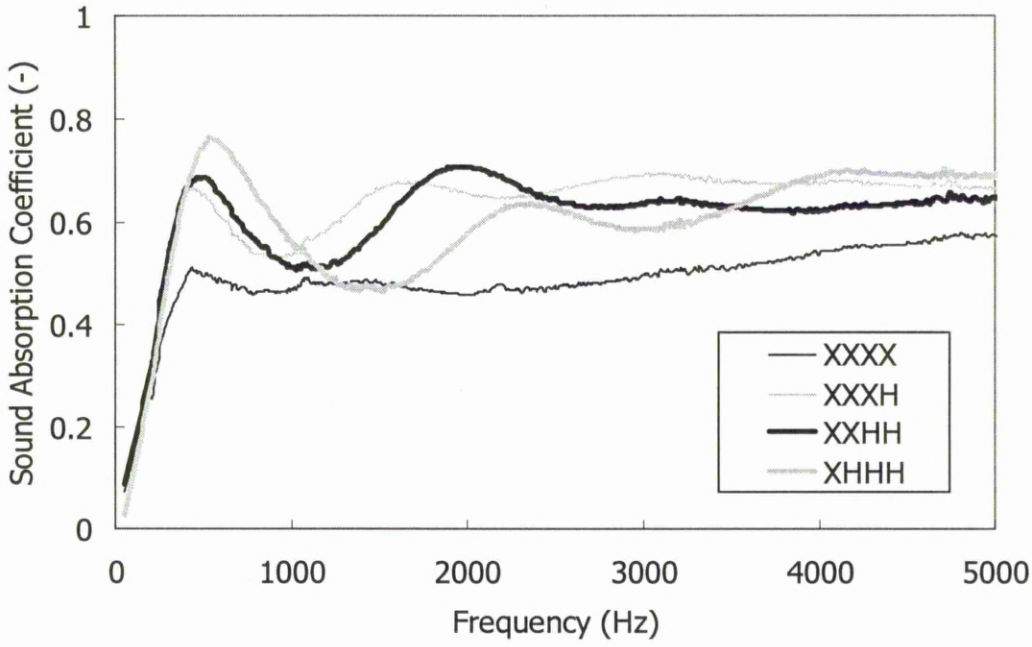

Figure 5.2.6 Sound absorption coefficient curves of four-layer assemblies with different nominal porosity orders with low porosity at front. X-60%, H-75%.

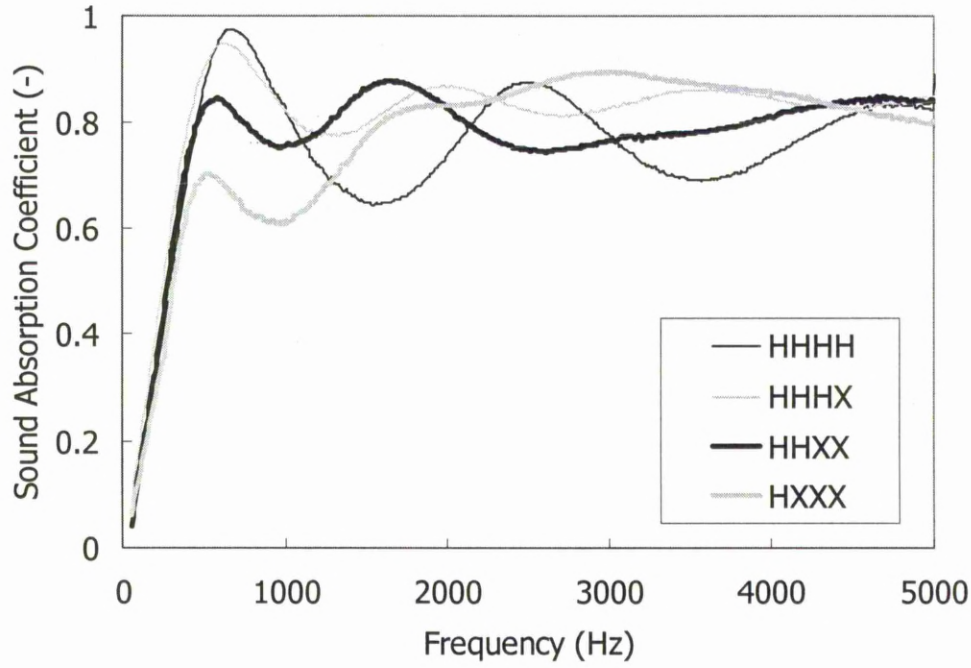

5.2.7 Sound absorption coefficient curves of four-layer assemblies with different nominal porosity orders with high porosity at front. X-60%, H-75%.

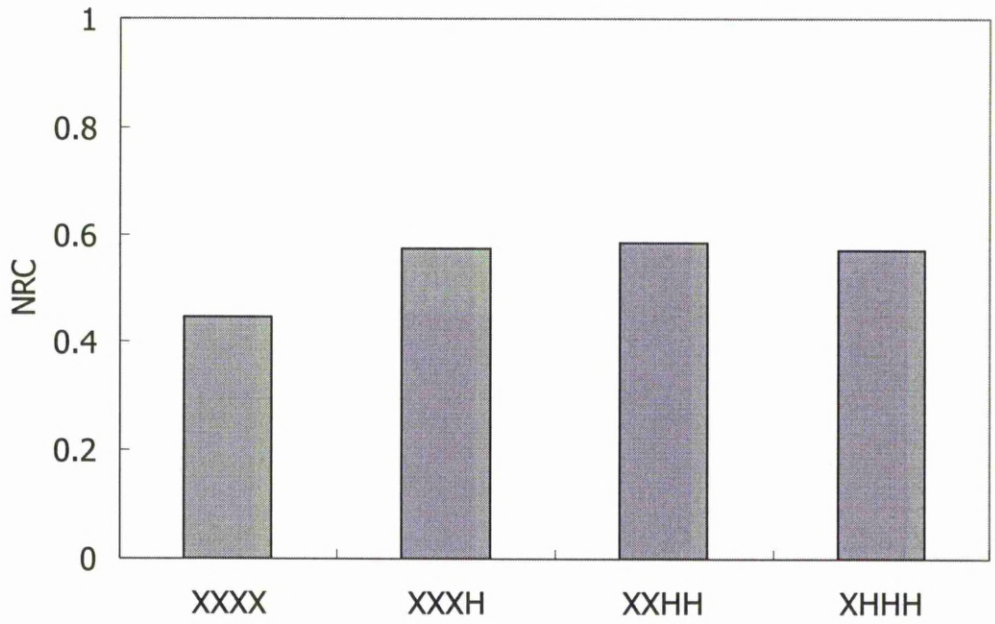

Figure 5.2.8 NRC of four-layer assemblies with different nominal porosity orders with low porosity at front. X-60%, H-75%.

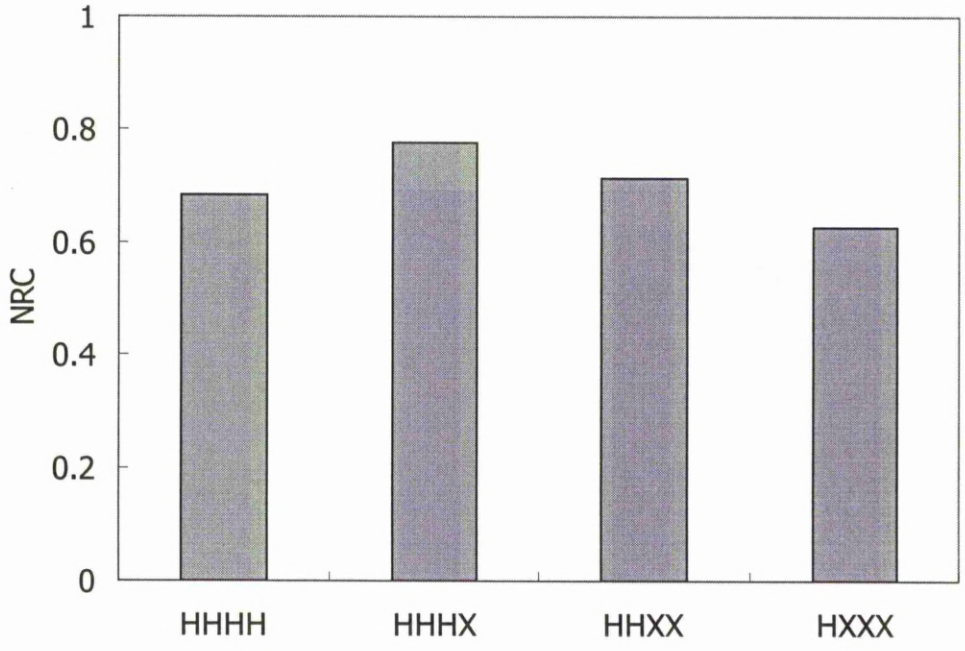

Figure 5.2.9 NRC of four-layer assemblies with different nominal porosity orders with high porosity at front. X-60%, H-75%.

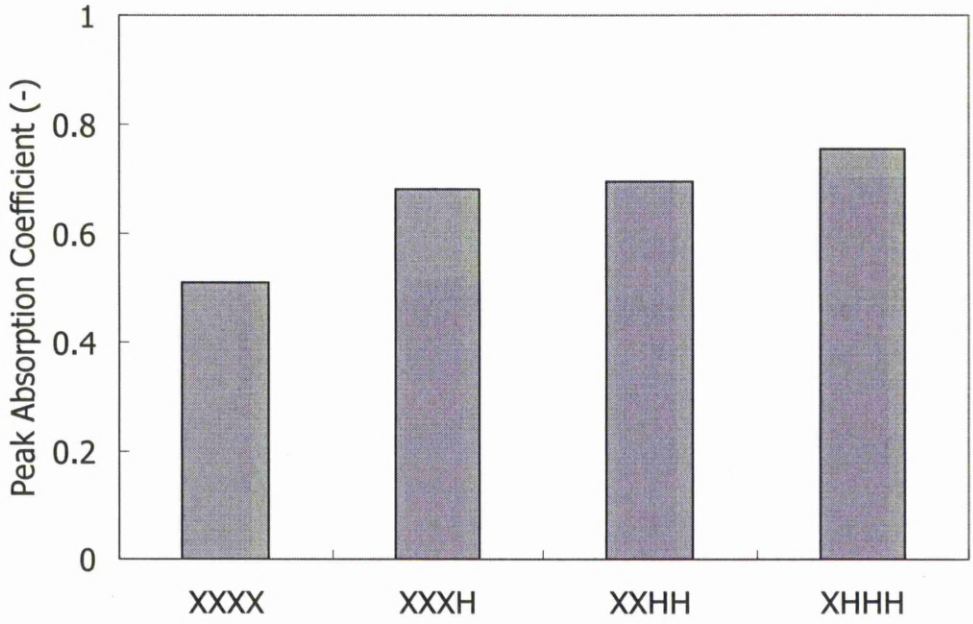

Figure 5.2.10 Peak absorption coefficients of four-layer assemblies with different nominal porosity orders with low porosity at front. X-60%, H-75%.

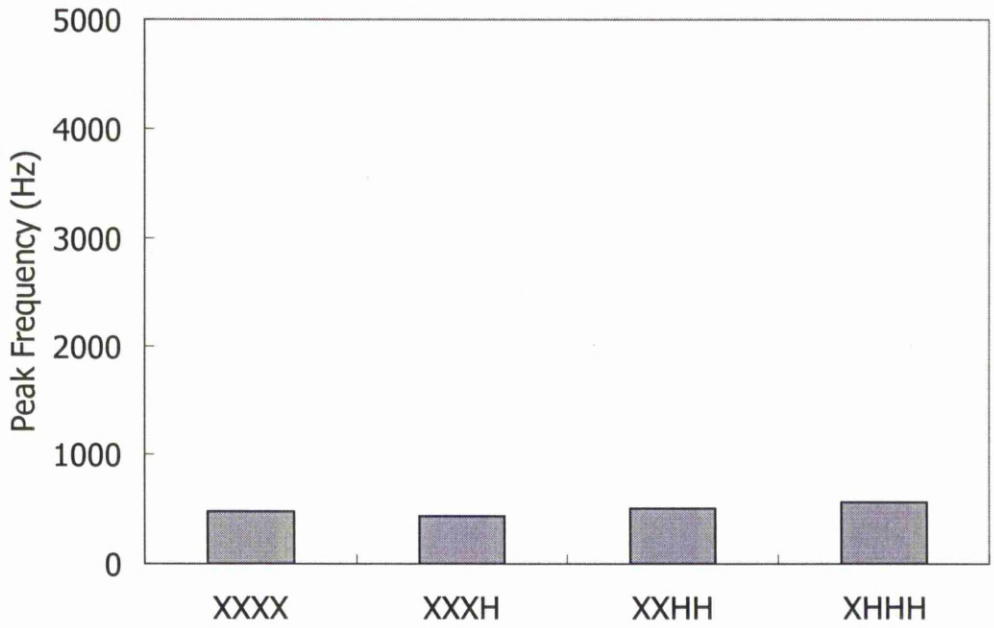

Figure 5.2.11 Peak frequencies of four-layer assemblies with different nominal porosity orders with low porosity at front. X-60%, H-75%.

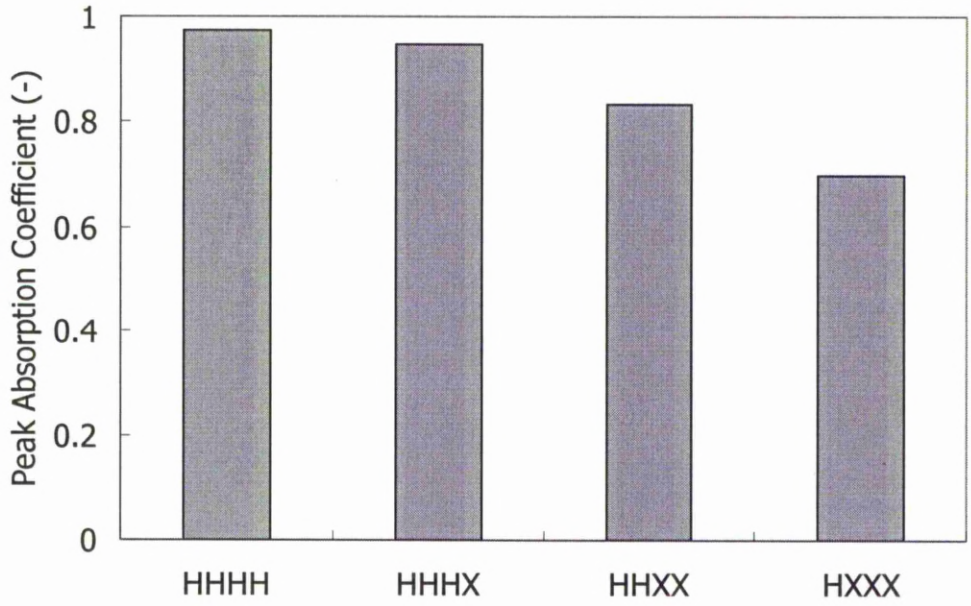

Figure 5.2.12 Peak absorption coefficients of four-layer assemblies with different nominal porosity orders with high porosity at front. X-60%, H-75%.

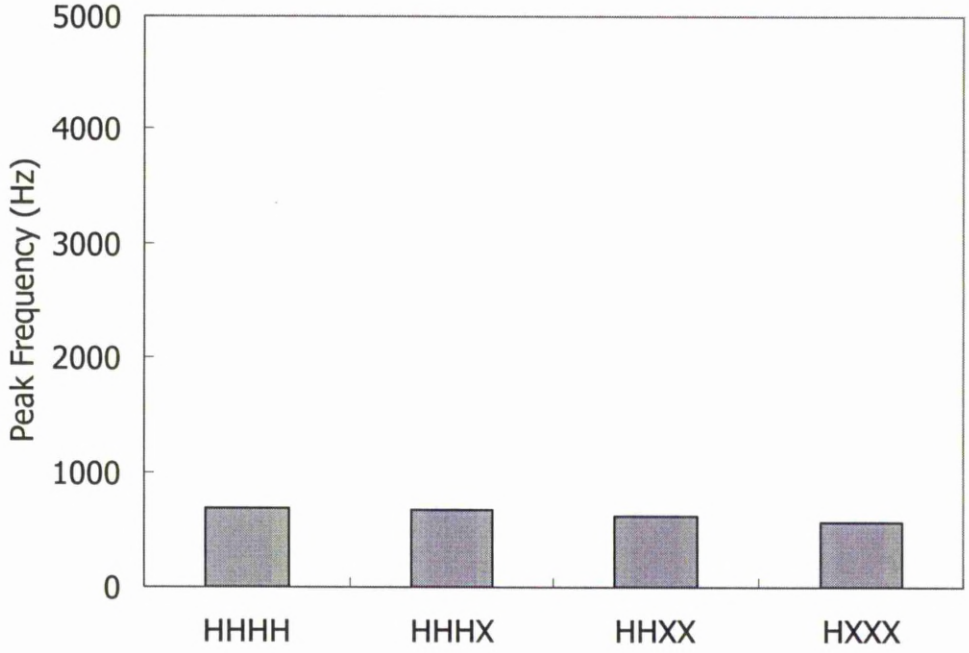

Figure 5.2.13 Peak frequencies of four-layer assemblies with different nominal porosity orders with high porosity at front. X-60%, H-75%.

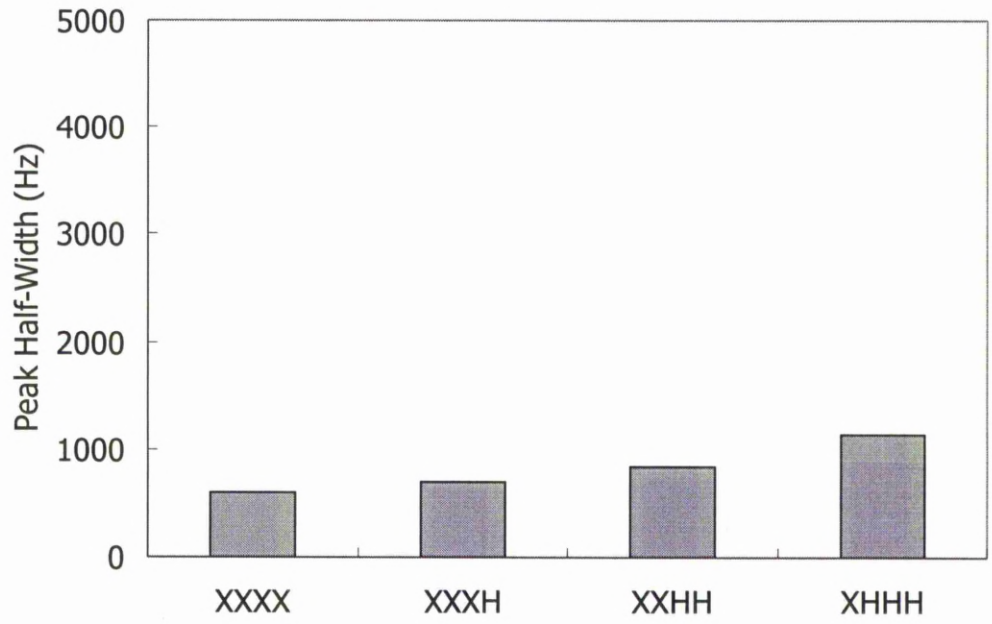

Figure 5.2.14 Peak half-widths of four-layer assemblies with different nominal porosity orders with low porosity at front. X-60%, H-75%.

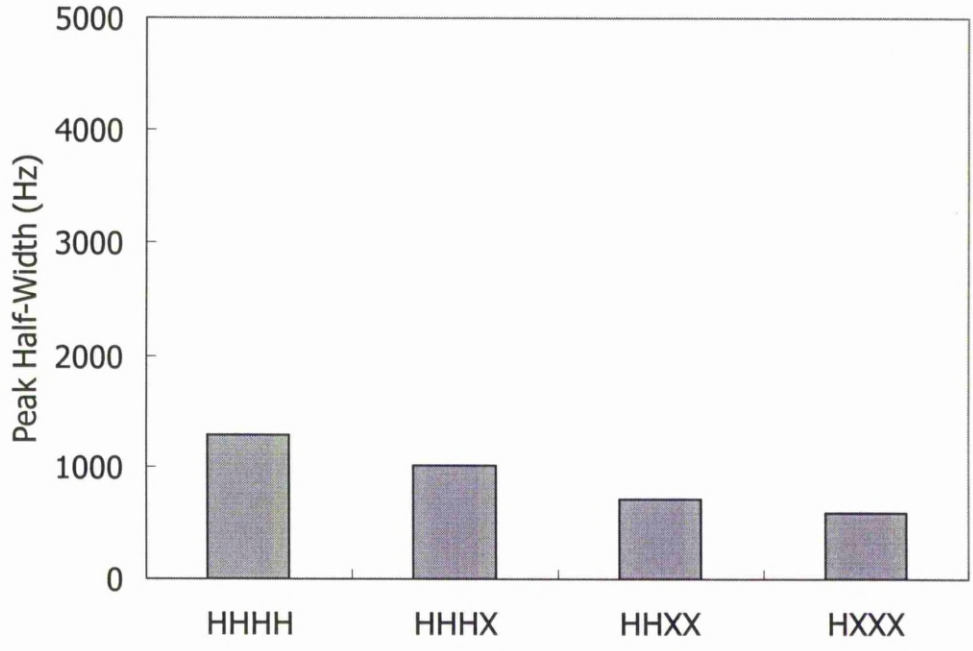

Figure 5.2.15 Peak half-widths of four-layer assemblies with different nominal porosity orders with high porosity at front. X-60%, H-75%.

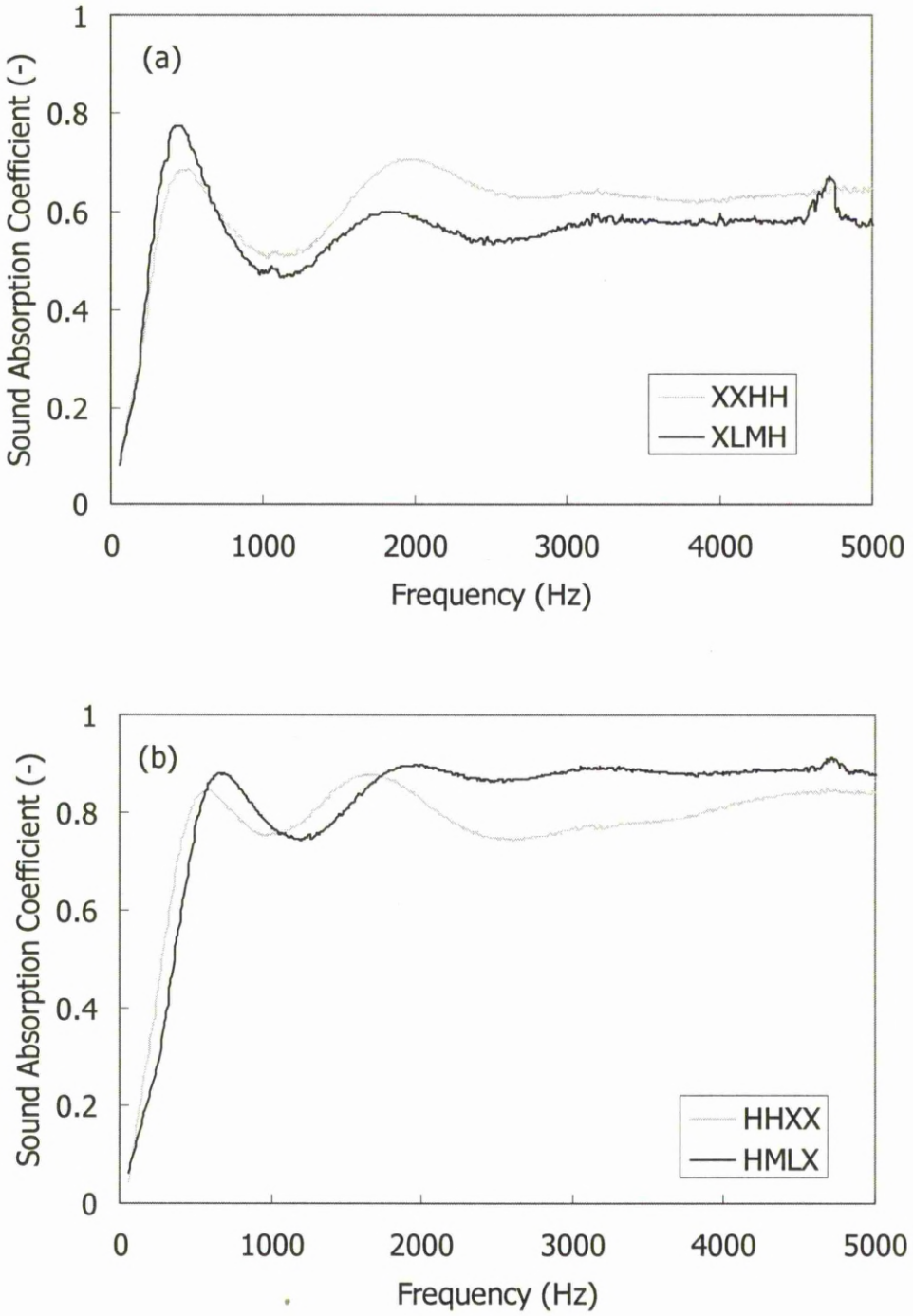

Figure 5.2.16 Sound absorption coefficient curves of four-layer assemblies with different nominal porosity orders: (a) low-high and (b) high-low. X-60%, L-65%, M-70%, H-75%.

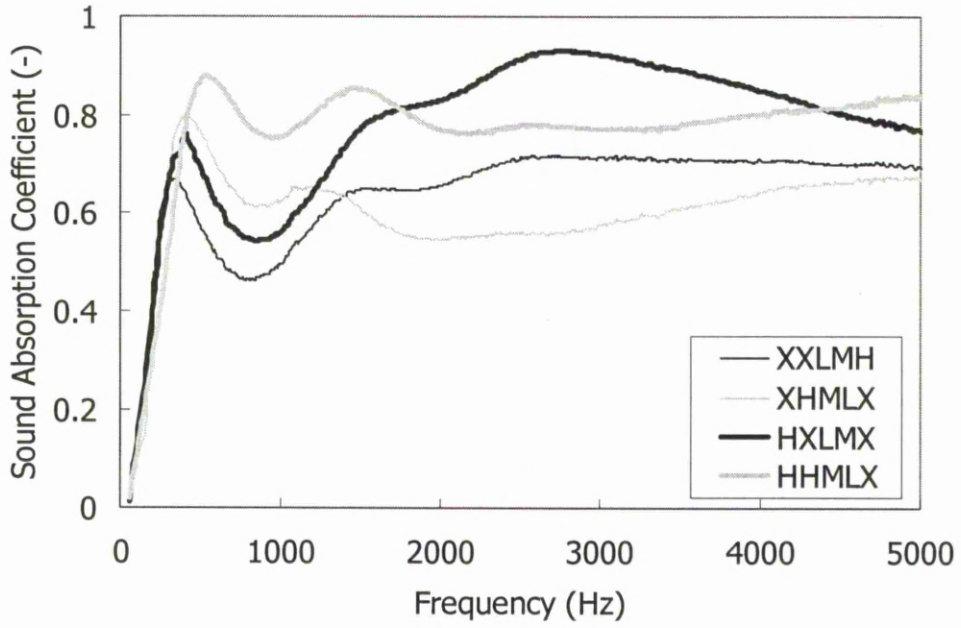

Figure 5.2.17 Sound absorption coefficient curves of fiver-layer assemblies with different nominal porosity orders. X-60%, L-65%, M-70%, H-75%.

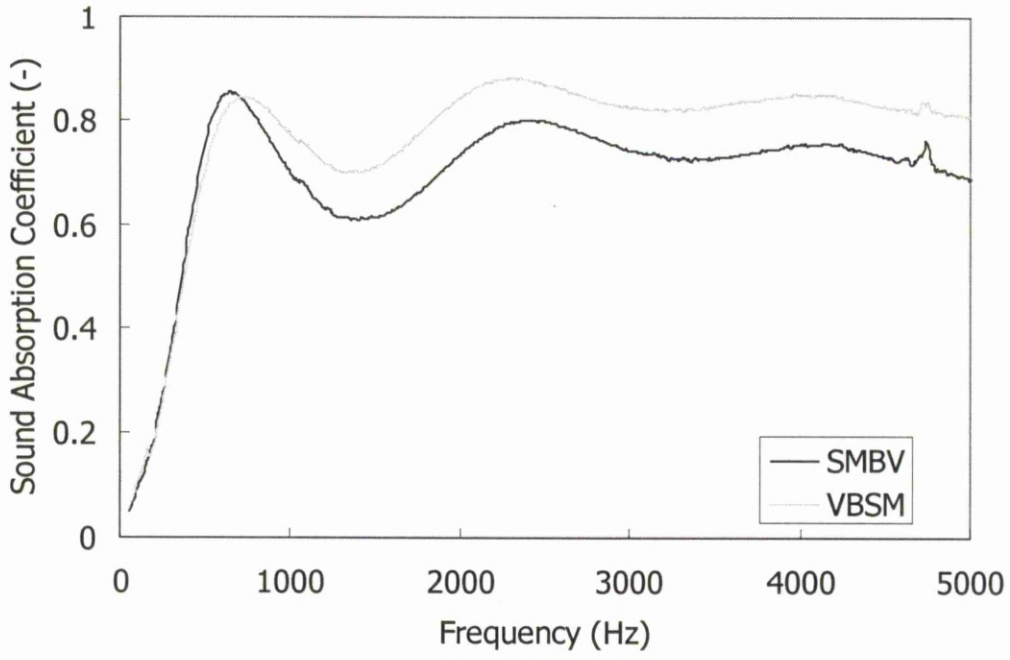

Figure 5.2.18 Sound absorption coefficient curves of four-layer assemblies with different pore size orders: (a) small-big and (b) big-small. S: 250-425μm, M: 415-710μm, B: 710-1000μm and V: 1000-1500μm.

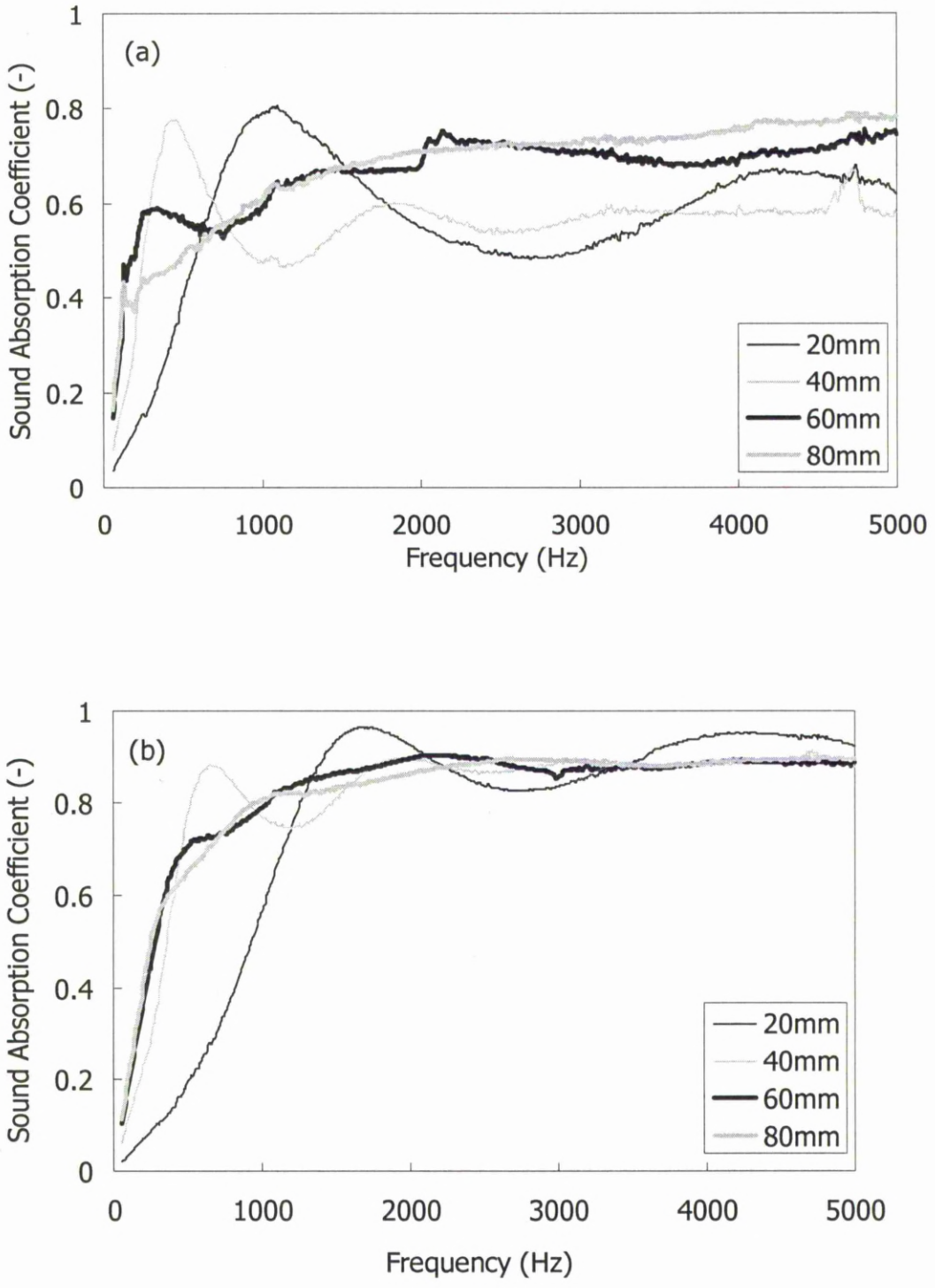

Figure 5.2.19 Sound absorption coefficient curves of four-layer assemblies with different thicknesses and porosity orders: (a) XLMH and (b) HMLX. X-60%, L-65%, M-70%, H-75%.

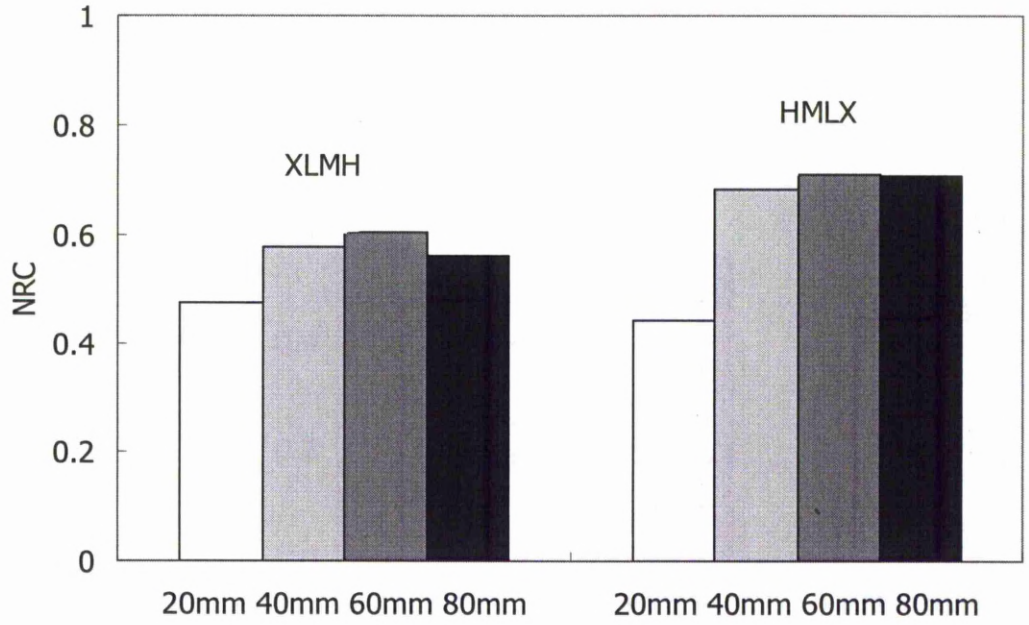

Figure 5.2.20 NRC of four-layer assemblies with different nominal porosity orders and thicknesses. X-60%, L-65%, M-70%, H-75%.

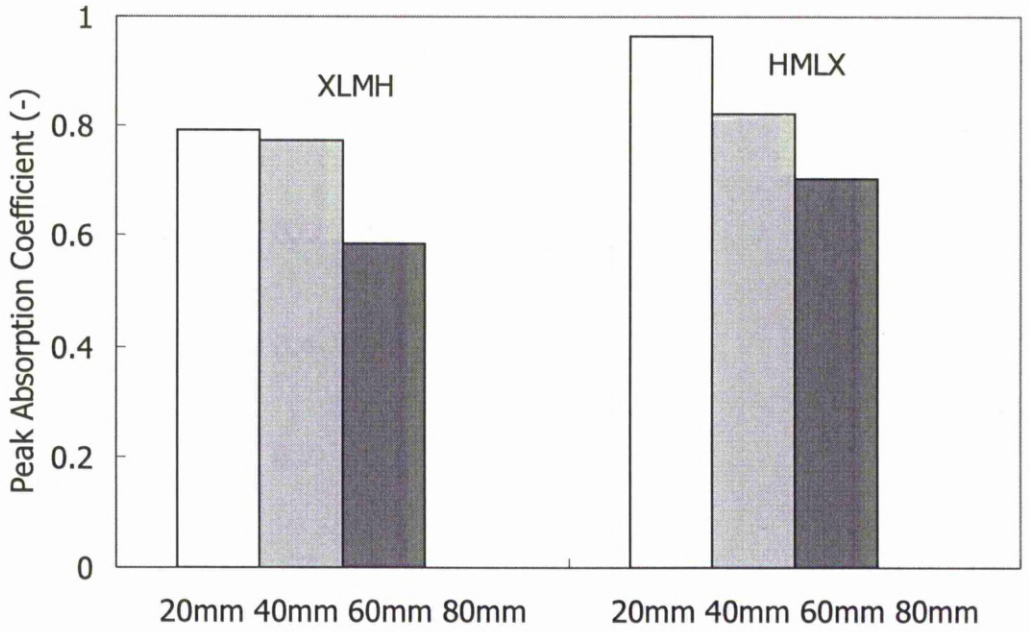

Figure 5.2.21 Peak absorption coefficients of four-layer assemblies with different nominal porosity orders and thicknesses. X-60%, L-65%, M-70%, H-75%.

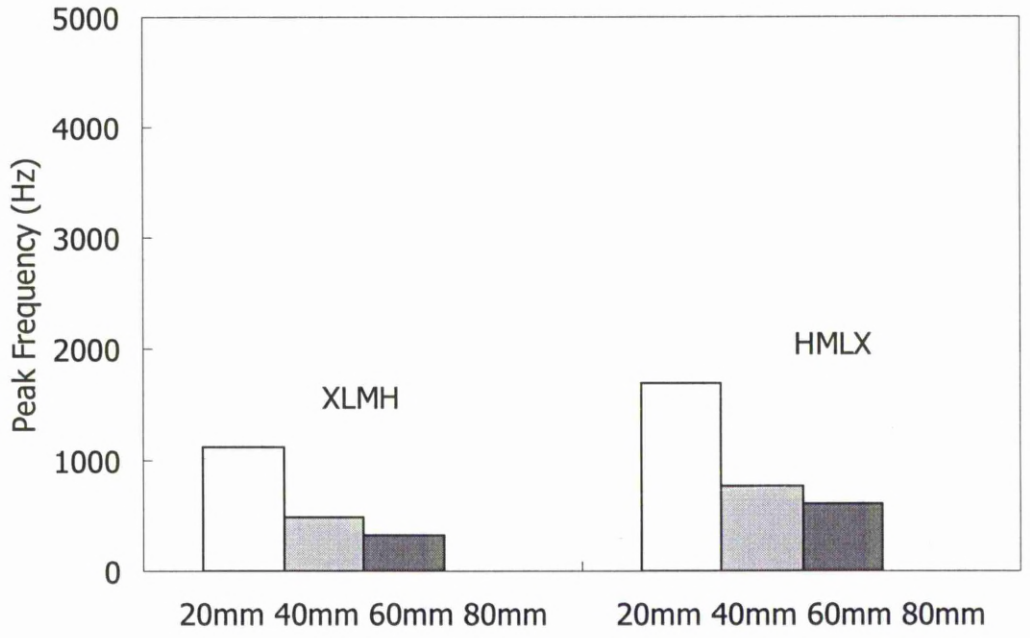

Figure 5.2.22 Peak frequencies of four-layer assemblies with different nominal porosity orders and thicknesses. X-60%, L-65%, M-70%, H-75%.

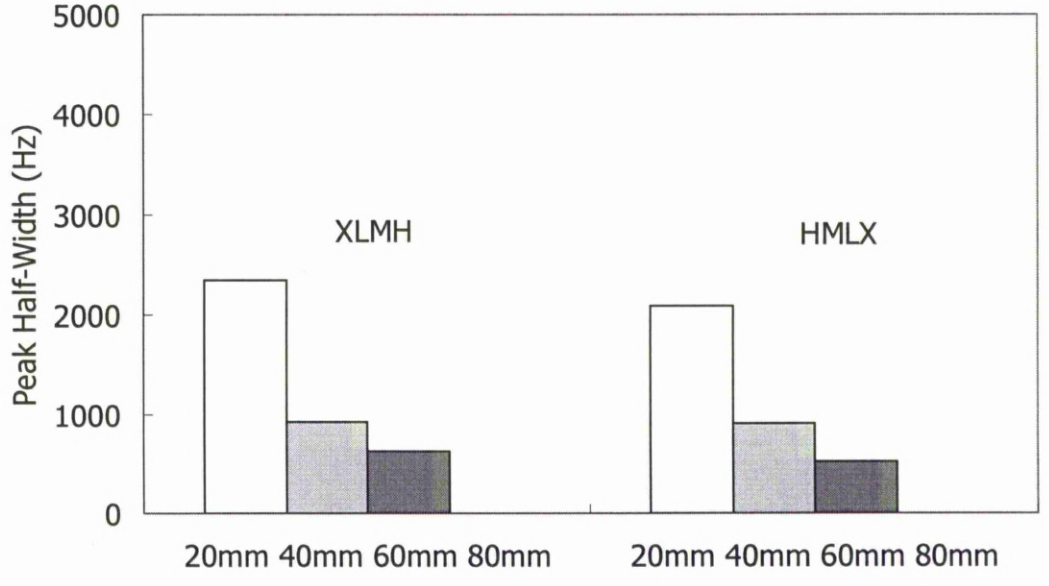

Figure 5.2.23 Peak half-widths of four-layer assemblies with different nominal porosity orders and thicknesses. X-60%, L-65%, M-70%, H-75%.

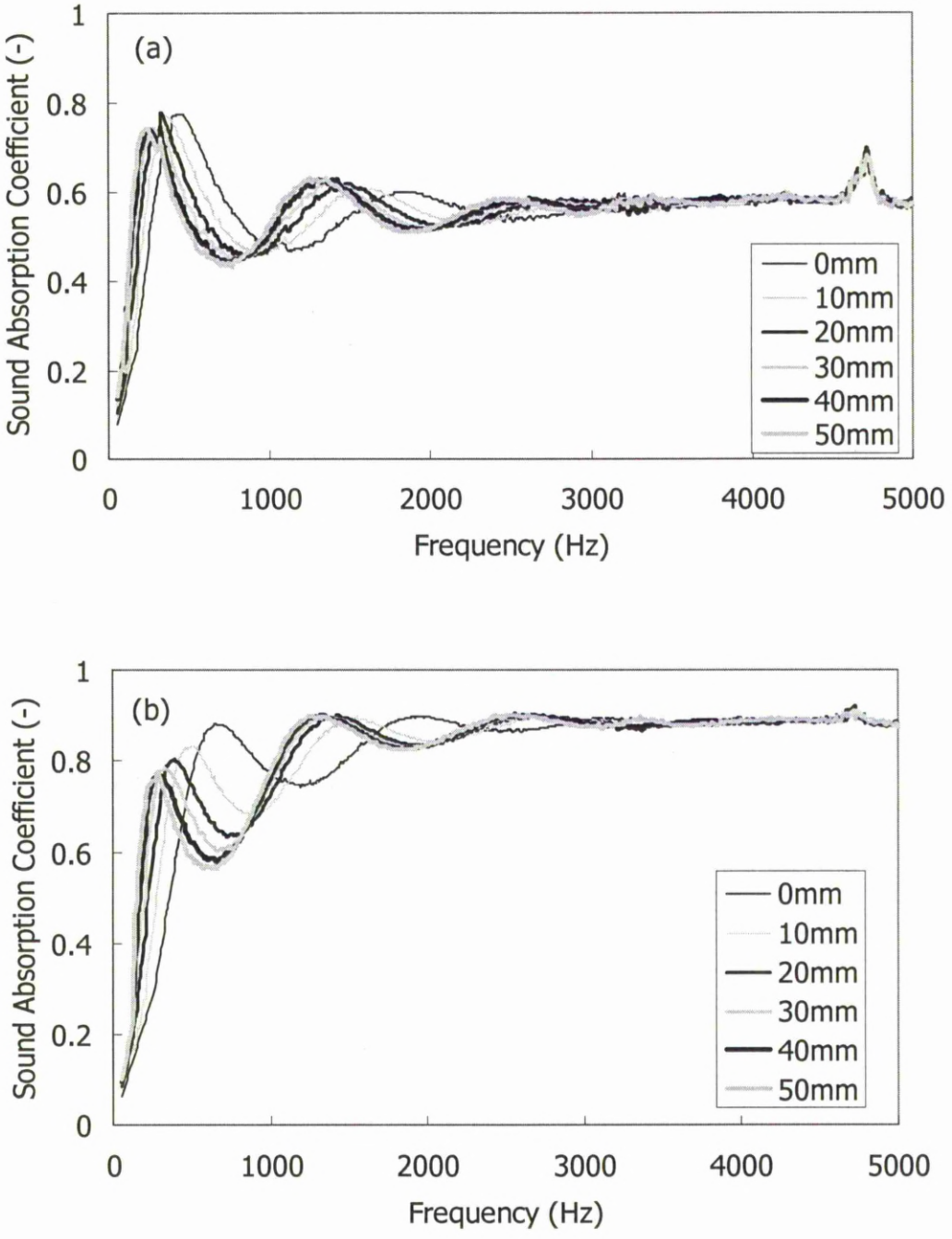

Figure 5.2.24 Sound absorption coefficient curves of four-layer assemblies with different air-gap depths and porosity orders: (a) XLMH and (b) HMLX. X-60%, L-65%, M-70%, H-75%.

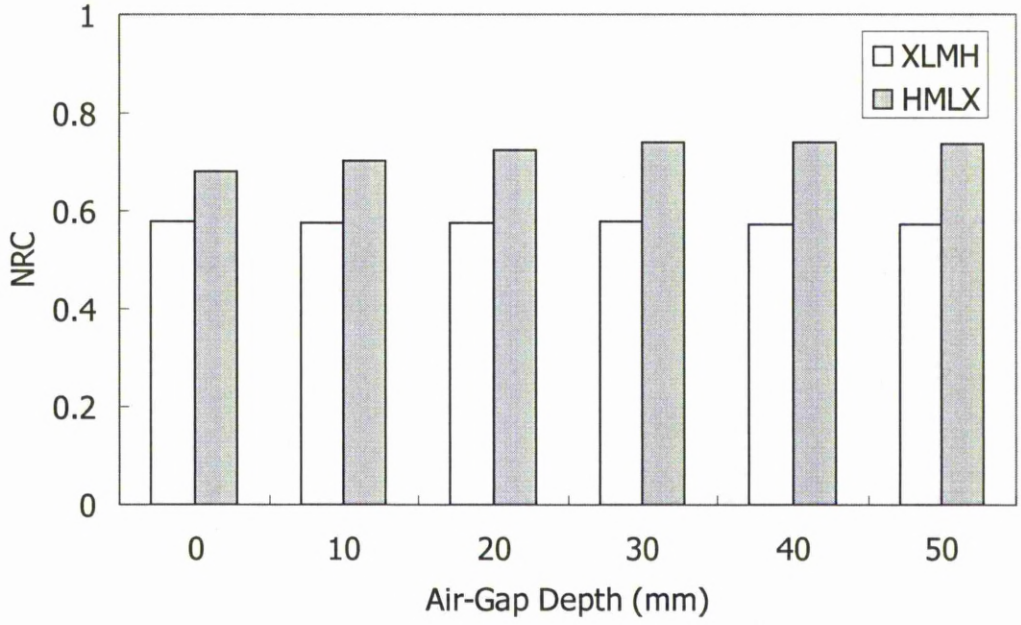

Figure 5.2.25 Variation of NRC with air-gap depth for four-layer assemblies with different nominal porosity orders. X-60%, L-65%, M-70%, H-75%.

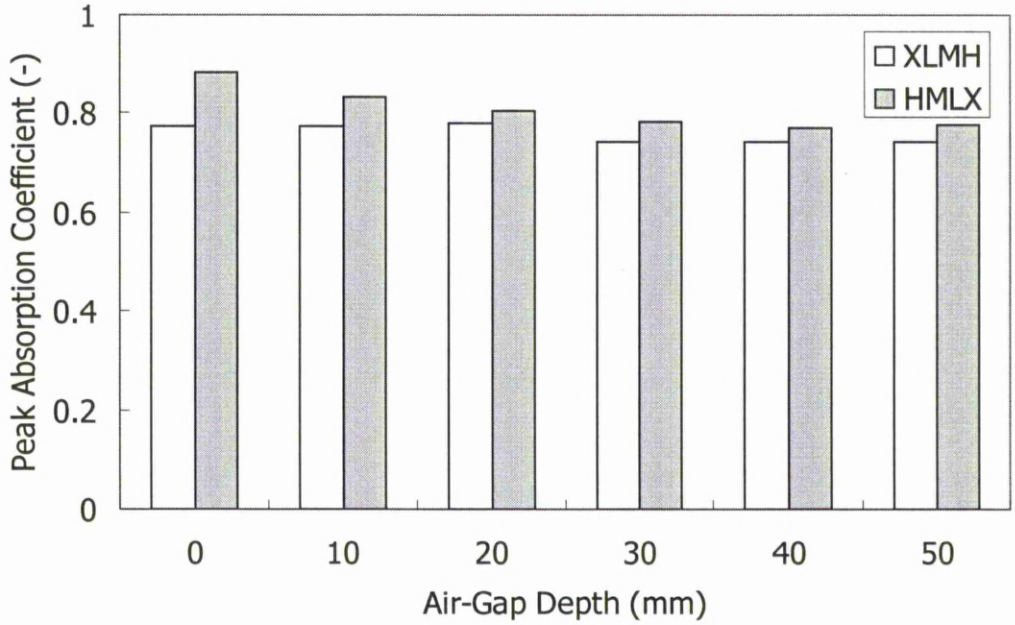

Figure 5.2.26 Variation of peak absorption coefficient with air-gap depth for four-layer assemblies with different nominal porosity orders. X-60%, L-65%, M-70%, H-75%.

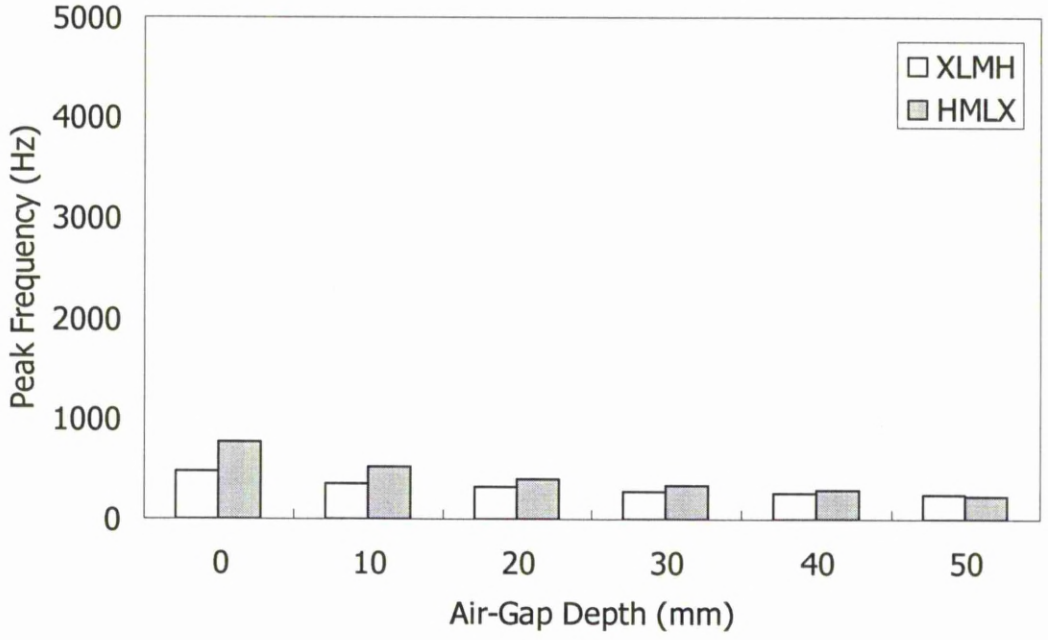

Figure 5.2.27 Variation of peak frequency with air-gap depth for four-layer assemblies with different nominal porosity orders. X-60%, L-65%, M-70%, H-75%.

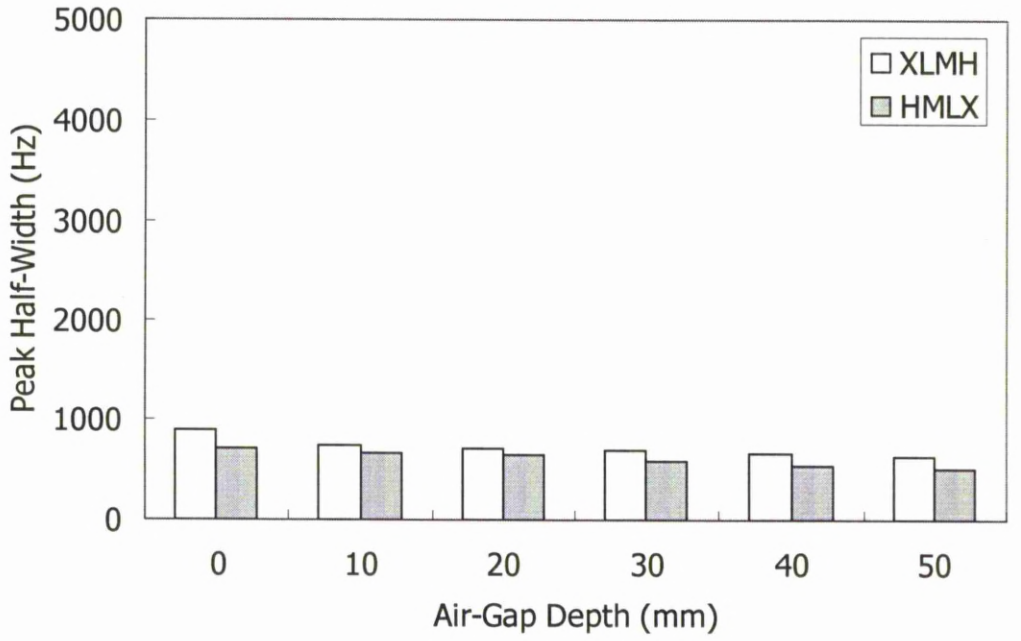

Figure 5.2.28 Variation of peak half-width with air-gap depth for four-layer assemblies with different nominal porosity orders. X-60%, L-65%, M-70%, H-75%.

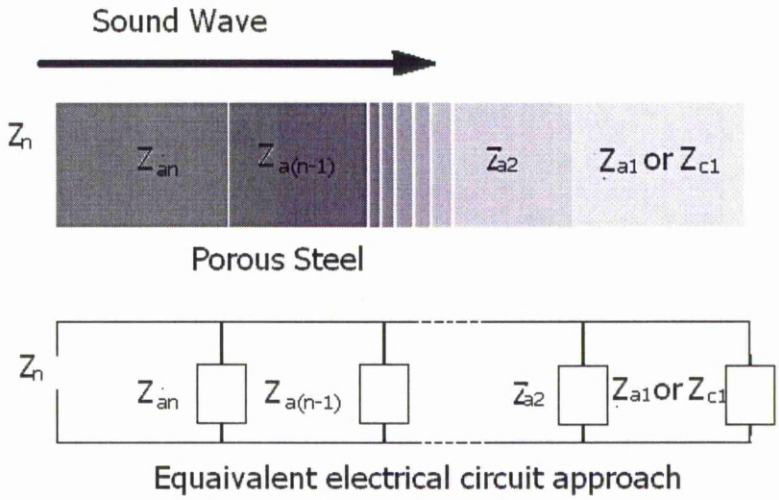

Figure 5.2.29 Schematic diagram showing EECA for sound absorption of multi-layer-assembled porous steel.

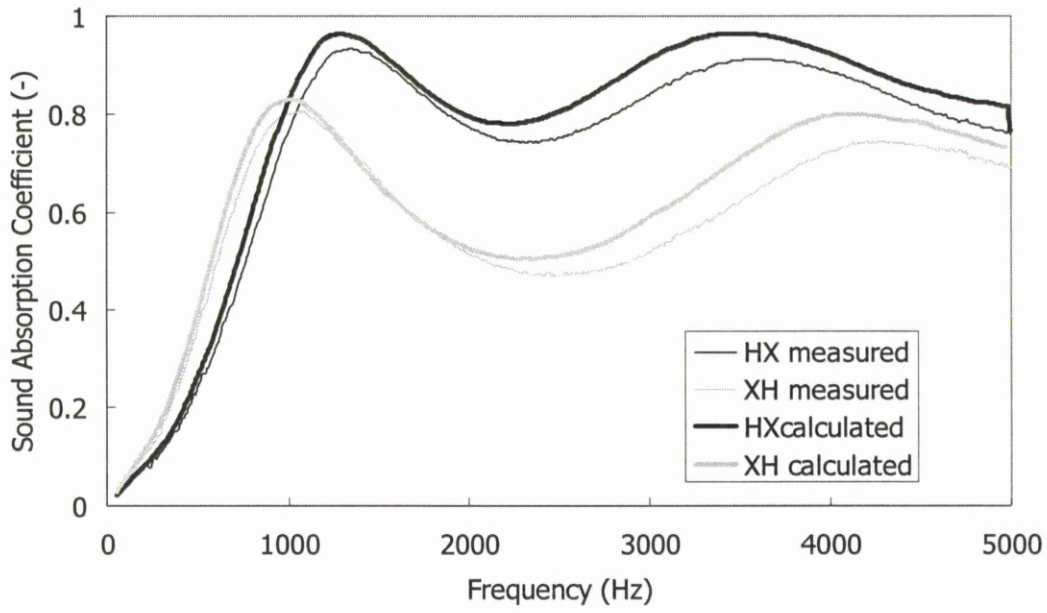

Figure 5.2.30 Calculated and measured sound absorption curves of open cell two-layer-assembled porous steel with different nominal porosities. X-60%, H-75%.

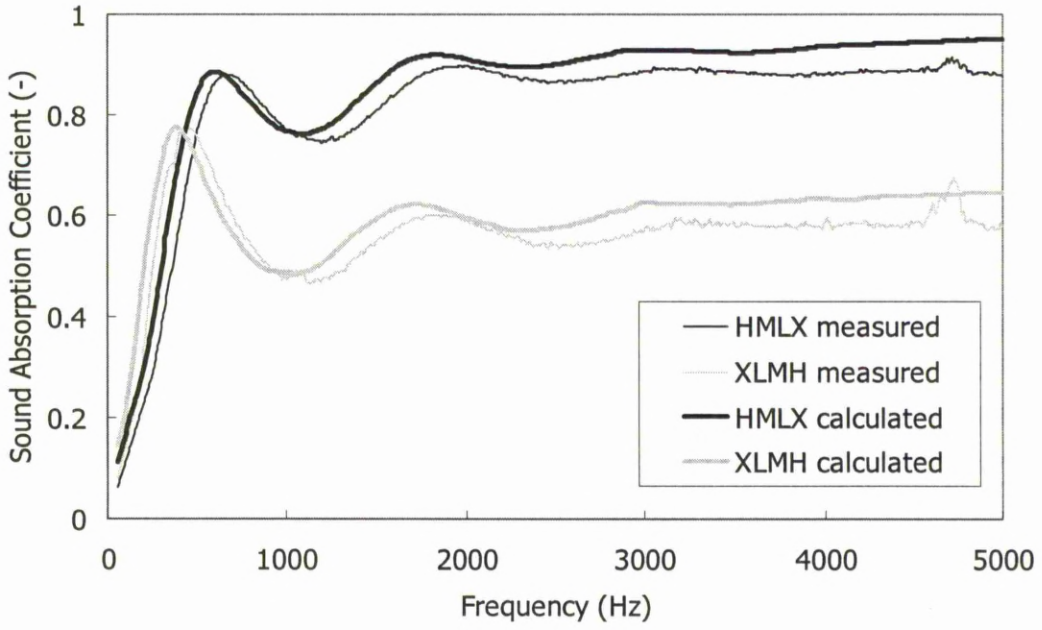

Figure 5.2.31 Calculated and measured Sound absorption curves of open cell four-layer-assembled porous steel with different nominal porosities. X-60%, L-65%, M-70%, H-75%.

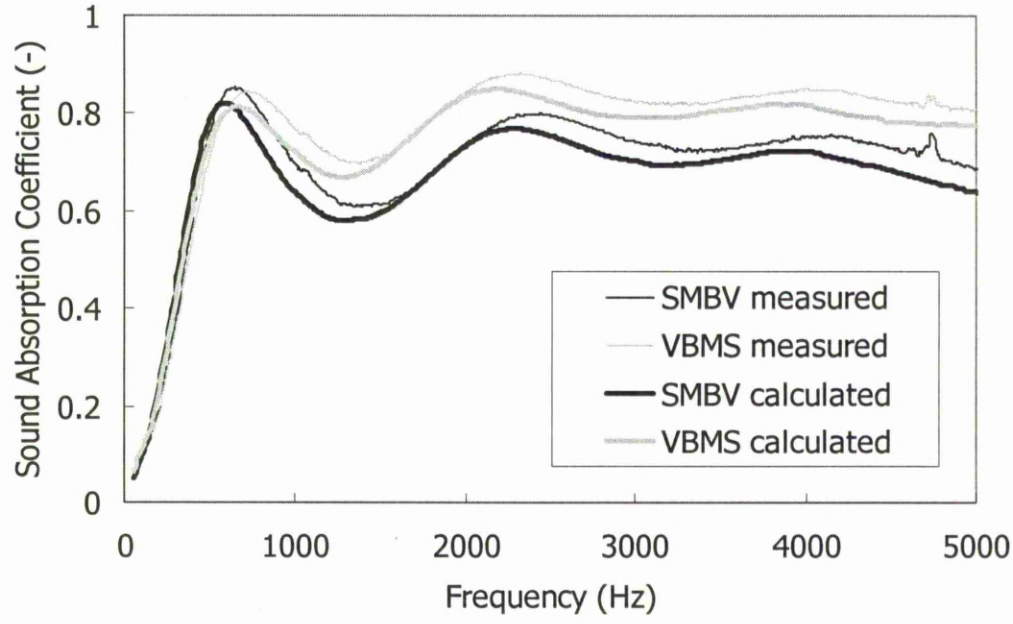

Figure 5.2.32 Calculated and measured sound absorption curves of open cell four-layer-assembled specimens with different pore sizes. S: 250-425μm, M: 415-710μm, B: 710-1000μm and V: 1000-1500μm.

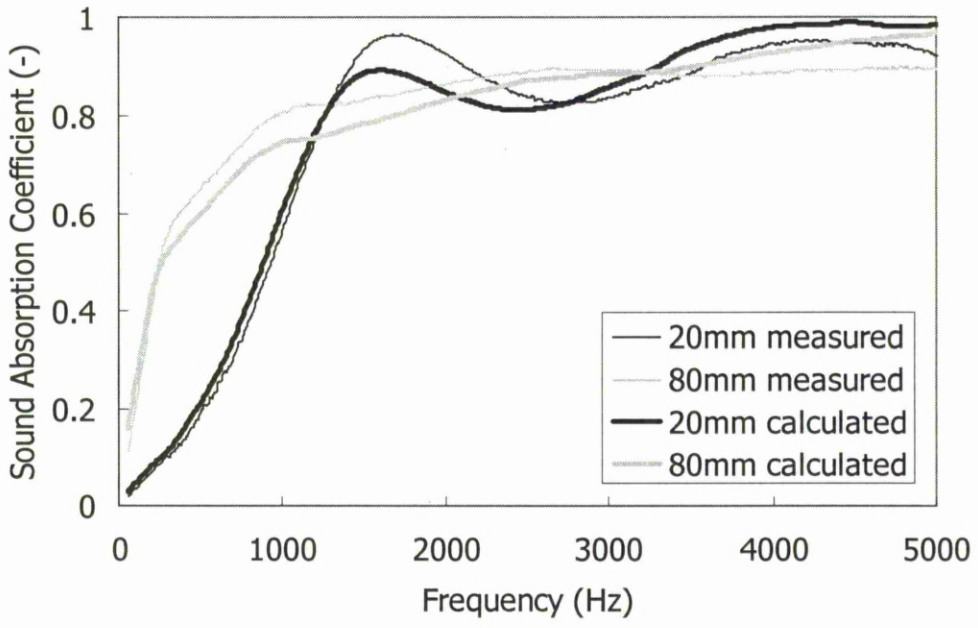

Figure 5.2.33 Calculated and measured sound absorption curves of open cell specimens with the order HMLX with different total thicknesses of 20mm and 80mm. X-60%, L-65%, M-70%, H-75%.

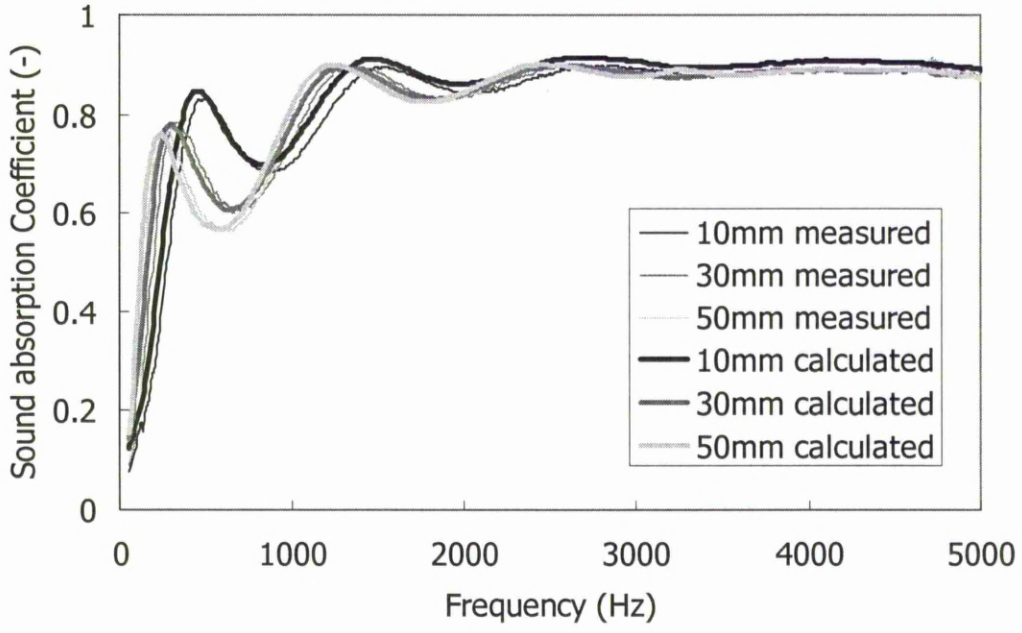

Figure 5.2.34 Calculated and measured sound absorption curves of open cell four-layer-assembled porous steel specimens with the order of HMLX and with different air-gap depths. X-60%, L-65%, M-70%, H-75%.

CHAPTER 6 CONCLUSIONS AND FUTURE WORKS

6.1 Conclusions

6.1.1 LCS process

Porous steel specimens with different pore structures have been manufactured using the LCS process via dissolution and decomposition routes under a range of conditions. The nominal relative density of the test specimens ranged between 0.25 and 0.4 and the pore size ranged between 250 and 1500 μm. The compaction pressure used in manufacturing the specimens ranged between 100 and 300MPa. In the dissolution route, the sintering temperature was 850°C and the sintering time was 4 hrs. In the decomposition route, the sintering temperature ranged between 950°C and 1100°C, and the sintering time ranged between 0.5 and 3 hrs.

The pore size and shape of the LCS porous steel closely match those of the K_2CO_3 particles. The pores have rough surfaces and are interconnected by interstices and voids. Porosities and pore sizes can be accurately controlled in the manufacturing stage, resulting in a porous structure with uniform pore distribution. The LCS process is highly controllable and efficient for producing high quality porous steel.

LCS porous steel displays a wide range of properties that can be exploited in a number of practical situations. It is the possibility of combining the structural, mechanical and acoustic properties that makes the material attractive for unique industrial applications.

6.1.2 Mechanical properties

Mechanical properties of the porous steel specimens manufactured by LCS via the dissolution and decomposition routes are measured and compared. The compressive strength, elastic modulus, and flexural strength of the porous steel increased with increasing relative density. Increasing the sintering temperature and time serves to increase the compressive strength, elastic modulus and flexural strength.

The scaling law was found to be applicable for compressive strength and elastic modulus as follow (Gibson & Ashby, 1988).

$$\frac{\sigma_C}{\sigma_S} = C\left(\frac{\rho}{\rho_S}\right)^n \tag{6.1}$$

$$\frac{E}{E_S} = C'\left(\frac{\rho}{\rho_s}\right)^{n'} \tag{6.2}$$

The values of the geometric constant C are all close to 0.3, not affected by pore size or sintering temperature. The values of the geometric constant C' are within 0.34-0.61 and increase with increasing pore size but are independent of sintering temperature. The values of the density exponents n and n' are within 1.2-2.6, and both increase with

decreasing pore size or sintering. In other words, pore sring temperature affect the property sensitivities to relative density.

The specimens manufactured by the decomposition retter mechanical properties than those manufactured by the dissolu The specimens manufactured by the re-sintering route have lower compexural strengths than the specimens manufactured by the decompos The specimens manufactured by the re-sintering route have lower elas than both the dissolution and decomposition routes.

6.1.3 Acoustic absorption properties

The acoustic absorption performance of LCS porousfactured by the dissolution route was assessed using the standing wave be method. The acoustic absorption coefficient has been measured betwd 5000Hz. The single layer specimens with a thickness of 10mm shoound absorption properties at high frequencies (>2KHz). This is mainly d frictional losses within the complex network of pores and interconnectinhe sintered steel particles, which form the pore wall, give rise to a unique surface, which contributes to the internal frictional and viscous losses. In gporosity leads to good sound absorption at low frequencies, and a high por good absorption at high frequencies. Varying pore size of the porous steelas no significant

effect on the sound absorption coefficient in the whole frequency range. Sound absorption at low frequencies can be improved by increasing the thickness of specimens, or by introducing an air gap behind the absorber. Increasing the thickness of specimen or the depth of the air gap behind the absorber shifts the sound absorption peak to lower frequencies

The sound absorption properties of the porous specimens of multi-layer assemblies with different porosities, pore sizes, thicknesses and air-gap depths have been assessed. The porosity of the first layer of multi-layer-assembled specimens has a critical effect on the sound absorption coefficient and frequency of peak. Increasing this porosity increases the sound absorption coefficient at all frequencies after the peak. The effects of the porosities of the subsequent layers are smaller. When the first layer has a high porosity, increasing the porosity of the second layer increases the frequency of peak. When the first layer has a low porosity, increasing the porosity of the second layer enhances the sound absorption coefficient of peak. The effects of pore size are not significant. Increasing the thickness of specimens and the depth of air-gap behind the specimens decreases the frequency and coefficient of the peak in the sound absorption curve.

The Equivalent Electrical Circuit Approach (EECA) is suitable for calculating the sound absorption properties of multi-layer assemblies. The calculated results are similar to the measured values at low frequencies but slightly higher than the measured values at high frequencies.

6.2 Future Work

The LCS porous steel specimens manufactured by the re-sintering route do not show any improvement in comparison with the specimens manufactured by the decomposition route although with additional sintering. They are inferior to the specimens manufactured by the other two routes. It appears there may be some residual potassium carbonate left in the samples, which may corrode the metal matrix. In the decomposition route, the liquid K_2O may also not be fully pushed out from the porous steel specimens and can damage the specimens. There is a need to study how clean the samples are, how to minimize the potassium carbonate or K_2O, and how to reduce the effect in the LCS porous steel. There are two possible approaches to improve the cleaning. One approach is to find a suitable chemical solvent to remove the potassium carbonate or K_2O without damaging the metal matrix. Another approach is to use a kind of steel powder which is not susceptible to the attack from potassium carbonate or K_2O.

The values of the geometric constant C' for elastic modulus for the LCS porous steel are much lower than those reported in the previous works, where the porous metals were produced by liquid state methods. This is probably because the LCS porous steels have many small pores in the cell-walls. Future work may investigate the feasibility of using steel powder with smaller particle sizes (< 45μm), together with higher sintering temperature (>1100°C) and longer sintering time (> 3 hrs) to reduce porosity in the metal matrix.

This thesis only studied the mechanical properties of LCS porous steel under static conditions. The applications of the LCS porous steel e.g. in vehicles as an energy absorber to protect the passengers in a crash, require the understanding of its dynamic behaviour. However, the strength, elastic modulus, and energy absorption of porous metal are sensitive to strain rate (Wang *et al*, 2001). There is a need to study the mechanical properties and energy absorption of LCS porous steel under impact by low (<4m/s) and high (10-40m/s) speed impact tests. Furthermore, porous metal sandwich structures showed good resistance to indentation (Gibson & Ashby, 1998). The behaviour of the LCS steel sandwich structure in compressive, three-point bending, impact, and indentation works are all in further studies.

Porous metals can be used for underwater sound absorption because of light weight and higher strength than traditional materials such as rubber (Wang, 2007). Whether LCS porous steels can be used as underwater sound absorbers or not remains unclear, because the impedance mismatch on the surface between the porous metal and water is usually greater than that with air. For the LCS porous steel to be used as an underwater sound absorber, the effects of porosity, pore size, thickness and water-gap depth on sound absorption characteristics under water need to be studied. The ultrasonic and infrasonic wave absorption characteristics of LCS porous steel can also be studied in the future.

REFERENCES

Adler J, Standke G, Stephani G, (2004), Sintered open-celled metal foams made by replication method - manufacturing and properties on example of 316L stainless steel foams, Proceedings of the Symposium on Cellular Metals and Polymers (CMaP). Deutsche Forschungsgemeinschaft (DFG), 12-14 October, Fürth, Germany, pp89-92.

Ahmed Y. M. Z, Iskander B. A, Ibrahim M, Shalabi M. E. H., (2009), Mechanical properties and porosity relationship of porous iron compacts, Powder Metallurgy, 52, No. 1.

Albracht F., Lotze G, (1999), Acoustical investigation of sintered highly porous metal fibre structures as sound absorbers, J. of Appl. Phys. 32, pp 22-29.

Allard J. F, (1993), Propagation of sound in porous media, modeling sound absorbing materials, New York: Elsevier Applied Science.

Apprill G. M, Poirier D. R, Maguire M. C, Gutsch T. C, (1998), Porous and cellular materials for structural applications, In: Schwartz D. S, Shih D. S, Evans A. G, Wadley H. N. G, editors. MRS Symp. Proc., vol. 521, pp 291.

Ashby M. F, (1983), The mechanical properties of cellular solids, Metall. Trans. A14, pp 1755-1757.

Ashby M. F, Evans A. G, Fleck N. A, Gibson L. J, Hutchinson J. W, Wadley H.N.G, (2000), Metal foams: a design guide, Boston: Butterworth–Heinemann, Oxford.

Asholt P, (1999), Metal foams and porous metal structures. In: Banhart J, Ashby M. F, Fleck N. A, editors. Int. Conf., Bremen, Germany, 14–16 June. Bremen: MIT

Press–Verlag, pp 133.

Babcsan N, Banhart J, Leitlmeier D,(2003), Metal foams – manufacture and physics of foaming, International Conference "Advanced Metallic Materials" 5-7, Smolenice, Slovakia.

Banhart J, Baumeister J, Weber M, (1995), Proceedings of the European conference on Advanced Materials, (PM '95), Birmingham, UK, 23–25 October 1995.pp 201.

Banhart J, Baumeister J, (1998), Deformation characteristics of metal foams, J Mater Sci 33, pp 1431-1440

Banhart J, Ashby M.F, and Fleck N.A, (1999), Metal foams and porous metal structures ,Bremen, Germany: MIT-Verlag

Banhart J, (2001), Manufacture, characterization and application of cellular metals and metal foams, Progress in Materials Science 46.

Banhart J, Ashby M.F, Fleck N.A, (2001), Cellular Metals and Metal Foaming Technology, MIT-Verlag Bremen and Special Issue of Adv. Eng. Mat. 2002, 4 (10).

Banhart J, Fleck N, Mortensen A, (2003), Cellular metals and manufacture properties applications, Metfoam 2003,

Baumeister J,(2010), Methods for filling hollow structures with aluminium foam, Materials science forum, . 638-642, pp 61-66.

Baumgartner F, Gers H, (1999), Metal foams and porous metal structures. In: Banhart J, Ashby M. F, Fleck N. A, Editors. Int. Conf., Bremen, Germany, 14–16. Bremen: MIT Press–Verlag, pp 72-73.

Baumgartner F, Duarte I, Banhart J, (2000), Industrialization of powder compact foaming process, Advanced Engineering Materials, 2:168.

Bell L. H, (1982), Industrial noise control, New York: Marcel Dekker, pp 199-205,

Beranek L. L, Ver I. L, (1992), Noise and vibration control engineering [M]. New York: John Wiley and Sons, pp 232-243.

Berg A, Maysenholder W, Heasche M,(2003), Noise reduction of open-pore aluminum foams, Cellular metals: manufacture, properties, Applications, by Banhart J, Fleck N. A, Mortensen A, MIT-Verlag.

Berrymann J. G, (1980), Confirmation of Biot's theory, Appl. Phys. Lett. 37, pp 382–384.

Biot M. A, (1956a), Theory of propagation of elastic waves in a fluid-saturated porous solid: I. Low frequency range, J. Acoust. Soc. Am. 28, pp 168–178

Biot M. A, (1956b), Theory of propagation of elastic waves in a fluid-saturated porous solid: II: High frequency range, J. Acoust. Soc. Am. 28, pp 179–191.

Biot M.A,(1962), Generalized theory of acoustic wave propagation in porous dissipative media, J. Acoust. Soc. Am. 54, pp 1254–1264.

Bjorksten J, Rock E. J, (1972), Method for foaming Metals, US Patent 3707367.

Blot M. A, (1956), Theory of propagation of elastic waves in a fluid-saturated porous solid. 1. Low-frequency range, J. Acoust. Soc. Am. 28, pp168-178.

Bram M, Stiller C, Buchkremer H. P, Stover D, Bauer H, (2000), Advanced engineering materials, 2:196.

Bray H, (1972), Design opportunities with metal foam, Engineering Materials and Design, Volume **16**, Issue 1, pp 19.

Brennan M. J, To W. M, (2001), Acoustic properties of rigid-frame porous materials -an engineering perspective, Appl. Acoust. 62 793.

Capus J.M, (2000), Metal Powders: A Global Survey of Production, Applications and Markets, Metal Powder Industries Federation (MPIF), 3rd edition.

Carman P. C, (1937), Fluid flow through granular beds, Trans. Inst. Chem. Eng. 15, pp150–166.

Carter V. E, (1977), Metallic coating for corrosion control, Butterworths, London.

Champou Y, Stinson M. R, (1991), On acoustical models for sound propagation in rigid frame porous materials and the influence of shape factors, J. Acoust. Soc. Am., 92, No. 2, Pt. 1.

Chen F, He D, (1999), Preparation, structure control and acoustic properties of porous aluminium with open cells, Metal foams and porous metal structures. In: Banhart. J, Ashby M: F, Fleck N. A, editors. Int. Conf., Bremen, Germany. Bremen: MIT Press–Verlag. pp 162-163.

Christensen, R.M., (1986), Mechanics of low density materials. J. Mech. Phys. Solids 34 (6), pp 563–578.

Clark J. L, Hurysz K. M, Lee K. J, Cochran J. K, Sanders T. H,(1999),Stainless steel sphere foams-fabrication, carburization, and properties, Metal foams and porous metal structures. In: Banhart J, Ashby M. F, Fleck N. A, editors. Int. Conf., Bremen, Germany. Bremen: MIT Press–Verlag. pp 170-171.

Davern W. A, (1977), Perforated facings backed with porous materials as sound absorbers-an experimental study, Applied Acoustics 10, pp 85-112.

Davies G. J, Zhen S, (1983), Metallic foams: their production, properties and applications, Chapman and Hall Ltd.

Degischer H. P, Kriszt B, (2002), Handbook of cellular metals, production, processing, applications, Wiley-VCH, Berlin.

Delany M. E., Bazley E. N,(1970), Acoustic properties of fibrous absorbent material, Applied Acoustics 3, pp 105-116.

Dilley D. C., (1974), Foametal - Its properties and applications, Mach. Prod. Eng. 125.

Drolet, J. P., (1977), Low density foams produced from aluminium powders, The International Journal of Powder Metallurgy & Powder Technology, 13(3), pp 221-225

Du G, Zhu Z, Gong X, (2001) The theory of sound [M], P.R.China: Nanjing University Press, pp116-163.

Dunn I. P, Davern W. A, (1986), Calculation of acoustic impedance of multi-layer absorbers, Applied Acoustics 19, pp 321-334.

Eisenmann M, (1998), Metal powder technologies and applications, ASM Handbook, vol. 7. Materials Park, USA: ASM International, pp 1031.

Elliot J. C, (1956), Method of producing metal foam, US Patent No. 2,751,289.

Ettel V. A, (1998), New Inco powders and foams for nickel batteries, NiVad 98, Prague.

Evans E. J, Bazley E. N, (1964), Sound absorbing materials, H.M.S.O., London.

Everest F. A, (2001), Master handbook of acoustics, 4th Ed, McGraw-Hill, New York.

Fazekas A, Dendiecel R, Salvo L, Brechet Y, (2002), Effect of microstructural topology upon the stiffness and strength of 2D cellular structures, Int J. Mech. Sci 44, pp 2047-2066.

Foroughi B, Degischer H.P, Kottar A, (2009), Simulation of deformation and damage of non-uniform cellular aluminium, Metfoam 2009.

Friedl O, Motz C, Peterlik H, Puchegger S, Reger N, and Pippan R, (2007), Experimental investigation of mechanical properties of metallic hollow sphere structures, Metallurgical and Materials Transactions B. 39(1), pp 135-146.

Garboczi, E.J, Day, A.R., (1995), An algorithm for computing the effective linear elastic properties of heterogeneous materials: three-dimensional results for composites with equal phase Poisson ratios, J. Mech. Phys. Solids 43, pp 1349–1362.

Gardner A. R, (1967), Transparent Plastics Open New Windows on Products, Product Engineering, pp 66-69.

Golovin I. S, Sinning H. R, (2004), Internal friction in metallic foams and some related cellular structures, Materials Science and Engineering A 370, pp 504-511.

Gibson L.J, Ashby M.F, (1982), The mechanics of three-dimensional cellular materials, Proc. R. Soc. Lond. A 382, pp 43-59.

Gibson L.J, Ashby M.F, (1988), Cellular solids: structure and properties, Pergamon Press, Oxford.

Gibson L. J, Ashby M. F, (1997), Cellular solids: structure and properties, 2nd edn, Cambridge University Press, Cambridge, UK, Chapter 7.

Goodall R, Despois J. F, Salvo L, Mortensen A, (2007), Replicated microcellular aluminum with spherical pores: Processing and influence on properties. Materials Science and Engineering: A Volume 465, Issues 1-2, 15 September, pp 124-135.

Hagiwara H, Green D. J, (1987), Elastic behaviour of open-cell alumina, J. Am. Ceram. Sor., 70 [11], 811-15

Han F, Cheng H, Wang J, Wang Q, (2003), Effect of pore combination on the mechanical properties of an open cell aluminium foam, Scripta Materialia 50, pp 13-17.

Han F, Seiffert G, Zhao Y, Gibbs B,(2003), Acoustic absorption behaviour of an open-celled aluminium foam, J Phys D: Appl Phys, 36, pp 294–302.

Han F, Zhu Z, Gao J, (1998), Compressive deformation and energy absorbing

characteristic of foamed aluminum, Metallurgical and materials transactions A, Volume 29A, pp 2497-2502.

Harris C. M, (1979), Handbook of noise control, New York: McGraw- Hill.

Hartmann M, Reindel K, Singer R. F, (1998), Porous and cellular materials for structural applications, In: Schwartz DS, Shih DS, Evans AG, Wadley HNG, editors. MRS Symp. Proc., 521, pp 210-211.

Hoganas, (2002), Hoganas Handbook of iron and steel powder.

Hintz C, Wagner I, Sahm P. R, Stojanov P,(1999), Investment cast near-net-shape components based on cellular metal materials, Metal foams and porous metal structures. In: Banhart J, Ashby M. F, Fleck N. A, editors. Int. Conf., Bremen, Germany, 14–16 June. Bremen: MIT Press–Verlag. pp 150-153.

Huang Q, (1999), Noise control in engineering [M], Wuhan: HUST express.

Hubbert M. K, (1956), Darcy's law and the field equations of the flow of underground fluids, Petroleum, Transaction, AIME, 207, pp 222–239.

Hyun S. K, Nakajima H, (2002), Anisotropic compressive properties of porous copper produced by unidirectional solidification, Mat. Sci. & Eng. A 340, pp 258-264.

Ingard U, (1953), Perforated facing and sound absorption. Journal of the Acoustical Society of America, 26(2), pp 151–154.

Instron Handbook, http://www.testresources.com/kw10_instron/instron_0616g1.aspx

Irwin J. D, Graf E .R, (1979), Industrial noise and vibration control, Englewood Cliffs, NJ: Prentice-Hall.

Ismail L, Ghazali M. I, Mahzan S, Zaidi A. M. A, (2010), Sound Absorption of Arenga Pinnata Natural Fiber, World Academy of Science, Engineering and Technology 67.

Jeon Y.P, Kang C. G, Lee S. M, (2009), Effects of cell size on compression and bending strength of aluminum-formed material by complex stirring in induction heating, Journal of Materials Processing Technology 209, pp 435-444.

Jinkyo L, George W, Swenson J, (1992), Compact sound absorbers for low frequencies, Noise Control Engineering Journal 38, pp 109-117.

John B, (2001), Manufacture, characterization and application of cellular metals and metal foams, Progress in Materials Science 46, pp 559–632

Kovacik J, Tobolka P, Simancik F, (1999), Noice attenuation using aluminum foams, Metal foams and porous metal structures. In: Banhart J, Ashby M. F, Fleck N. A, editors. Int. Conf., Bremen, Germany, 14–16 June. Bremen: MIT Press–Verlag. pp 405-406.

Kunze H. D, Baumeister J, Banhart J, Weber M, (1993), P/M technology for the production of metal foams, Powder Metall Int **25**, pp 182.

Kwan Y. B. P, Stephenson D. J, Alcock J. R, (2000), The porosity dependence of flexural modulus and strength for capsule-free hot isostatically pressed porous alumina, Journal of Materials Science, Volume 35, Number 5, pp 1205-1211.

Lavernia E.J, Grant N. J, (1988), Spray deposition of metals: a review, Materials Science and Engineering, 98, pp 381-390.

Lee F, Chen W,(2001),Acoustic transmission analysis of multi-layer absorbers, Journal of Sound and vibration, 248(4), pp 621-634

Lefebvre L P, Banhart J, Dunand D. C, (2008), Porous metals and metallic foams: current status and recent developments, Advanced Engineering Materials, No. 9.

Lenel F. V, (1980), Powder metallurgy: principles and applications, Metal Powder Industries Federation. Princeton, NewJersey, pp 240-241.

Li C, Zhu Z, (2006), Dynamic Young's modulus of open-porosity titanium measured by the electromagnetic acoustic resonance method, J Porous Mater 13, pp 21–26.

Liu P.S, (2010), Mechanical relations for porous metal foams under several typical loads of shearing, torsion and bending, Materials Science and Engineering A 527, pp 7961–7966.

Lu M, Hopkins C, Zhao Y. Y, Seiffert G, (2009), Sound Absorption Characteristics of Porous Steel Manufactured by Lost Carbonate Sintering, Materials Research Society 2009, Mater. Res. Soc. Symp. Proc. Vol. 1188.

Lu M, Zhao Y. Y, (2010), Mechanical properties of LCS porous steel, Supplement proceedings: Volume 2, TMS, 2010.

Lu T. J, Hess A, Ashby M. F, (1999), Sound absorption in metallic foam, J. Appl. Phys. 85, No. 11, pp 7528-7539.

Lu T. J, Chen F, He D, (2000), Sound absorption of cellular metals with semi open cells. J Acoustic Soc Am, 108, pp 1697–709.

Ma D, (1983), Noise control science, China science, pp 355-358.

Ma L, Song Z,(1998), Cellular structure control of aluminium foams during foaming process of aluminium melt, Scripta Materialia, 39, No. 11, pp 1523–1528.

Meller M.A, (1925), Produit métallique pour l'obtention d'objets laminés, moulés ou autres, et procédés pour sa fabrication, French Patent 615.147.

Morse P. M, (1948), Vibration and sound, McGraw-Hill, New York.

Morse P. M, Ingard K. U, (1968), Theoretical acoustics. Princeton, chapter 6.

Mukai T, Kanahashi H, Miyoshi T, Mabuchi M, Nieh T. G, Higashi K, (1999), Experimental study of energy absorption in a close-celled aluminum foam under dynamic loading, Scripta Materialia, Vol. 40, No. 8, pp 921–927.

Munjal M. L, (1987) Acoustics of ducts and mufflers with application to exhaust and ventilation system design, 53-88. New York: John Wiley and Sons, Chapter 2.

Nakajima H, Kanetake N, (2006), Porous Metals and Metal Foaming Technology, The Japan Institute of Metals, Sendai and Special Issue of Adv. Eng. Mat. 2006, 8 (9).

Neumann P, (1999), Porous metal structures made by sintering: process and application, Metal foams and porous metal structures. In: Banhart J, Ashby M. F, Fleck N. A, editors. Int. Conf., Bremen, Germany, 14–16 June. Bremen: MIT Press–Verlag. pp 167-169.

Niebylski L. M, Jarema C. P, Immethun P. A, (1974), Metal Foams and Process Therefore, in U.S. Patent 3,794,481.

Norris A. N, (1986), On the Viscodynamic operator in biot's equations of poroelasticity, J. Wave Mater. Interact. 1, pp 367-379.

Park C, Nutt S. R, (2000), PM synthesis and properties of steel foams, Materials Science and Engineering, A288, pp 111–118.

Prakash O, Sang H, Embury J.D, (1995), Structure and properties of Al---SiC foam, Mater Sci Eng A 199, pp 195.

Pizzirusso J, (1981), Acoustic of plastic foam, Mach. Des. 53, pp 135-137.

Plona T, (1980), Observation of a second bulk compressional wave in a porous medium at ultrasonic frequencies, Appl. Phys. Lett. 36, pp 259–261.

Qiao J, Xi Z, Tang H, Wang J, Zhu J, (2009), Mechanical properties of porous stainless steel metal fibre media, Materials Science Forum, 618-619, pp 109-112.

Queheillalt D. T, Sypeck D. J, Wadley H. N, (2002),Ultrasonic characterization of cellular metal structures, Materials Science and Engineering A323, pp138-147.

Rabiei A, Vendra L J, (2009), A comparison of composite metal foam's properties and other comparable metal foams, Materials Letters 63, pp 533-536.

Rezanezhad F, Quinton W. L, Price J. S, Elrick D, Elliot T. R, Heck R. J, (2009), Examining the effect of pore size distribution and shape on flow through unsaturated peat using 3-D computed tomography, Hydrol. Earth Syst. Sci. Discuss., 6, pp 3835–3862.

Rice R. W, (1996 a), Comparison of physical property-porosity behavior with minimum solid area models, Journal of Materials Science 31, pp1509-1528.

Rice R. W, (1996 b), Evaluation and extension of physical property-porosity models based on minimum solid area, Journal of Materials Science. 31, pp 102-118.

San Marchi C, Mortensen A, (2001), Deformation of open-cell aluminum foam, Acta Mater 49, pp 3959.

Santosa S, Wierzbicki T, (1998), Crash behavior of box columns filled with aluminum honeycomb or foam, Computers and Structures 68, pp 343-367.

Silva M. G, Ramesh K. T, (1997), The rate-dependent deformations of porous pure iron, Int J Plast 13, pp 587.

Simone A. E, Gibson L. J, (1998), Aluminum foams produced by liquid-state processes, Acta Materialia, Volume 46, Issue 9, 22 May, pp 3109-3123.

Shapovalov V. I, (1998), Porous and cellular materials for structural applications, In: Schwartz D. S, Shih D. S, Evans A. G, Wadley H. N. G, editors. MRS Symp. Proc., vol. 521, pp 281.

Silva M. G, Ramesh K. T, (1997), The rate-dependent deformations of porous pure iron, International Journal of Plasticity, 13, Nos. 6-7, pp 587-610.

Stiller C, Buchkremer H. P, Joos R, Stover D, Nelles H, (1998), Manufacturing and characterization of low density titanium parts, Proc. 1998 PM World Congress, European Powder Metallurgy Association. vol. 5, pp 189.

Stinson M. R, (1991), The Propagation of plane sound waves in narrow and wide circular tubes, and generalization to uniform tubes of arbitrary cross-sectional shape, J. Acoust. Soc. Am. 89, pp 550-558.

Stinson M. R, Champoux Y, (1992), Propagation of sound and the assignment of shape factors in model porous material shaving simple pore geometries, J. Acoust. Soc. Am. 91, pp 685-695.

Sun D, Zhao Y, (2003), Static and dynamic energy absorption of Al foams produced by the sintering and dissolution process, Metall Mater Trans 34B, pp 69-74.

Tao X. F, Zhang L. P, Zhao Y. Y, (2007) Mechanical response of porous copper manufactured by Lost Carbonate Sintering process, Materials Science Forum Vols. 539-543, pp 1863-1867.

Takemoto M, Fujibayashi S, Neo M, Suzuki J, Kokubo T, Nakamura T, (2005), Mechanical properties and osteoconductivity of porous bioactive titanium, Biomaterials. 2005 Oct; 26(30): 6014-23.

Tao X, Zhang L, Zhao Y, (2007), Mechanical response of porous copper manufactured by the lost carbonate sintering method, Mat. Sci. Forum. 539-543, pp 1863-1867.

Theis E, (2002), Flattening solutions and the anatomy of a bend in flat-rolled metals, Coil Processing Article, http://www.thefabricator.com/article/coilprocessing.

Thewsey D. J, (2009), Multifunctionality of porous copper manufactures by lost carbonate sintering, Thesis for the degree of PhD, University of Liverpool.

Thiele W, (1972), Aluminium foam used as an impact energy absorbing material. Met Mater 8, pp 349–351.

Thornton P. H, Magee C. L, (1975), The deformation of aluminum foams, Metall Trans A **6**, pp 1253.

Wang X, Lu T, (1999), Optimized acoustic properties of cellular solids, J. Acoust. Soc. Am. 106 756.

Wang B, Klepaczko J. R, Lu G, and Kong L. X, (2001), Viscoplastic behavior of porous bronzes and irons, J Mater Process Technol 113, pp 574.

Wang X, (2007), Porous metal absorbers for underwater sound, J. Acoust. Soc. Am., Vol. 122, No. 5, pp 2626–2635.

Warren, W.E., Kraynik, A.M., (1997), Linear elastic behavior of a low density Kelvin foam with open cells. J. Appl. Mech. 64, pp 787–794.

Wassilieff C, (1996), Sound absorption of wood-based materials Applied Acoustics, Vol. 48, No. 4, pp 339-356.

Wen C, Yamada Y, Shimojima K, Chino Y, Asahina T, Mabuchi M, (2002), Processing and mechanical properties of autogenous titanium implant materials, Journal of Materials Science: Materials in Medicine, 13, Number 4, pp 397-401.

Wen C.E, Yamada Y, Asahina T, Kato K, Sonoda T, Watazu A, Sonoda, T, Watazu, A, Mabuchi, M, (2004), Effects of the Density on Compressive Properties in Cellular Aluminum Produced by the Sintering Method, Mater Trans 45, pp 327.

Wu J, Li C, Wang D, Gui M, (2002), Damping and sound absorption properties of particle reinforced Al matrix composite foams, Composites Science and Technology 63, Issues 3-4, pp 569-574.

Wu Q, (1988), Empirical relations between acoustic properties and flow resistivity of porous plastic open-cell foam, Applied Acoustics 25, pp 141-148.

Xie Z. K, Ikeda T, Okuda. Y, Nakajima H, (2004), Sound absorption characteristics of lotus-type porous copper fabricated by unidirectional solidification, Mater Sci Eng, pp 386-390.

Yamada Y, Shimojima K, Sakaguchi Y, Mabuchi M, Nakamura M, Asahina T, Mukai T, Kanahashi H, Higashi K, (2000), Processing of Cellular Magnesium Materials, Advanced Engineering Materials 2000.2, No. 4.

Yarnton D, Davies T. J, (1963), The Effect of Lubrication on the Pressing of Metal Powder Compacts", Powder Met., Vol. 6. pp 130-152.

Zhang B, Chen T, (2009), Calculation of sound absorption characteristics of porous sintered fibre metal, Applied Acoustics 70, pp 337-346.

Zhang E, Wang B, (2004), On the compressive behaviour of sintered porous coppers with low to medium porosities-part1: experimental study, Int J. of mech. Sci. 47, pp 744-756.

Zhang L, Zhao Y, (2007), Fabrication of high melting-point porous metals by lost carbonate sintering process via decomposition route, Journal of Engineering Manufacture, 222, pp 267-271.

Zhao Y, Sun D, (2001), A Novel sintering-dissolution process for manufacturing Al foams, Scr. Mater. 44, pp 105-110.

Zhao Y, Fung T, Zhang L, (2005), Lost carbonate sintering process for manufacturing metal foams, Scripta Materialia, 52, pp 295-298.

Zhu C, Huang Q, (2005), A method for calculating the absorption coefficient of a multi-layer absorbent using the electro-acoustic analogy, Applied Acoustics 66, pp 879–887

Zhu, H. X, Knott, J. F, Mills, N. J, (1997). Analysis of the elastic properties of open-cell foams with tetrakaidecahedral cells. J. Mech. Phys. Solids 45, pp 319–343.

Zhu M, Chung D. D. L, (1991), Resilient composite of silicone and foamed tin as a new material for electrical and thermal contacts, COMPOSITES. 22. number 3, 219.

Zhou H, Li B, Huang G, (2006), Sound absorption characteristics of polymer micro-particles, JOURNAL OF APPLIED POLYMER SCIENCE VOL 101; NUMBER 4, pp 2675-2679.

Zwikker C, Kosten C. W, (1949), Sound Absorbing Materials, Elsevier, New York.